Universitat Autònoma de Barcelona

Ruthenium and Platinum Nanoparticles For Artificial Photosynthesis

Luis Ignacio Álvarez Prada

Universitat Autònoma de Barcelona

Ruthenium and Platinum Nanoparticles For Artificial Photosynthesis

Luis Ignacio Álvarez Prada

PhD Thesis

Programa de Doctorat en Química

Supervisors:

Dr. Lluís Escriche, Dr. Nuria Romero & Dr. Jordi García-Antón

Tutor:

Dr. Xavier Sala Román

Departament de Química

Facultat de Ciències

2021

Memòria presentada per aspirar al Grau de Doctor en Química per:

Luis Ignacio Álvarez Prada

Vist i plau

Directors:

Dr. Jordi García-Antón Aviñó Dr. Nuria Romero Fernández Dr. Lluís Escriche Martínez

Tutor:

Dr. Xavier Sala Román

Departament de Química
Facultat de Ciències
Universitat Autònoma de Barcelona

Bellaterra, 28 de Juliol de 2021

Table of contents

Aknowledgements/Agradecimientos

Me gustaría empezar agradeciendo a mis directores, el Dr. Lluís Escriche, la Dr. Nuria Romero y el Dr. Jordi García-Antón, sin los cuales no hubiera podido llevar a cabo esta tesis. Gracias Lluís por tu buen humor, lecciones vitales y por el puesto de doctorando privilegiado. Jordi y Nuria por toda su ayuda dentro y fuera del laboratorio, y por guiarme tan bien que solo os ha faltado escribirme la tesis. El doctorado se ha hecho largo y duro por momentos, pero nunca me he sentido solo y os estaré agradecido siempre por ello.

Mencionar también al resto del núcleo de SelOxCat. A Xavi por acogerme en su grupo y por todo lo que he aprendido de él en este tiempo. Y a Roger, sus ocurrencias, sus aportes, y por supuesto por la inmersión lingüística nada más poner un pie en Barcelona. Moltes gràcies per tot. Y a toda la gente que ha ido pasando por el grupo, desde los (por entonces) veteranos Marcos, Jonathan, Jordi, Rosa y Bing, hasta Laura, Heting, Gerard, y todos los estudiantes de TFG y TFM. Pocos sitios con tan buen ambiente para trabajar como ese laboratorio.

Tampoco quiero olvidarme del resto de doctorandos del departamento, que también han colaborado en el buen recuerdo que me llevo de estos años, ya sea en pausas de café, congresos o en prácticas. Merche, no me puedo ni imaginar la aburrida línea temporal en la que no hubiéramos sido vecinos de labo. Anna, ha sido un honor compartir el título de doctorando emérito (o eterno) contigo.

Aprovecho para extender mi gratitud a toda la gente involucrada en este trabajo, desde los colaboradores en los diferentes proyectos hasta los servicios técnicos de la UAB (Servei d'Anàlisi Química (SAQ) i el Servei de Difracció de Raigs X (SDRX). También Al Prof. Santiago Suriñach por su ayuda con los TGA. Al Dr. Guillaume Sauthier (ICN2) por su paciencia con los XPS. Quisiera acordarme especialmente del Servei de Microscòpia Electrònica de la UAB, el segundo sitio donde más tiempo he pasado en el campus. Gracias a Martí, Emma y Àlex por toda la ayuda en esas incontables sesiones de TEM. Por supuesto al personal de administración del Departamento de Química, por todo el trabajo y el papeleo que les he dado en estos años.

I cannot forget to mention Dr. Karine Philippot, who welcomed me into her laboratory and allowed me to return two other times. Thanks to all Equipe L from the LCC-CNRS in Toulouse, especially Rosa, Sam, Elena and Miquel for their hospitality and help in each of my visits.

También quiero mencionar a la Dr. Zoraida Freixa y al Dr. Miguel Huertos que, durante mis estudios de máster en la UPV/EHU, fueron determinantes en que prosiguiera mi carrera investigadora con estos estudios de doctorado.

Por ultimo, y casi lo más importante, agradecer a mis padres el haber tenido siempre la suficiente confianza en mí como para darme la libertad de hacer lo que quisiera, sin cuestionarme. Siento mamá que no vayas a poder leer estas palabras. Si hoy presento esta tesis es gracias a vosotros. Un recuerdo especial al resto de mi familia y amigos en Gijón, porque no importa los tumbos que dé por el mundo ni lo desconectado que esté, siempre siguen ahí.

The work performed in the present doctoral thesis has been possible thanks to the funding of Ministerio de Economía y Competitividad and Ministerio de Ciencia, Innovación y Universidades, through Projects: CTQ2015-64261-R (MINECO, FEDER-UE) and PID2019-104171RB-I00.

I would like to express my gratitude to Universitat Autònoma de Barcelona for the predoctoral PIF-UAB grant. Finally, I would like to thank again the UAB and the HC3A-GDRI for the mobility grants, facilitating my research stays abroad.

Ruthenium and Platinum Nanoparticles for Artificial Photosynthesis

The increasing energy demand, necessary to meet the needs of the growing world population, has accelerated climate change in recent decades, due to the predominantly use of fossil fuels, which in addition to being pollutants are non-renewable and ill-distributed. This has aroused interest in cleaner energetic alternatives. Thus, taking Nature as an example, Artificial Photosynthesis emerges as a way to store the enormous amount of solar radiation received by the Earth, in the form of chemical bonds of a fuel. This process includes, besides the oxidation of water to dioxygen, the reduction of protons and the reduction of CO_2, obtaining, respectively, dihydrogen and products derived from carbon such as methane or methanol. In both cases, the use of a catalyst is required to make the process efficient, and a photoactive material that triggers the process induced by light.

Chapter I further develops the problem of climate change and the current state of the proton and CO_2 reduction processes, pointing out the use of semiconductors such as carbon nitride as photoactive material and metallic nanoparticles as catalysts. In addition, the use of the organometallic method for the preparation of these catalysts is highlighted, under mild reaction conditions and with great control over their physical and chemical features.

In Chapter II, the objectives of this work are exposed, centered on the design, multi-technique characterization and testing of materials based on metallic nanoparticles to carry out these processes.

In Chapter III, ruthenium nanoparticles are prepared using different ligands as stabilizers, observing differences in their activity and electrocatalytic stability in the reduction of protons, related to their physical properties and composition.

In Chapter IV, mesoporous graphitic nitrogen carbide (mpg-CN) is used as a photoactive material for photoinduced CO_2 reduction. The effect of the loading of platinum nanoparticles to the semiconductor is tested, notably improving the efficiency and selectivity of the process.

In Chapter V, mpg-CN is used again but with ruthenium and platinum nanoparticles for the photoreduction of protons. Ruthenium nanoparticles are prepared in

different ways, using stabilizing ligands, carbon materials or directly deposited in the semiconductor. It is found that, regardless of the technique, the observed catalytic efficiency is similar in all these systems, and much lower than the performance of Pt. The catalytic observations are supported by photophysical studies.

In Chapter VI, Pt nanoparticles supported on four different carbon materials (carbon nanohorns, carbon nanotubes, reduced graphene oxide and grahpite) are prepared and incorporated into an electroanalytical sensing platform, proving effective for the detection of parabens at ultra-trace levels.

Finally, in Chapter VII the global conclusions are presented.

Nanopartículas de Rutenio y Platino para Fotosíntesis Artificial

La creciente demanda energética, necesaria para cubrir las necesidades de una población cada vez más numerosa, ha acelerado el cambio climático en las últimas décadas, debido al empleo predominantemente de combustibles fósiles, que además de contaminantes son finitos y están mal distribuidos globalmente. Esto ha propiciado el interés por emplear energías más limpias. Así, tomando la naturaleza como ejemplo, surge la Fotosíntesis Artificial, una forma de almacenar la ingente energía solar que recibimos en la Tierra en forma de enlaces químicos en diferentes sustancias. Este proceso incluye, además de la oxidación de agua a dioxígeno, la reacción de reducción de protones y la reducción de CO_2, obteniéndose, respectivamente, dihidrógeno y productos derivados del carbono como metano o metanol. En ambos casos se requiere el empleo de un catalizador para hacer el proceso eficiente, y un material fotoactivo que desencadene el proceso inducido por la luz.

En el Capítulo I, se desarrolla aún más la problemática del cambio climático y el estado actual de los procesos de reducción de protones y CO_2, señalando el empleo de semiconductores como el nitruro de carbono como material fotoactivo y de nanopartículas metálicas como catalizadores. Se destaca, además, el empleo del método organometálico para la preparación de estos catalizadores, en condiciones suaves de reacción y con un gran control sobre sus características físicas y químicas.

En el Capítulo II, se exponen los objetivos de este trabajo, centrados en el diseño, caracterización multitécnica y uso de materiales basados en nanopartículas metálicas para llevar a cabo estos procesos.

En el Capítulo III, se preparan nanopartículas de rutenio empleando diferentes ligandos como estabilizadores, observando diferencias en su actividad y estabilidad electrocatalítica en la reducción de protones, relacionados con sus propiedades y composición.

En el Capítulo IV, se emplea carburo de nitrógeno grafítico mesoporoso (mpg-CN) como material fotoactivo para la reducción fotoinducida de CO_2. Se comprueba el

efecto que tiene la incorporación de nanopartículas de platino al semiconductor, mejorando notablemente la eficiencia y la selectividad del proceso.

En el Capítulo V, vuelve a utilizarse mpg-CN pero con nanopartículas de rutenio y platino para la fotorreducción de protones. Las nanopartículas de rutenio se preparan de diferentes maneras, utilizando ligandos estabilizadores, materiales de carbono o directamente en el semiconductor. Se comprueba que, independientemente de la técnica, la eficiencia catalítica observada es similar en todos estos sistemas, y muy inferior a la obtenida con Pt. Las observaciones catalíticas se respaldan con estudios fotofísicos.

En el Capítulo VI, se perparan nanopartículas de Pt soportadas en cuatro materiales de carbono diferentes (nanohorns y nanotubos de carbono, óxido de grafeno reducido y grafito), que son incorporadas a un sistema de detección electroanalítica, mostrándose eficaces para la detección de parabenos a niveles de ultratraza.

Finalmente, en el Capítulo VII se exponen las conclusiones globales.

Nanopartícules de Ruteni i Platí per Fotosíntesi Artificial

La creixent demanda energètica, necessària per a cobrir les necessitats d'una població cada vegada més nombrosa, ha accelerat el canvi climàtic en les últimes dècades, a causa de l'ús predominant de combustibles fòssils, que a més de contaminants són finits i estan mal distribuïts globalment. Això ha propiciat l'interès per emprar energies més netes. Així, prenent la naturalesa com a exemple, sorgeix la Fotosíntesi Artificial, una forma d'emmagatzemar la ingent energia solar que rebem a la Terra en forma d'enllaços químics en diferents substàncies. Aquest procés inclou, a més a més de l'oxidació de l'aigua a dioxigen, la reacció de reducció de protons i la reducció de CO_2, obtenint-se, respectivament, dihidrogen i productes derivats del carboni com són el metà o el metanol. En tots dos casos es requereix l'ús d'un catalitzador per fer el procés eficient, i un material fotoactiu que desencadeni el procés induït per la llum.

En el Capítol I, es desenvolupa encara més la problemàtica del canvi climàtic i l'estat actual dels processos de reducció de protons i CO_2, fent èmfasi en l'ús de semiconductors com el nitrur de carboni com a material fotoactiu i de nanopartícules metàl·liques com a catalitzadors. Es destaca, a més, l'ús del mètode organometàl·lic per a la preparació d'aquests catalitzadors, en condicions suaus de reacció i amb un gran control sobre les seves característiques físiques i químiques.

En el Capítol II, s'exposen els objectius d'aquest treball, centrats en el disseny, caracterització multitècnica i l'ús de materials basats en nanopartícules metàl·liques per dur a terme aquests processos.

En el Capítol III, es preparen nanopartícules de ruteni emprant diferents lligands com estabilitzadors, observant diferències en la seva activitat i estabilitat electrocatalítica en la reducció de protons, relacionats amb les seves propietats i composició.

En el Capítol IV, es fa servir carbur de nitrogen grafític mesoporós (mpg-CN) com a material fotoactiu per a la reducció de CO_2 fotoinduïda. Es comprova l'efecte que té la incorporació de nanopartícules de platí al semiconductor, millorant notablement l'eficiència i la selectivitat del procés.

En el Capítol V, torna a utilitzar-se mpg-CN però amb nanopartícules de ruteni i platí per a la fotoreducció de protons. Les nanopartícules de ruteni es preparen de diferents maneres, utilitzant lligands estabilitzadors, materials de carboni o directament en el semiconductor. Es comprova que, independentment de la tècnica, l'eficiència catalítica observada és similar en tots aquests sistemes, i molt inferior a l'obtinguda amb Pt. Les observacions catalítiques es recolzen amb estudis fotofísics.

En el Capítol VI, es preparen nanopartícules de Pt suportades en quatre materials de carboni diferents (nanohorns y nanotubs de carboni, òxid de grafè reduït i grafit), que són incorporades a un sistema de detecció electroanalítica, essent eficaces per a la detecció de parabens a nivells ultratraça.

Finalment, en el Capítol VII s'exposen les conclusions globals.

Glossary of Terms and Abbreviations

ACN	Acetonitrile
ADP	Adenosine diphosphate
APS	Artificial Photosynthesis
ATP	Adenosine triphosphate
b	Tafel slope [mV·dec-1]
b6f	Cytochrome b6f complex
BET	Brunauer-Emmet-Teller method
CDL	Double-Layer capacitance [mF]
CB	Conduction band
CN	Carbon nitride
CNH	Carbon nanohorns
CNM	Carbon nanomaterial
CNT	Carbon nanotubes
coe	Cyclooctadienyl
cod	1,5-Cyclooctadiene
CP	Chronopotentiometry
CV	Cyclic voltammetry
CVD	Chemical vapor deposition
dba	dibenzylideneacetone
DFT	Density functional theory
DPV	Differential pulse voltammetry
DRS	Diffuse Reflectance Spectroscopy
EA	Elemental analysis
ECSA	Electrochemically active surface area
EDX	Energy-dispersive X-ray spectroscopy
EIS	Electrochemical impedance spectroscopy
Eq.	Equivalent
FE	Faradaic efficiency
FID	Flame ionization detector
FLIM	Fluorescence-lifetime imaging microscopy
FTO	Fluorine-doped tin oxide electrode
GC/GCE	Glassy Carbon Electrode
GC-MS	Gas chromatography-mass spectrometry
GHG	Green-House Gases
GP	Graphite
HEC	Hydrogen Evolution Catalyst
HER	Hydrogen Evolution Reaction
HPLC	High-performance liquid chromatography
hcp	Hexagonal close-packed structure
i	Current intensity [mA]
ICP	Inductive-Coupled Plasma

j	Current density [mA·cm^{-2}]
*j*0	Exchange Current Density [mA·cm^{-2}]
LOD	Limit of detection
LSV	Linear sweep voltammetry
MeP	Methylparaben
MNP	Metal nanoparticle
MOF	Metal-Organic Framework
mpg-CN	Mesoporous graphitic carbon nitride
MPT	4'-(4-methylphenyl)-2,2':6',2"-terpyridine
M-H	Metal-Hydride
NPs	Nanoparticles
OEC	Oxygen Evolving Complex/Center
OER	Oxygen Evolution Reaction
OES	Optical Emission Spectrometry
PB	Parabens
PBS	Phosphate Buffer Solution
PCET	Proton-Coupled Electron Transfer
PEC	Photoelectrochemical cell
PEM	Polymer Electrolyte Membrane
PP	Phenylpyridine
PS	Photosensitizer
PS-I/PS-II	Photosystem I-II
PVCs	Photovoltaic Cells
PVP	Polyvinylpyrrolidone
RDE	Rotating disk electrode
rGO	Reduced graphene oxide
RHE	Reversible hydrogen electrode
rds	Rate-determining step
Rub	Ruthenium black
S_{BET}	Specific surface area via BET method
SA	Sample
SEM-FEG	Scanning Electron Microscopy-Field Emission Gun
SSA	Specific surface area
SMR	Steam Methane Reforming
TC-SPC	Time-Correlated Single Photon Counting
TCD	Thermal Conductivity Detector
TEM	Transmission Electron Microscopy
TEOA	Triethanolamine
TGA	ThermoGravimetric Analysis
THF	Tetrahydrofuran
TOF	Turnover frequency
TON	Turnover number
UPD	Under-Potential Deposition

UV-vis	Ultraviolet-visible
Vs.	Versus
VB	Valence band
WAXS	Wide-Angle X-ray Scattering
WE	Working Electrode
WOC	Water Oxidation Catalyst
WS	Water Splitting
XPS	X-Ray Photoelectron Spectroscopy
XRD	X-Ray Diffraction spectroscopy
0-3D	Zero/three-dimensional
e^-	Electron
η	Overpotential
$\eta 0$	Onset overpotential
$\eta 10$	Overpotential at j=10 mA·cm-2
λ	Wavelenght
τ	Lifetime

Chapter I

General Introduction

This chapter aims to offer insight into the state of the art in the field of artificial photosynthesis, including the light-driven water splitting and CO_2 reduction towards the production of solar fuels, as well as the motivation behind the growing interest in these processes and the main challenges they face.

Table of contents

1.1 Environmental concern and global energy transformation

Since the first scientific papers addressing climate change were published two centuries ago, the concern about this problem has grown to become one of the main challenges in our world [1]. In 1896, Svante Arrhenius already pointed out how the emission into the atmosphere of certain substances, now known as greenhouse gases (GHG) (such as carbon dioxide, methane or nitrous oxide), could impact on the average temperature of Earth, based on theoretical calculations [2].

Since then, numerous studies have tried to prove the role that human activity plays in climate changes, such as global mean temperature rise, shrinking cryosphere, sea level rise, change on precipitation patrons, droughts, extreme climate events (e. g. hurricanes or winter storms), ocean acidification, etc. [3–6]. Most of the environmental research points to the increase in world population, motivated by improvements in life quality and expectancy, especially on the developed and industrialized countries, as the main cause of climate change. A larger population means a greater demand of resources and energy consumption, with fossil fuels (oil, gas and coal) being the main source of energy, according to the data collected in **Figure 1** [7].

Fossil fuels are an abundant and cheap source of energy, but release large amounts of CO_2 and other harmful gases and particles, thus increasing the concentration of GHG in the atmosphere [4,8–10]. The problem of fossil fuels is not only related to its contribution to a negative environmental impact through climate change. They are a major source of pollution, with subsequent health problems on the population. In addition, their distribution is unbalanced, so that not all countries have equal access to them, thus bringing economic and political factors (energy dependence) as well as logistics (transport and distribution) into play [9]. Fossil fuels are also non-renewable energy sources, and although right now their production is only increasing and there are many deposits to be exploited, their use for future generations is not guaranteed. All these reasons have led to a peak in the search for cleaner and renewable alternatives.

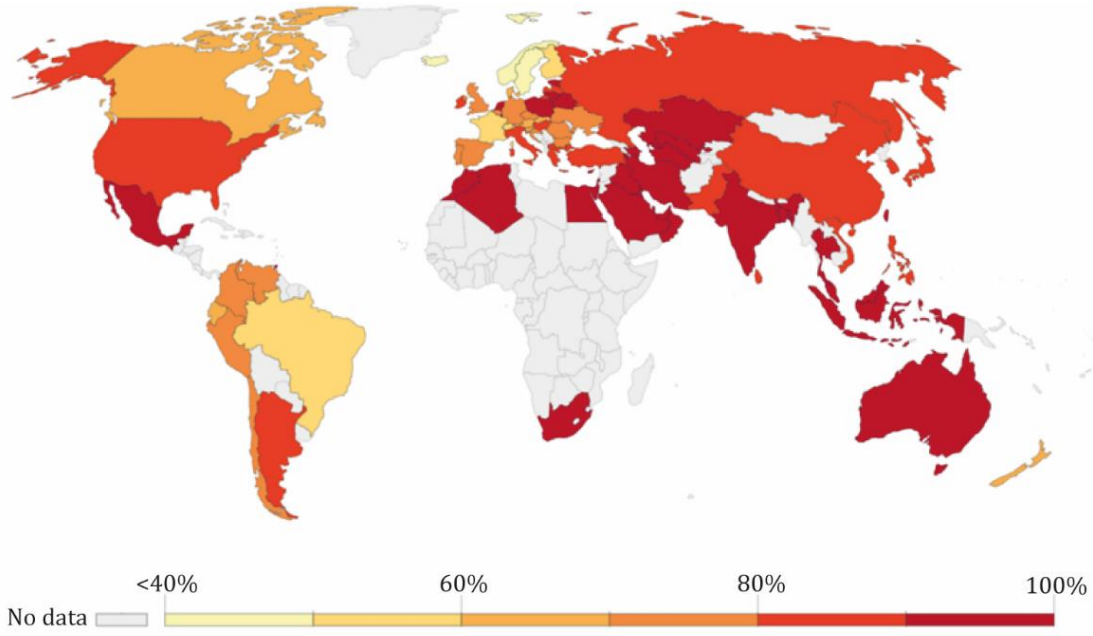

Figure 1. Share of primary energy from fossil fuels (2019) (Source: OurWorldInData based on reference [7]).

Renewable energies also come from natural sources, but are virtually inexhaustible (rapid regeneration), and are also cleaner, as they do not generate polluting gases during their exploitation [11]. These sources include wind, solar, hydro and tidal power, as well as geothermal or biofuels. However, this does not imply that their carbon footprint is zero. Renewable-energy power plants also require installation and maintenance, that being so, there will be other manufacturing industries indirectly involved in the process in which there will probably be emission of CO_2 and other substances. In spite of that, this is minimal compared to the use of fossil fuels. It is also important to point out that using some of these power facilities can have a negative impact on the environment. Many hydroelectric power plants require the creation of artificial water dams and reservoirs, which negatively affect the environment and wildlife.

One of the joint actions that has been carried out globally to overcome the issues related with fossil fuels took place in 2015, when all members of the United Nations adopted the 2030 Agenda for Sustainable Development, a total of 17 objectives to be met within a 15 years period. Two of the agreements are to "ensure access to affordable, reliable, sustainable and modern energy for all" and to "take urgent

action to combat climate change and its impacts" [12]. Since the last decades, renewable, cleaner and more sustainable energy sources have been implemented [7]. However, with less than ten years to meet the purposes of the 2030 Agenda, the prospect of ceasing to be dependent on fossil fuels seems still distant.

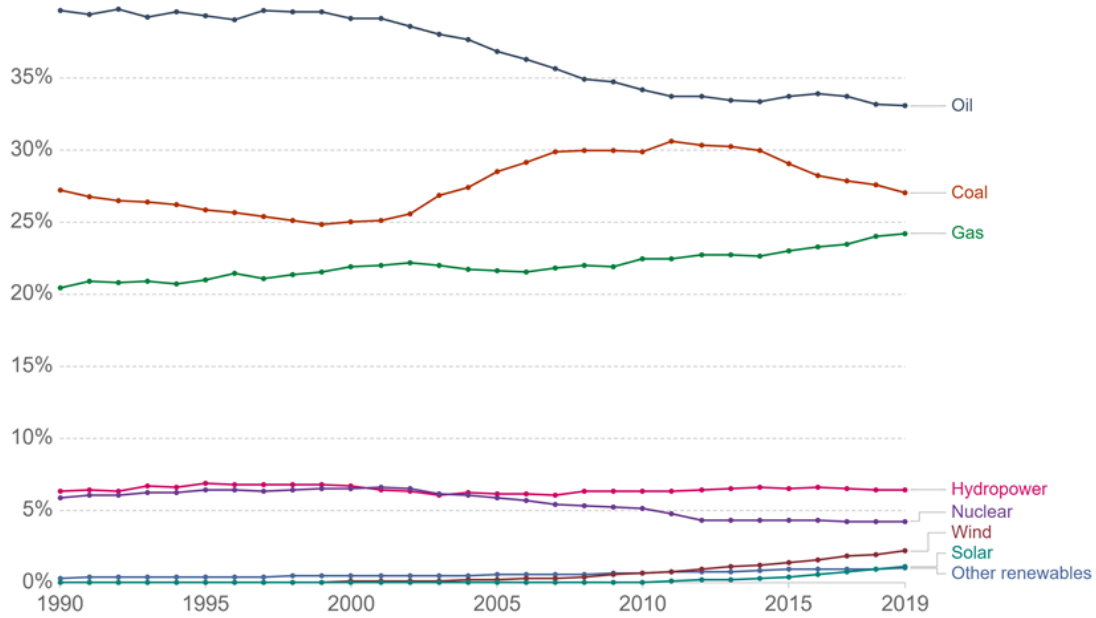

Figure 2. Share of global energy consumption by source (right) from 1990 to 2019. (Source: OurWorldIndata based on reference [7]).

Even though the use of renewable energy, especially solar or wind power, has increased in recent years, their total share with respect to fossil fuels has barely been altered for the past decades (**Figure 2**). Thus, both climate change and the development of an efficient and sustainable energy alternative will continue to be hot topics for years to come.

1.2 Solar energy

Among the most developed renewable energies, there are many reasons to highlight solar energy as the ideal alternative. It is a sustainable, non-polluting and totally inexhaustible source, and one of the most abundant, since the Earth intercepts 1.8×10^{14} kW per second from the Sun, although almost half of it is reflected, scattered or absorbed in the atmosphere before reaching the surface [13]. The remaining energy could be collected and directly used in a wide variety of ways [14,15]:

- It can be concentrated to generate heat, which could be used as collected for thermal purposes, or it could be transformed into mechanical or electrical energy using an appropriate type of engine.
- It could be directly converted into electricity using photovoltaic cells (PVC). The great advantage of these forms of exploitation is that they are already sufficiently developed, thus easy to implement from domestic to industrial purposes.

Despite its abundance, there are places where or situations in which it is not possible to have access to solar energy. It is also necessary to take into account fluctuations in energy production, caused by weather conditions or at night, when the solar collectors or PVC are not operative [15]. Wind power and other renewable energies also suffer from this intermittency issue. Therefore, a storage system is necessary to optimize the use of captured solar power and, at the same time, ensure that the energy demand is covered in any situation.

An attractive alternative is to harvest and store sunlight into the chemical bonds of a material, in a process similar to what happens in natural photosynthesis. This would allow energy consumption regardless of solar radiation availability. This kind of materials are the so-called solar fuels [16–18]. Besides being able to be transported and stored until further use, most of these solar fuels are compatible with existing infrastructure and engines, thereby facilitating their implementation.

1.3 Hydrogen as energy carrier candidate

The use of hydrogen to meet the energy demand is one of the most viable alternatives to fossil fuels. Unlike the latter, hydrogen combustion is totally clean, generating only water, instead of greenhouse gases such as carbon dioxide. However, affirming that hydrogen is a totally clean energy nowadays is misleading. To understand this, the first thing is to classify hydrogen as an energy carrier.

The concept of energy carrier is used to define those substances or energy systems that, like hydrogen, are capable of storing energy that can be used, at any time and situation, in a controlled manner [19,20]. The differential factor with other forms of energy is that they are manufactured products, in which a significant amount of energy has been invested for their production. Aside from hydrogen, electric batteries, capacitors, compressed air, dammed water and even springs could be categorized as energy carriers.

Hydrogen, despite being the most abundant element in the universe, and the third on the Earth's crust, is hardly present naturally as H_2 gas in the atmosphere. Therefore, to have hydrogen as an energy carrier, it is required both a substance that contains atoms of the mentioned element, and a source of energy.

The common mistake of classifying hydrogen as clean energy carrier lies in the manufacturing process. Considering only its combustion, it could be considered a "green" energy. The trick is that its production normally involves the use of non-renewable energy sources, or raw materials whose collection is not sustainable, for example steam-methane reforming and water-gas shift reactions (explained in detail in section 1.3.2), in which H_2 is obtained from methane and ultimately releasing CO_2 to the atmosphere [21]. This required clean-energy utilization/production cycle (**Figure 3**) represents another challenge on the way towards a non-polluting and sustainable energy source.

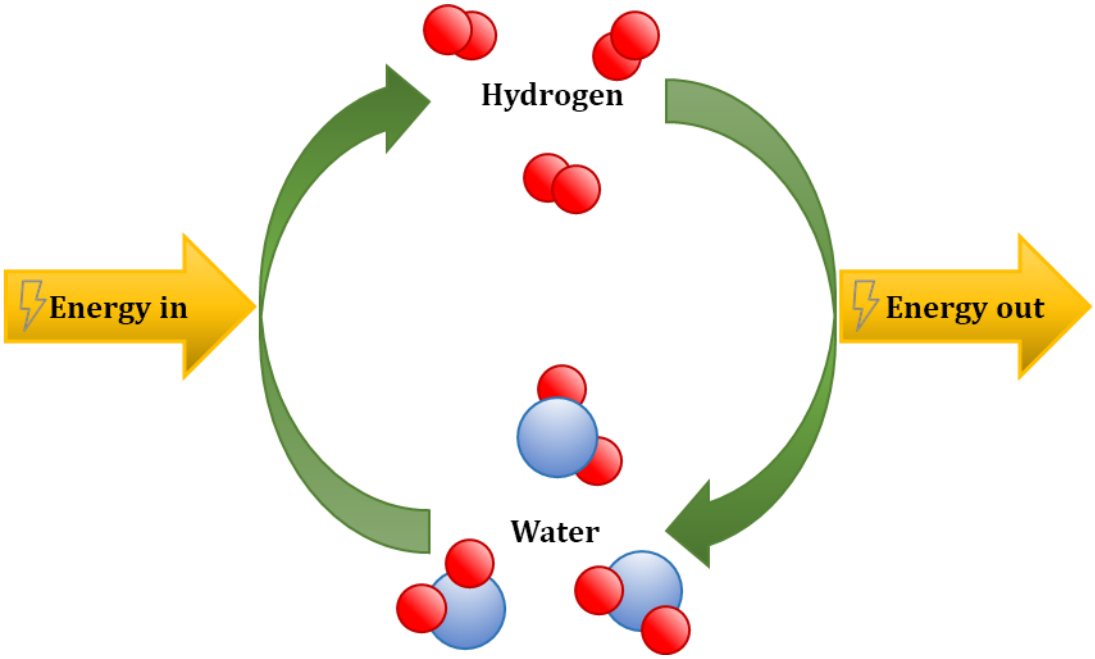

Figure 3. The water-hydrogen cycle as a clean way to produce energy [20].

1.3.1 Hydrogen properties as fuel

Hydrogen is a very light gas. Hence, its non-existent abundance in the Earth's atmosphere, as it easily escapes from the Earth's gravity. Although it is not toxic, like any gas other than oxygen, hydrogen can be a suffocating gas. However, its hazards are fundamentally due, as with most traditional and widely used fuels, in its flammable and explosive nature. Compared to gasoline or methane, the use of hydrogen can present more dangers due to its wide flammability range, low ignition energy or higher deflagration index [22]. However, when making a hazard comparison, other factors must be taken into account, such as the fact that hydrogen is a very light molecule that is easily dispersible in air, so the risks and their consequences could be offset, especially in wide or open spaces.

From an energy point of view, hydrogen, whether in gas, liquid or compressed high pressure form, provides more energy per unit mass than any of the more common fuels [19,23]. However, hydrogen has a high energy density when it is compressed or in a liquid state, but lower compared to conventional fuels (**Table 1**). Thus, hydrogen storage tanks must be larger than gasoline tanks to provide the same amount of energy, which makes it more challenging to store and adapt to non-stationary applications like transportation, as will be discussed later.

Fuel type	Energy per mass unit ($J \cdot kg^{-1}$)	Energy per volume unit ($J \cdot m^{-3}$)	Specific carbon emission ($kg_C \cdot kg_{fuel}^{-1}$)
Hydrogen gas	143	0.0107	0.00
Hydrogen (liq.)	143	10.1	0.00
Methane	55.6	0.0378	-
Natural gas	53.6	0.0364	0.46
Natural gas (liq.)	53.6	22.2	-
Gasoline	46.4	34.2	0.86

Table 1. Comparison of the main energetic properties of gas or liquefied hydrogen, with the most commonly used fuels. Energy densities (per mass or volume units) refer to stored energy by each material, and released in combustion. Adapted from references [19,23].

1.3.2 Hydrogen production

Hydrogen can be obtained from different resources. As discussed above, a hydrogen-containing material is required in order to be extracted from it. Water is the ideal substance, due to its abundance and availability almost anywhere (even in deserts it can be obtained from air humidity) [24]. There are three main ways to get hydrogen from water. The first one is electrolysis, using electricity to "break" the water molecule into its components. If this power comes from renewable sources, such as wind or solar energy, the final product could be labelled as "green hydrogen" [25]. The other two methods are thermochemical. On the one hand, there is gasification, which uses coal, and on the other hand, there is the steam reforming, which uses natural gas. These two techniques today represent the main routes of hydrogen production [19,21]. One way to lower the carbon footprint of these fossil fuel-dependant strategies would be to capture and store carbon emissions [25,26]. It might not be considered as a totally green hydrogen production route, but it would help reduce polluting gas emissions while completing the transition to fully renewable energy sources.

1.3.2.1 Electrolysis of water

The electrolysis of water is an electrochemical process that uses an electrical current to split water molecules directly into dihydrogen and dioxygen gases (**Eq. 1**). Contrary to its reverse process, which is spontaneous under different reaction conditions (**Eq. 2**), the electrolysis of pure water is a thermodynamically demanding process.

$$2H_2O \rightarrow 2H_2 + O_2 \qquad \Delta H^0 = 285.85\ \text{kJ} \cdot \text{mol}^{-1} \qquad \text{Eq. 1}$$

$$2H_2 + O_2 \rightarrow 2H_2O \qquad \text{Eq. 2}$$

There is also a dependence of the thermodynamic potential with pH, according to the Nernst equation (**Eq.3-4**), from which the corresponding Pourbaix diagram can be obtained (**Figure 4**).

$$E^0_{O_2/H_2O}(\text{V}) = 1.229 - (0.059 \cdot \text{pH}) \qquad \text{Eq.3}$$

$$E^0_{H_2/H_2O}(\text{V}) = 0.000 - (0.059 \cdot \text{pH}) \qquad \text{Eq. 4}$$

In addition to the thermodynamic potential, water electrolysis requires a large amount of extra energy, referred as overpotential (η). This is mainly due to the kinetic barriers derived from the breaking and formation of chemical bonds during the process, but also to overcome the ohmic resistance of the aqueous electrolyte or ions mobility (drift and diffusion). In this way, many electrolytic cells require electrocatalysts to counteract the effect of this overpotential [27].

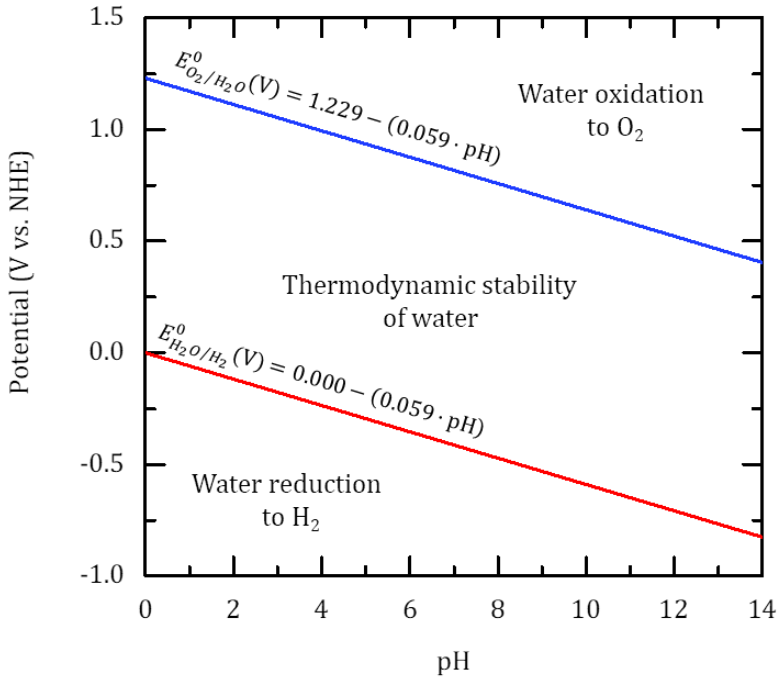

Figure 4. Thermodynamic water splitting oxidation and reduction potentials as a function of pH at standard conditions for temperature and pressure, according to Nernst equation.

Alkaline water electrolysers have played a very relevant role in the production of hydrogen by electrolysis at an industrial level [21]. These alkaline electrolysis cells (AECs) (**Figure 5**) use an alkaline electrolyte solution (usually sodium hydroxide or potassium hydroxide), in which two electrodes are submerged, separated by a diaphragm. The latter was historically made of porous white asbestos and more recently made of ceramic-polymers composites, due to the toxicity-related problem of the former. The diaphragm acts as an impermeable membrane to dihydrogen and dioxygen gases but allowing the flow of OH^- between the two electrodes. When the electric current is applied, oxygen begins to form at the anode (**Eq. 5**), as well as water molecules, which flow into the cathode compartment as the reduction of water molecules takes place, releasing hydrogen (**Eq. 6**).

$$4OH^-_{(aq)} \rightarrow 2H_2O_{(liq)} + 2O_{2(g)} + 4e^- \quad \text{anode} \quad \text{Eq. 5}$$

$$4H_2O_{(liq)} + 4e^- \rightarrow 2H_{2(g)} + 4OH^-_{(aq)} \quad \text{cathode} \quad \text{Eq. 6}$$

The electrodes of AECs are usually nickel-based, offering resistance to corrosion in alkaline medium at a reasonable price. Also, cobalt could be used as an additive for the anode and iron for the cathode [28,29].

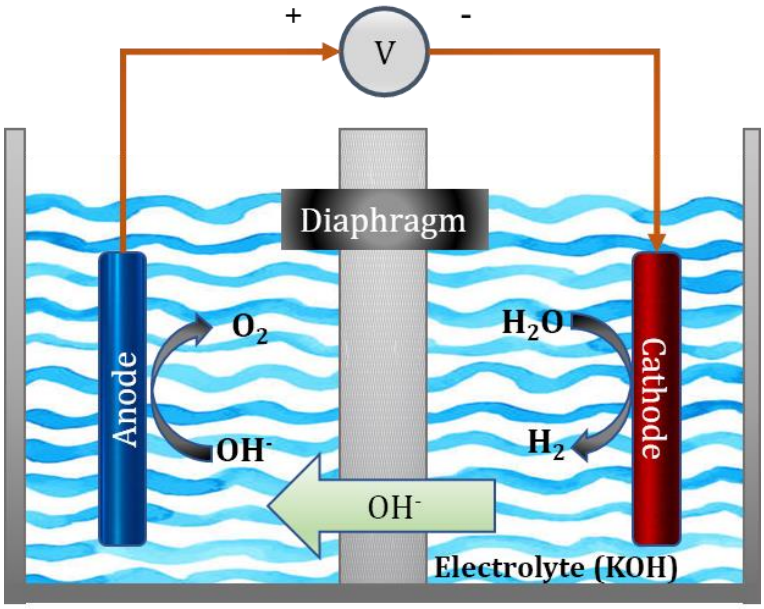

Figure 5. Schematic representation of an alkaline water electrolysis cell. Adapted from reference [29].

The other system that has been gaining prominence at large-scale hydrogen production are proton electrolyte membrane (PEM) based electrolyzers (**Figure 6**). Water is pumped through a stack of two electrodes and a polymer electrolyte membrane, only allowing protons to pass through [29]. By applying a current, water is oxidized, releasing oxygen and protons at the anode. The latter pass through the PEM reaching the cathode, where protons and electrons recombine to generate hydrogen (**Eq. 8**). Platinum black and mixed Ir and Ru oxides are commonly used as electrocatalyst, at the cathode and anode, respectively, in PEM electrolyzers [27].

$$2H_2O_{(liq)} \rightarrow 4H^+_{(aq)} + O_{2(g)} + 4e^- \qquad \text{anode} \qquad \text{Eq. 7}$$

$$4H^+_{(liq)} + 4e^- \rightarrow 2H_{2(g)} \qquad \text{cathode} \qquad \text{Eq. 8}$$

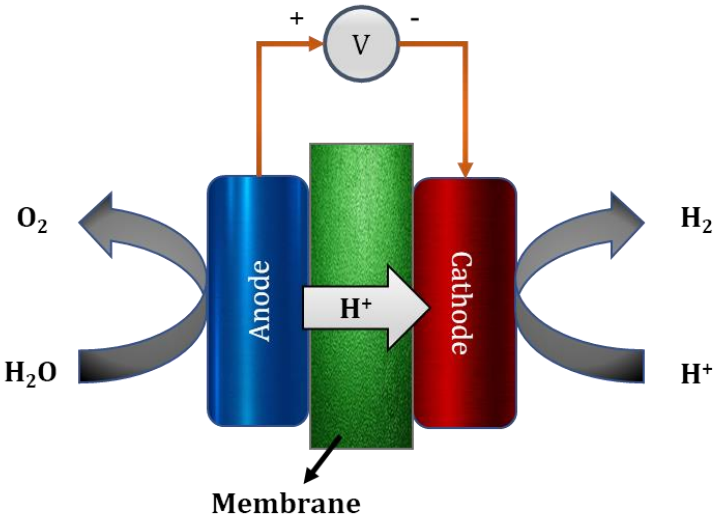

Figure 6. Schematic representation of a water electrolysis PEM cell. Adapted from reference [29].

Compared to alkaline electrolysis, PEM electrolysis delivers higher efficiency and does not suffer from corrosion problems derived from the use of an alkaline medium, which also facilitates its maintenance [30]. On the contrary, the use of scarce metals such as Pt and Ir increases the cost of manufacture. Employing renewable energy sources in electrolysis processes is key, not only to reduce the carbon footprint, but also to maximize the profitability of the process, as they are energy-demanding techniques. The high purity of the hydrogen obtained is also remarkable, as it is obtained in the form of an easily recoverable gas and not mixed with oxygen.

1.3.2.2 Coal gasification

Normally, the use of coal is associated with the direct production of energy by combustion. Coal gasification process, however, chemically treats this fossil fuel to produce synthetic natural gas (**Figure 7**). Water steam and oxygen gas are used to partially oxidize coal, inside a reactor at high temperature and pressure, thus yielding H_2 and CO (syngas) (**Eq. 9**) [31,32].

$$3C_{(s)/coal} + O_2 + H_2O_{(liq)} \rightarrow H_{2(g)} + 3CO_{(g)} \qquad \text{Eq. 9}$$

The H_2/CO ratio can be increased if the syngas is treated with water (steam), in a catalysed process known as water-gas shift (WGS). It is a moderately exothermic

reaction (ΔH^0 = -41.09 kJ·mol^{-1}), which is thermodynamically favoured when operating at lower temperatures but kinetically favoured at elevated temperatures, which is why suitable catalysts are required [33]. WGS reaction step is essential when the final objective of coal gasification is the production of hydrogen (**Eq. 10**).

$$CO_{(g)} + H_2O_{(g)} \rightleftarrows H_{2(g)} + CO_{2(g)} \qquad \text{Eq. 10}$$

The benefits of this method are that coal is an accessible and affordable substance, allowing the generation of a low-cost synthetic fuel. The main drawback of coal gasification is that CO_2 emissions are very high, due to the high carbon content of coal compared to other feedstocks. This also requires investment in carbon capture and storage strategies. Operating at high temperatures and pressures also makes the process and reactor maintenance more expensive. The efficiency of the system is not very reliable either, as it depends on the quality (impurities) of the starting coal [31,32].

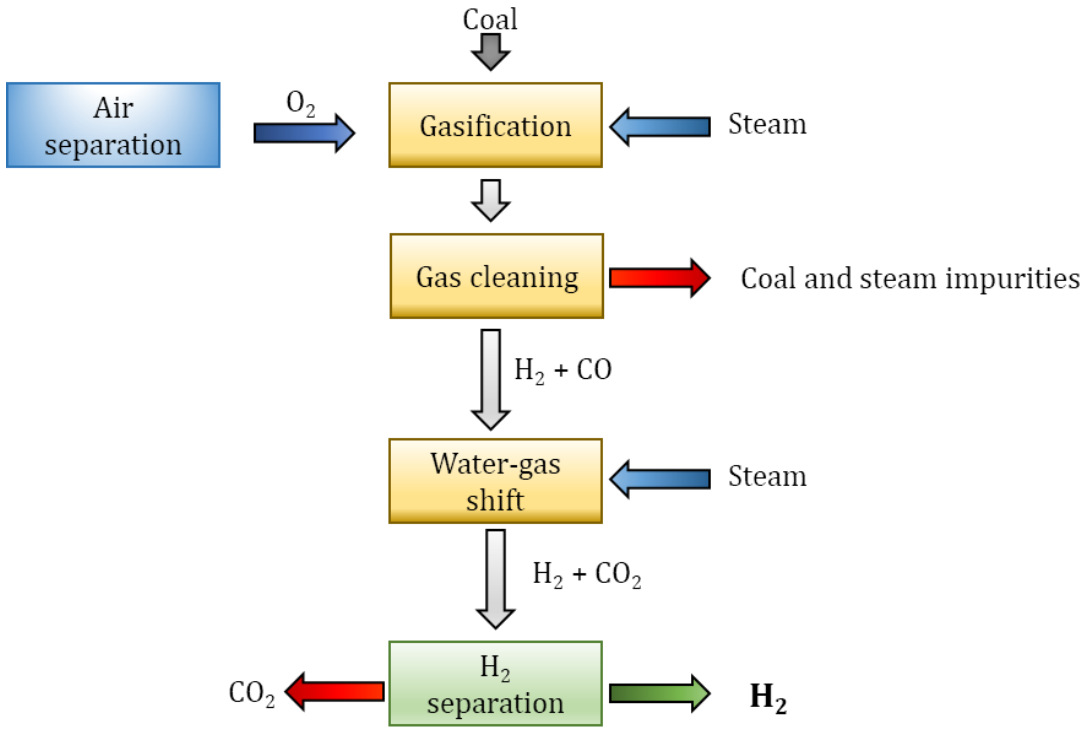

Figure 7. Outline of the main steps of coal gasification for hydrogen production. Adapted from reference [34].

1.3.2.3 Steam methane reforming

Natural gas, whose main component is methane, is the main feedstock for steam reforming, an economic and the most widely used industrial process for the production of hydrogen [19,32]. Steam methane reforming is a highly endothermic reaction, which requires natural gas treated with water steam, to convert it into hydrogen in the presence of a catalyst (commonly Ni). As with coal gasification, SMR reaction is followed by WGS reaction to increase hydrogen yield [33]. Carbon dioxide is captured for further use or storage, before hydrogen purification, where H_2 gas is obtained and the tail gas reconducted to the first step, serving as supporting fuel to restart the process (**Figure 8**).

$$CH_{4(g)} + H_2O_{(liq)} \rightarrow 3H_{2(g)} + CO_{(g)} \qquad \text{Eq. 11}$$

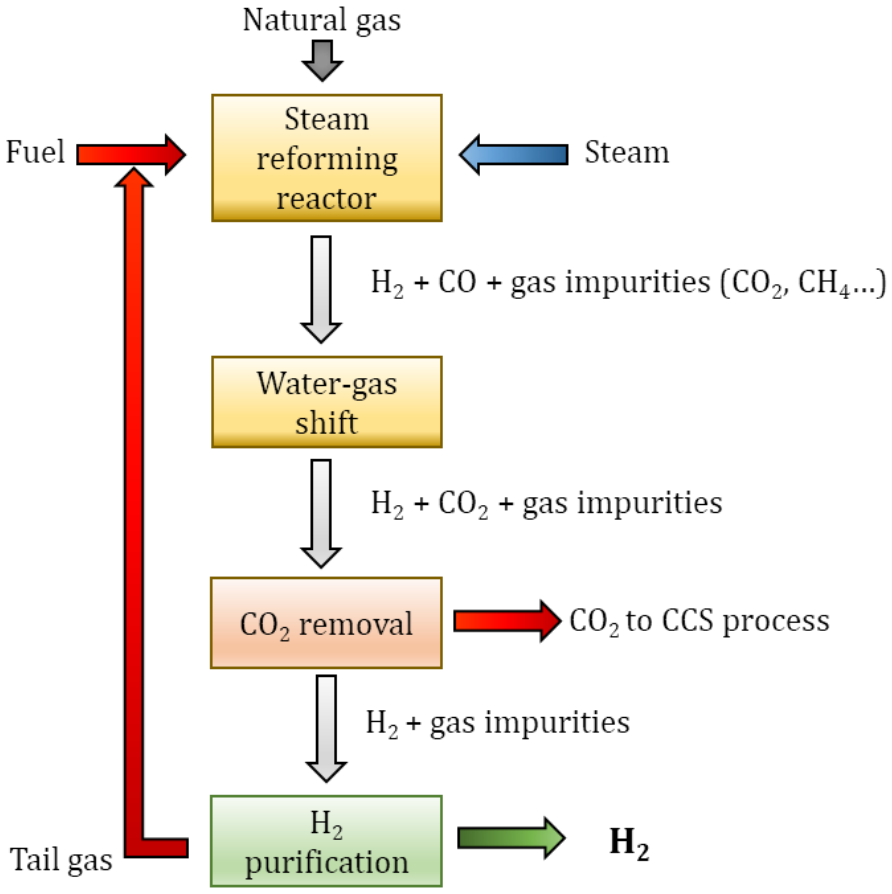

Figure 8. Main steps in hydrogen production via steam methane reforming, including carbon capture and storage (CCS) techniques for the sequestration and exploitation of CO_2. Adapted from reference [32].

The disadvantages of this technique lie, once again, in the use of commodities (methane or natural gas) with high carbon content and the consequent pollution or investment in carbon capture techniques. On the contrary, SMR is a well-known and established technology, so its exploitation involves very few risks [31,32].

1.3.3 Hydrogen storage and distribution

At room temperature, molecular dihydrogen is a gas (boiling point at −252.879 °C) and the most efficient way to store it in its pure form is to compress or liquefy it (compression process followed by cryogenization). Additionally, working with a compressed or cryogenic gas requires an energy investment and makes its maintenance more expensive, plus additional security measures. Even yet, hydrogen can easily be transported in gaseous form through pipes or, after liquefaction, in metal vessels or road tankers, using the existing transport logistics network, to storage facilities or directly to end-use locations (**Figure 9**) [19,21,35,36].

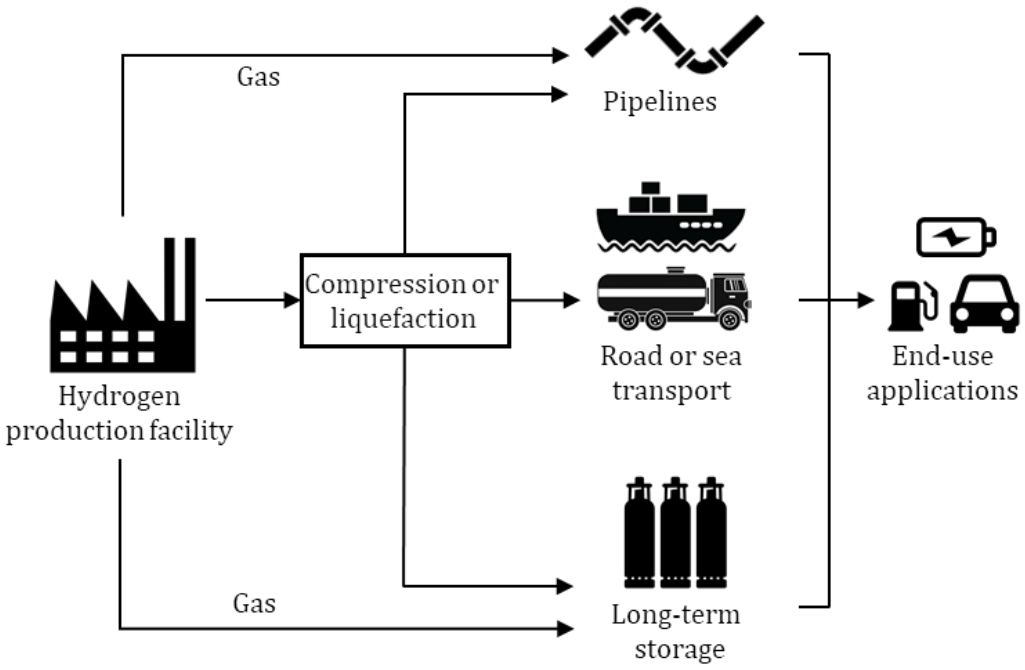

Figure 9. Large-scale hydrogen production, storage and transport.

A large-scale storage option, gaining importance as hydrogen emerges as an energy alternative, is the underground hydrogen storage. This technique takes as an example the underground storage of natural gas, which has been used in the oil

industry for years and goes hand in hand with the underground storage of CO_2, also on the rise. Helium, a gas that diffuses faster than hydrogen, was successfully stored in this way years ago [37]. It involves injecting the gas into large existing geological underground spaces, such as aquifers, salt mines or depleted deposits of oil or natural gas [26,38–40]. Mines could also be dug for this purpose, although the environmental impact would no longer be zero. Underground hydrogen storage offers a series of advantages, such as storage security (deposits are buried dozens of meters under the ground), optimization of space (not requiring conventional warehouses), and also economic, as long as existing geological facilities are used, which are also very common in most places [40].

Another efficient resource is material-based hydrogen storage. This category includes hydrides (mainly metal hydrides or boron-based compounds), by forming chemical bonds with hydrogen atoms, and the use of adsorbent materials (with a very high surface area), such as carbon nanotubes (CNTs), metal-organic frameworks (MOFs), covalent-organic frameworks (COFs) or zeolites, which accommodate hydrogen molecules on their surface through physicochemical interactions [41]. Although these alternatives allow hydrogen to be stored and transported under ambient temperature and pressure conditions, reducing handling risks and saving on infrastructure maintenance costs, hydrogen storage remains a major drawback for the implementation of this energy alternative, and many researchers continue to focus on the development and improvement of these techniques.

1.3.4 Hydrogen applications overview

Hydrogen is used mainly in industry as a reagent, for the preparation of ammonia and as the main feedstock for the synthesis of fertilizers. It is also used in oil refiners and in the pharmaceutical or food industries [35]. However, the appeal of hydrogen as an energy carrier attaches increasing importance of its use directly as fuel or via more recently developed fuel cells (FC), being transportation the main target-application.

Any device capable of transforming, by means of a chemical reaction, the energy stored in a fuel into electrical energy, could be labelled as fuel cell. One type

of FC is polymer electrolyte membrane (PEM-FC), which have been marketed for decades for niche applications, but whose interest as a source of energy for mass applications such as transport or portable electronic devices is more recent [42]. Hydrogen is fed into the cell, where it is catalytically oxidized according to **Eq. 12**. The electrons are then conducted through an external circuit, performing electrical work before being redirected to the anode. The protons migrate to the cathode through the special proton-conducting polymer electrolyte membrane where they react with oxygen, which is reduced (**Eq. 13**).

Hydrogen oxidation $H_2 \rightarrow 2H^+ + 2e^-$ Eq. 12

Oxygen reduction $4H^+ + 4e^- + O_2 \rightarrow 2H_2O$ Eq. 13

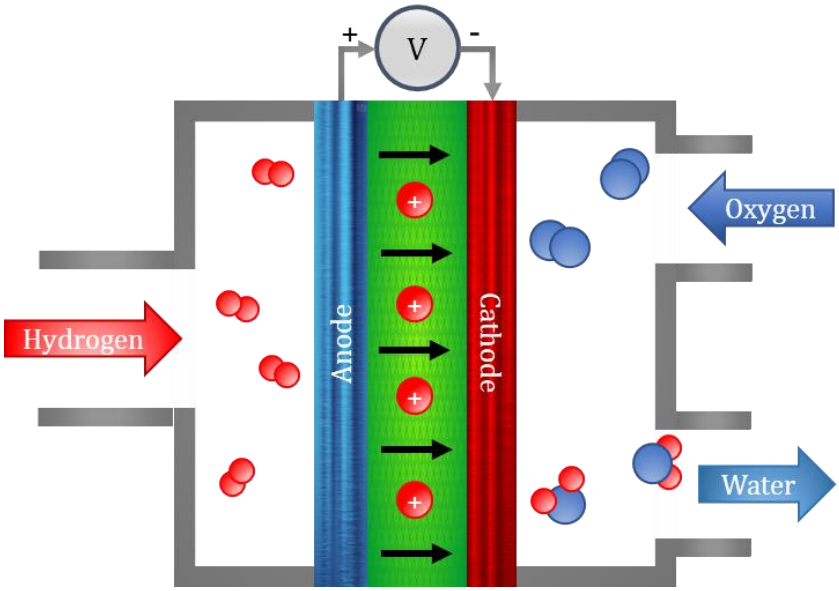

Figure 10. Basic operation of a hydrogen fuel cell [20].

The higher the purity of the hydrogen fed, the cleaner the energy produced, since only water and heat are generated as by-products of the whole process [20]. Platinum usually serves as a catalyst, but being a scarce metal makes the process more expensive, so the development of equally efficient and more affordable catalysts is today one of the challenges when mass-implementing hydrogen-fuelled cells. A fuel cell works essentially like a conventional battery, except that it is not depleted or needs to be recharged, as long as the fuel supply is maintained. Fuel cells are more efficient than using hydrogen directly as fuel in conventional internal combustion engines. This is mainly due to, as already discussed, hydrogen's low

energy density by volume. Thanks to the high efficiency of hydrogen fuel cells in real motor vehicles (it is already capable of exceeding its competitors [43]) the principal ambition now is to match the cost and durability of the still dominant fossil fuel-powered traditional engines.

1.4 Carbon capture and storage

In a deeply industrialized world dependent on fossil fuels, the shift to cleaner energy has to be gradual. Carbon capture and storage (CCS) technologies play an important role in this energy transition to a low carbon economy [44]. These techniques seek to reduce the carbon footprint derived from the consumption of fossil fuels, either for their direct use or, as previously stated, for the production of hydrogen.

We can classify CO_2 capture techniques into three main categories (**Figure 11**), depending on the stage of the industrial or energy process in which it is carried out [45,46]:

- Post-combustion carbon capture: Separates CO_2 from exhaust after the combustion process. It is the most used in power plants, since they can be easily adapted. One of the great challenges of this strategy is separating the low concentration of CO_2 from the exhaust gas (4-14% depending on the fuel).
- Pre-combustion carbon capture: Before using the fuel, it undergoes a treatment. In the case of coal, a gasification process (**Eq. 9**, page 13) is performed followed by WGS reaction (**Eq. 10**, page 14). In this case, the final CO_2 concentration is high enough (> 20%) to facilitate its separation. In case of using natural gas (methane), the previous step to the WGS reaction would be steam reforming (**Eq. 11**, page 15). It is a technique devised for newly built power plants.
- Oxy-fuel combustion carbon capture: It is a type of post-combustion carbon capture, in which high purity oxygen is used for combustion, instead of using air. This means that in the exhaust gases there are not so many by-products (such as NOx), which makes the subsequent separation of CO_2 easier.

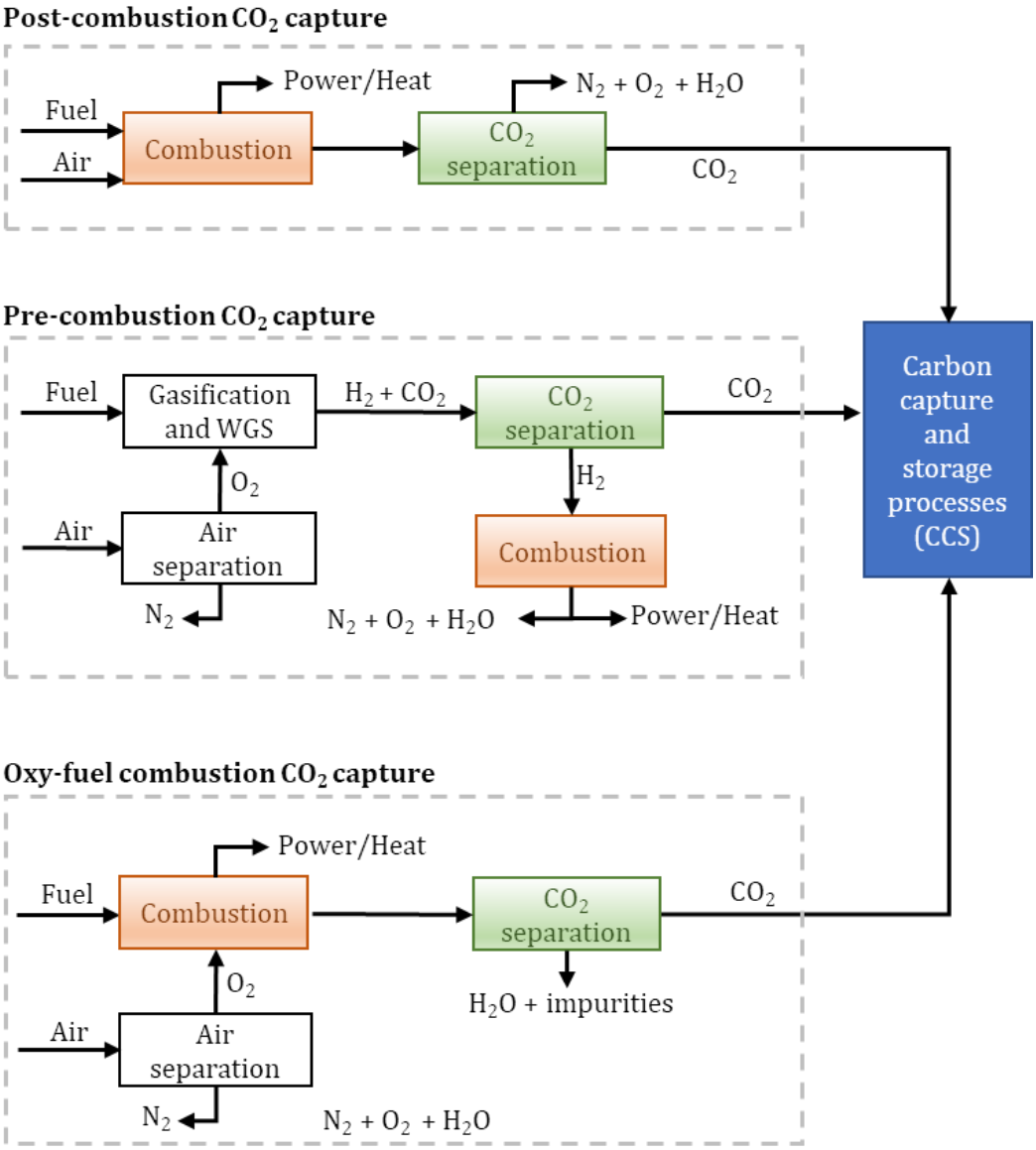

Figure 11. Main strategies for the capture of CO_2 derived from the consumption of fossil fuels. Based on reference [50].

In terms of transport and storage, CO_2 presents challenges similar to those seen with hydrogen. It is a gas at room temperature (boiling point at −78 °C). It can be transported similarly to natural gas through pipes, or it can be even compressed or liquefied, stored in pressurized vessels or in tankers trucks for transport [47,48]. All these techniques suppose an energetic investment, and therefore economic. Thus, a very attractive solution for long-term storage of large amounts of CO_2 would be geological storage underground (e.g. depleted hydrocarbon deposits) [48,49].

The implementation of CO_2 capture systems represents an economic outlay, either to create new infrastructure or adapt the existing one. Many countries regulate

carbon emissions through economic sanctions when limits are exceeded, which encourages the adoption of this type of measures by the industry.

1.5 Natural Photosynthesis

Nature has its own mechanisms, developed and perfected through millions of years of evolution. This is the reason why, whenever possible, scientists have taken Nature as a mirror to look at. One of these natural processes, very relevant because it supports the vast majority of life on Earth, is the photosynthesis, where sunlight is used to convert water and carbon dioxide in oxygen and sugar molecules [51]. Plants or algae are photosynthetic organisms capable of carrying out this transformation, using water as an electron donor, thus involving molecular oxygen in the mechanism. Although they are not of interest to this work, there are other organisms, such as bacteria, that use reduced inorganic compounds as a source of electrons, meaning no oxygen is produced [52]. Natural photosynthesis is usually condensed into a single reaction (**Eq. 14**), although it is actually a more complex process.

$$\text{sunlight} + a\text{H}_2\text{O} + b\text{CO}_2 \rightarrow c(\text{CH}_2\text{O})_n + d\text{O}_2 \qquad \text{Eq. 14}$$

This process takes place in the so-called thylakoid membranes (**Figure 12**) in the cells of oxygenated photosynthetic organisms. Inside the cells, the multi-protein complexes responsible for photosynthesis are located. There are two types of these multi-protein complexes, known as photosystem I (PSI) and photosystem II (PSII), each of which has a characteristic chlorophyll-based reaction centre, capable of absorbing light, called P700 for PSI, and P680 for PSII, where the number refers to the wavelength at which they absorb the light. Additionally, they also have other pigments that collaborate in this light harvesting process.

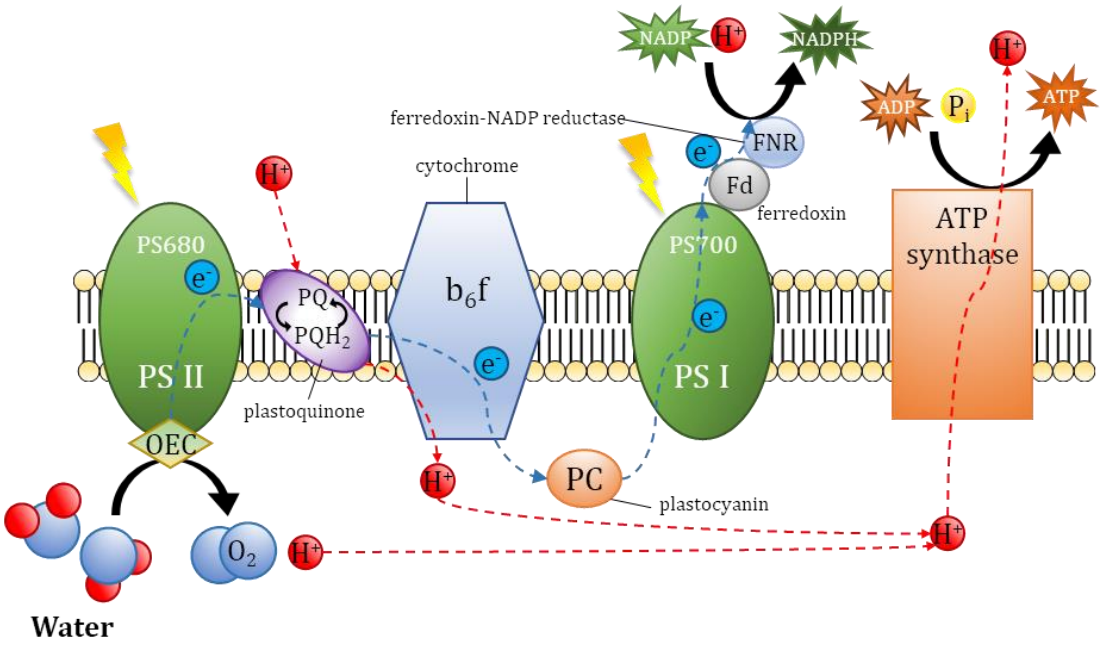

Figure 12. Photosynthetic electron-transfer chain of the thylakoid membrane. Adapted from [53].

Once the PSII begins the light absorption, the energy is transmitted from one pigment to another until it reaches the reaction centre. When P680 receives enough energy, an electron is excited and released from PSII and passed through the electron transport chain, consisting first of plastoquinone (PQ), a lipid molecule, then the enzymatic complex b6f, the plastocyanin (PC) protein, before reaching PSI. The lost electron on the PSII reaction centre is later replenished by water splitting. This reaction takes place after the electron donation from the oxygen-evolving complex (OEC), a metal cluster consisting of a cubane-type oxo-bridged structure of four Mn and one Ca ions (**Figure 13**). Additionally, the proposed structure is completed by adding four water molecules which are bound to one Mn and the Ca atoms [54].

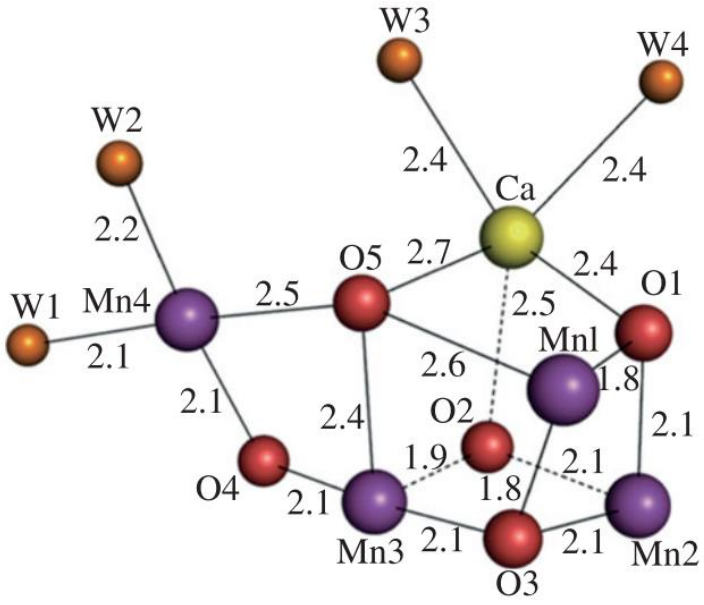

Figure 13. Structure of the Mn_4CaO_5 cluster present in PSII, extracted from the reference [55].

Although mechanistically the water oxidation reaction that takes place in the OEC is debatable, it has been demonstrated that the Mn_4CaO_5 cluster could store four equivalent oxidative charges, thus facilitating the four-electron oxidation of two water molecules (**Eq. 15**) [55,56]. This reaction only generates oxygen as a by-product, but of paramount importance because it maintains the oxygenated life of the planet.

$$2H_2O + 4hv \rightarrow O_2 + 4H^+ + 4e^- \qquad \text{Eq. 15}$$

Electrons reaching PSI through the electron transport chain, together with protons released in water splitting are used at the end of this step of photosynthesis to form adenosine triphosphate (ATP) and nicotinamide adenine dinucleotide phosphate (NADPH), energy-carrying organic molecules necessary in the next step of photosynthesis, the Calvin cycle or the "dark reactions", referring to the absence of light, where the fixation of carbon dioxide takes place, being incorporated into organic molecules and reduced, finally forming carbohydrates [51,52,55].

1.6 Water Splitting

The concept of manufacturing fuels using sunlight takes Nature as an example, as it is based on natural photosynthesis. In this manner, Artificial photosynthesis (APS), starting from water and using sunlight, is capable of carrying out the oxidation of water to oxygen (**Eq. 15**), releasing also protons and electrons, being able to use the latter in a reduction process, typically either protons or CO_2 to H_2 (**Eq. 16**) or hydrocarbons (which will be further discussed later on), respectively. Thus, substances with high-energy content are generated that could be consumed as fuels.

$$4H^+ + 4e^- \rightarrow 2H_2 \qquad \text{Eq. 16}$$

$$2H_2O \rightarrow 2O_2 + 4H_2 \qquad \text{Eq. 17}$$

When the processes in **Eq. 15** and **Eq. 16** are combined, the **Eq. 17** is obtained. This reaction is called water splitting, in which the water molecule is broken down into its components, dioxygen and dihydrogen gases. It is the reverse of the process previously described in section 1.3.4, page 17, which explained the operation of the hydrogen fuel cell.

Solar-driven photoelectrochemical water splitting is emerging as one of the most interesting techniques to produce clean hydrogen [57]. This process would take place in electrolysers analogous to those used for the electrolysis of water. Photovoltaic cells (PVC) could be used to transform solar radiation into electrical energy that promotes water splitting. However, the high cost of PVCs is a drawback when it comes to scaling the process [21]. The alternative is the use of a photosensitive substance (PS), a light-harvesting material or molecule that allows direct use of sunlight, without its prior conversion into electricity.

The typical photoelectrochemical cell (PEC) assembly for the photoinduced production of hydrogen from water splitting would be the one shown in **Figure 14**. It consists of an anodic and a cathodic compartment where the oxidation and reduction semi-reactions would take place, respectively. Each compartment consists of an electrode, linked together by an external circuit suitable for the electron flow. Electrodes are generally semiconductor materials, which can serve as light-harvesting units. Photosensitive molecules (photosensitizers, PS) can also be

used to modify the electrodes and promote light absorption. Furthermore, at the anode we find the Water Oxidation Catalyst (WOC) and at the cathode the Hydrogen Evolution Catalyst (HEC). A polymer electrolyte membrane (PEM) serves as junction between compartments, allowing the flow of protons and facilitating the collection of O_2 and H_2 [58].

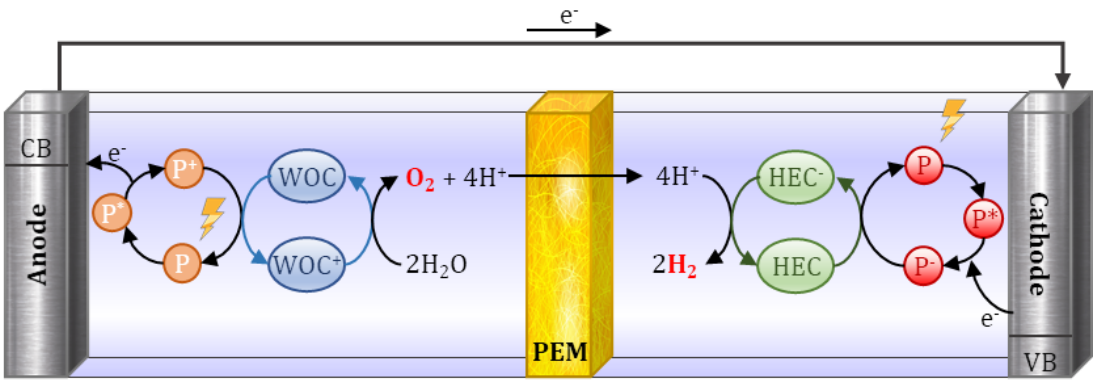

Figure 14. Scheme of a photoelectrochemical (PEC) cell that operates the overall light-driven water-splitting reaction. Adapted from reference [58].

Titanium dioxide (TiO_2) has been one of the most studied materials, not only as a light-harvesting unit but also as a catalyst (photocatalyst if we take into account the aforementioned photo-absorbent properties), since Honda and Fujishima reported in 1972 the first photocatalytic water splitting reaction [59,60]. When irradiated with UV light, the migration of electrons from the photoanode (TiO_2) to the photocathode (Pt) occurred, and the formation of oxygen and hydrogen, respectively, was observed on the surface of the electrodes (**Figure 15**).

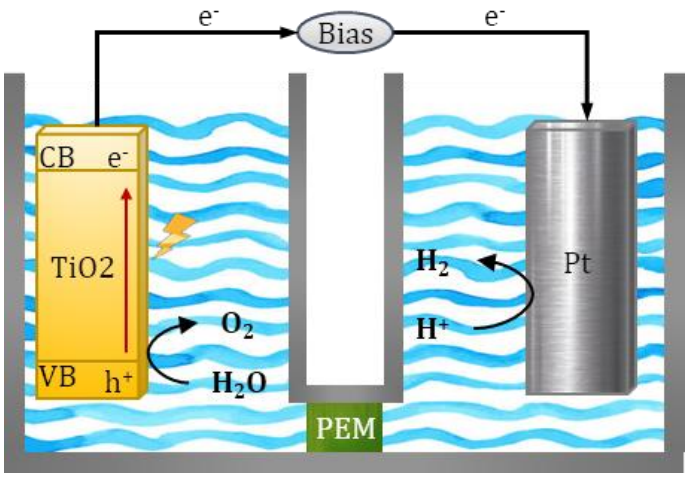

Figure 15. Photoelectrochemical water splitting with TiO_2 as photoanode and Pt as counter electrode, separated with a polymer electrolyte membrane. Adapted from reference [61].

Although TiO_2 draws a lot of interest because it is very stable and affordable, its photocatalytic activity is limited to the range of ultraviolet light. Over the past years, different strategies have been developed for the visible light-activation of TiO_2 [62,63]. Additionally, other photocatalytically active materials used for water splitting are Ta_2O_5,[64], WO_3 [65], ZnO [66], ZrO_2 [67], or Fe_2O_3 [68]. PEC electrodes could also be decorated with photo-responsive molecules such as dyes and pigments (such as chlorophyll in artificial photosynthesis). $[Ru(bpy)_3]^{2+}$ (bpy = 2,2'-bipyridine) and its analogues are among the most developed photosensitizers in this field [69,70].

In order to ensure the efficiency of a PEC, each component should be optimized separately. Besides the photoactive species, the other key aspect when building a PEC is the design of both the WOC and HEC. These catalysts can be tested in a conventional single-compartment three electrode configuration, an electrochemical set-up consisting of a potentiostat to apply the desired potential, a working electrode where the catalyst would be immobilized, a reference electrode and a counter electrode. These catalysts are used to speed up the water oxidation and

proton reduction reactions, respectively, offsetting the overpotential required for the formation of O_2 and H_2 (concept introduced in page 10).

After carrying out the electrochemical study of a species as a catalyst for OER or HER, a polarization curve similar to the ones shown in **Figure 16** is obtained, plotting the applied potential against the measured current density (normalizing the intensity of the current with the area working electrode). Overpotential is typically assessed at onset (η_0), resulting from the difference between the thermodynamic potential at equilibrium (E^0) and the current potential at which the catalyst begins to operate, but also at a given current density, being $|j|$ = 10 mA·cm^{-2} (η_{10}) the most commonly used convention for the water splitting electrocatalysts [57,71].

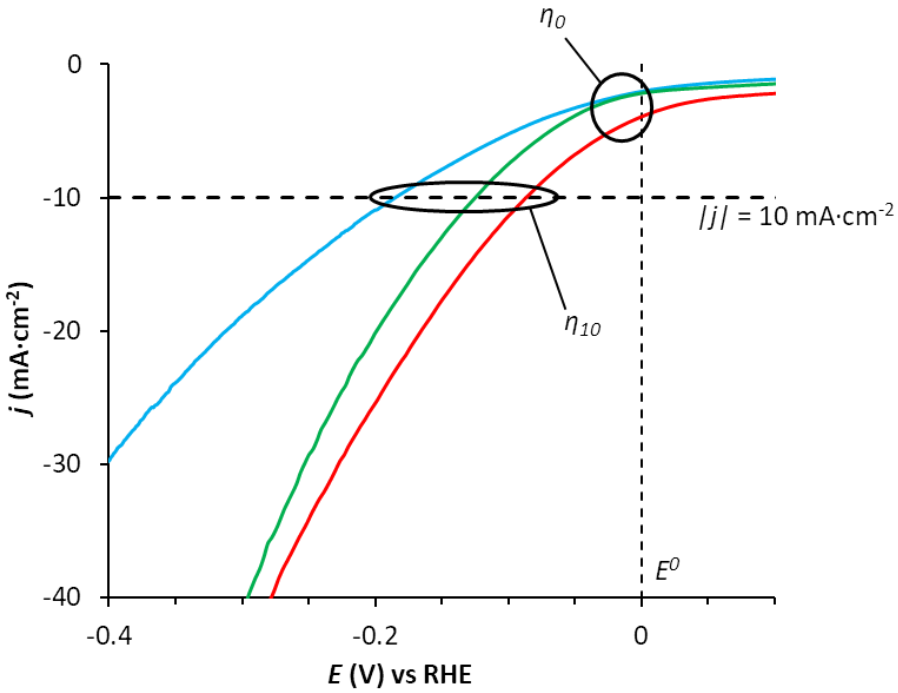

Figure 16. Typical polarization curves obtained for the electrocatalytic evaluation of HECs at pH0.

As the value of the current density *j* is already normalized according to the electrode area, this allows the comparison between different systems under similar reaction conditions (pH, catalyst load) but different surface area. Generally, the best overpotentials reported for OECs are around 200 mV, while for HECs they are less than 100 mV [72]. Although there are many considerations when evaluating the

different catalysts, the one that offers the lowest overpotential at a given current density is considered more efficient.

Additionally, there are other analyses and parameters that serve to evaluate the efficiency of the catalysts used for OER and HER in water splitting. Tafel analysis allow to know more details about the mechanism and the reaction rate through the calculation of two different parameters, the so-called Tafel slope and the exchange current density (j_0). This analysis also starts from a voltammogram, like the one in **Figure 16**, transforming the data to obtain a "log (j)" vs. "overpotential (η)" plot. The Tafel equation is calculated by fitting the linear segment to a line, whose slope (Tafel slope), yields kinetic information about the rate determining step of the reaction (this will be further elaborated when discussing the HER mechanism) [73]. The exchange current density (j_0), a descriptor of the catalytic activity, can also be deduced from the Tafel analysis, resolving the Tafel equation for η = 0 mV. It corresponds to the obtained current in the lack of faradaic processes.

Two other parameters to take into account when working with catalysts, regardless of their application, are the turnover number (TON) and the turnover frequency (TOF) [74]. Given a simple catalytic reaction, where the products are obtained directly from the reactants by the action of a catalyst, the TON is a measure of the lifetime robustness of the catalyst. It corresponds to the total number of cycles that a catalyst can achieve at a given time. Although TON does not depend on time, since it is a unitless parameter, it is generally calculated for a certain time range (t = T), thus facilitating the comparison between catalysts. TON values can be calculated from the **Eq. 18**, dividing the number of mol of product formed at a certain time $n_{P(t=T)}$, by the number of mol of catalyst (n_{cat}). TOF, meanwhile, is a kinetic parameter that measures the instantaneous efficiency of the catalyst. It is calculated by dividing the TON value by a certain period of time (**Eq. 19**).

$$TON_{(t=T)} = \frac{n_{P(t=T)}}{n_{ccat}} \qquad \text{Eq. 18}$$

$$TOF_{(t=T)}(s^{-1}) = \frac{TON_{(t=T)}}{T} = \frac{n_{P(t=T)}}{n_{cat} \cdot T} \qquad \text{Eq. 19}$$

The main objective of this Doctoral Thesis is to develop nanomaterial-based systems to catalyse the reductive half-reaction of water splitting, i.e. generating H_2 through the Hydrogen Evolution Reaction (HER). Additionally, and still within the framework of artificial photosynthesis, the suitability of some of the prepared catalysts in the reduction of CO_2 will also be studied. In the following sections, the mechanistic aspects and current state of these two processes will be further studied.

1.6.1 Hydrogen Evolution Reaction

The hydrogen evolution reaction (HER) is the cathodic half-reaction of the splitting of water and, therefore, one of the electrocatalytic processes that arouses most interest nowadays. From a thermodynamic point of view, it is a simpler process than its counterpart, the oxygen evolution reaction (OER). HER is a two-electron transfer reaction, which involves the formation of a H-H bond, and it requires a suitable catalyst (HEC) to reduce the overpotential of each step of the reaction. The general consensus is that when designing an electrocatalyst, it must be able to catalyse the HER reaction within an overpotential of 100 mV or less [75].

1.6.1.1 Mechanism of the HER by heterogenous catalysts

Proton electroreduction can take place under acidic or alkaline conditions. The potential required to carry out the transformation will depend on the pH, according to the Nernst equation (**Eq. 4**, page 10), and also on the overpotential of the system.

Focusing solely on nanomaterials like HECs, there are two generally accepted pathways for the HER, either the Volmer-Heyrovsky or the Volmer-Tafel mechanism [73,76–78]. Thus, in acidic media, the processes consist of the following steps:

Volmer step	$H^+ + e^- \rightarrow H_{ads}$	Eq. 20
Heyrovsky step	$H_{ads} + H^+ + e^- \rightarrow H_2$	Eq. 21
Tafel step	$H_{ads} + H_{ads} \rightarrow H_2$	Eq. 22

Volmer's reaction is the first step and is common to all HECs. It involves the adsorption of a proton on the catalyst surface, through a single electron transfer process. Desorption can occur in two ways: i) the Heyrovsky reaction, which means the electron assisted coupling of the adsorbed hydrogen atom with a proton in solution, or ii) the Tafel reaction, in which two adsorbed hydrogen atoms recombine.

Either way, the process ends releasing hydrogen. **Figure 17** shows the scheme of the different mechanisms in acidic media. **Eq. 23-25** represent the corresponding reactions in alkaline media, occurring analogously to the acidic counterpart.

Volmer step	$H_2O + e^- \rightarrow H_{ads} + OH^-$	Eq. 23
Heyrovsky step	$H_2O + e^- + H_{ads} \rightarrow H_2 + OH^-$	Eq. 24
Tafel step	$H_{ads} + H_{ads} \rightarrow H_2$	Eq. 25

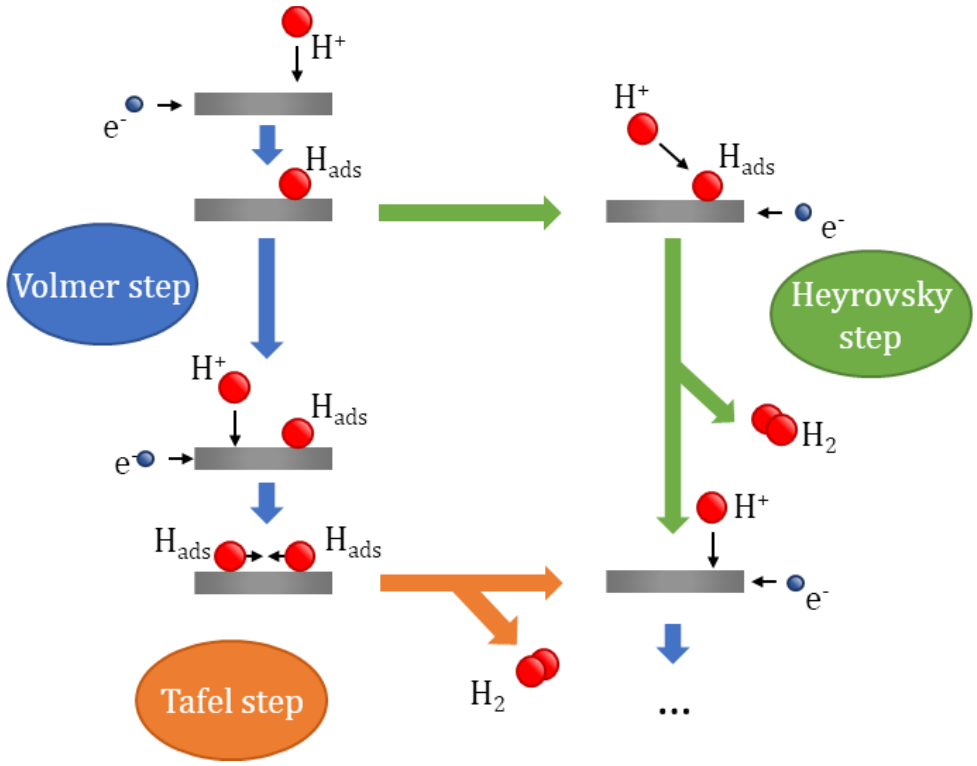

Figure 17. Outline of the proposed mechanisms for the hydrogen evolution reaction in an acidic medium. Adapted from reference [79].

The specific interaction between the hydrogen atoms and each possible HEC at the surface of the electrode make the choice of the HECs a fundamental decision for the process to proceed in one way or another. Tafel analyses help to propose a mechanism when we use different HECs, and it also helps us to compare the catalytic activity of different electrocatalysts. The Tafel slope calculated for each electrocatalyst, explained above, provides information related to the rate-determining steps when compared with the values calculated through kinetic models [73]. The Tafel equation used in HER is actually a simplification of the Butler-Volmer equation (**Eq. 26**), where j is the current density, j_0 is the exchange

current density, α is the charge transfer coefficient, η is the number of electrons transferred, F is the Faraday constant, R is the ideal gas constant, and T is the temperature [75].

$$j = j_0[-e^{-\frac{\alpha n F \eta}{RT}} + e^{\frac{(1-\alpha) n F \eta}{RT}}] \quad \text{Eq. 26}$$

Butler-Volmer equation shows the strong electrochemical potential-dependence of the kinetics of the HER reaction. At low overpotentials ($\eta \leq 0.005$ V), **Eq. 26** can be simplified, resulting in equation **Eq. 27**, showing a linear correlation between the overpotential and the current density when we are close to the equilibrium potential.

$$\eta = \left(\frac{RT}{nFj_0}\right) \cdot j \quad \text{Eq. 27}$$

Oppositely, by approximating the Butler-Volmer equation to overpotentials farther from the equilibrium potential ($\eta > 0.005$ V), Tafel equation is obtained (**Eq. 28**). This indicates that there is a linear dependence between the overpotential and, in this case, the log *j*, where the slope *b* would correspond to the aforementioned Tafel slope.

$$\eta = \frac{-2.3RT}{\alpha nF} \cdot \log j_0 + \frac{2.3RT}{\alpha nF} \cdot \log j = a + b \cdot \log j \quad \text{Eq. 28}$$

The value of *b* observed for the different HECs is used to discern the rate-determining steps (RDS) of the reaction in each case. A Tafel slope value around 120 mV·dec^{-1} indicates that the RDS corresponds to the Volmer reaction. Instead, the limiting stage will be either Heyrovsky or Tafel reaction when the value of the slope b is much lower, usually around 40 or 30 mV·dec^{-1} respectively [75,80].

1.6.1.2 Nanomaterial-based catalysts in the HER

Efficient catalysts are required to improve HER performance. Almost a century ago, Bowden and Rideal [81] were already studying the effect that a variety of metals, in the form of films, could have on the electrocatalytic HER. Noble metal-based materials, and more specifically platinum, is the one that has offered the best

performance in this reaction, offering high exchange current densities and low overpotentials [82].

This trend could be explained through the HER mechanism, detailed in the previous section. Both Volmer-Tafel and Volver-Heyrowsky pathways involve the adsorption of hydrogen, thus forming intermediates (H_{ads}) on the surface of the electrode/catalyst. The strength of this interaction (hydrogen adsorption free energy, ΔG_H), will determine the RDS of the reaction, as it can affect both the initial adsorption step and the subsequent desorption, as originally described by Parsons [83]. Therefore, an ideal efficient HEC should offer an optimal $\Delta G_H \approx 0$ [84–87]. As a result of this, and based on experimental studies and theoretical calculations, a Volcano-like relation (**Figure 18**) has been elaborated, where optimal M-H binding energy (not too low or too high), and hence maximum activity, could be found at the top of the Volcano graph.

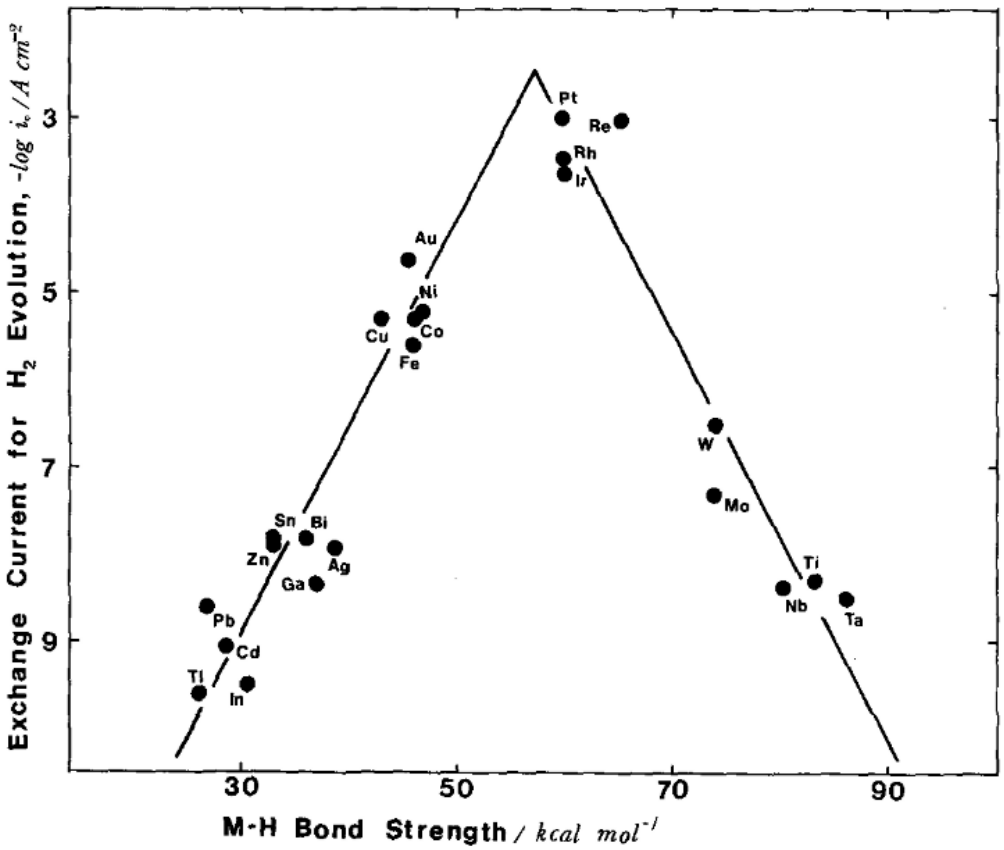

Figure 18. Volcano-plot based on intermediate metal-hydrogen bond formed during HER, as originally proposed by Trasatti [88].

Volcano plots are built by plotting the exchange current densities of HER versus the strength of the metal-hydrogen bonds of different metals. Since the publication of the first Volcano plot, by Trasatti in 1972 [88], new studies have emerged that modify some of the assumptions used for the Volcano-dependence calculations [89–91]. Nonetheless, common agreement seems to suggest that platinum-group metals have surface characteristics that make them more suitable as HECs [75].

The main drawbacks of the use of Pt as a HER electrocatalyst are its high demand and high cost due to its scarcity. This limitation is exacerbated when going from laboratory scale to real applications. However, its appeal as a catalyst has stimulated the search for strategies that are more affordable and scalable without giving up the use of this noble metal. An efficient way to reduce the amount of Pt required for catalysis is to use ultra-small platinum nanoparticles (Pt NPs). There are several studies that relate the drastic reduction in the size of the nanoparticles with the increase of the exchange current densities and the reduction of the overpotential [92–97].

Additionally, supports could be used to ensure the stability and dispersibility of these systems, preventing the aggregation of the nanoparticles, both during the synthesis and the electrochemical studies, thus maintaining their efficiency. In 2014, Y. Lei *et al.* reported a system of ultra-small platinum nanoparticles (1-3 nm) grafted on cellulose-derived carbon nanofibers (CNFs), with a Pt mass loading inferior to 1wt% [98]. A working electrode was prepared by dispersing the electrocatalyst in a Nafion® solution, and depositing it via spin-coating on a carbon paper. Whereas the commercial Pt/C electrode (Pt 10 wt%) shows a very low overpotential at $|j|$= 10 mA·cm^{-2} (η_{10} = 19 mV), this system with a Pt loading ten times lower shows just a slightly worse overpotential (η_{10} = 55 mV), maintaining its performance for more than 1000 linear sweep voltammetry (LSV) cycles in acidic conditions.

Similarly, Devadas and Imae presented in 2016 a Pt-based composite, consisting of dendrimers-encapsulated Pt nanoparticles, supported on carbon materials, such as nanohorns (CNHs) or nanotubes (CNTs) [99]. In this case, Pt NPs were presynthesized by chemical reduction of the Pt precursor ($Na_2PtCl_6 \cdot 6H_2O$) in the presence of the dendrimer, and subsequently impregnation on the carbon material. For the electrochemical test, the material was immobilized on a glassy carbon (GCE)

electrode using a Nafion® solution. With a platinum loading of about 1wt%, and Pt NPs mean size of 5 nm, these composite catalysts delivered low onset overpotentials (η_0 = 16 mV) and high stability in 0.5 M H_2SO_4 solution, being able to hold the activity of the catalyst towards the HER up to 500 LSV cycles. It can be considered a more than reasonable HER efficiency when compared to the commercially available Pt/C performance, which delivers $\eta_0 \approx 0$ mV, but with a much higher Pt content (40 wt%).

Following this path of decreasing Pt loading without compromising catalyst efficiency, J. Chen and co-workers designed in 2010 a low-cost monolayer Pt-based catalyst on tungsten monocarbide substrates, to operate the hydrogen evolution reaction in acid conditions. The electronic and chemical properties of this hybrid material matches that of bulk Pt, thus demonstrating that the topmost layer of bulk platinum is probably the determining factor in its catalytic activity, being able to replace the rest with a more affordable carbon-based material [100].

Combining both strategies of lowering the metal content on the NPs and the use of supporting materials, X. Sun *et al.* reported a Pt-nanoclusters as catalyst for the HER. The synthesis was carried out by means of atomic layer deposition (ALD), in a reactor that contained, in addition to the Pt precursor, nitrogen-doped graphene nanosheets. A glassy carbon rotating-disk electrode (GC-RDE) serves as the working electrode. These systems present negligible overpotentials towards HER, comparable with commercial Pt/C, the Tafel slope being even lower (29 mV dec^{-1} vs 31 mV dec^{-1} for the Pt species) in 0.5M H_2SO_4 solution. Stability was also studied, not losing catalytic activity in 100 LSV cycles [101].

More recently, Fang et al. developed an atomically dispersed Pt on metal-organic framework (MOF) derived N-C framework, following the same synthetic route. The combination of ALD technique and a well-defined MOF structure were shown as key in the uniform deposition of single-atom Pt. The electrocatalyst was tested, after immobilization on a carbon cloth as working electrode, in 0.5M H_2SO_4 and 1.0M KOH solutions The overpotentials achieved were 19 mV and 46 mV in the acidic and basic media respectively, surprisingly also demonstrating excellent durability (up to 20h) in a wide pH range [102].

Preparing single-atom and nanoclusters as catalysts is challenging, given the tendency of atoms to diffuse and agglomerate, forming larger nanoparticles, which can be difficult to control when scaling up the synthesis [103,104]. Thus, these promising atom-scale catalytic systems are required not only to be very efficient, but also to offer satisfactory stability [105].

Despite efforts to develop economically affordable Pt-based catalysts, other factors must be considered. Most studies focus on the acidic medium because that is where Pt outshines all other metal-based candidates to catalyze the HER. However, its performance in an alkaline medium is more irregular, frequently presenting stability problems [97,106].

Ruthenium nanoparticles have been widely studied as catalysts in different applications [107]. However, within the field of HER for water splitting, the available literature is not as extensive as that found for platinum, and most of the publications are concentrated in recent years. This sudden interest in Ru as a substitute for Pt as a catalyst is due to the fact that it is more affordable, it is more stable in a wider pH range, and considering the strength of M-H bond, Ru-H bond is slightly weaker than for Pt, but according to experimental results and theoretical calculations, it does not represent a great concern in terms of catalytic efficiency [107,108]. Ru NPs of different sizes and morphologies have been reported. One of the most common problems with these materials is that they are prone to aggregation. In this way, much of the research on Ru NPs as an electrocatalyst for HER resorts to the use of supports as stabilizers, similar to what has already been discussed regarding Pt, prior to immobilization on the electrodes [97].

J. Baek *et al.* used a 2-dimensional (2D) nitrogenated-carbon (C_2N) structure to stabilize the Ru NPs. C_2N is a holey-structure in which nitrogen atoms serve as active sites to accommodate Ru (**Figure 19a**). Overpotentials in both acid and basic media are slightly lower than in commercial Pt/C (η_{10} = 13.5 mV and η_{10} = 17 mV in acid and basic media, respectively). Stability was also tested at 10,000 LSV cycles, with barely any shift in the curve [109]. Baek's group also reported a system of Ru NPs uniformly deposited on edge-carboxylic-acid-functionalized graphene nanoplatelets (CGnP) whose HER performance in both acid and basic media surpasses that of commercial Pt/C catalysts, with Tafel slopes of 30 mV·dec^{-1} in 0.5M

H_2SO_4 and 28 mV·dec^{-1} in 1M KOH), and low overpotentials (η_{10} = 13 mV and η_{10} = 22 mV in acid and basic media respectively). The substrate was prepared via ball-milling graphite, in the presence of dry ice. In this way, the resulting CGnPs have improved electrical conductivity and numerous active sites (carboxylic acid groups) that allow simple metal ion anchoring. In this case, the ruthenium ions are subsequently reduced to Ru^0 NPs (~2nm) by a thermal annealing treatment (**Figure 19b**) [110]. This shows that the preparation and functionalization of the support is also key to ensure the efficiency of the Ru-based catalyst. The use of amorphous or highly defective materials can affect their performance (electrical conductivity or availability of active sites).

Other commonly used supports for Ru NPs are carbon microfibers [111], carbon nanotubes (CNT) or [112] metal-organic frameworks (MOF) [113]. X. Xu *et al.*, recently reported Ru NPs dispersed on N-doped carbon hollow nanospheres (Ru@NCHNS). The morphology of the 3D matrix is expected to increase the surface area of the support and facilitate access to the active sites. A facile synthetic method is proposed, based on the SiO_2-template approach (**Figure 19c**). The resulting Ru-based composites delivers an overpotential of η_{10} = 28.9 in 1.0M KOH, outperforming both commercial Pt/C (50.5 mV) and a Ru@NC hybrid (185.6 mV), prepared under the same conditions without the SiO_2-templating step, thus demonstrating the influence of the 3D-matrix. Almost no changes in the polarization curve were observed after 1000 LSV cycles, strongly consolidating its position as one of the best reported Ru-based nanocatalysts towards HER in alkaline conditions [114].

As was the case with Pt, examples of ruthenium atomically dispersed in carbon supports are also found, such as that reported by Chen's group [115]. The atomic-Ru dispersed on N-doped carbon nanowires (CNW) outperformed the results of commercial Pt catalysts in alkaline medium (η_{10} = 12 mV vs. -49 mV for Pt/C). Outstanding results were also obtained by R. Tan *et al.* [116] who prepared a modulable nanoporous MoS_2 structure, to accommodate dispersed single-atom Ru, serving as highly efficient HER catalyst.

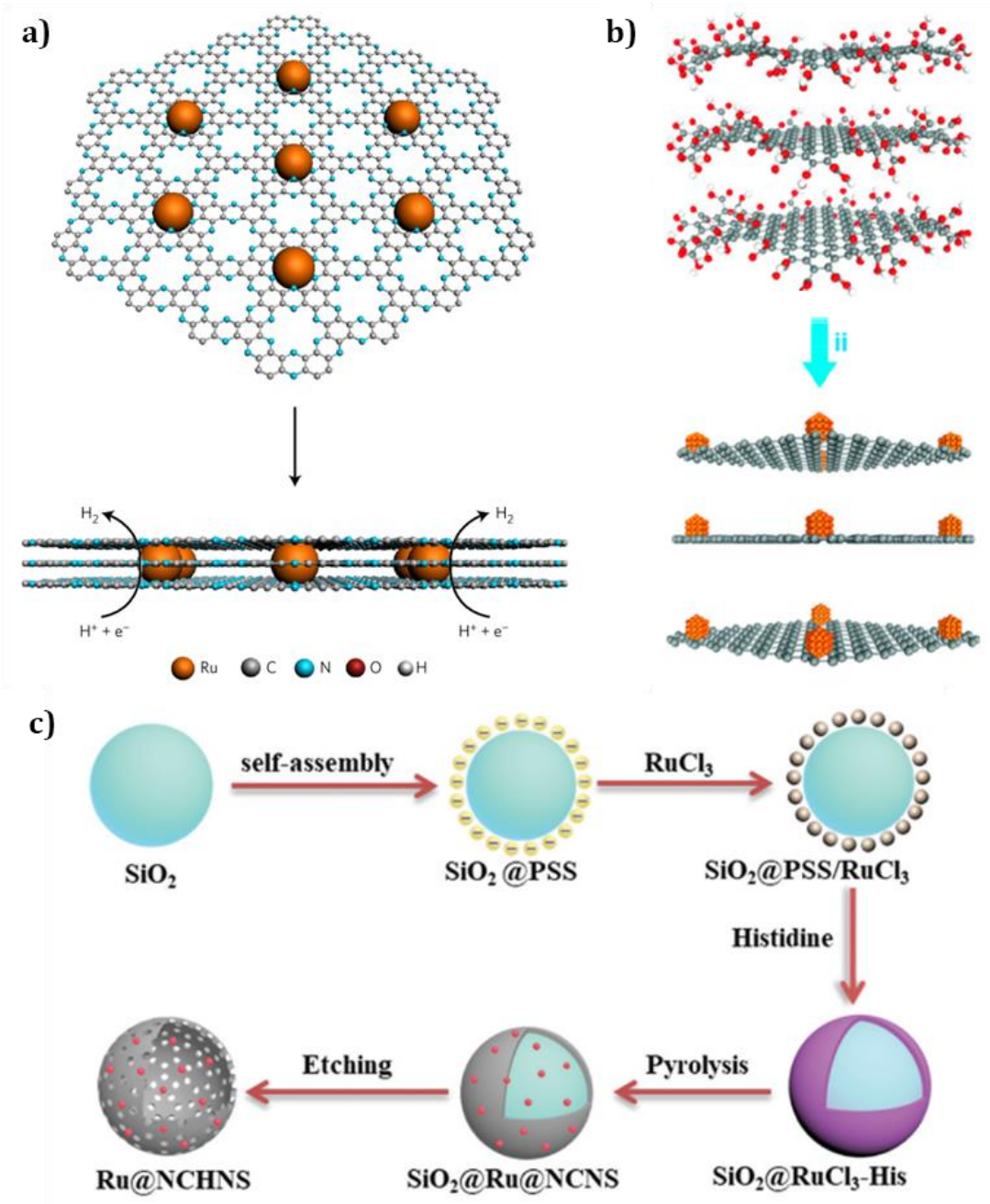

Figure 19. (a) Ru NPs dispersed on the 2D nitrogenated carbon structure [109], (b) reduction of Ru ions and formation of Ru NPs on the surface of the graphene nanoplatelets (CGnPs) [110], (c) schematic representation of the synthetic procedure of Ru NPs dispersed on carbon hollow nanospheres (Ru@NCHNS) from a self-assembled SiO_2@PSS (poly(sodium 4-styrenesulfonate) composite. After wrapping with Ru (III) and histidine and a subsequent heat treatment, SiO_2@Ru@NCNS (Ru NPs on carbon nanospheres and SiO_2 template) are obtained. After selective etching treatment of the SiO_2 template with HF solution, Ru@NCHNS are yielded [114].

Unlike with Pt, when working with Ru, it is necessary to take into account the oxidation state on the surface of the nanomaterials. Changes, usually between Ru^0 and Ru^{IV}, may occur when Ru-based materials are exposed to air or when a given potential is applied during electrochemical processes. This can affect its performance as a catalyst, since the efficiency will vary, depending on the acidic or basic medium, if the ruthenium is as metallic-Ru^0 or as Ru^{IV} oxidation state [111].

The choice of the appropriate synthetic route allows control over the key parameters in the activity and stability of the nanoparticulated co-catalyst, such as size and shape, surface environment, structure and homogeneity. The organometallic approach is a reproducible synthetic method that allows the preparation of Ru NPs in mild reaction conditions controlling most of these parameters. (**Figure 20**) [117]. During the synthetic procedure, H_2 pressure triggers the decomposition of the olefinic ligands normally present in the organometallic precursor, and the by-products can be easily removed. Importantly, the presence of a stabilizing molecule is required to control the growth of the nanoparticles and ensure their stability, preventing them from agglomerating. Through this route, well-defined and dispersed nanoparticles can be obtained, which can also serve as catalysts in HER for water splitting [118].

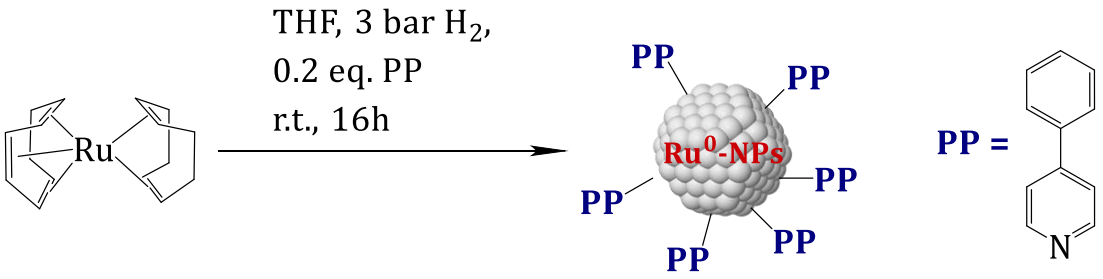

Figure 20. Synthesis of ruthenium nanoparticles stabilized by 4-phenylpyridine (PP) following the organometallic approach [119].

Following this method, the research group recently reported on a HER catalyst consisting of Ru NPs stabilized with 4-phenylpyridine [119]. A layer of RuO_2 was formed on the surface of the NPs after controlled exposure to air. It was observed that by applying a reductive potential in a 1M H_2SO_4 aqueous solution, this partial oxidation could be reversed, "recovering" the synthesized Ru^0 NPs, and maintaining the coordination of the pyridine ligand. This step enhances the catalytic efficiency of

the NPs, reaching impressive overpotentials of $\eta_0 \approx 0$ mV and $\eta_{10} = 20$ mV, with hardly any changes in activity or the morphology of the nanoparticles during 12h. In 1M NaOH solution, reduction of the catalyst could not be reversed, but the pyridine-stabilized RuO_2/Ru^0 NPs still exhibit excellent activity and stability for 12h towards HER ($\eta_0 \approx 0$ mV and $\eta_{10} = 25$ mV). Under both pH conditions, these nanocatalysts overshadow the catalytic performance of both Pt/C and Ru-black commercial catalysts. Additionally, density-functional theory (DFT) calculations suggest that the coordinated ligands on the surface of NPs may play a role in their electrochemical performance.

This justifies the interest in the design of ligand-capped nanoparticles for HER. The use of different ligands makes these systems easily tunable, being able to modify their morphology and surface composition, hence their catalytic activity.

1.6.1.3 Benchmarking methodology for heterogeneous materials for HER electrocatalysis

Different parameters have been previously detailed in the literature in order to compare the efficiency of catalysts. However, it is often difficult to make an appropriate comparison when the reaction conditions or the nature of the catalysts are very different. In 2015, Jaramillo *et al*. elaborated a standard benchmarking protocol for comparing different catalysts, applicable to both WOCs and HECs [120]. To develop this methodology, they subjected catalysts to different electrochemical processes under extreme acid (1M H_2SO_4) or alkaline (1M NaOH) conditions. The different techniques involved in this protocol are shown in **Figure 21** and explained below**.**

These experiments can be classified into groups depending on the disclosed information:

- **Surface characterization**: Includes X-ray photoelectron spectroscopy (XPS), a qualitative analysis technique that allows knowing the nature and oxidation state of the chemical species responsible for catalysis. Once the electrode has been prepared, immobilizing the catalyst, it is necessary to determine the area of the electrode available to carry out the electrochemical process, which usually differs from the geometric surface area. This

parameter is referred as the electrochemically active surface area (ECSA). The roughness factor (RF) expresses the ratio between active surface and geometric area. ECSA value can be estimated by means of double-layer capacitance (C_{DL}) measurements, by carrying out cyclic voltammograms (CV) in a non-Faradaic region. The calculation is based on the assumption that, in this region, the measured current is due to the double-layer charging. Based on this, the load current (i_c) is directly proportional to the product of C_{DL} and the scan rate (ν) (**Eq. 29**).

$$i_c = \nu \cdot C_{DL} \qquad \text{Eq. 29}$$

After plotting i_c as a function of ν, a linear equation is obtained and whose slope equals C_{DL}. Then, ECSA of a given catalyst can be calculated by dividing the obtained C_{DL} value by the specific capacitance (C_S) of the sample, intrinsic to the material and solution used (**Eq. 30**). Finally, RF value can be calculated using the ECSA and the value of the geometric area of the electrode ($S_{elec.}$) (**Eq. 31**).

$$\text{ECSA}\ (cm^2) = \frac{C_{DL}}{C_S} \qquad \text{Eq. 30}$$

$$RF = \frac{ECSA}{S_{elec.}} \qquad \text{Eq. 31}$$

- **Catalytic activity**: The characterization of the catalytic efficiency of the materials is carried out by means of a combination of rotary-disk electrode (RDE) voltammetry measurements at 10 $mV \cdot s^{-1}$ scan rate, and both current-controlled chronopotentiometric and potential-controlled chronoamperometric measurements by 30 s steps. From this study of catalytic activity, the overpotential (η_{10}) is obtained, a value indicating the overpotential required to achieve a current density of $|j|$ = 10 $mA \cdot cm^{-2}$.
- **Short and long-term stability**: The study of the stability of the catalyst over time is carried out by applying constant current density of $|j|$ = 10 $mA \cdot cm^{-2}$ to the electrode containing the catalyst, measuring the potential fluctuations during a given time. Shorter stability tests last 2 hours, while long-term studies can take up to 24 hours.

- **Faradaic efficiency (ε)**: It is used to verify that all electrones transferred to the system are devoted to the OER or HER. To do this, the amount of O_2 or H_2 generated in the electrocatalytic OER or HER, respectively, is measured and divided by the expected amount of each gas based on the electrons transferred during electrocatalysis.

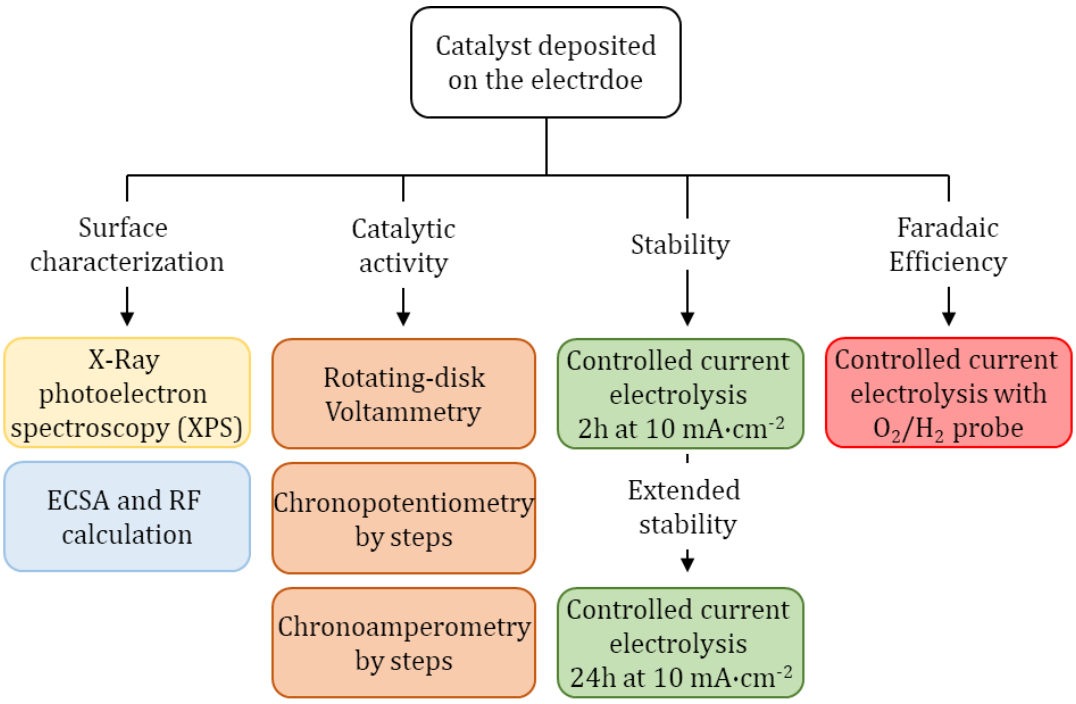

Figure 21. Jaramillo's benchmarking protocol of heterogeneous catalyst for both OER and HER [120].

1.6.1.4 Light-driven HER

As was introduced in section 1.6, page 25, semiconductor materials are an interesting option to carry out the HER in water splitting, both for their abilities as light harvesters as for their catalytic performance. This duality brings closer the final objective of achieving a device for the generation of fuels from sunlight and water.

The efficiency of a semiconductor will be determined not only by its catalytic performance, but also by its light absorbing abilities, which are dictated by its band structure (bandgap, energy difference between the conduction band (CB) and the valence band (VB)). At the same time, the position of the CB and VB will determine the capacity of the photogenerated charge carriers (electron-hole pairs) to promote oxidation and reduction reactions. TiO_2 has been one of the traditionally most

studied materials as a photocatalyst, given its versatility in adapting to numerous applications [59,121]. However, its wide bandgap value (3.2 eV) restrains application to UV-light region to achieve the photoactivation, thus hindering its implementation in sunlight-driven photocatalysis frameworks [63,122].

Graphitic carbon nitride (g-CN) is a polymeric *n*-type semiconductor that exhibits a stacked structure, similar to graphite. Although it is not a newly developed material, is emerging as an ideal alternative to the use of the more widespread TiO_2, mainly because it can be activated by visible light (bandgap ~2.7 eV), a determining factor in sunlight-triggered reactions. Its other virtues include its simple preparation compared to other metal-based semiconductors, non-toxicity, composition based on Earth-abundant elements, and high thermal and chemical stability [123–125]. Although there are different phases of g-CN and its structure may vary slightly depending on the precursor and the polymerization method chosen, the basic structure of mpg-CN is considered to consist of tri-s-triazine units interconnected through planar amino groups, forming stacked sheets interconnected by van der Waals forces (**Figure 22**). The result of this is a porous structure, in which the nitrogen atoms are located, and that can serve as active sites in catalysis, or as anchor points to modify the surface of the g-CN.

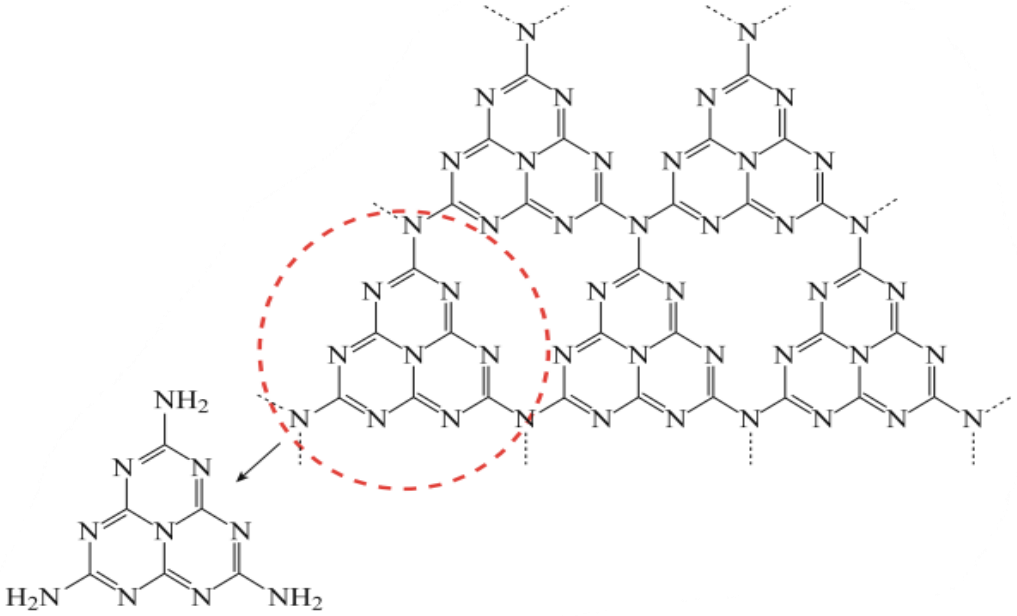

Figure 22. Tri-s-triazine unit and a g-CN sheet. Based on reference [125].

Despite its benefits, when using bare g-CN as a photocatalyst in HER, the results are not entirely satisfactory. The reason is mainly the rapid recombination of photogenerated charge carriers (electron-hole pairs) [126,127]. One way to achieve a photocatalyst with lower recombination rates, and therefore more efficient, is to modify the structure of g-CN, by preparing it through different synthetic routes, applying thermochemical treatments or doping the structure with heteroatoms [128–132]. In this way, it is also possible to narrow the semiconductor bandgap, thereby improving visible-light absorption.

Another strategy would be loading the g-CN with substances that could serve as co-catalysts [133,134]. In this context, any of the materials studied in the previous section, whose efficiency as catalysts in HER is more than proven, would fit for this task. Thus, while loaded metal nanoparticles improve the photoefficiency of g-CN, the structure of the latter will also serve to stabilize them. In the literature, there are many examples of these symbiotic systems for HER, mainly based on Pt [135–138], although there are also examples with non-noble metals [139–143]. For Ru, on the other hand, it is an area yet to be explored.

In order to test these systems for photocatalytic HER, a cell containing g-CN loaded with the corresponding co-catalyst is normally used in an aqueous suspension with triethanolamine (TEOA), which acts as a sacrificial agent donating electrons to the semiconductor. By light-irradiating the semiconductor, photons are absorbed, promoting the excitation of electrons in the valence band (VB) of the semiconductor, and being able to "jump" to the conduction band (CB), where they are devoted to proton reduction. Co-catalyst on the surface accelerates the transfer of electrons in this step, thus suppressing the recombination of the charge carriers. Vacancies (holes) are generated in the VB, which are quickly replenished by the TEOA. This joint action between the g-CN and the co-catalyst considerably improves the catalytic performance of the semiconductor material (**Figure 23**).

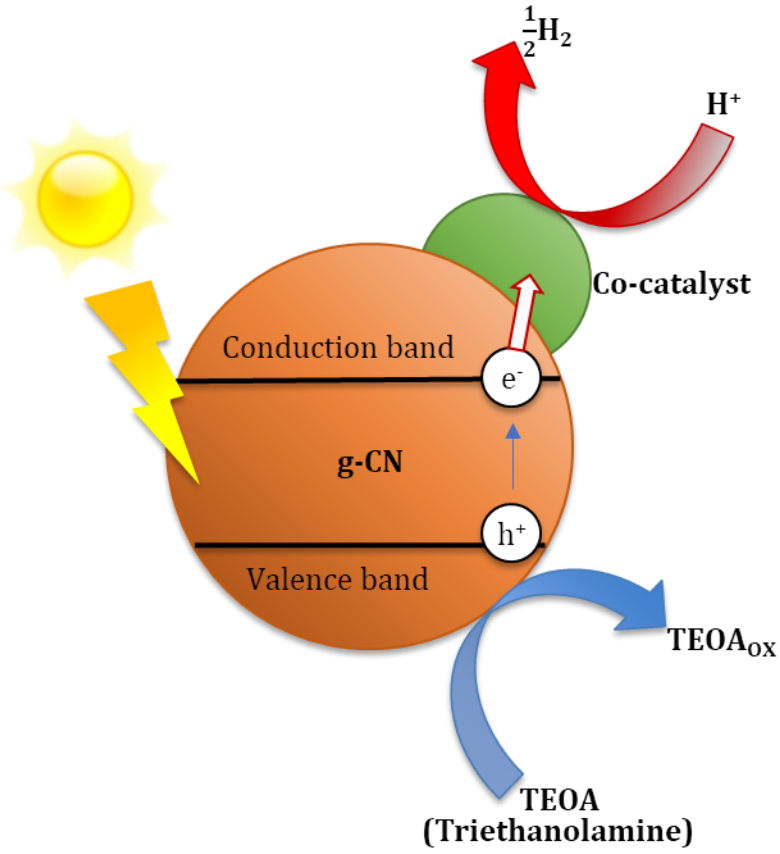

Figure 23. Proposed mechanism of the charge carriers transfer process of photocatalytic HER using triethanolamine as sacrificial agent [134].

1.7 Photocatalytic CO_2 reduction

Solar-induced water splitting to generate O_2 and H_2 is not the only way to convert sunlight, using water molecules, into fuels. Carbon dioxide reduction uses the released protons and electrons from the oxidative half reaction in artificial photosynthesis (**Eq. 15,** page 23) to produce hydrocarbons, analogously to the production of sugar molecules during the Calvin Cycle in natural photosynthesis (section 1.5). CO_2 reduction is a way to help reduce this greenhouse gas from the atmosphere, derived from the burning of fossil fuels and other industrial processes. These manufactured substances could be used as fuels, although a significant share of them is used as feedstocks in the industry [144].

CO_2 reduction is a costly process, not only because of the investment involved in capturing and storing this gas, but also because it is a relatively inert gas ($\Delta G_f^0 =$

$-394.39\ \mathrm{KJ \cdot mol^{-1}}$), thus requiring an adequate strategy for its fixation in useful fuels. As in the generation of hydrogen by photoelectrochemical water splitting, the first examples of photocatalyzed carbon dioxide reduction, by Inoue and co-workers in 1979,[145] also employed TiO_2 and other photoactive semiconductors. Due to the energy input required, the most studied semiconductors are those with a wide bandgap, capable of providing the necessary energy to promote both the CO_2 reduction and H_2O oxidation [144].

CO_2 reduction is a complex mechanism that involves the breaking of C=O double bonds, whose first step undergoes with the absorption of a CO_2 molecule onto the catalyst surface, where the photoexcited electrons are transferred to it, coming from the CB of the semiconductor, thus forming the $CO_2^{\bullet -}$ radical [146]. However, given the CB edges of the semiconductors listed in **Figure 24**, all of them below the highly negative redox potential at pH 7 of the anion radical (**Eq. 32**), this single-reduction intermediate step requires an external force to evolve. It is important to note that there are other more thermodynamically favoured pathways, involving proton-coupled electron transfer (PCET) processes [147]. Thus, reducing CO_2 can lead to a wide range of high-added value chemicals, commonly methane (CH_4), formic acid (HCOOH), formaldehyde (HCOH) and methanol (MeOH) (**Eq. 33**-36), and also typically CO, which hinders the selectivity of the transformation.

$CO_2 + e^- \rightarrow CO_2^{\bullet -}$	$E^0_{redox} = -1.90\ V$	Eq. 32
$CO_2 + 8H^+ + 8e^- \rightarrow CH_4 + 2H_2O$	$E^0_{redox} = -0.24\ V$	Eq. 33
$CO_2 + 2H^+ + 2e^- \rightarrow HCOOH$	$E^0_{redox} = -0.61\ V$	Eq. 34
$CO_2 + 4H^+ + 4e^- \rightarrow HCOH + H_2O$	$E^0_{redox} = -0.48\ V$	Eq. 35
$CO_2 + 6H^+ + 6e^- \rightarrow CH_3OH + H_2O$	$E^0_{redox} = -0.38\ V$	Eq. 36

Despite being a process studied for decades, the mechanisms involved in the photoreduction of carbon dioxide towards its different products is still under discussion [148,149]. This lack of knowledge about the key steps of the reaction greatly hampers the development of fully efficient photocatalysts. At the same time, the interest in understanding more about this process increases.

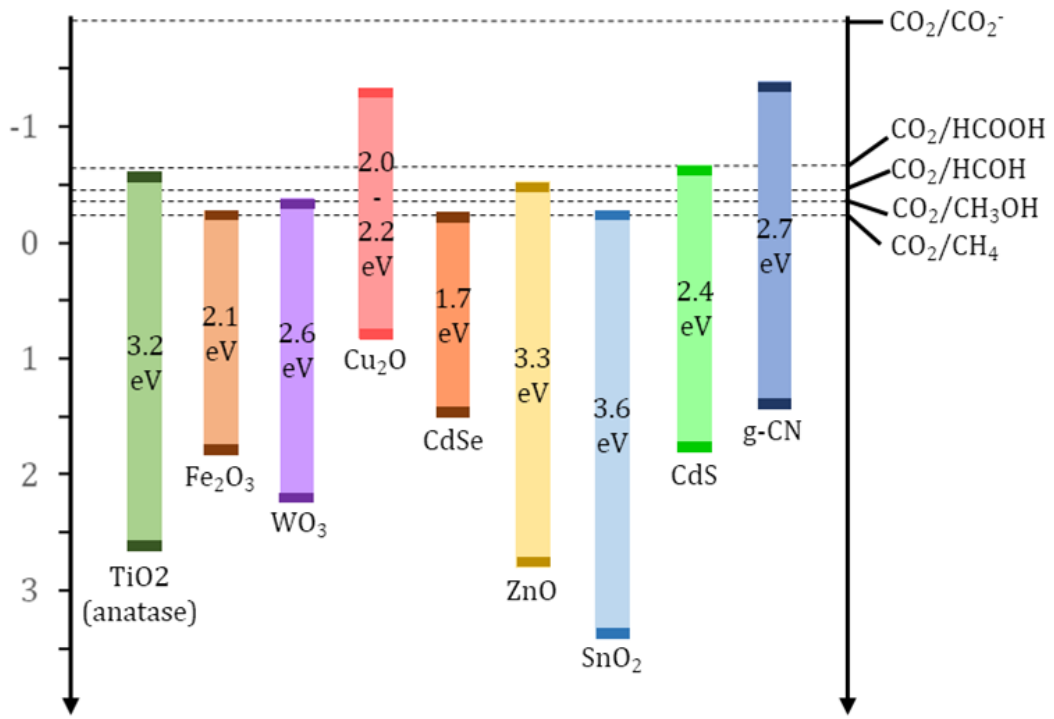

Figure 24. Characteristic bandgap energies of typical semiconductor photocatalytic materials and their VB and CB positions, relative to the redox potentials of compounds involved in CO_2 reduction, at pH = 7. Adapted from references [148,150].

TiO_2 is, despite its known drawback of limited visible light absorption , the most widely used semiconductor also in the reduction of CO_2 [151]. For this transformation, the choice of a suitable co-catalyst is key, not only to improve catalytic efficiency and absorbance of visible light by the semiconductor, by reducing both the recombination rates of the electron-hole pairs and the bandgap value, but also to achieve adequate selectivity towards the desired end-products. As seen for the photocatalytic proton reduction, metal-loaded based nanomaterials as co-catalyst is a simple and effective way to meet these requirements [152].

Wang's group studied the effect of the noble metal-loading in the efficiency of TiO_2 as photocatalytic CO_2 reduction catalyst [153]. Pt, Pd, Rh, Au and Ag were photo-deposited onto the semiconductor surface and tested as co-catalyst under UV light. In all cases, the presence of the metal enhanced the selectivity of the reduction towards CH_4, with formation rates corresponding to the ascending order Ag < Rh < Au < Pd < Pt. This matches with the expected results based on the electro donor/acceptor abilities of these metals, which follow the same trend. Thereby, Pt

offers less probability of charge carrier recombination, and therefore the efficiency of the transformation is higher.

However, not only the nature of the co-catalyst is important, also, in the case of working with nanomaterials, it is its size and morphology. P. Biswas *et al.* prepared 1D TiO_2 films, coated with Pt NPs with sizes varying from 0.5 to 2 nm. These Pt-TiO_2 films proved to be efficient for CO_2 photoreduction, in the UV light range, with a high selectivity towards the formation of CH_4. Top performance occurred at Pt NPs size around 1 nm, whereas smaller nanoparticles exhibited poorer performance, which they attributed to a greater energy band separation, caused by quantum confinement [154].

M. Tasbihi *et al.* reported a Pt NPs-based TiO_2 photocatalyst, prepared with different loadings of Pt following a deposition-precipitation method. H_2, CO and CH_4 were detected as the main reduction products after UV light irradiation. Even if bare TiO_2 produced CO as the principal product, the selectivity towards CH_4 increased when incorporating platinum, being almost 100% at the optimal loading [155]. More recently, C. Matranga *et al.* designed a visible light-triggered TiO_2 photocatalyst. In order to enhance the visible light sensitivity of TiO_2, not only they doped the semiconductor with Pt NPs, but also with nanocrystal quantum dots of another semiconductor, CdSe, whose band alignment makes it more appropriate to visible-light absorption [156]. They managed to carry out the photoreduction of CO_2 into CH_4 and MeOH using only visible light.

Despite the efforts to design efficient photocatalysts triggered by visible light modifying TiO_2, a more straightforward strategy goes through the use of semiconductors with a suitable bandgap. As was the case with the HER, carbon nitride (g-CN) has attracted a lot of interest in this field [124,157].

B.Cheng *et al.* improved the catalytic performance of bare g-CN in the photoreduction of CO_2 into CH_4, CH_3OH and HCOH, under simulated solar irradiation, by deposition of Pt NPs [158]. Pt co-catalyst not only had an effect on production rates, but also the selectivity increased towards CH_4 and CH_3OH, or towards HCOH, depending on the metal content. Likewise, J. Zhang *et al.* demonstrated the effect of nanoparticle size [159]. Pt NPs of different sizes were

synthesized on the surface of g-CN, and it was observed that the smallest NPs (1.8 nm) delivered higher activity, in terms of generation rates. In contrast, with the largest ones (7 nm), the selectivity to produce CH_4 was higher. The experiments were carried out with the same amount of Pt as co-catalyst and under simulated sunlight. These examples highlight, once again, the importance of a suitable synthetic method for the application of metal-based nanoparticles as co-catalysts.

Research focused carbon dioxide photoreduction is on the rise. The full knowledge of its mechanism and the development of efficient, selective, and applicable catalysts on an industrial scale are pending issues that, together with the need to deal with the huge amounts of CO_2 emitted into the atmosphere, are responsible for encouraging research in this field.

1.8 Nanochemistry

"Nano", derived from the Greek νᾶνος (dwarf), is currently used as a unit prefix used by the International System of Units (SI), equivalent to a factor 10^{-9}, which in length units corresponds to the Anglo-Saxon billionth of a meter, in other words, a nanometer. In 2004, the Royal Society of London reported a consensual definition of nanoscience and nanotechnologies, defining nanoscience as the study and manipulation of materials at the atomic, molecular or macromolecular scales, whose properties differ from materials at larger scales. They also defined nanotechnology as everything that involves the design, characterization, production and application of materials or devices on a nanometric scale, controlling their shape and size [160].

Regardless of the terminology or the precise definition, these sciences have as their object of study all that matter, of both organic and inorganic nature, whose size is in the order of nanometers. Specifically in the range of 100 nm down to the atomic scale [160,161]. This scale is considered because it is where the properties of matter differ significantly from their corresponding bulk materials. By working at the nanoscale, the surface area increases significantly compared to materials of the same total volume (**Figure 25**). This means that, in many cases, the same materials are more reactive, having more exposed surface, or in the case of a catalyst, more

active sites, and therefore greater efficiency. It is also necessary to consider the changes in the optical, electrical or magnetic properties, the result of quantum effects, which become relevant when working in very small size ranges [162,163].

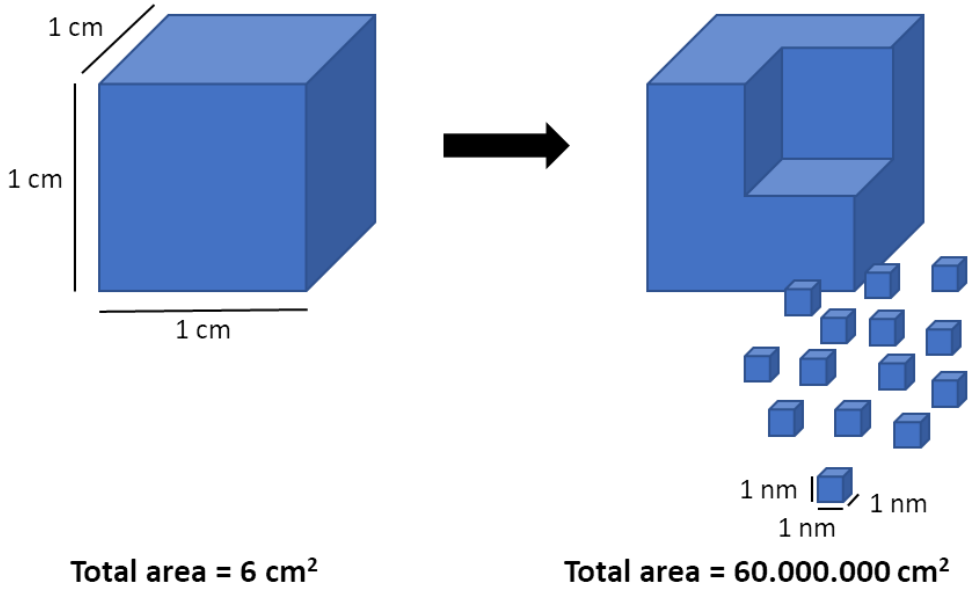

Figure 25. Surface area comparison of a cube-shaped material before and after cutting off into nano-cubes.

Nanomaterials can be classified according to their dimensions. To be considered a nanomaterial, at least one of its dimensions must be in the nanoscale range. 3D materials are not strictly confined to the nanoscale in any dimension, although they can be made up of nanomaterials. For example, graphite (3D) can be defined as stacked sheets of graphene (2D), a carbon structure with a dimension at the nanoscale. Carbon can also be in the form of nanotubes (1D) or fullerenes (0D) (**Figure 26**). Those nanomaterials whose three dimensions are confined to the nanoscale are defined as nanoparticles.

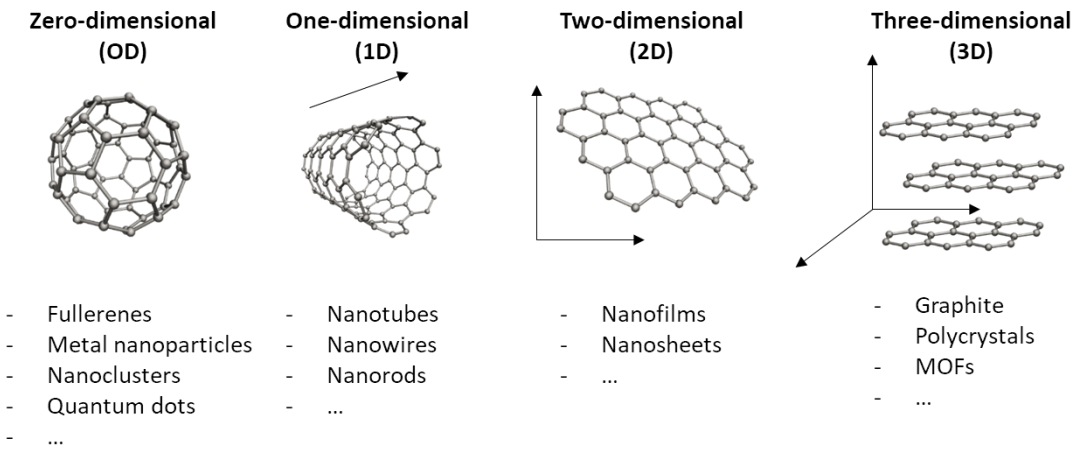

Figure 26. Classification of nanomaterials according to their dimensions, using carbon structures as a reference. Based on reference [164].

The enhanced properties of nanomaterials have awakened a nano-fever over the past years, and there are already many industrial applications that have incorporated them into their operating routine (coatings, dyes and pigments, cosmetics, biomedicine, sensors, electronics, catalysis, etc.) [165–168].

1.8.1 Strategies for the preparation of nanoparticles

Nanoparticles can have a natural origin, in volcanic activity, plants or algae, and also derived from human activity, in combustion processes (at the industrial or domestic level) or in the exhaust gases of vehicles [160]. Artificially, nanoparticles can be prepared following two strategies:

- **Top-down techniques**: This involves breaking or scaling down the bulk material into nanosized structures. These are the cases of mechanical grinding [169] or lithography [170]. The prepared nanoparticles are not completely homogeneous in shape and size and may present surface defects (due to physical treatment) that affect their final properties.
- **Bottom-up approach**: It implies using smaller building blocks, such as atoms, molecules, or nanoparticles which, after self-assembly, will form larger and more complex nanostructures. This approach includes chemical vapor deposition (CVD), chemical reduction of ionic salts or sol-gel methods, to name a few [171]. They allow control of the growth and shape of the nanoparticles, diminishing the problems of top-down techniques [172,173].

In previous pages, the importance of metal-based nanoparticles as catalysts has been highlighted, both for the reduction of protons and carbon dioxide reduction. Bottom-up strategies described above are the most suitable for the preparation of metal-based nanoparticles, based on the reproducibility in the preparation, a key aspect for catalysts. Coming up next, the most outstanding methods for the preparation of metallic nanoparticles will be addressed.

1.8.1.1 Chemical reduction method

This method consists of reducing an ionic salt of a transition metal, under suitable reaction conditions in the presence of a reducing agent. An additional stabilizing agent is usually also required to control the growth and prevent the coalescence of the nanoparticles. Silver NPs are commonly prepared by this method, using $AgNO_3$ as the salt, and $NaBH_4$, ethylene glycol or DMF as reducing agents. Sometimes, the reducing agent itself also serves as a stabilizer (e.g. trisodium citrate), although others such as polyvinylpyrrolidone (PVP) or oleylamine are generally added [174]. It is a very simple method of preparation NPs, in which the main disadvantages are related not only to the cost or toxicity of the reagents, but also the effect on the catalytic activity that ions and other substances (impurities) involved in the preparation may have, which are difficult to remove and could poison the surface of the NPs [175].

1.8.1.2 Thermal, sonochemical, or photochemical decomposition

These chemical reactions are triggered by temperature, sound or light irradiation. In some cases, the stabilizers can act as reductants, not requiring additional chemical agents to reduce or decompose the metal precursor prior to the assembly of the nanoparticles, thus reducing the probability of impurities in the catalyst.

F. Davar *et al.* proposed a facile thermal method for the preparation of Cu and Cu_2O NPs.[176] Metal precursor, [bis(salicylaldiminate)copper(II)], was heated up to 230 °C in the presence of oleylamine, serving as both solvent and stabilizer of the formed Cu^0 NPs (Figure 27). Cu_2O NPs can be easily obtained by air exposure of the former NPs, displaying great stability to both oxidation and agglomeration.

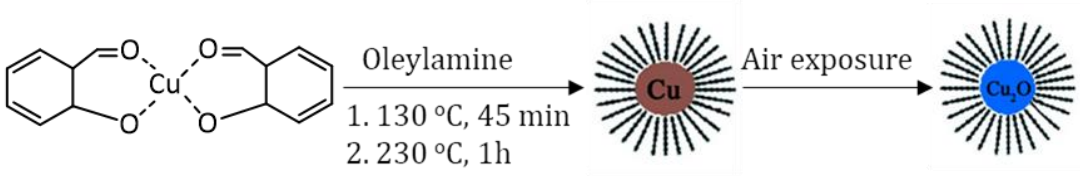

Figure 27. Simple thermochemical preparation of Cu and Cu_2O NPs using oleylamine as stabilizer. Adapted from reference [176].

Regarding sonochemical decomposition, F. Griesser *et al.* [177]. prepared Au NPs after irradiation of an $HAuCl_4$ aqueous solution. In this case, 1-propanol was added to accelerate the Au(III) reduction, and PVP to prevent agglomeration. Through this study, they were able to demonstrate that the ultrasound frequency had an influence on both the Au(III) rate of reduction and the final size of the nanoparticles.

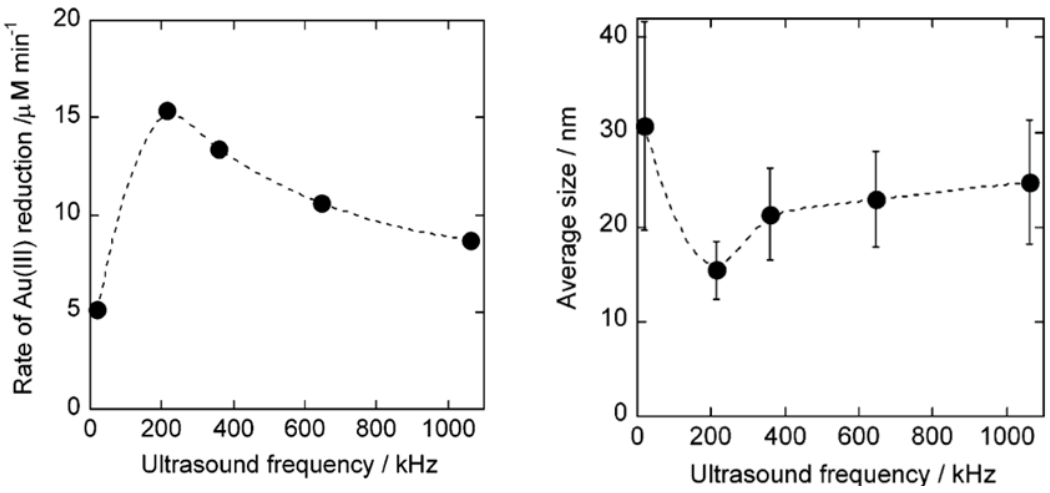

Figure 28. Left: Rate of Au (III) reduction as a function of ultrasound frequency; Right: Au NPs mean size as a function of ultrasound frequency. Extracted from reference [177].

L. Paterno and co-workers followed the photochemical route to prepare gold nanoparticles stabilized with polyethylenimine (PEI) [178]. The procedure involves irradiating a reactor containing the gold precursor ($HAuCl_4 \cdot 3H_2O$) with PEI in aqueous solution. PEI controls the nucleation process of the NPs by forming strongly associated ionic pairs with $AuCl_4^-$ ions, which are easily reduced to the zero-valent gold species, by the PEI amino groups, under UV radiation.

1.8.1.3 Chemical vapor deposition (CVD)

This method is based on the vaporization and subsequent decomposition, on a substrate or surface, of the metallic precursors. H. Kim *et al.* developed bi-metallic Pt-Co NPs, suitable and very stable for electrochemical applications [179]. Starting from vaporized $[Pt(Me)_3(MeCp)]$, Pt NPs were deposited on a carbon support inside the CVD chamber, followed by the injection of $[Co(CO)_2(Cp)]$ also in the gas phase after which the Co atoms are deposited on the existing Pt NPs. By-products and volatile fragments (mainly hydrocarbons) are removed by flowing hydrogen gas from the chamber. Applying a subsequent heat treatment of at least 500 °C, it is also possible to transform the NPs into ordered bimetallic alloys (**Figure 29**).

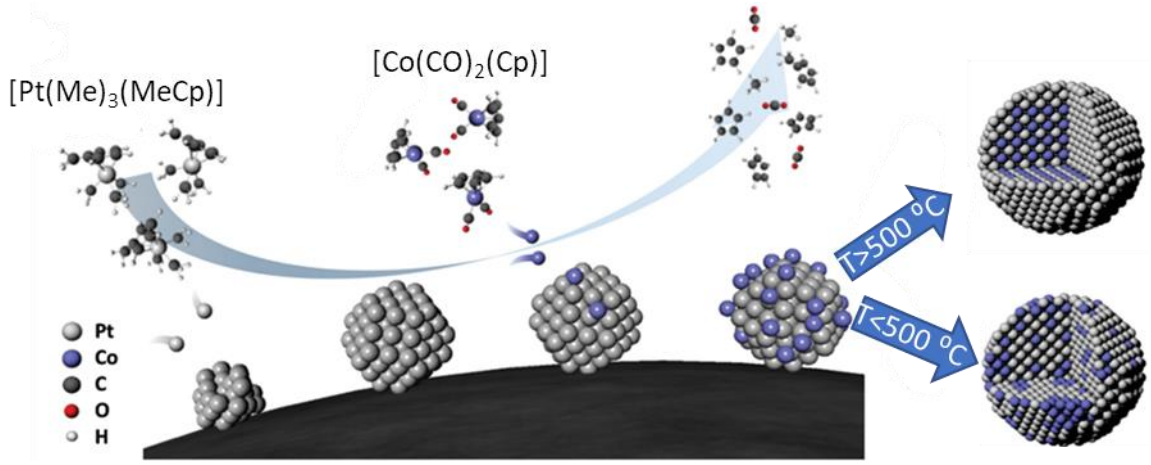

Figure 29. Schematic representation of the synthesis of Pt-Co bimetallic NPs on a carbon support with the effect of the final annealing treatment in the atomic ordering. Adapted from reference [179].

1.8.1.4 Electrochemical reduction

The electrochemical reduction method, developed by M. T. Reetz requires a sacrificial anode as the metal precursor, in the presence of a quaternary ammonium salt serving as electrolyte and stabilizer [180]. This anode is first oxidized (Eq. 37), generating ions in solution, that are later reduced at the cathode (Eq. 38), thus forming metallic nanoparticles (**Figure 30**). This method allows to control the size of the nanoparticles by varying the current intensity. The NPs are also easily recoverable, by precipitating them once formed, and offers high yields.

Anode $M_{bulk} \rightarrow M^{n+} + ne^-$ Eq. 37

Cathode $M^{n+} + ne^- + stabilizer \rightarrow M_{NPs}/stabilizer$ Eq. 38

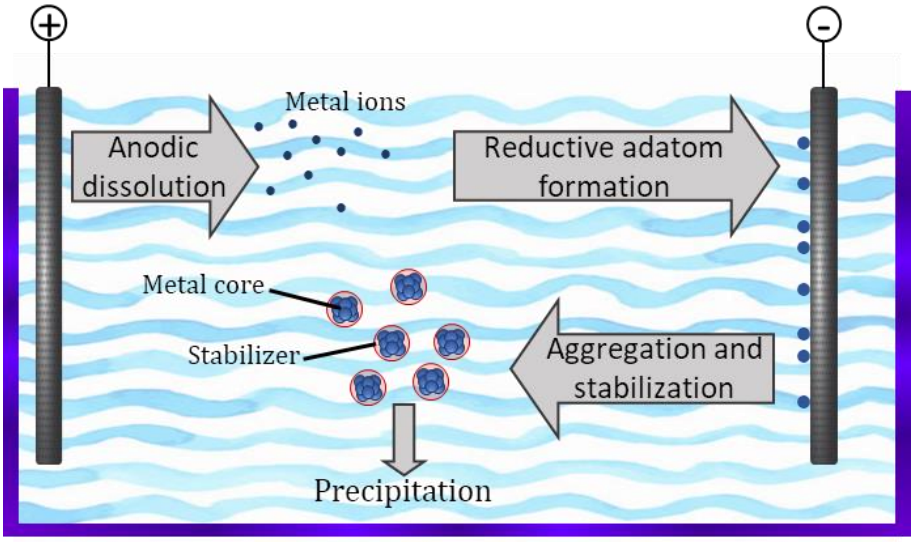

Figure 30. Synthesis of electrochemically reduced metal nanoparticles. Based on reference [180].

Another strategy would be to employ, as a metallic precursor, a transition metal salt instead of the sacrificial anode. It is the accurate alternative with metals that do not oxidize easily, such as Pt, Rh or Ru [181].

1.8.1.5 Organometallic approach

This synthetic method was previously introduced when discussing HER catalysts (section 1.6.1.2, page 38). This methodology, developed by B. Chaudret and K. Philippot [117,182], starts, like the previous techniques, from a metallic precursor (organometallic complex) which, under hydrogen pressure, decomposes, thus yielding the nanoparticles.

Ideally, the precursor contains a zero or low-valent metal, and olefinic ligands. In this way, when the ligands in the coordination sphere of the metal are hydrogenated, they are reduced to the corresponding alkanes, which are easily eliminated and do not interact with the surface of the NPs. Some examples of suitable metallic precursors are [Ru(cod)(cot)](cod = 1,5-cyclooctadiene, cot = 1,3,5-cyclooctatriene), employed to prepare the ligand-capped Ru NPs system previously

discussed as HEC[119], [Co(coe)(cod)] (coe = cyclooctenyl) [183], [Ni(cod)$_2$] [184], or [Pt(dba)$_2$] (dba= dibenzylideneacetone) [185], all of them decomposing at relatively low hydrogen pressures.

Additionally, the method requires a stabilizing agent. For this purpose, different organic ligands have been studied [117]. These capping ligands are present from the beginning of the reaction, often mixed with the metallic precursor at low temperature, to avoid the formation of intermediates that are difficult to decompose. As soon as the atoms are released, these ligands can interact with their surface and thus influence their growth into nanoparticles (**Figure 31**).

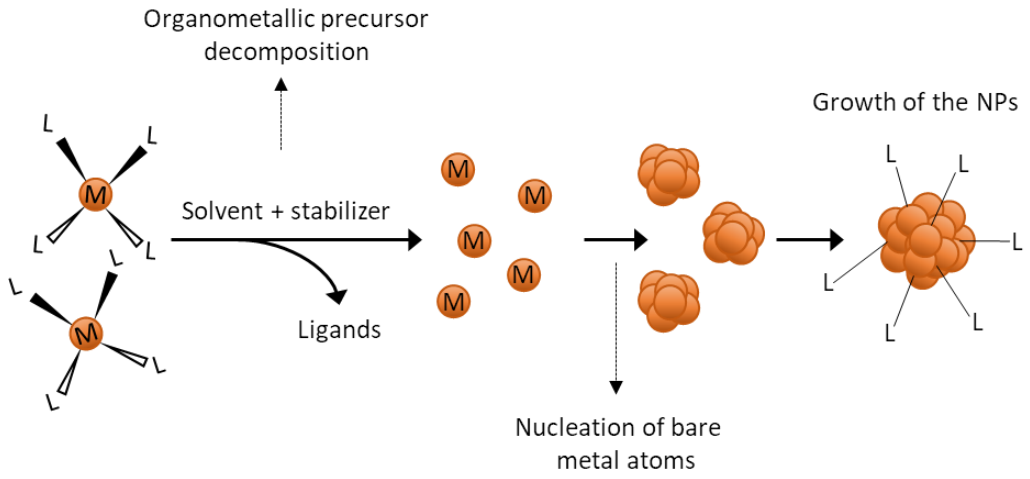

Figure 31. Schematic illustration of the organometallic approach for the synthesis of metallic nanoparticles. Based on reference [117].

The organometallic method not only focuses on colloidal solutions of nanoparticles, also hybrid materials or composites can be prepared, by decomposition of the organometallic precursor in the presence of a supporting material, which can also help controlling the growth and promoting the dispersion of the nanoparticles (e.g. carbon nanotubes (CNT) [186], carbon microfibers (CFs) [187], MOF [188], etc.).

Therefore, the organometallic approach offers an alternative for the synthesis of nanoparticles in mild conditions, narrow size distribution and well-controlled surface state.

1.9 References

[1] Lashof, D. A. and Ahuja, D. R. "Relative global warming potentials of greenhouse gas emissions" *Nature*, **1990** (344) 529–31

[2] Björsne, A.-K.; Rütting, T. and Ambus, P. "Belowground heathland responses after 2 years of combined warming, elevated CO_2 and summer drought" *Biogeochemistry.*, **2014** (120) 27–42

[3] Le Treut, H.; Cubasch, U. and Allen, M. "Historical Overview of Climate Change Science" *Notes*, **2005** (16)

[4] Satterthwaite, D. "The implications of population growth and urbanization for climate change" *Environ. Urban.*, **2009** (21) 545–67

[5] Stephenson, J.; Newman, K. and Mayhew, S. "Population dynamics and climate change: What are the links?" *J. Public Health (Bangkok).*, **2010** (32) 150–6

[6] McMichael, A. J. "Globalization, Climate Change, and Human Health" *N. Engl. J. Med.*, **2013** (368) 1335–43

[7] Looney, B. "Statistical Review of World Energy, 2020 | 69th Edition" *Bp*, **2020** (69) 66

[8] Abas, N.; Kalair, A. and Khan, N. "Review of fossil fuels and future energy technologies" *Futures*, **2015** (69) 31–49

[9] Martins, F.; Felgueiras, C.; Smitkova, M. and Caetano, N. "Analysis of fossil fuel energy consumption and environmental impacts in european countries" *Energies*, **2019** (12) 1–11

[10] Vakulchuk, R.; Overland, I. and Scholten, D. "Renewable energy and geopolitics: A review" *Renew. Sustain. Energy Rev.*, **2020** (122) 109547

[11] Gielen, D.; Boshell, F.; Saygin, D.; Bazilian, M. D.; Wagner, N. and Gorini, R. "The role of renewable energy in the global energy transformation" *Energy Strateg. Rev.*, **2019** (24) 38–50

[12] Johnston, R. B. "Arsenic and the 2030 Agenda for sustainable development" *Arsen. Res. Glob. Sustain. - Proc. 6th Int. Congr. Arsen. Environ. AS 2016*, **2016** 12–4

[13] Thirugnanasambandam, M.; Iniyan, S. and Goic, R. "A review of solar thermal technologies" *Renew. Sustain. Energy Rev.*, **2010** (14) 312–22

[14] Mekhilef, S.; Saidur, R. and Safari, A. "A review on solar energy use in industries" *Renew. Sustain. Energy Rev.*, **2011** (15) 1777–90

[15] Kannan, N. and Vakeesan, D. "Solar energy for future world: - A review" *Renew. Sustain. Energy Rev.*, **2016** (62) 1092–105

[16] Tuller, H. L. "Solar to fuels conversion technologies: A perspective" *Mater. Renew. Sustain. Energy*, **2017** (6)

[17] Nocera, D. G. "Solar fuels and solar chemicals industry" *Acc. Chem. Res.*, **2017** (50) 616–9

[18] Barber, J. "Photosynthetic energy conversion: natural and artificial." *Chem. Soc. Rev.*, **2009** (38) 185–96

[19] Mazloomi, K. and Gomes, C. "Hydrogen as an energy carrier: Prospects and challenges" *Renew. Sustain. Energy Rev.*, **2012** (16) 3024–33

[20] Crabtree, G. W. and Dresselhaus, M. S. "The hydrogen fuel alternative" *MRS Bull.*, **2008** (33) 421–8

[21] Hosseini, S. E. and Wahid, M. A. "Hydrogen production from renewable and sustainable energy resources: Promising green energy carrier for clean development" *Renew. Sustain. Energy Rev.*, **2016** (57) 850–66

[22] Crowl, D. A. and Jo, Y. Do. "The hazards and risks of hydrogen" *J. Loss Prev. Process Ind.*, **2007** (20) 158–64

[23] Midilli, A.; Ay, M.; Dincer, I. and Rosen, M. A. "On hydrogen and hydrogen energy strategies I : Current status and needs" *Renew. Sustain. Energy Rev.*, **2005** (9) 255–71

[24] Liu, X.; Wang, X. and Kapteijn, F. "Water and Metal-Organic Frameworks: From Interaction toward Utilization" *Chem. Rev.*, **2020** (120) 8303–77

[25] Acar, C. and Dincer, I. "Review and evaluation of hydrogen production options for better environment" *J. Clean. Prod.*, **2019** (218) 835–49

[26] Brandon, N. P. and Kurban, Z. "Clean energy and the hydrogen economy" *Philos. Trans. R. Soc. A Math. Phys. Eng. Sci.*, **2017** (375)

[27] Xiang, C.; Papadantonakis, K. M. and Lewis, N. S. "Principles and implementations of electrolysis systems for water splitting" *Mater. Horizons*, **2016** (3) 169–73

[28] Hernández-Gómez, Á.; Ramirez, V. and Guilbert, D. "Investigation of PEM electrolyzer modeling: Electrical domain, efficiency, and specific energy consumption" *Int. J. Hydrogen Energy*, **2020** (45) 14625–39

[29] Shiva Kumar, S. and Himabindu, V. "Hydrogen production by PEM water electrolysis – A review" *Mater. Sci. Energy Technol.*, **2019** (2) 442–54
[30] Guo, Y.; Li, G.; Zhou, J. and Liu, Y. "Comparison between hydrogen production by alkaline water electrolysis and hydrogen production by PEM electrolysis" *IOP Conf. Ser. Earth Environ. Sci.*, **2019** (371)
[31] Acar, C. and Dincer, I. "Comparative assessment of hydrogen production methods from renewable and non-renewable sources" *Int. J. Hydrogen Energy*, **2014** (39) 1–12
[32] Mueller-Langer, F.; Tzimas, E.; Kaltschmitt, M. and Peteves, S. "Techno-economic assessment of hydrogen production processes for the hydrogen economy for the short and medium term" *Int. J. Hydrogen Energy*, **2007** (32) 3797–810
[33] Pal, D. B.; Chand, R.; Upadhyay, S. N. and Mishra, P. K. "Performance of water gas shift reaction catalysts: A review" *Renew. Sustain. Energy Rev.*, **2018** (93) 549–65
[34] Demirel, Y. "Technoeconomics and Sustainability of Renewable Methanol and Ammonia Productions Using Wind Power-based Hydrogen" *J. Adv. Chem. Eng.*, **2015** (5)
[35] Abdalla, A. M.; Hossain, S.; Nisfindy, O. B.; Azad, A. T.; Dawood, M. and Azad, A. K. "Hydrogen production, storage, transportation and key challenges with applications: A review" *Energy Convers. Manag.*, **2018** (165) 602–27
[36] Züttel, A. "Hydrogen storage and distribution systems" *Mitig. Adapt. Strateg. Glob. Chang.*, **2007** (12) 343–65
[37] Tade, M. D. "Helium Storage in Cliffside Field" *J. Pet. Technol.*, **1967** (19) 885–8
[38] Lord, A. S.; Kobos, P. H. and Borns, D. J. "Geologic storage of hydrogen: Scaling up to meet city transportation demands" *Int. J. Hydrogen Energy*, **2014** (39) 15570–82
[39] Moradi, R. and Groth, K. M. "Hydrogen storage and delivery: Review of the state of the art technologies and risk and reliability analysis" *Int. J. Hydrogen Energy*, **2019** (44) 12254–69
[40] Tarkowski, R. "Underground hydrogen storage: Characteristics and prospects" *Renew. Sustain. Energy Rev.*, **2019** (105) 86–94
[41] Kayfeci, M. and Keçebaş, A. "Hydrogen storage" *Sol. Hydrog. Prod. Process. Syst. Technol.*, **2019** 85–110
[42] Kreuer, K. D. "On the development of proton conducting polymer membranes for hydrogen and methanol fuel cells" *J. Memb. Sci.*, **2001** (185) 29–39
[43] Acar, C. and Dincer, I. "The potential role of hydrogen as a sustainable transportation fuel to combat global warming" *Int. J. Hydrogen Energy*, **2020** (45) 3396–406
[44] Kätelhön, A.; Meys, R.; Deutz, S.; Suh, S. and Bardow, A. "Climate change mitigation potential of carbon capture and utilization in the chemical industry" *Proc. Natl. Acad. Sci. U. S. A.*, **2019** (166) 11187–94
[45] Olajire, A. A. "CO2 capture and separation technologies for end-of-pipe applications - A review" *Energy*, **2010** (35) 2610–28
[46] Leung, D. Y. C.; Caramanna, G. and Maroto-Valer, M. M. "An overview of current status of carbon dioxide capture and storage technologies" *Renew. Sustain. Energy Rev.*, **2014** (39) 426–43
[47] Jensen, M. D.; Schlasner, S. M.; Sorensen, J. A. and Hamling, J. A. "Operational flexibility of CO2 transport and storage" *Energy Procedia*, **2014** (63) 2715–22
[48] Onyebuchi, V. E.; Kolios, A.; Hanak, D. P.; Biliyok, C. and Manovic, V. "A systematic review of key challenges of CO2 transport via pipelines" *Renew. Sustain. Energy Rev.*, **2018** (81) 2563–83
[49] Vilarrasa, V. and Rutqvist, J. "Thermal effects on geologic carbon storage" *Earth-Science Rev.*, **2017** (165) 245–56
[50] Widjanarko, S. and Ubaydullaev, B. "The role of carbon capture and storage in the global energy portfolio" *Int. J. Technol.*, **2011** (2) 65–73
[51] Dogutan, D. K. and Nocera, D. G. "Artificial Photosynthesis at Efficiencies Greatly Exceeding That of Natural Photosynthesis" *Acc. Chem. Res.*, **2019**
[52] El-Khouly, M. E.; El-Mohsnawy, E. and Fukuzumi, S. "Solar energy conversion: From natural to artificial photosynthesis" *J. Photochem. Photobiol. C Photochem. Rev.*, **2017** (31) 36–83
[53] Matuszyńska, A. and Ebenhöh, O. "A reductionist approach to model photosynthetic self-regulation in eukaryotes in response to light" *Biochem. Soc. Trans.*, **2015** (43) 1133–9
[54] Umena, Y.; Kawakami, K.; Shen, J. R. and Kamiya, N. "Crystal structure of oxygen-evolving photosystem II at a resolution of 1.9Å" *Nature*, **2011** (473) 55–60
[55] Barber, J. and Tran, P. D. "From natural to artificial photosynthesis" *J. R. Soc. Interface*, **2013** (10)
[56] Yano, J. and Yachandra, V. "Mn4Ca cluster in photosynthesis: Where and how water is oxidized to dioxygen" *Chem. Rev.*, **2014** (114) 4175–205

[57] Walter, M. G.; Warren, E. L.; McKone, J. R.; Boettcher, S. W.; Mi, Q.; Santori, E. A. and Lewis, N. S. "Solar water splitting cells" *Chem. Rev.*, **2010** (110) 6446–73
[58] Berardi, S.; Drouet, S.; Francàs, L.; Gimbert-Suriñach, C.; Guttentag, M.; Richmond, C.; Stoll, T. and Llobet, A. "Molecular artificial photosynthesis" *Chem. Soc. Rev.*, **2014** (43) 7501–19
[59] Fujishima, A. and Honda, K. "Electrochemical Photolysis of Water at a Semiconductor Electrode" *Nature*, **1972** (238) 37–40
[60] Hashimoto, K.; Irie, H. and Fujishima, A. "TiO 2 photocatalysis: A historical overview and future prospects" *Japanese J. Appl. Physics, Part 1 Regul. Pap. Short Notes Rev. Pap.*, **2005** (44) 8269–85
[61] Zheng, Z.; Xie, W.; Huang, B. and Dai, Y. "Plasmon-Enhanced Solar Water Splitting on Metal-Semiconductor Photocatalysts" *Chem. - A Eur. J.*, **2018** (24) 18322–33
[62] Yang, J.; Yan, H.; Zong, X.; Fuyuwen.; Liu, M. and Li, C. "Roles of cocatalysts in semiconductor-based photocatalytic hydrogen production" *Philos. Trans. R. Soc. A Math. Phys. Eng. Sci.*, **2013** (371)
[63] Etacheri, V.; Di Valentin, C.; Schneider, J.; Bahnemann, D. and Pillai, S. C. "Visible-light activation of TiO2 photocatalysts: Advances in theory and experiments" *J. Photochem. Photobiol. C Photochem. Rev.*, **2015** (25) 1–29
[64] Zhang, P.; Zhang, J. and Gong, J. "Tantalum-based semiconductors for solar water splitting" *Chem. Soc. Rev.*, **2014** (43) 4395–422
[65] Erbs, W.; Desilvestro, J.; Borgarello, E. and Grätzel, M. "Visible-light-induced O2 generation from aqueous dispersions of WO3" *J. Phys. Chem.*, **1984** (88) 4001–6
[66] Maeda, K.; Takata, T.; Hara, M.; Saito, N.; Inoue, Y.; Kobayashi, H. and Domen, K. "GaN:ZnO solid solution as a photocatalyst for visible-light-driven overall water splitting" *J. Am. Chem. Soc.*, **2005** (127) 8286–7
[67] Sayama, K. and Arakawa, H. "Photocatalytic decomposition of water and photocatalytic reduction of carbon dioxide over zirconia catalyst" *J. Phys. Chem.*, **1993** (97) 531–3
[68] Lin, Z.; Du, C.; Yan, B. and Yang, G. "Amorphous Fe2O3 for photocatalytic hydrogen evolution" *Catal. Sci. Technol.*, **2019** (9) 5582–92
[69] Müller, P. and Brettel, K. "[Ru(bpy)3]2^{+} as a reference in transient absorption spectroscopy: Differential absorption coefficients for formation of the long-lived 3MLCT excited state." *Photochem. Photobiol. Sci.*, **2012** (11) 632
[70] Kärkäs, M. D.; Laine, T. M.; Johnston, E. V. and Akermark, B. "Visible Light-Driven Water Oxidation Catalyzed by Ruthenium Complexes" *Appl. Photosynth. - New Prog.*, **2016**
[71] Gorlin, Y. and Jaramillo, T. F. "A bifunctional nonprecious metal catalyst for oxygen reduction and water oxidation" *J. Am. Chem. Soc.*, **2010** (132) 13612–4
[72] Creus, J.; De Tovar, J.; Romero, N.; García-Antón, J.; Philippot, K.; Bofill, R. and Sala, X. "Ruthenium Nanoparticles for Catalytic Water Splitting" *ChemSusChem*, **2019** (12) 2493–514
[73] Shinagawa, T.; Garcia-Esparza, A. T. and Takanabe, K. "Insight on Tafel slopes from a microkinetic analysis of aqueous electrocatalysis for energy conversion" *Sci. Rep.*, **2015** (5) 1–21
[74] Costentin, C.; Drouet, S.; Robert, M. and Savéant, J. M. "Turnover numbers, turnover frequencies, and overpotential in molecular catalysis of electrochemical reactions. Cyclic voltammetry and preparative-scale electrolysis" *J. Am. Chem. Soc.*, **2012** (134) 11235–42
[75] Zeng, M. and Li, Y. "Recent advances in heterogeneous electrocatalysts for the hydrogen evolution reaction" *J. Mater. Chem. A*, **2015** (3) 14942–62
[76] Conway, B. E. and Tilak, B. V. "Interfacial processes involving electrocatalytic evolution and oxidation of H2, and the role of chemisorbed H" *Electrochim. Acta*, **2002** (47) 3571–94
[77] Shinagawa, T. and Takanabe, K. "Towards Versatile and Sustainable Hydrogen Production through Electrocatalytic Water Splitting: Electrolyte Engineering" *ChemSusChem*, **2017** (10) 1318–36
[78] Lasia, A. "Mechanism and kinetics of the hydrogen evolution reaction" *Int. J. Hydrogen Energy*, **2019** (44) 19484–518
[79] Wei, J.; Zhou, M.; Long, A.; Xue, Y.; Liao, H.; Wei, C. and Xu, Z. J. "Heterostructured Electrocatalysts for Hydrogen Evolution Reaction Under Alkaline Conditions" *Nano-Micro Lett.*, **2018** (10) 1–15
[80] Murthy, A. P.; Theerthagiri, J. and Madhavan, J. "Insights on Tafel Constant in the Analysis of Hydrogen Evolution Reaction" *J. Phys. Chem. C*, **2018** (122) 23943–9
[81] Bowden, F. P. and Rideal, E. K. "The electrolytic behaviour of thin films. Part I.—Hydrogen" *Proc. R. Soc. London. Ser. A, Contain. Pap. a Math. Phys. Character*, **1928** (120) 59–79

[82] Greeley, J.; Jaramillo, T. F.; Bonde, J.; Chorkendorff, I. and Nørskov, J. K. "Computational high-throughput screening of electrocatalytic materials for hydrogen evolution" *Nat. Mater.*, **2006** (5) 909–13
[83] Parsons, R. "The rate of electrolytic hydrogen evolution and the heat of adsorption of hydrogen" *Trans. Faraday Soc.*, **1958** (54) 1053–63
[84] Benck, J. D.; Hellstern, T. R.; Kibsgaard, J.; Chakthranont, P. and Jaramillo, T. F. "Catalyzing the hydrogen evolution reaction (HER) with molybdenum sulfide nanomaterials" *ACS Catal.*, **2014** (4) 3957–71
[85] Ruqia, B. and Choi, S. Il. "Pt and Pt–Ni(OH)2 Electrodes for the Hydrogen Evolution Reaction in Alkaline Electrolytes and Their Nanoscaled Electrocatalysts" *ChemSusChem*, **2018** (11) 2643–53
[86] Zhou, W.; Jia, J.; Lu, J.; Yang, L.; Hou, D.; Li, G. and Chen, S. "Recent developments of carbon-based electrocatalysts for hydrogen evolution reaction" *Nano Energy*, **2016** (28) 29–43
[87] Ekspong, J.; Gracia-Espino, E. and Wagberg, T. "Hydrogen evolution reaction activity of heterogeneous materials: A theoretical model" *J. Phys. Chem. C*, **2020** (124) 20911–21
[88] Trasatti, S. "Work function, electronegativity, and electrochemical behaviour of metals. III. Electrolytic hydrogen evolution in acid solutions" *J. Electroanal. Chem.*, **1972** (39) 163–84
[89] Nørskov, J. K.; Bligaard, T.; Logadottir, A.; Kitchin, J. R.; Chen, J. G.; Pandelov, S. and Stimming, U. "Trends in the Exchange Current for Hydrogen Evolution" *J. Electrochem. Soc.*, **2005** (152) J23
[90] Zeradjanin, A. R.; Grote, J. P.; Polymeros, G. and Mayrhofer, K. J. J. "A Critical Review on Hydrogen Evolution Electrocatalysis: Re-exploring the Volcano-relationship" *Electroanalysis*, **2016** (28) 2256–69
[91] Exner, K. S. "Hydrogen electrocatalysis revisited: Weak bonding of adsorbed hydrogen as the design principle for active electrode materials" *Curr. Opin. Electrochem.*, **2021** (26) 100673
[92] Tan, T. L.; Wang, L. L.; Zhang, J.; Johnson, D. D. and Bai, K. "Platinum nanoparticle during electrochemical hydrogen evolution: Adsorbate distribution, active reaction species, and size effect" *ACS Catal.*, **2015** (5) 2376–83
[93] Klein, J.; Engstfeld, A. K.; Brimaud, S. and Behm, R. J. "Pt nanocluster size effects in the hydrogen evolution reaction: Approaching the theoretical maximum activity" *Phys. Chem. Chem. Phys.*, **2020** (22) 19059–68
[94] Anantharaj, S.; Karthik, P. E.; Subramanian, B. and Kundu, S. "Pt Nanoparticle Anchored Molecular Self-Assemblies of DNA: An Extremely Stable and Efficient HER Electrocatalyst with Ultralow Pt Content" *ACS Catal.*, **2016** (6) 4660–72
[95] Zheng, Y.; Jiao, Y.; Jaroniec, M. and Qiao, S. Z. "Advancing the electrochemistry of the hydrogen-Evolution reaction through combining experiment" *Angew. Chemie - Int. Ed.*, **2015** (54) 52–65
[96] Qu, Y.; Chen, B.; Li, Z.; Duan, X.; Wang, L.; Lin, Y.; Yuan, T.; Zhou, F.; Hu, Y.; Yang, Z.; Zhao, C.; Wang, J.; Zhao, C.; Hu, Y.; Wu, G.; Zhang, Q.; Xu, Q.; Liu, B.; Gao, P.; You, R.; Huang, W.; Zheng, L.; Gu, L.; Wu, Y. and Li, Y. "Thermal Emitting Strategy to Synthesize Atomically Dispersed Pt Metal Sites from Bulk Pt Metal" *J. Am. Chem. Soc.*, **2019** (141) 4505–9
[97] Zhu, J.; Hu, L.; Zhao, P.; Lee, L. Y. S. and Wong, K. Y. "Recent Advances in Electrocatalytic Hydrogen Evolution Using Nanoparticles" *Chem. Rev.*, **2020** (120) 851–918
[98] Mi, Y.; Wen, L.; Wang, Z.; Cao, D.; Zhao, H.; Zhou, Y.; Grote, F. and Lei, Y. "Ultra-low mass loading of platinum nanoparticles on bacterial cellulose derived carbon nanofibers for efficient hydrogen evolution" *Catal. Today*, **2016** (262) 141–5
[99] Devadas, B. and Imae, T. "Hydrogen evolution reaction efficiency by low loading of platinum nanoparticles protected by dendrimers on carbon materials" *Electrochem. commun.*, **2016** (72) 135–9
[100] Esposito, D. V.; Hunt, S. T.; Stottlemyer, A. L.; Dobson, K. D.; McCandless, B. E.; Birkmire, R. W. and Chen, J. G. "Low-cost hydrogen-evolution catalysts based on monolayer platinum on tungsten monocarbide substrates" *Angew. Chemie - Int. Ed.*, **2010** (49) 9859–62
[101] Cheng, N.; Stambula, S.; Wang, D.; Banis, M. N.; Liu, J.; Riese, A.; Xiao, B.; Li, R.; Sham, T. K.; Liu, L. M.; Botton, G. A. and Sun, X. "Platinum single-atom and cluster catalysis of the hydrogen evolution reaction" *Nat. Commun.*, **2016** (7) 1–9
[102] Fang, S.; Zhu, X.; Liu, X.; Gu, J.; Liu, W.; Wang, D.; Zhang, W.; Lin, Y.; Lu, J.; Wei, S.; Li, Y. and Yao, T. "Uncovering near-free platinum single-atom dynamics during electrochemical hydrogen evolution reaction" *Nat. Commun.*, **2020** (11) 1–8

[103] MacKus, A. J. M.; Verheijen, M. A.; Leick, N.; Bol, A. A. and Kessels, W. M. M. "Influence of oxygen exposure on the nucleation of platinum atomic layer deposition: Consequences for film growth, nanopatterning, and nanoparticle synthesis" *Chem. Mater.*, **2013** (25) 1905–11
[104] Uzun, A.; Ortalan, V.; Hao, Y.; Browning, N. D. and Gates, B. C. "Nanoclusters of gold on a high-area support: Almost uniform nanoclusters imaged by scanning transmission electron microscopy" *ACS Nano*, **2009** (3) 3691–5
[105] Yang, X.; Wang, A.; Qiao, B. and Li, J. U. N. "Single-Atom Catalysts : A New Frontier" **2013** (46)
[106] Strmcnik, D.; Lopes, P. P.; Genorio, B.; Stamenkovic, V. R. and Markovic, N. M. "Design principles for hydrogen evolution reaction catalyst materials" *Nano Energy*, **2016** (29) 29–36
[107] Axet, M. R. and Philippot, K. "Catalysis with Colloidal Ruthenium Nanoparticles" *Chem. Rev.*, **2020** (120) 1085–145
[108] Bae, S.-Y.; Mahmood, J.; Jeon, I.-Y. and Baek, J.-B. "Recent advances in ruthenium-based electrocatalysts for the hydrogen evolution reaction" *Nanoscale Horizons*, **2019** 43–56
[109] Mahmood, J.; Li, F.; Jung, S. M.; Okyay, M. S.; Ahmad, I.; Kim, S. J.; Park, N.; Jeong, H. Y. and Baek, J. B. "An efficient and pH-universal ruthenium-based catalyst for the hydrogen evolution reaction" *Nat. Nanotechnol.*, **2017** (12) 441–6
[110] Li, F.; Han, G. F.; Noh, H. J.; Ahmad, I.; Jeon, I. Y. and Baek, J. B. "Mechanochemically Assisted Synthesis of a Ru Catalyst for Hydrogen Evolution with Performance Superior to Pt in Both Acidic and Alkaline Media" *Adv. Mater.*, **2018** (30) 1–7
[111] Creus, J.; Mallón, L.; Romero, N.; Bofill, R.; Moya, A.; Fierro, J. L. G.; Mas-Ballesté, R.; Sala, X.; Philippot, K. and García-Antón, J. "Ruthenium Nanoparticles Supported on Carbon Microfibers for Hydrogen Evolution Electrocatalysis" *Eur. J. Inorg. Chem.*, **2019** (2019) 2071–7
[112] Kweon, D. H.; Okyay, M. S.; Kim, S. J.; Jeon, J. P.; Noh, H. J.; Park, N.; Mahmood, J. and Baek, J. B. "Ruthenium anchored on carbon nanotube electrocatalyst for hydrogen production with enhanced Faradaic efficiency" *Nat. Commun.*, **2020** (11) 1–10
[113] Qiu, T.; Liang, Z.; Guo, W.; Gao, S.; Qu, C.; Tabassum, H.; Zhang, H.; Zhu, B.; Zou, R. and Shao-Horn, Y. "Highly exposed ruthenium-based electrocatalysts from bimetallic metal-organic frameworks for overall water splitting" *Nano Energy*, **2019** (58) 1–10
[114] Li, J. Sen.; Huang, M. J.; Chen, X. N.; Kong, L. X.; Zhou, Y. W.; Wang, M. Y.; Li, J. L.; Wu, Z. X. and Xu, X. F. "Synergistically enhanced hydrogen evolution reaction by ruthenium nanoparticles dispersed on N-doped carbon hollow nanospheres" *Chem. Commun.*, **2020** (56) 6802–5
[115] Lu, B.; Guo, L.; Wu, F.; Peng, Y.; Lu, J. E.; Smart, T. J.; Wang, N.; Finfrock, Y. Z.; Morris, D.; Zhang, P.; Li, N.; Gao, P.; Ping, Y. and Chen, S. "Ruthenium atomically dispersed in carbon outperforms platinum toward hydrogen evolution in alkaline media" *Nat. Commun.*, **2019** (10)
[116] Jiang, K.; Luo, M.; Liu, Z.; Peng, M.; Chen, D.; Lu, Y. R.; Chan, T. S.; de Groot, F. M. F. and Tan, Y. "Rational strain engineering of single-atom ruthenium on nanoporous MoS2 for highly efficient hydrogen evolution" *Nat. Commun.*, **2021** (12)
[117] Amiens, C.; Chaudret, B.; Ciuculescu-Pradines, D.; Collière, V.; Fajerwerg, K.; Fau, P.; Kahn, M.; Maisonnat, A.; Soulantica, K. and Philippot, K. "Organometallic approach for the synthesis of nanostructures" *New J. Chem.*, **2013** (37) 3374–401
[118] Drouet, S.; Creus, J.; Collière, V.; Amiens, C.; García-Antón, J.; Sala, X. and Philippot, K. "A porous Ru nanomaterial as an efficient electrocatalyst for the hydrogen evolution reaction under acidic and neutral conditions" *Chem. Commun.*, **2017** (53) 11713–6
[119] Creus, J.; Drouet, S.; Suriñach, S.; Lecante, P.; Collière, V.; Poteau, R.; Philippot, K.; García-Antón, J. and Sala, X. "Ligand-Capped Ru Nanoparticles as Efficient Electrocatalyst for the Hydrogen Evolution Reaction" *ACS Catal.*, **2018** (8) 11094–102
[120] McCrory, C. C. L.; Jung, S.; Ferrer, I. M.; Chatman, S. M.; Peters, J. C. and Jaramillo, T. F. "Benchmarking Hydrogen Evolving Reaction and Oxygen Evolving Reaction Electrocatalysts for Solar Water Splitting Devices" *J. Am. Chem. Soc.*, **2015** (137) 4347–57
[121] Nakata, K. and Fujishima, A. "TiO 2 photocatalysis: Design and applications" *J. Photochem. Photobiol. C Photochem. Rev.*, **2012** (13) 169–89
[122] Angel, R. Del.; Durán-Álvarez, J. C. and Zanella, R. "TiO2-Low Band Gap Semiconductor Heterostructures for Water Treatment Using Sunlight-Driven Photocatalysis" *Titan. Dioxide - Mater. a Sustain. Environ.*, **2018**
[123] Ong, W. J.; Tan, L. L.; Ng, Y. H.; Yong, S. T. and Chai, S. P. "Graphitic Carbon Nitride (g-C3N4)-Based Photocatalysts for Artificial Photosynthesis and Environmental Remediation: Are We a Step Closer to Achieving Sustainability?" *Chem. Rev.*, **2016** (116) 7159–329
[124] Kumar, S.; Karthikeyan, S. and Lee, A. "g-C3N4-Based Nanomaterials for Visible Light-Driven Photocatalysis" *Catalysts*, **2018** (8) 74

[125] Wang, A.; Wang, C.; Fu, L.; Wong-Ng, W. and Lan, Y. "Recent Advances of Graphitic Carbon Nitride-Based Structures and Applications in Catalyst, Sensing, Imaging, and LEDs" *Nano-Micro Lett.*, **2017** (9)
[126] Yan, S. C.; Li, Z. S. and Zou, Z. G. "Photodegradation of rhodamine B and methyl orange over boron-doped g-C 3N4 under visible light irradiation" *Langmuir*, **2010** (26) 3894–901
[127] Zhang, J.; Zhang, M.; Sun, R. Q. and Wang, X. "A facile band alignment of polymeric carbon nitride semiconductors to construct isotype heterojunctions" *Angew. Chemie - Int. Ed.*, **2012** (51) 10145–9
[128] Zhou, L.; Zhang, H.; Sun, H.; Liu, S.; Tade, M. O.; Wang, S. and Jin, W. "Recent advances in non-metal modification of graphitic carbon nitride for photocatalysis: A historic review" *Catal. Sci. Technol.*, **2016** (6) 7002–23
[129] Caux, M.; Fina, F.; Irvine, J. T. S.; Idriss, H. and Howe, R. "Impact of the annealing temperature on Pt/g-C3N4 structure, activity and selectivity between photodegradation and water splitting" *Catal. Today*, **2017** (287) 182–8
[130] Jiang, L.; Yuan, X.; Pan, Y.; Liang, J.; Zeng, G.; Wu, Z. and Wang, H. "Doping of graphitic carbon nitride for photocatalysis: A reveiw" *Appl. Catal. B Environ.*, **2017** (217) 388–406
[131] Fang, X. X.; Ma, L. B.; Liang, K.; Zhao, S. J.; Jiang, Y. F.; Ling, C.; Zhao, T.; Cheang, T. Y. and Xu, A. W. "The doping of phosphorus atoms into graphitic carbon nitride for highly enhanced photocatalytic hydrogen evolution" *J. Mater. Chem. A*, **2019** (7) 11506–12
[132] Katsumata, H.; Sakakibara, K.; Tateishi, I.; Furukawa, M. and Kaneco, S. "Structurally modified graphitic carbon nitride with highly photocatalytic activity in the presence of visible light" *Catal. Today*, **2020** (352) 47–53
[133] Teixeira, I. F.; Barbosa, E. C. M.; Tsang, S. C. E. and Camargo, P. H. C. "Carbon nitrides and metal nanoparticles: From controlled synthesis to design principles for improved photocatalysis" *Chem. Soc. Rev.*, **2018** (47) 7783–817
[134] Huang, J.; Liu, J.; Yan, J.; Wang, C.; Fei, T.; Ji, H.; Song, Y.; Ding, C.; Liu, C.; Xu, H. and Li, H. "Enhanced photocatalytic H2 evolution by deposition of metal nanoparticles into mesoporous structure of g-C3N4" *Colloids Surfaces A Physicochem. Eng. Asp.*, **2020** (585) 124067
[135] Han, C.; Lu, Y.; Zhang, J.; Ge, L.; Li, Y.; Chen, C.; Xin, Y.; Wu, L. and Fang, S. "Novel PtCo alloy nanoparticle decorated 2D g-C3N4 nanosheets with enhanced photocatalytic activity for H2 evolution under visible light irradiation" *J. Mater. Chem. A*, **2015** (3) 23274–82
[136] Nazir, R.; Fageria, P.; Basu, M.; Gangopadhyay, S. and Pande, S. "Decoration of Pd and Pt nanoparticles on a carbon nitride (C3N4) surface for nitro-compounds reduction and hydrogen evolution reaction" *New J. Chem.*, **2017** (41) 9658–67
[137] Shiraishi, Y.; Kofuji, Y.; Kanazawa, S.; Sakamoto, H.; Ichikawa, S.; Tanaka, S. and Hirai, T. "Platinum nanoparticles strongly associated with graphitic carbon nitride as efficient co-catalysts for photocatalytic hydrogen evolution under visible light" *Chem. Commun.*, **2014** (50) 15255–8
[138] Ghosh, K.; Kumar, M.; Wang, H.; Maruyama, T. and Ando, Y. "Facile decoration of platinum nanoparticles on carbon-nitride nanotubes via microwave-assisted chemical reduction and their optimization for field-emission application" *J. Phys. Chem. C*, **2010** (114) 5107–12
[139] Yue, X.; Yi, S.; Wang, R.; Zhang, Z. and Qiu, S. "Cadmium sulfide and nickel synergetic co-catalysts supported on graphitic carbon nitride for visible-light-driven photocatalytic hydrogen evolution" *Sci. Rep.*, **2016** (6) 1–9
[140] Chen, J.; Zhao, D.; Diao, Z.; Wang, M. and Shen, S. "Ferrites boosting photocatalytic hydrogen evolution over graphitic carbon nitride: a case study of (Co, Ni)Fe2O4 modification" *Sci. Bull.*, **2016** (61) 292–301
[141] Cao, M.; Zhang, X.; Qin, J. and Liu, R. "Enhancement of Hydrogen Evolution Reaction Performance of Graphitic Carbon Nitride with Incorporated Nickel Boride" *ACS Sustain. Chem. Eng.*, **2018** (6) 16198–204
[142] Oliveira, R. C. P.; Sevim, M.; Šljukić, B.; Sequeira, C. A. C.; Metin, Ö. and Santos, D. M. F. "Mesoporous graphitic carbon nitride-supported binary MPt (M: Co, Ni, Cu) nanoalloys as electrocatalysts for borohydride oxidation and hydrogen evolution reaction" *Catal. Today*, **2019**
[143] Deng, P.; Gan, M.; Zhang, X.; Li, Z. and Hou, Y. "Non-noble-metal Ni nanoparticles modified N-doped g-C3N4 for efficient photocatalytic hydrogen evolution" *Int. J. Hydrogen Energy*, **2019** (44) 30084–92
[144] Albero, J.; Peng, Y. and García, H. "Photocatalytic CO2Reduction to C2+ Products" *ACS Catal.*, **2020** (10) 5734–49

[145] Inoue, T.; Fujishima, A.; Konishi, S. and Honda, K. "Photoelectrocatalytic reduction of carbon dioxide in aqueous suspensions of semiconductor powders [3]" *Nature*, **1979** (277) 637–8
[146] Stolarczyk, J. K.; Bhattacharyya, S.; Polavarapu, L. and Feldmann, J. "Challenges and Prospects in Solar Water Splitting and CO2 Reduction with Inorganic and Hybrid Nanostructures" *ACS Catal.*, **2018** (8) 3602–35
[147] Huynh, M. H. V. and Meyer, T. J. "Proton-Coupled Electron Transfer" **2007** 5004–64
[148] Fresno, F.; Villar-García, I. J.; Collado, L.; Alfonso-González, E.; Renones, P.; Barawi, M. and De La Pena O'Shea, V. A. "Mechanistic View of the Main Current Issues in Photocatalytic CO 2 Reduction" *J. Phys. Chem. Lett.*, **2018** (9) 7192–204
[149] Thompson, W. A.; Sanchez Fernandez, E. and Maroto-Valer, M. M. " Review and Analysis of CO 2 Photoreduction Kinetics " *ACS Sustain. Chem. Eng.*, **2020** (8) 4677–92
[150] Habisreutinger, S. N.; Schmidt-Mende, L. and Stolarczyk, J. K. "Photocatalytic reduction of CO2 on TiO2 and other semiconductors" *Angew. Chemie - Int. Ed.*, **2013** (52) 7372–408
[151] Corma, A. and Garcia, H. "Photocatalytic reduction of CO2 for fuel production: Possibilities and challenges" *J. Catal.*, **2013** (308) 168–75
[152] Sagir, M.; Tahir, M. B.; Rafique, M.; Rafique, M. S. and Nawaz, T. *Photocatalytic nanomaterials for CO2 photoreduction and disinfection of bacteria* (Elsevier Inc.)
[153] Xie, S.; Wang, Y.; Zhang, Q.; Deng, W. and Wang, Y. "MgO- and Pt-promoted TiO2 as an efficient photocatalyst for the preferential reduction of carbon dioxide in the presence of water" *ACS Catal.*, **2014** (4) 3644–53
[154] Wang, W. N.; An, W. J.; Ramalingam, B.; Mukherjee, S.; Niedzwiedzki, D. M.; Gangopadhyay, S. and Biswas, P. "Size and structure matter: Enhanced CO 2 photoreduction efficiency by size-resolved ultrafine Pt nanoparticles on TiO 2 single crystals" *J. Am. Chem. Soc.*, **2012** (134) 11276–81
[155] Tasbihi, M.; Fresno, F.; Simon, U.; Villar-García, I. J.; Pérez-Dieste, V.; Escudero, C. and de la Peña O'Shea, V. A. "On the selectivity of CO2 photoreduction towards CH4 using Pt/TiO2 catalysts supported on mesoporous silica" *Appl. Catal. B Environ.*, **2018** (239) 68–76
[156] Wang, C.; Thompson, R. L.; Baltrus, J. and Matranga, C. "Visible light photoreduction of CO2 using CdSe/Pt/TiO2 heterostructured catalysts" *J. Phys. Chem. Lett.*, **2010** (1) 48–53
[157] Ong, W. J.; Tan, L. L.; Ng, Y. H.; Yong, S. T. and Chai, S. P. "Graphitic Carbon Nitride (g-C3N4)-Based Photocatalysts for Artificial Photosynthesis and Environmental Remediation: Are We a Step Closer to Achieving Sustainability?" *Chem. Rev.*, **2016** (116) 7159–329
[158] Yu, J.; Wang, K.; Xiao, W. and Cheng, B. "Photocatalytic reduction of CO2 into hydrocarbon solar fuels over g-C3N4-Pt nanocomposite photocatalysts" *Phys. Chem. Chem. Phys.*, **2014** (16) 11492–501
[159] Dong, C.; Lian, C.; Hu, S.; Deng, Z.; Gong, J.; Li, M.; Liu, H.; Xing, M. and Zhang, J. "Size-dependent activity and selectivity of carbon dioxide photocatalytic reduction over platinum nanoparticles" *Nat. Commun.*, **2018** (9) 1–11
[160] Dowling, a.; Clift, R.; Grobert, N.; Hutton, D.; Oliver, R.; O'neill, O.; Pethica, J.; Pidgeon, N.; Porritt, J.; Ryan, J. and Et Al. "Nanoscience and nanotechnologies : opportunities and uncertainties" *London R. Soc. R. Acad. Eng. Rep.*, **2004** (46) 618–618
[161] Sanchez, F. and Sobolev, K. "Nanotechnology in concrete - A review" *Constr. Build. Mater.*, **2010** (24) 2060–71
[162] Volokitin, Y.; Sinzig, J.; De Jongh, L. J.; Schmidt, G.; Vargaftik, M. N. and Moiseev, I. I. "Quantum-size effects in the thermodynamic properties of metallic nanoparticles" *Nature*, **1996** (384) 621–3
[163] Loss, D. "Editorial: Quantum phenomena in Nanotechnology" *Nanotechnology*, **2009** (20) 8–9
[164] Poh, T. Y.; Ali, N. A. T. B. M.; Mac Aogáin, M.; Kathawala, M. H.; Setyawati, M. I.; Ng, K. W. and Chotirmall, S. H. "Inhaled nanomaterials and the respiratory microbiome: Clinical, immunological and toxicological perspectives" *Part. Fibre Toxicol.*, **2018** (15) 1–16
[165] Stark, W. J.; Stoessel, P. R.; Wohlleben, W. and Hafner, A. "Industrial applications of nanoparticles" *Chem. Soc. Rev.*, **2015** (44) 5793–805
[166] Salata, O. V. "Applications of nanoparticles in biology and medicine" *J. Nanobiotechnology*, **2004** (6) 1–6
[167] Luo, X.; Morrin, A.; Killard, A. J. and Smyth, M. R. "Application of nanoparticles in electrochemical sensors and biosensors" *Electroanalysis*, **2006** (18) 319–26
[168] Astruc, D. "Introduction: Nanoparticles in Catalysis" *Chem. Rev.*, **2020** (120) 461–3

[169] Prasad Yadav, T.; Manohar Yadav, R. and Pratap Singh, D. "Mechanical Milling: a Top Down Approach for the Synthesis of Nanomaterials and Nanocomposites" *Nanosci. Nanotechnol.*, **2012** (2) 22–48
[170] Colson, P.; Henrist, C. and Cloots, R. "Nanosphere lithography: A powerful method for the controlled manufacturing of nanomaterials" *J. Nanomater.*, **2013** (2013)
[171] Jamkhande, P. G.; Ghule, N. W.; Bamer, A. H. and Kalaskar, M. G. "Metal nanoparticles synthesis: An overview on methods of preparation, advantages and disadvantages, and applications" *J. Drug Deliv. Sci. Technol.*, **2019** (53) 101174
[172] Roucoux, A.; Schulz, J. and Patin, H. "Reduced transition metal colloids: A novel family of reusable catalysts?" *Chem. Rev.*, **2002** (102) 3757–78
[173] Iqbal, P.; Preece, J. A. and Mendes, P. M. "Nanotechnology: The "Top-Down" and "Bottom-Up" Approaches" *Supramol. Chem.*, **2012**
[174] Iravani, S.; Korbekandi, H.; Mirmohammadi, S. V. and Zolfaghari, B. "Synthesis of silver nanoparticles: Chemical, physical and biological methods" *Res. Pharm. Sci.*, **2014** (9) 385–406
[175] Zhang, Q. L.; Yang, Z. M.; Ding, B. J.; Lan, X. Z. and Guo, Y. J. "Preparation of copper nanoparticles by chemical reduction method using potassium borohydride" *Trans. Nonferrous Met. Soc. China (English Ed.*, **2010** (20) s240–4
[176] Salavati-niasari, M. and Davar, F. "Synthesis of copper and copper (I) oxide nanoparticles by thermal decomposition of a new precursor" *Mater. Lett.*, **2009** (63) 441–3
[177] Okitsu, K.; Ashokkumar, M. and Grieser, F. "Sonochemical synthesis of gold nanoparticles: Effects of ultrasound frequency" *J. Phys. Chem. B*, **2005** (109) 20673–5
[178] Teixeira, P. R.; Santos, M. S. C.; Silva, A. L. G.; Báo, S. N.; Azevedo, R. B.; Sales, M. J. A. and Paterno, L. G. "Photochemically-assisted synthesis of non-toxic and biocompatible gold nanoparticles" *Colloids Surfaces B Biointerfaces*, **2016** (148) 317–23
[179] Choi, D. S.; Robertson, A. W.; Warner, J. H.; Kim, S. O. and Kim, H. "Low-Temperature Chemical Vapor Deposition Synthesis of Pt–Co Alloyed Nanoparticles with Enhanced Oxygen Reduction Reaction Catalysis" *Adv. Mater.*, **2016** (28) 7115–22
[180] Reetz, M. T. and Helbig, W. "Size-Selective Synthesis of Nanostructured Transition Metal Clusters" *J. Am. Chem. Soc.*, **1994** 7401–2
[181] Reetz, M. T. and Quaiser, S. A. "A New Method for the Preparation of Nanostructured Metal Clusters" *Angew. Chemie Int. Ed. English*, **1995** (34) 2240–1
[182] Pelzer, K.; Vidoni, O.; Philippot, K.; Chaudret, B. and Collière, V. "Organometallic synthesis of size-controlled polycrystalline ruthenium nanoparticles in the presence of alcohols" *Adv. Funct. Mater.*, **2003** (13) 118–26
[183] Osuna, J.; De Caro, D.; Amiens, C.; Chaudret, B.; Snoeck, E.; Respaud, M.; Broto, J. M. and Fert, A. "Synthesis, characterization, and magnetic properties of cobalt nanoparticles from an organometallic precursor" *J. Phys. Chem.*, **1996** (100) 14571–4
[184] Ely, T. O.; Amiens, C.; Chaudret, B.; Snoeck, E.; Verelst, M.; Respaud, M. and Broto, J. "Synthesis of Nickel Nanoparticles . Influence of Aggregation Induced by Modification of Poly (vinylpyrrolidone) Chain Length on Their Magnetic Properties attracting increasing interest , because they may differ surface or quantum size effects . 1 Howeve" *Chem. Mater.*, **1999** (11) 526–9
[185] Moraes, L. C.; Figueiredo, R. C.; Espinós, J. P.; Vattier, F.; Franconetti, A.; Jaime, C.; Lacroix, B.; Rojo, J.; Lara, P. and Conejero, S. "Platinum nanoparticles stabilized by N-heterocyclic thiones. Synthesis and catalytic activity in mono- A nd di-hydroboration of alkynes" *Nanoscale*, **2020** (12) 6821–31
[186] Castillejos, E.; Debouttière, P. J.; Roiban, L.; Solhy, A.; Martinez, V.; Kihn, Y.; Ersen, O.; Philippot, K.; Chaudret, B. and Serp, P. "An efficient strategy to drive nanoparticles into carbon nanotubes and the remarkable effect of confinement on their catalytic performance" *Angew. Chemie - Int. Ed.*, **2009** (48) 2529–33
[187] Mallón, L.; Romero, N.; Jiménez, A.; Martín Morales, E.; Alemán, J.; Mas-Ballesté, R.; Bofill, R.; Philippot, K.; García-Antón, J. and Sala, X. "The role of catalyst-support interactions in oxygen evolution anodes based on Co(OH)2nanoparticles and carbon microfibers" *Catal. Sci. Technol.*, **2020** (10) 4513–21
[188] Schröder, F.; Esken, D.; Cokoja, M.; Van Den Berg, M. W. E.; Lebedev, O. I.; Van Tendeloo, G.; Walaszek, B.; Buntkowsky, G.; Limbach, H. H.; Chaudret, B. and Fischer, R. A. "Ruthenium nanoparticles inside porous [Zn4O(bdc)3] by hydrogenolysis of adsorbed [Ru(cod)(cot)]: A solid-state reference system for surfactant-stabilized ruthenium colloids" *J. Am. Chem. Soc.*, **2008** (130) 6119–30

Chapter II

Objectives

After introducing the state-of-the-art in the field of artificial photosynthesis and electrochemical-induced water splitting, the main goals of these PhD thesis are presented in this chapter. Essentially, they involve the preparation of Ru-based nanoparticles as catalyst in the hydrogen evolution reaction, and Ru and Pt-based photocatalyst for CO_2 reduction into fuels and other chemicals. In the first part, the objectives common to all the studied processes are exposed, and then the specific objectives for each chapter are detailed.

1.1. General objectives

For the past decades, one of the great issues of researchers within the energy field has been focused on developing reliable catalyst for the processes involved in artificial photosynthesis. This process, which emerges as an alternative to the fossil fuels utilization and a strategy to reduce the CO_2 emissions in the atmosphere, uses water and sunlight to produce fuels. During artificial photosynthesis, and after water is oxidized into oxygen, protons and electrons are released, which can be reduced into H_2 (in the overall process known as water splitting). Electrons can also be used to reduce CO_2, yielding fuels and other value-added chemicals. The main challenge of both Hydrogen Evolution Reaction (HER) and CO_2 reduction is the development of robust and efficient catalysts to carry out these transformations. Thus, the overall objectives, and the backbone of this PhD thesis, can be summarized as follow:

- Design of metal-based catalysts, within the nanoscale, for the HER and CO_2 reduction.
- Lean on the organometallic approach as synthetic tool in order to carry out the preparation of the catalysts under mild reaction conditions, with a controlled surface state.
- Select the adequate photoactive material both to support the catalytically active metal-based nanoparticles and to carry out the HER and CO_2 reduction induced by light irradiation.
- Complement the (photo)catalytic studies with diverse characterization techniques, to be aware of the surface environment, oxidation state, morphology or the evolution of species before and after the catalytic conditions.
- Based on these observations, rationally design new (photo)catalysts by tuning their features, with the aim of improving their catalytic performances.

1.2. Specific objectives

In the case of the HER, the reductive half-reaction of the water splitting process, Ru-based NPs have been recently reported as a more affordable and, in some cases, more stable alternative to the state-of-the-art Pt. Thus, the specific objectives of this part are:

- Synthesis and characterization of Ru-NPs, through the organometallic method, stabilized with pyridine-type ligands. Study the effect that reaction conditions (nature of the ligand and ligand-to-metal ratio) has on the size, surface composition or oxidation state of the nanoparticles.
- Test the prepared Ru-based nanosystems as catalyst in the electrochemical HER, evaluate both their activity and stability under extreme pH conditions, and correlate their catalytic output with their physical and chemical features to better understand the mechanism involved in this transformation. Finally, compare with reported analogous systems.

For the light-driven HER, in addition to the suitable catalyst, a photoactive species is required, such as semiconductor materials. The challenge with this process is the election of the semiconductor, which should feature the adequate bandgap to be visible light responsive, and an optimal communication with the metallic catalyst (co-catalyst), in order to facilitate the electron-transfer process, thus adding further goals:

- Study of carbon nitride as photoactive material triggered by visible light, and also as support for the stabilization of the metal (Ru or Pt) nanoparticles used as co-catalyst.
- Evaluate different strategies for the deposition of the metal nanoparticles on the surface, including direct deposition following the organometallic approach, or physical mixture with metal nanoparticles pre-deposited on different carbon-based conductive materials.
- Elucidate the role of the different metal-loading methods and the nature of the co-catalyst in their corresponding photocatalytic outputs, based on photocatalytic HER experiments and complementary photophysical studies.

The major challenge concerning CO_2 photoreduction is to achieve control over the selectivity towards each of the possible products of the reduction, including the competitive proton reduction. In this case, the election of the adequate co-catalyst (generally Pt) to load on the photoactive material not only affects the photocatalytic performance of the system, but also the selectivity of the process. Thus, in addition to the objectives described for the light-driven HER regarding the choice of photoactive support, as specific goals for this part are:

- Preparation of carbon nitride-supported Pt NPs, with different loads, directly deposited using the organometallic approach.
- Study the activity towards CO_2 photoreduction and the selectivity towards different C-products, correlating the results with the absence/presence of the co-catalyst, the load of Pt, and the use of UV or visible as light sources.

Finally, and as an additional objective, it is intended to test the versatility of nanoparticles prepared following the organometallic approach towards applications other than energy production. Sensors are one of the main applications of nanoparticles nowadays. The combination of their catalytic features with the electric conductivity of carbonaceous supports leads to an increase in the analytical signal, which is of paramount importance in this particular field. In this regard, the objectives for this final part are:

- Preparation of Pt-based nanoparticles supported on carbon (nano)allotropes, by direct deposition following organometallic approach.
- Test the prepared hybrid materials as electrochemical sensing platforms towards methylparaben (MeP) determination, a potential endocrine-disrupting chemical present in many cosmetic and pharmaceutical formulations.
- Validate the proposed electroanalytical method, with real samples, using the traditional, but more tedious, chromatographic technique (HPLC).

Chapter III

Ligand-capped Ruthenium Nanoparticles as Hydrogen Evolution Catalysts

Two ruthenium-based nanocatalysts have been prepared, following the organometallic approach, and stabilized by pyridine-type ligands. After thorough characterization, including TEM, WAXS, ICP, EA and TGA analyses, the electrochemical output of both systems for the Hydrogen Evolution Reaction has been tested in acidic and basic conditions, trying to understand their behaviour based on their distinguished surface properties.

Table of contents

3.1 Abstract

Ruthenium nanoparticles (NPs) have been easily prepared following the organometallic method, by hydrogenation of the organometallic compound [Ru(cod)(cot)] (cod = 1,5-cyclooctadiene; cot = 1,3,5-cyclooctatriene) in THF, in the presence of pyridine-type ligands as stabilizers, either 4'-(4-methylphenyl)-2,2':6',2"-terpyridine (MPT) or 2-phenylpyridine (2PP). Ligand to metal ratio during the synthesis of the NPs was optimized to study the effect of the ligand, obtaining small, well-defined and homogeneous nanoparticles. After properly isolating and characterizing the NPs by the commonly used state characterization techniques, they were deposited onto a glassy carbon electrode, and tested as electrocatalysts in the hydrogen evolution reaction (HER). In 1 M H_2SO_4, the activity of these materials was highly dependent on the oxidation state on the surface of the NPs, being metallic Ru more active than RuO_2, whereas in 1 M NaOH the Ru/RuO_2 of the as-deposited nanomaterials is maintained even after reductive treatment. Both 2PP and MPT-stabilized Ru NPs systems were benchmarked after estimation of the active sites on the NPs surface and the electrochemically active surface area (*ECSA*), and they have proved to be active and highly stable in acidic and basic pH under turnover conditions. Furthermore, in 1 M H_2SO_4, the 2PP-stabilized system displayed low overpotentials and Tafel slope ($\eta_0 \approx 0$ mV and η_{10} = 30 mV and 42 mV·dec^{-1}, respectively) and high TOF (ca. 10 s^{-1} at η = 100 mV), values fairly competitive to the ones obtained for Ru NPs stabilized with 4-phenylpyridine recently reported, which outshines the state-of-the-art Pt and most of the HER electrocatalyst reported under acidic (and also basic) conditions.

3.2 Introduction

Hydrogen evolution reaction (HER), as part of the sunlight-driven water splitting process, plays an important role in the global energy economy, promoting hydrogen production from water and sunlight as a clean and sustainable energy alternative to the still dominant, but highly polluting and ill-distributed fossil fuels [1,2]. This transformation of protons into hydrogen, and also its redox counterpart (the oxygen evolution reaction, OER), require catalysts operating at low overpotentials and under fast kinetic conditions, thereby making the whole hydrogen production from water splitting process efficient.

Among all HER catalysts reported, Pt-based catalyst show the best performance, especially in acidic conditions. This could be explained through the HER mechanism: when Pt-H species are formed, they are stable enough due to the strength of the bond, but weak enough to promote dihydrogen gas formation afterwards [3]. However, stability problems in basic pH, together with its scarcity and high cost, hampers its implementation on large scale applications [4,5]. In this way, Ru is postulated as the ideal alternative, being cheaper than Pt, and more stable in alkaline medium, and with a Ru-H bond strength that does not differ much from the Pt-H one. Therefore, the small difference in bond strength should not have a great impact on the overpotentials achieved by these catalysts [6,7].

More concretely, the use of Ru-based nanoparticles (NPs) as (electro)catalysts for HER has attracted lots of attention in recent years [8]. This nanostructured heterogeneous systems, with a surface area to volume ratio significantly larger than the corresponding bulk material, offer high stability in both acidic and basic pH [3], although electron transfer is generally less facilitated compared to molecular complexes. This issue can be overcome by depositing the NPs on a support such as a conductive carbon-based matrix (e.g. carbon nanotubes or graphitic carbon nitride)[9,10], or by immobilizing them in a glassy carbon (GC) electrode [11], to directly test their electrocatalytic performance towards HER.

One great advantage of preparing ex-situ Ru-based NPs as electrocatalysts for HER is that, as their intrinsic catalytic properties are not altered by the supporting electrodes, they allow greater control over the characteristics of the NPs when

choosing the adequate synthetic method, thus facilitating the correlation of their chemical and physical properties with their HER electrocatalytic output. In this regard, the organometallic approach is a very powerful tool for the preparation of small, homogeneous nanoparticles, with great control of the surface composition and under mild reaction conditions [12]. The organometallic precursor and the reaction conditions (temperature, solvent) are important for the final characteristics of the nanoparticles. An stabilizing ligand is generally required to ensure the nanosized structure of the obtained particles and also to prevent their aggregation. These ligands, coordinated on the surface of the nanoparticles, will influence the active sites of the electrocatalysts, thus affecting their performance. This makes the organometallic approach a rapid and easy alternative to prepare nanocatalysts with tunable properties playing with different types of ligands.

Recently, the research group reported a Ru NPs system, prepared from the decomposition of the organometallic precursor [Ru(cod)(cot)] (cod = 1,5-cyclooctadiene; cot = 1,3,5-cyclooctatriene) under 3 bars of hydrogen in THF, with 4-phenylpyridine (4PP) as stabilizing ligand [13]. These small (1.5 ± 0.3 nm) Ru NPs were well-defined with a narrow size-distribution and, most important, with a well-known surface composition after an exhaustive characterization study involving diverse techniques. After being immobilized onto a GC electrode, the nanomaterial was tested for the HER in extreme pH conditions, outperforming both commercial ruthenium black (Rub) and Pt/C in 1 M H_2SO_4, displaying really low overpotentials ($\eta_0 \approx 0$ mV and $\eta_{10} = 20$ mV) and high TOF (ca. 17 s^{-1}), and also in 1 M NaOH ($\eta_0 \approx 0$ mV and $\eta_{10} = 25$ mV), with outstanding stability in both acidic and alkaline conditions, thus being one of the best HER electrocatalysts reported to date.

The objective of this chapter is to prepare analogous systems of Ru NPs stabilized by pyridine-type ligands via the organometallic approach, under the same reactions conditions as the previously reported system. These ligands are 2-phenylpyridine (2PP) and 4'-(4-methylphenyl)-2,2':6',2"-terpyridine (MPT). Through the different characterization techniques, we will be able to study the effect that these ligands can have on the morphology of the Ru NPs, as well as on their surface properties, and later correlate the effect these characteristics have on their catalytic output in acidic and basic media.

3.3 Experimental part

3.3.1 Reagents and materials

All procedures involved the synthesis of the Ru NPs stabilized by pyridine-type ligands were carried out using standard Schlenk-line and Fischer-Porter bottle techniques. A glovebox (MBRAUN Unilab) with argon atmosphere is also employed to handle the metal precursors. Glassware was dried at 120 ˚C before use. The following chemicals were used as purchased: [Ru(cod)(cot)] (cod = 1,5-cyclooctadiene; cot = 1,3,5-cyclooctatriene) from NanoMePS, the pyridine-type ligand used as stabilizers, 2-phenylpyridine (**2PP**) and 4'-(4-methylphenyl)-2,2':6',2"-terpyridine (**MPT**), from Sigma-Aldrich; hydrogen (H_2) gas from Air Liquide (Alphagaz). Tetrahydrofuran (THF) and pentane, used as solvents, were treated in a purification apparatus (MBRAUN) and degassed by freeze-pump-thaw cycling prior to use.

3.3.2 Synthesis procedure

All Ru-NPs systems were prepared following the same procedure, solvent and ruthenium organometallic precursor, only varying the pyridine-type ligand and the ligand to metal (L/M) ratio. For **MPT** ligand, 0.05, 0.1, 0.2 and 0.5 L/M molar equivalents (eq.) where employed, whereas 0.2, 0.3, 0.4 and 0.5 L/M molar eq. were used when preparing **2PP**-stabilized Ru-NPs. Ru NPs stabilized by 0.05 molar eq. of **MPT** will serve as example, detailed as follow. A Fisher-Porter bottle, containing [Ru(cod)(cot)], (80 mg, 0.253 mmol) under argon atmosphere, is placed in an EtOH/N_2 bath. A solution of **MPT** (4.1 mg, 0.012 mmol) ligand in THF (80 mL), prepared also under inert conditions, was transferred into the reactor, which was then pressurized with 3 bars of H_2 gas and kept under stirring at room temperature (r.t.) for 16 h. Colour change from yellow to dark brown could be observed in the solution within the first minutes of reaction. The nanoparticles were precipitated by pentane addition under Ar atmosphere and washed also with pentane. Afterwards, they were isolated and dried under vacuum, and finally transferred into a vial inside the glovebox. The vial containing Ru NPs remained closed, outside the glovebox, for

several days (minimum 30 days), before opening, for a slow oxidation (i.e., passivation process) of the metallic surface.

3.3.3 Characterization techniques

Transmission Electron Microscopy (TEM) and High Resolution TEM (HRTEM). Transmission electron microscopy at low and high resolution (TEM and HRTEM) analyses were performed in Servei de Microscòpia at the UAB, using a JEM-2011 unit with an acceleration voltage of 200 kV. TEM samples were prepared by drop-casting method, depositing a small drop of the colloidal solution after synthesis and after cleaning process onto a carbon-coated copper grid. TEM micrographs were treated with the Fiji-ImageJ image processing freeware. An average of 200 NPs were measured to obtain the mean size and size distribution of each Ru NPs system.

Wide-Angle X-Ray Scattering (WAXS). WAXS analyses were carried out at Centre d'Élaboration de Matériaux et d'Études Structurales (CEMES-CNRS) in Toulouse, France. Samples were placed in 1.0 mm diameter glass capillaries (Lindermann) under Argon, and the measurements were taken after irradiation with graphite monochromatized molybdenum Kα (0.071069 nm) radiation, while two-axis diffractometer was employed to carry out X-ray scattering intensity measurements. After Fourier transformation of the reduced and corrected data, Radial distribution functions (RDF) were estimated.

X-Ray Photoelectron Spectroscopy (XPS). XPS analyses were carried out at Institut Català de Nanociència i Nanotecnologia (ICN2), in Barcelona. A Phoibos 150 analyzer from SPECS GmbH (Berlin, Germany) at ultra-high vacuum conditions (base pressure of $5 \cdot 10^{-10}$ mbar), with a monochromatic aluminum Kα X-ray source (1486.74 eV), was employed to perform the measurements. The energy resolution was measured by the FWHM of the Ag 3d5/2 peak, which for a sputtered silver foil was 0.62 eV.

Elemental analysis (EA). EA was performed at Servei d'Anàlisi Química (SAQ) at the UAB in Barcelona, using a Flash EA 2000 CHNS from Thermo Fisher Scientific.

Inductively Coupled Plasma - Optical Emission Spectrometry (ICP-OES). The amount of Ru (wt.%) on each ligand-stabilized Ru NPs system was determined by an ICP-OES in an Agilent Optima model system at the "Servei d'Anàlisi Química (SAQ)" of the Universitat Autònoma de Barcelona.

Thermogravimetric Analysis (TGA). Thermogravimetric analyses were performed using a Perkin Elmer TGA 7 analyzer under Ar atmosphere, in a temperature range from 30 ˚C to 500 ˚C and a heating rate of 2 ˚C·min^{-1}. Measurements were performed per triplicate, showing the average results obtained.

Ligand/Ru ratio calculation. The number of mol (n) of either **MPT** or **2PP** ligands were calculated from a) N wt.% value obtained by EA, and Ru wt.% estimated after subtracting organics (CHN) from EA data or b) remaining wt.% after the drop observed in TGA analysis (attributed to the ligand) in the 150-300 °C range

Surface hydride titration. This experiment was done for the crude colloidal solution of **RuMPT** and **Ru2PP**, using [Ru(cod)(cot)] (30 mg, 0.095 mmol) and **MPT** (1.54 mg, 0.005 mmol) or **2PP** (2.94 mg, 0.019 mmol) to prepare the nanoparticles, following the method described at the beginning of this section. Synthesis was stopped by removing the excess of hydrogen, applying vacuum and refilling with argon, repeating the cycle three times. Then, 2-norbornene (45 mg, 0.475 mmol) was weighted and placed into the reactor, under inert atmosphere. The mixture was kept under stirring for three days, in which each two surface hydrides were able to hydrogenate one double bond from 2-norbornene to yield norbornane. After this time, an aliquot was taken, filtered through celite and kept in a vial for GC-MS analysis, experiment performed at the SAQ in UAB using a Gas Chromatograph HP 6890 Series II with a SGE BP1 non polar 100% dimethyl polysiloxane capillary column of 50mx0.32mmx0.25µm, coupled with a MS detector model 5973 (Hewlett-Packard).

Calculations were performed as follows, using **RuMPT** as example. After analysing the samples and treating the data, the hydrogenation conversion of 2-norbornene to norbornane was estimated at 4.3 %, which is equivalent to 0.020 mol of norbornane, and therefore 0.040 mol of hydrides titrated.

Eq. 1 is used to calculate the total number of metal atoms per nanoparticle (N_T), being d the density of Ru atom (12.45 g·cm^{-3}), N_A the Avogadro constant, V the volume of the nanoparticle considering a mean size of 1.4 nm and assuming each NP is a perfect sphere, and MW the molecular weight of Ru.

$$N_T = \frac{d \cdot N_A \cdot V}{MW} = \frac{(12.45 \cdot 10^6) \cdot (6.022 \cdot 10^{23}) \cdot (\frac{4}{3} \cdot \pi \cdot \left(\frac{1.4}{2} \cdot 10^{-9}\right)^3)}{101.07} = 107\ atoms \qquad \textbf{Eq. 1}$$

Once N_T was determined, surface Ru atoms (N_S) number was calculated following the magic-number clusters concept,[14,15] assuming that there are layers around the central atom, composed of the optimal number of atoms to achieve a stable configuration, while maintaining a certain structure. Whereas hexagonal close-packed (hcp) is the bulk Ru crystalline structure, at the nanoscale, face-centered cubic (fcc) structure is also possible, even a combination of both of them [16–18]. The atoms of each shell around the central unit could be calculated using ($10n^2$+2), where n is the number of each layer. **Table 1** exemplifies various magic-number clusters, with the percentage of surface atoms considering a full shell[19],[20].

Number of shells (n)	1	2	3	4	5
Number of atoms per cluster	13	55	147	309	561
Percentage of surface atoms (Complete shell)	92 %	76 %	63 %	52 %	45 %

Table 1. Building of close-shell clusters by applying the magic number rule

As calculated before, there are 107 atoms per nanoparticle of **RuMPT**, thus being in and intermediate situation between clusters of 2 and 3 full shells. Considering the initial quantity of [Ru(cod)(cot)] as 30 mg (0.095 mmol), and the percentage of surface atoms reflected on Table 1, the amount of surface Ru would be 0.072 mol in the case of 2 full-shell cluster, and 0.060 mol for a 3 full-shell cluster. With the previous calculation of titrated hydrides (0.040 mol) and considering the contribution of both full-shell clusters possibilities, a H/Ru$_{surface}$ ratio of ca. 0.7 was estimated.

Electrochemical characterization. Electrochemical measurements were carried out in a BioLogic SP-150 potentiostat, using a three-electrode set-up. A glassy carbon rotating disk electrode (GC-RDE, 0.07 cm^2 surface area) was employed as

working electrode (WE), connected to a R11V016 Radiometer CTV101 speed control unit fixed at 3000 rpm, which allows the removal of H_2 bubbles as they form. A Pt mesh electrode and a saturated calomel electrode (SCE) (KCl sat.) were used as counter electrode (CE) and reference electrode (RE) respectively. This electrode configuration was employed for all the experiments unless otherwise noted. 1 M H_2SO_4 solution (pH 0) and 1M NaOH (pH 14) solution were prepared by dilution of 95-97 % H_2SO_4 (56.1 mL) and dissolving NaOH (40.0 g), respectively, in Mili-Q water (1 L). The solutions were degassed by bubbling N_2 gas prior to the experiments. Automatic correction of ohmic potential (*i*R) drop was adjusted to 85% using the Biologic EC-Lab software. The *E* values of the different experiments were expressed as V vs RHE adding +0.244 V in the case of using SCE as a reference, and +0.200 V in the case of using Ag/AgCl electrode. The measured or applied current intensity (*i*) is transformed into current density (*j*) dividing by the surface of the WE used in each case.

Electrode Preparation. To prepare RDE-supported Ru NPs, a 2 mg·mL^{-1} colloidal solution was prepared (1 mg of the selected Ru NPs in 500 µL of THF, or 495 µL of THF and 5 µL of Nafion® solution when indicated), sonicating for 30 minutes. Three 5 µL aliquots of the dispersion were added to the surface of the RDE, allowing the solvent to evaporate under an air current between each drop.

In the case of the FTO-supported Ru NPs, a single 25 µL drop of NPs solution was added onto the surface of the electrode.

Linear Seep Voltammetry (LSV). To obtain LSV curves, the voltage was scanned from E_i = 0.2 V vs NHE to E_f = -0.4 V vs NHE, at 10 m·Vs^{-1} scan rate.

Chronopotentiometry (CP). To activate the surface of the NPs, a CP technique was employed. A current (*i*) of -0.7 mA was applied on the WE, when using the RDE, in order to have a current density (*j*) of -10 mA·cm^{-2}, during at least 30 min. This activation process was required before carrying out the rest of the electrochemical studies. For CP experiments, *i*R drop was manually adjusted at 85% ($E_{mod} = E_{meas} + E_{iR}$; *mod* = modified; meas = measured) after estimating the value corresponding to $E_{iR} = i_{exp} \cdot (R_{mes} \cdot 0.85)$, where i_{exp} is the applied current and R_{mes} the measured resistance of the 1 M H_2SO_4 or NaOH solutions.

Faradaic Efficiency. For the faradaic efficiency experiments, a fluorine-doped tin oxide (FTO) electrode (1 cm^2 surface area) was used as WE, a Ag/AgCl (KCl sat.) electrode as RE, and a Pt mesh as CE. A two-compartment cell was employed, separated with a permeable membrane, equipped with a stirring bar and filled with either 1M H_2SO_4 or 1M NaOH solution. A Clark-type microsensor, Unisense H_2-NP, was employed to monitor the hydrogen gas generation during bulk electrolysis. This Clark-type electrode was placed in the chamber containing the WE and the RE, whereas the CE was placed in the other one. The Clark-type electrode was calibrated by adding known volumes of pure hydrogen at the end of bulk electrolysis, applying the ideal gas law

Double-layer capacitance (C_{DL}) and ElectroChemically Active Surface Area (ECSA) determination. Double-layer capacitance (C_{DL}) value was determined by performing successive cyclic voltammetry (CV) experiments, at increasing scan rates, starting from 5 mV/s up to 500 mV/s, and holding for ten seconds the potential vertex between each scan (up and down) of the CV. By doing this, a double layer of opposite charges will be created in the WE, thus acting as a capacitor, as reflected in the **Eq. 2**, where Q is the charge of each layer (absolute value) and V the electric potential difference between layers. This equation is divided by time, obtaining **Eq. 3**, where i_c is for current density, and v the scan rate. Plotting i_c as function of v leads to a line whose slope is equal to C_{DL}.

$$Q = V \cdot C_{DL} \qquad \text{Eq. 2}$$

$$i_C = v \cdot C_{DL} \qquad \text{Eq. 3}$$

The measurements were taken after each NPs system had been electrochemically activated, and the CVs were carried out in a potential range with no redox processes (non-Faradaic region). To calculate *ECSA* (**Eq. 4**), this C_{DL} value was divided by the specific capacitance, C_S, whose value depends on the nature of the WE and the solution used (for a carbon electrode in 1 M H_2SO_4, C_S = 13-17 $\mu F \cdot cm^{-2}$, and in 1 M NaOH C_S = 40 $\mu F \cdot cm^{-2}$). Roughness Factor (*RF*) was calculated through **Eq. 5**, where S is the geometrical surface area of the WE.

$$ECSA = \frac{C_{DL}}{C_S} \qquad \text{Eq. 4}$$

$$RF = \frac{ECSA}{S} \qquad \text{Eq. 5}$$

Copper Under Potential Deposition (Cu UPD). To determine the number of the active sites through Cu UPD, which will allow TOF calculation and therefore benchmarking the electrocatalysts, a chronoamperometry (constant potential bulk electrolysis) (CA) was performed. Potential was fixed at 0.194 V vs NHE for **RuMPT NPs**, and at 0.244 V vs NHE for **Ru2PP NPs**, for 100 seconds, using a glassy carbon as WE, submerged in a 1M H_2SO_4 solution, in the presence of $CuSO_4$ (5 nM). A linear sweep voltammetry (LSV) was run before and after the CA in the absence of $CuSO_4$, observing an oxidation wave in the later LSV, due to the deposited Cu during the CA experiment (**Eq. 6**). **Eq. 7** allowed the calculation of the active sites number (n) based on the UPD copper stripping charge (Q_{Cu}, Cu_{UPD}), where *F* is the Faraday constant (96485 C·mol^{-1}) [21].

$$Cu_{UPD} = Cu^{2+} + 2e^- \qquad \text{Eq. 6}$$

$$n = \frac{Q_{Cu}}{2 \cdot F} \qquad \text{Eq. 7}$$

Turnover Frequency (TOF) (s^{-1}) calculation. Eq. 8 was used to determine the TOF value, where *i* is the current intensity measured in the LSV experiments, *F* the Faraday constant and *n* the active sites number calculated above.

$$\mathrm{TOF}(s^{-1}) = \frac{\mathrm{i}}{2 \cdot \mathrm{F} \cdot \mathrm{n}} = \frac{\mathrm{i}}{2 \cdot \mathrm{Q_{Cu}}} \qquad \text{Eq. 8}$$

3.4 Results and discussion

3.4.1 Synthesis and characterization of Ru NPs stabilized with pyridine-type ligands Reagents and materials

Ruthenium nanoparticles (Ru NPs) stabilized by pyridine-type ligands were prepared following the previously described organometallic approach, summarized in **Figure 1**. The process starts with the decomposition of the Ru organometallic precursor, [Ru(cod)(cot)] (cod = 1,5-cyclooctadiene; cot = 1,3,5-cyclooctatriene), after being pressurized under 3 bars of H_2 gas, and in the presence of the selected pyridine-type ligand; namely 4'-(4-methylphenyl)-2,2':6',2"-terpyridine (**MPT**) or 2-phenylpyridine (**2PP**). THF was selected as solvent. The reactions were left running for 16 h at room temperature. In all cases, the initial yellowish solution rapidly became a black colloidal dispersion after pressurizing the Fisher-Porter reactor.

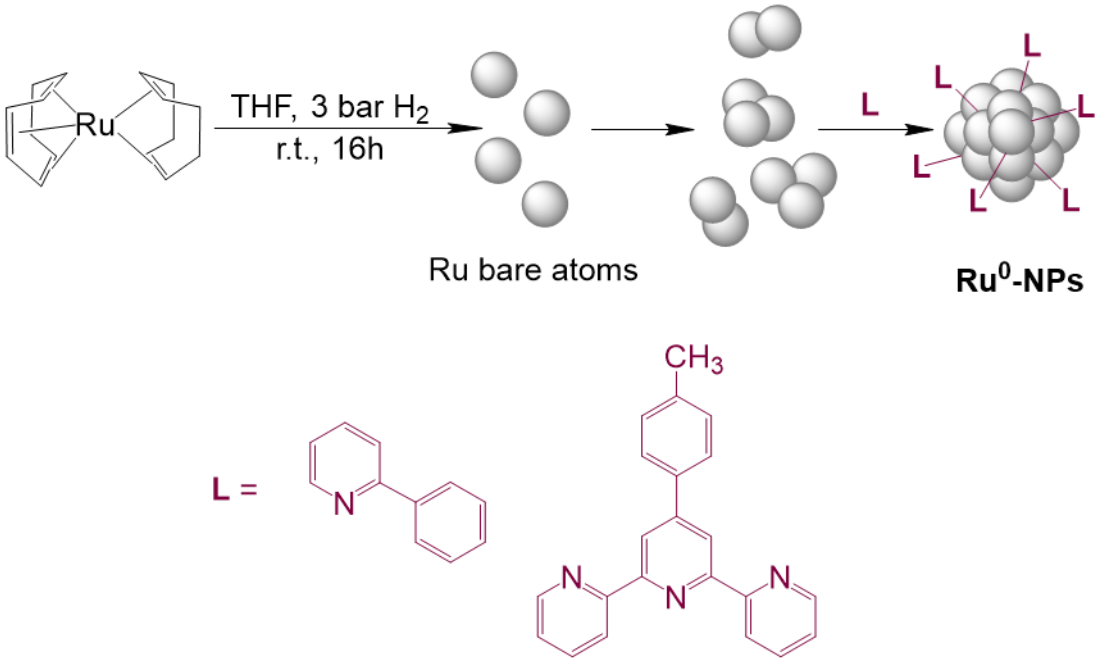

Figure 1. General synthesis of ligand-stabilized Ru NPs following the organometallic approach.

The H_2 pressure was removed, and pentane was added to clean the Ru NPs of any remaining uncoordinated ligand or precursor residue, under Ar atmosphere, which also favours the precipitation of the NPs. The cleaning process was repeated twice, after which the supernatant pentane was removed and the NPs were dried under

vacuum, obtaining at the end a blackish powder. All the systems are collected into a closed vial under argon.

Transmission electron microscopy (TEM) analyses

Due to the use of different type of ligands, in addition to the modification of the ligand-to-metal ratio (L/M), the properties of nanoparticles, in terms of mean size, shape or dispersion, could be affected [22]. The study of how all these variables influence the morphology of the Ru NPs was followed by Transmission Electron Microscopy (TEM). Samples for TEM analyses were taken, in all cases, from both crude colloidal dispersion and re-dispersed NPs after isolation, by depositing a single drop on the surface of a carbon-coated copper grid, not observing significant variations between both samples.

To prepare Ru NPs with **MPT** ligand, a range of ligand to metal (L/M) ratio between 0.05 and 0.5 equivalents was used. Based on previous studies within the research group, this range of MPT ligand concentrations led to the stabilization of small and well dispersed nanoparticles [23]. Dispersion of the NPs was remarkable throughout the ligand concentration range. At the same time, nanoparticles get drastically smaller by increasing the L/M ratio (**Figure 2**). This evidences the suitability of **MPT** as stabilizer ligand. The large size gap between Ru NPs depending on the L/M ratio suggests that **MPT** greatly influences nanoparticle growth.

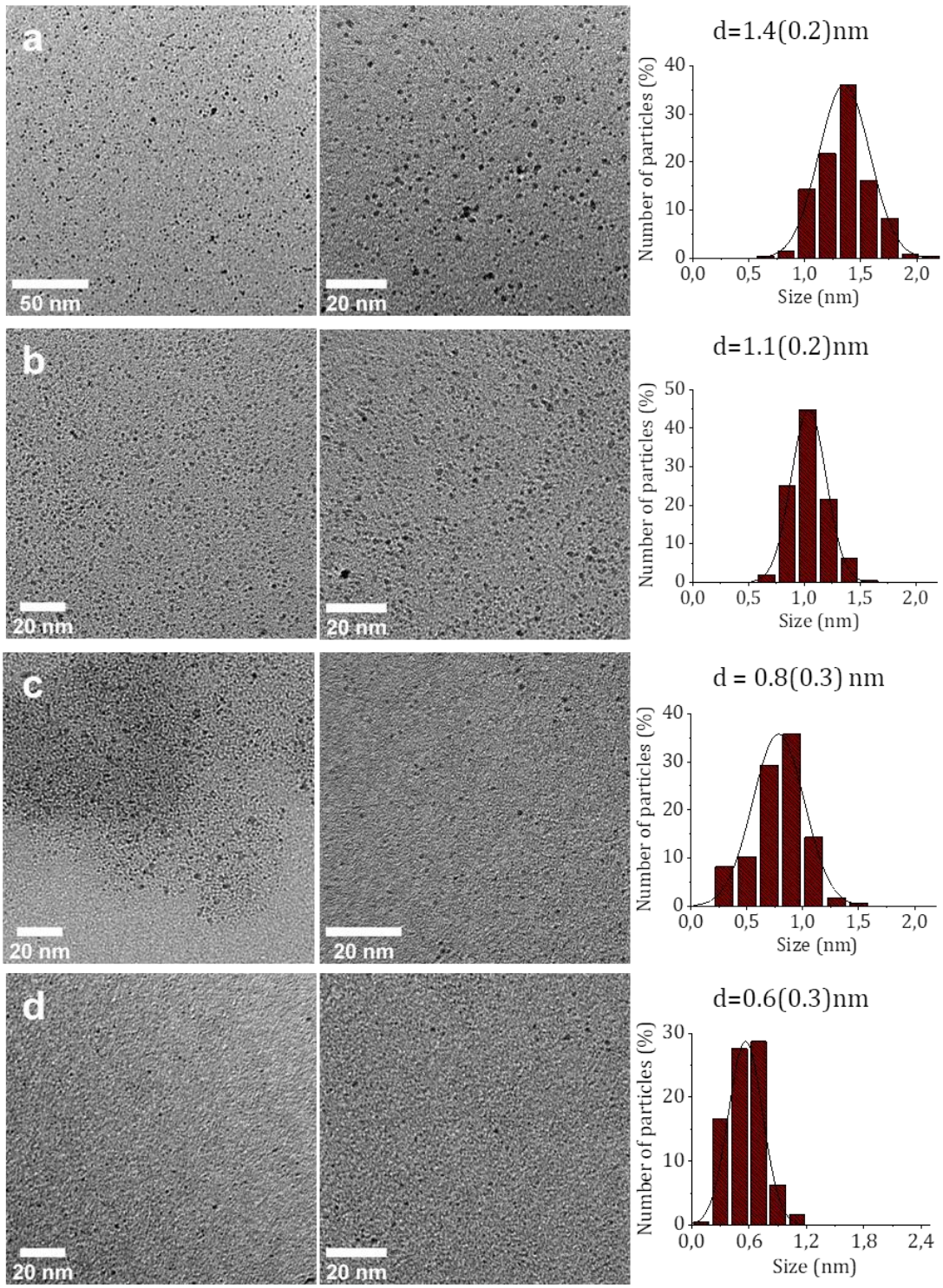

Figure 2. TEM micrographs and histograms of **Ru-MPT NPs** stabilized with different L/M ratios: a) 0.05, b) 0.1, c) 0.2 and d) 0.5 molar eq. of MPT.

In the case of the **2PP** ligand, the L/M ratios tested varied from 0.2 to 0.5 molar equivalents. Initially, only the 0.2 molar eq. system was prepared, as we expected a comparable result than when using the similar 4-phenylpyridine (**4PP**) ligand to prepare the **Ru4PP** reported system [13]. However, as observed in **Figure 3a**, the Ru NPs were slightly bigger than the reported ones with the **4PP** ligand (1.8 nm vs 1.5 nm). That is why higher L/M ratios were tested, expecting a decrease in the mean size of the NPs. However, it can be observed that ligand concentration affects the size of the NPs, although only slightly (**Figure 3b to c**), being the mean size of 1.6 ± 0.3 nm when using 0.3 molar eq. of **2PP** in the synthesis of the NPs, and a mean size ca. 1.5 with 0.4 and 0.5 molar eq. of **2PP**. Thus, increasing the amount of ligand leads to a minimal decrease in the average size of the nanoparticles, while increasing the level of agglomeration thereof. At 0.2 molar eq. of **2PP** NPs are still fairly dispersed, starting to increase the number of agglomerates observed at 0.3 molar eq. Thus, when using 0.4 molar eq. of ligand, NPs are mostly forming large aggregates whereas isolated nanoparticles are hardly observed. By increasing L/M ratio to 0.5 molar eq. the system is fully agglomerated, hindering the identification and subsequently measurement of the NPs accurately.

The efficiency of pyridine-type ligands, functionalized with phenyl groups, as stabilizers of NPs has been previously demonstrated [24]. In addition to L/M ratio, other ligand-related factors such as steric effects or coordination modes of the ligand with the nanoparticle surface can influence its stabilizing capacity, which may explain the different behaviour between these ligands. If the results obtained by using both **MPT** and **2PP** ligands are compared, different stabilizing effects could be observed. For instance, **2PP** presents a simple pyridine structure with an extra phenyl group in ortho position. One possible hypothesis is that the initial interaction with the Ru-NPs surface would be through the pyridyl-N (σ-coordination), which allows the approaching of the phenyl group to the surface, thus resulting in π-coordination from the phenyl ring [25]. However, the position of the phenyl ring could sterically hamper initial coordination through the nitrogen atom, impairing the stabilizing capacity of the ligand. **MTP** structure, in the other hand, displays three pyridyl groups, meaning that one single molecule has three different N-coordination sites, vs. the single pyridyl-N unit of the **2PP** molecule. This could lead

to a stronger coordination with the NPs surface and, therefore, more impact in their growth, which may explain the noteworthy difference regarding the L/M ratio when using **MPT**, as opposed to **2PP**. The variety of coordination modes, depending on the nature of each ligand, and their effect on the growth and stabilization of nanoparticles has been previously reported, using, pyrazole-derived ligands to prepare palladium nanoparticles [26]. In that case they conclude that, at least two pyrazolyl groups were necessary in the ligand in order to stabilize the Pd NPs efficiently. Such stabilization would be, at the same time, influenced by the position of the pyrazolyl groups relative to the phenyl group, as certain positions facilitate the coordination of both pyrazolyl moieties to the NPs better than others.

In order to compare the catalytic performance with the reported system stabilized with 4-phenylpyridine (**Ru4PP**) [13], from now on we will focus on the systems prepared using, on the one hand, 0.05 eq. of MPT (labelled as **RuMPT**), and on the other hand 0.2 eq. of 2PP (**Ru2PP**), as they are similar enough in terms of size and dispersibility, making the main differential factor between them the structure of the pyridine-type ligand. Interestingly, although the molar equivalents of ligand are not the same, if we consider the N-coordination sites the values are closer (0.05 molar eq. for the MPT, with 3 N-coordination sites/mol vs 0.2 molar eq. for the 2PP or 4PP, with 1 N coord. site/mol).

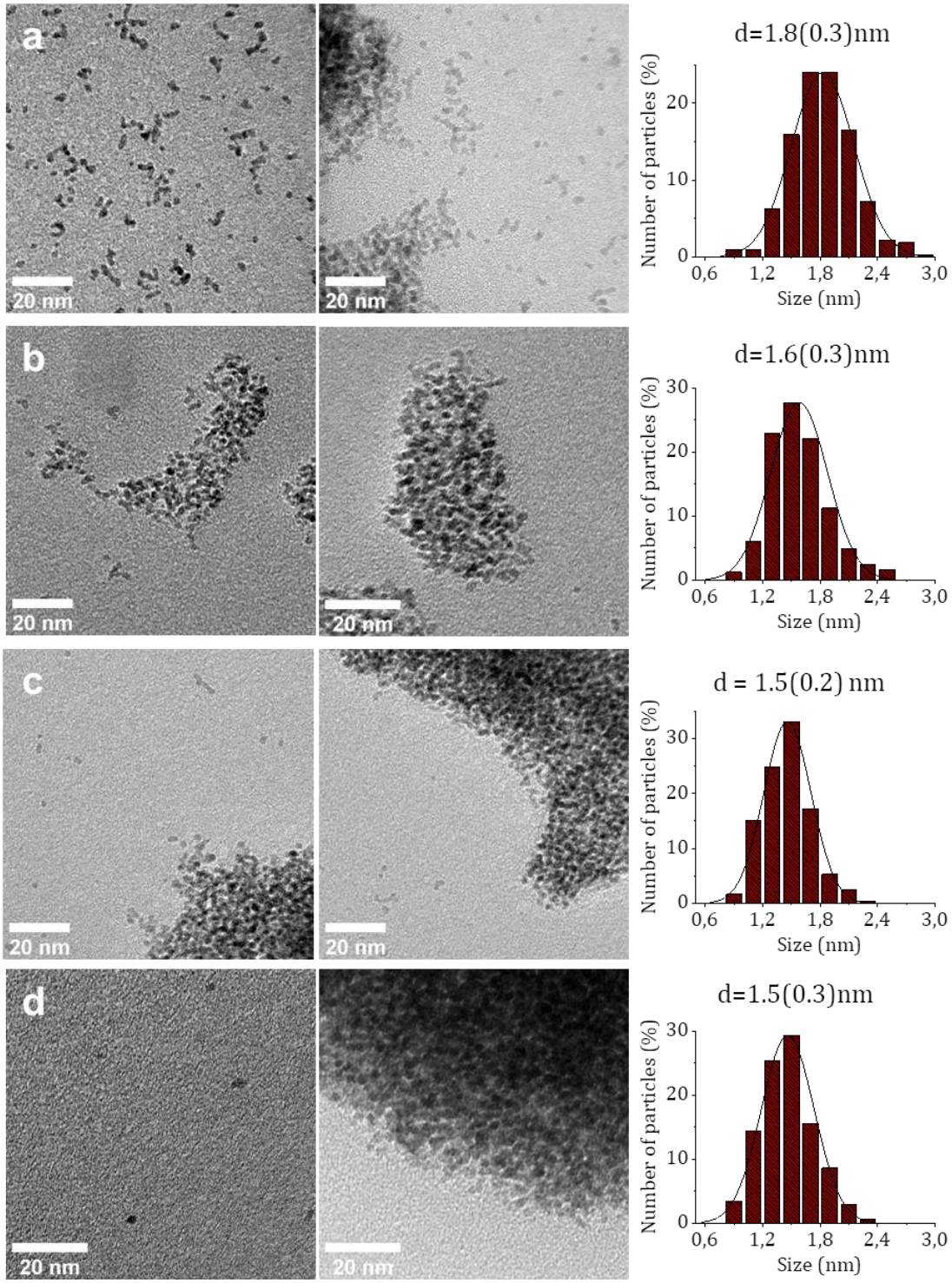

Figure 3. TEM micrographs and histograms of **Ru-2PP-NPs** stabilized with different L/M ratios: a) 0.2, b) 0.3, c) 0.4 and d) 0.5 molar eq. of 2PP.

Study of the oxidation state of pyridine-stabilized Ru-NPs

The oxidation state and crystalline structure of the as-formed **RuMPT** and **Ru2PP** systems was studied by Wide Angle X-ray Scattering (WAXS). The preparation of the sample requires working under an Ar atmosphere, depositing the powder from both NP systems in 1µm glass capillaries, subsequently sealed until analysis. The pattern observed for the **Ru2PP** sample, kept under Ar atmosphere, corresponds to hexagonal close-packed (hcp) metallic Ru structure (**Figure 4**). A peak around 4° could be observed, attributed to the presence of a few agglomerated nanoparticles. The **RuMPT** sample was also analysed, but within the framework of a previously PhD work from the research group, yielding similar results [23].

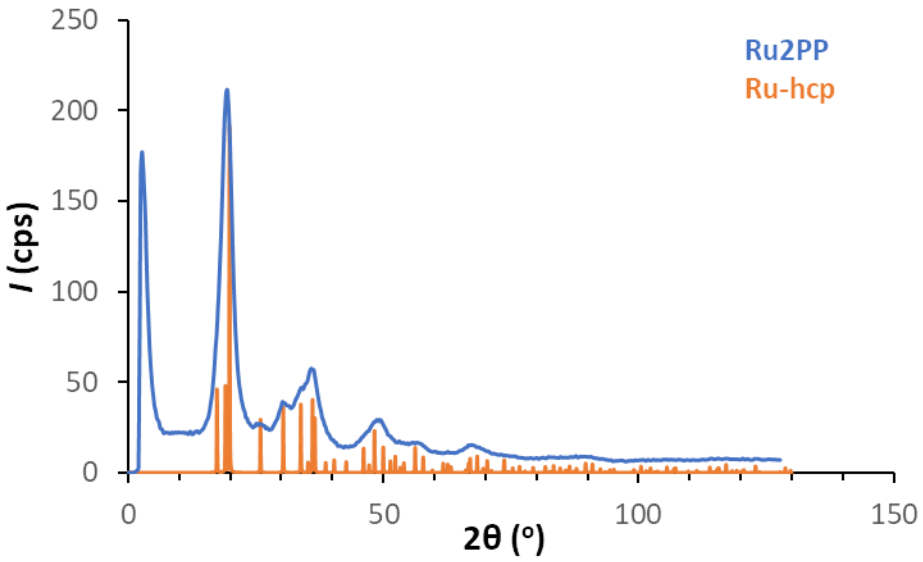

Figure 4. WAXS analysis for **Ru2PP** after synthesis, with no air exposure, in comparison with hcp Ru phase diagram.

From previous studies within the research group, when exposing these pyridine-stabilized NPs in the solid state directly into air, they burned [13]. To overcome this high reactivity on the metal surface, a slow passivation processed is preferred, keeping the NPs powder in a closed vial under argon, and allowing the slow diffusion of air for several days before opening.

X-ray photoelectron spectroscopy (XPS) analyses were performed after the passivation process on **RuMPT**-passivated(**p**) and **Ru2PP**-passivated(**p**). In both cases, Ru 3d5/2 peaks centered at 279.8 eV (Ru^0) and 280.6 eV (RuO_2) were

observed, thus confirming the presence of a Ru/RuO_2 mixture on the NPs surface (**Figure 5**) [27].

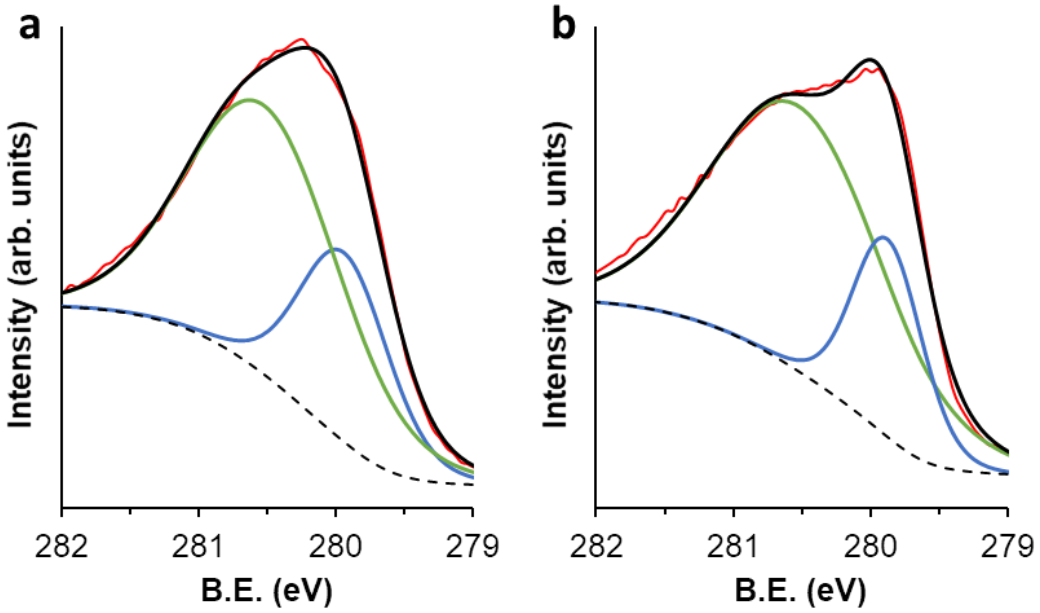

Figure 5. Powder XPS analysis of a) **RuMPT-p** (red) and b) **Ru2PP-p** (red). Fit for the signals: in blue line, metallic Ru (Ru $3d_{5/2}$ 278.8 eV); in green line, RuO_2 (Ru $3d_{5/2}$ 280.6 eV; in bold, envelope; in dashed line, background.

Elemental composition

With the aim of shedding light on the elemental composition and to estimate the ligand-metal ratio of **RuMPT-p** and **Ru2PP-p**, inductively coupled plasma optical emission spectroscopy (ICP-OES) analyses, elemental analyses (EA), and thermogravimetric analyses (TGA) of the samples were performed.

ICP-OES analyses exhibited a lower content on Ru than expected (56 and 68 Ru wt.% for **RuMPT-p** and **Ru2PP-p** respectively, vs. ca. 85 Ru wt.% expected for both systems, based on experimental synthetic calculations). However, the research group has previously had problems with the determination of Ru wt.% by ICP-OES in Ru NPs with an organic or inorganic matrix [23]. After acidic digestion of the samples, before ICP-OES analysis, a black residue attributed to Ru undissolved has been repeatedly detected, and this could explain the lower-than-expected Ru content.

EA, on the other hand, showed that the organic content was of 11.82 wt.% for **RuMPT-p** and 13.47 wt.% for **Ru2PP-p** (**Table 2**)

	EA results			
	C wt.%	**H wt.%**	**N wt.%**	**CNH wt.%**
RuMPT-p	9.32	1.14	1.35	11.81
Ru2PP-p	10.93	1.55	0.99	13.47

Table 2. Elemental analysis (C, H, N) results for **RuMPT-p** and **Ru2PP-p** samples.

Apart from the stabilizing ligand, on the surface of the nanoparticles other coordinating molecules could be expected, such as the synthesis solvent (THF) or hydrides (as hydrogen gas is used to decomposed Ru precursor). From EA data, calculations could be performed to estimate ligand-metal (L/M), THF-metal (THF/M) and hydrides-metal (H/M) ratios, and also the metal content. Thus, the ligand content (either MPT or 2PP) was calculated from N wt.% value, as ligands are the only source of nitrogen during the synthesis. Subtracting C wt.% and H wt.% corresponding to each ligand, the remaining C wt.% would indicate the amount of THF present on the Ru NPs (and assuming cyclooctane has been eliminated after the pentane-cleaning). Finally, the remaining amount of H was attributed to the hydrides on the surface (**Table 3**).

	Calculations performed				
	L/M	**THF/M**	**H/M**	**Total organics wt.%**	**Ru wt.%**
RuMPT-p	0.04	0.02	0.85	12.13	87.87
Ru2PP-p	0.08	0.04	0.94	13.79	86.21

Table 3. Estimated ligand, THF or hydride/metal ratios and total Ru from the EA results.

The different ratios were calculated using Ru wt.% estimation derived from EA. For **RuMPT-p**, L/M value was 0.04, almost the 0.05 molar equivalents used for the synthesis of the RuNPs. In the case of the **Ru2PP-p**, the estimated value through EA was much lower (0.08 vs 0.2 molar eq. introduced for the synthesis). As seen in the TEM analyses, in the case of the synthesis with 2PP ligand, L/M ratio had low influence on the size of the NPs, unlike what happens with MPT ligand. As previously explained, the different modes of ligand coordination and possible steric hindrances may be responsible for these differences in the stabilization of NPs. The low

influence of L/M ratio on the NPs size was also observed by some collaborators when using different type of ligands, such as alkyl sulfonated diphosphines or a betaine adduct of N-heterocyclic carbene and carbodiimide [28,29].

Thermogravimetric (TGA) analyses were performed on both samples to confirm the presence of the ligand, and the L/M ratio estimated after EA analyses. The as-synthesized **RuMPT** and **Ru2PP** samples were subjected to a heating process, detecting a variation in their weight in the temperature range 150-300 °C, attributed to the loss of the respective ligand. The mass variations, as well as the estimated L/M ratio and the Ru wt.% are shown in **Table 4**, while **Figure 6** displays the obtained "weight vs. temperature" curves for the NPs samples and the free **MPT** and **2PP** ligands. Ru wt.% values are comparable to those estimated with EA analyses (ca. 83 wt.% with TGA vs. ca. 87 wt.% with EA, for both samples). In the case of the **RuMPT**, the L/M ratio of 0.06 was also close to the expected value (0.05 molar eq.), and for the **Ru2PP**, the estimated value of 0.13 molar eq. of ligand was lower than the employed for the synthesis (0.2 molar eq.), also in accordance with the estimated values through EA analyses. TGA were also performed after the passivation process on **RuMPT-p** and **Ru2PP-p**, samples, observing a comparable weight drop in the same temperature range (**Figure S1**).

	TGA data		**Estimated values**	
	Δm (mg)	**Weight drop (%)**	**L/M**	**Ru wt.%**
RuMPT	0.292	17.46	0.06	82.54
Ru2PP	0.375	16.72	0.13	83.28

Table 4. Data from TGA analyses regarding the weight variation in the temperature range 150-300 °C, and the subsequent estimated values of L/M and Ru content in the samples, assuming that any mass variation corresponds to the loss of the ligand at that temperature range.

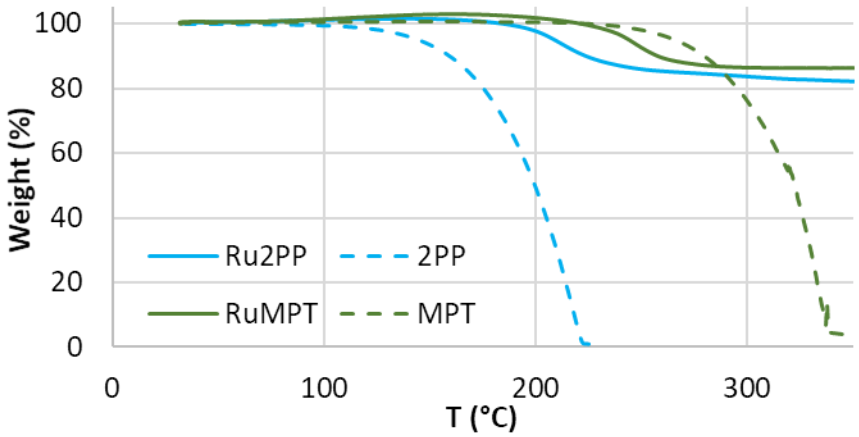

Figure 6. TGA curves for **RuMPT** (green) and **Ru2PP** (blue) samples and the corresponding **MPT** (dashed green) and **2PP** (dashed blue) ligands.

Surface hydrides' titration

Hydrogen plays a key role in the decomposition of the metal precursor, acting as a reducing agent. For this reason, hydrides are expected to be found onto the surface of the Ru nanoparticles, besides the chosen stabilizer and/or molecules of solvent [30]. In fact, the presence of hydrides has been previously confirmed through various NMR methods [31,32].

In the present case, we have demonstrated and quantified the presence of hydrides through a titration method previously reported [33], based on the hydrogenation of a simple olefin, such as 2-norbornene (**Figure 7**). The gas chromatography–mass spectrometry (GC-MS) technique was employed to monitor the conversion of norbornene into the corresponding alkane (norbornane).

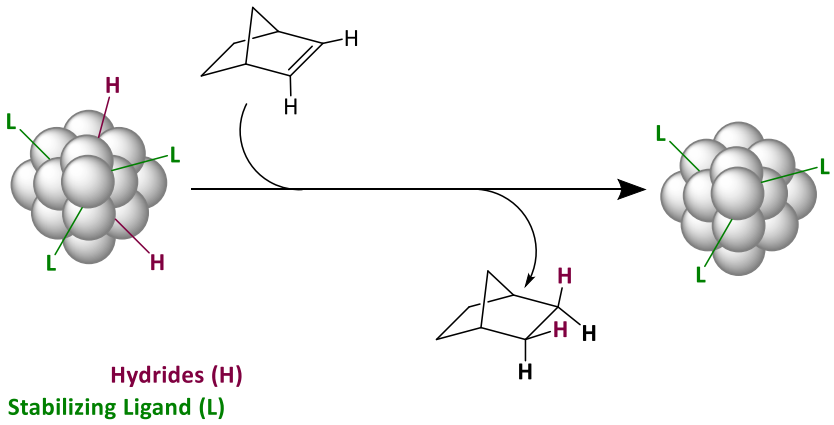

Figure 7. Hydrogenation of 2-norbornene by hydrides onto the nanoparticles surface.

This study was carried out with freshly prepared **RuMPT** or **Ru2PP** dispersions. The system was degassed to remove the remaining H_2, necessary for the synthesis, by three purge-and-refill cycles, using Ar gas. This ensured that the hydrides required for hydrogenation all came from the nanoparticles surface hydrides. The reactor was placed inside the glove box where a known quantity of norbornene (an excess of 5 molar eq. of the olefin per Ru atom) is added into the Fisher-Porter bottle. After 72 hours of continuous stirring, an aliquot was filtered through celite to retain the Ru NPs, and the collected sample was taken to the GC-MS for analysis. The whole process was repeated three times, starting from the synthesis, and three aliquots were taken in total from each of them to ensure the reproducibility of the method.

After calculations, detailed in the experimental section, it was estimated a $H/Ru_{surface}$ ratio of ca. 0.73 for **RuMPT** and 1.00 for **Ru2PP**. These values are similar to the estimated with the EA analyses (0.85 and 0.94 respectively), and comparable to other ligand-stabilized Ru NPs previously reported by the research group and collaborators, prepared with the same methodology [13,33], such as 1.2 $H/Ru_{surface}$ for Ru4PP (4PP = 4-phenylpyridine) NPs or 1.1 $H/Ru_{surface}$ for Ru-dppd [dppd = 1,10-bis(diphenylphosphino)decane] NPs.

3.4.2 Electrocatalytic HER studies in 1 M H_2SO_4

RuMPT-p and **Ru2PP-p** were first evaluated as hydrogen evolution reaction electrocatalysts under extreme acidic conditions (1 M H_2SO_4). Both Ru-based systems were redispersed in THF, in order to prepare an ink to drop-cast on the surface of a glassy carbon rotating disk electrode (RDE/GC), which served as Working Electrode (WE) in a typical three-electrode configuration electrochemical set-up, together with a Saturated Camel Electrode (SCE, KCl saturated) as reference electrode (RE) and a Pt mesh as counter electrode (CE). The obtained hydrogen evolution linear sweep voltammetry (LSV) polarization curves for both systems, at a scan rate of 10 $mV \cdot s^{-1}$ and RDE speed of 3000 rpm, are collected in **Figure 8** (dashed lines). It should be noted that, as with the reported Ru4PP system [13], after applying a fixed current density of j = -10 $mA \cdot cm^{-2}$ during at least 30 min, both systems show a change on the corresponding LSV curves (bold curves in **Figure 8**).

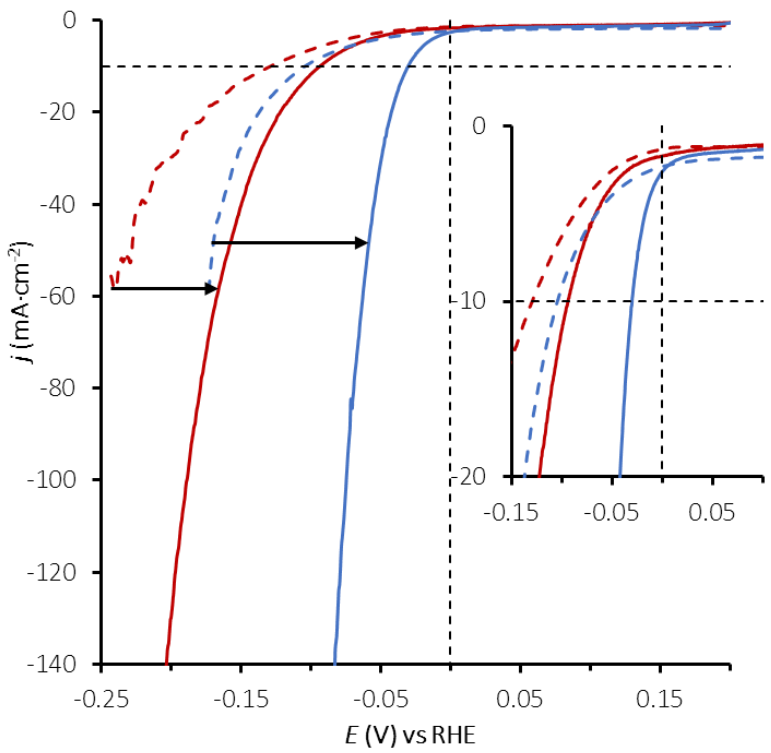

Figure 8. Polarization curves of **RuMPT** and **Ru2PP** before (dashed red and dashed blue, respectively) and after 30 min bulk electrolysis at j = -10 mA·cm^{-2} (bold red and bold blue, respectively), in 1 M H_2SO_4. Inset: Onset overpotential zone enlarged.

This behaviour can be explained by a change in the oxidation state on the surface of the NPs. Even if the initially passivated NPs present a partially oxidized surface, as previously demonstrated (section 3.4.1), by applying a reduction potential the surface is reduced, obtaining again the as-synthesized Ru^0 NPs, a more active species in the HER in acidic medium as it can be concluded from the benchmarking parameters that are extracted from the polarization curves. Before activation, **RuMPT-p** and **Ru2PP-p** show onset overpotentials (η_0) around 50 mV and 100 mV, respectively, and a η_{10} (the overpotential required to reach a current density of j = -10 mA·cm^{-2}) of 129 mV for **RuMPT-p** and 104 mV for **Ru2PP-p**. After activation through bulk electrolysis, overpotential towards HER were improved in all cases, reaching values of η_0 = 60 mV and η_{10} = 93 mV for **RuMPT**-activated in acid medium(**a_H**), and η_0 close to 0 mV and η_{10} = 30 mV for **Ru2PP-**activated in acid medium(**a_H**). Interestingly, the values of the latter were closer to those reported by the **Ru4PP** system after activation, a system with a more similar capping-ligand, and that outperformed the results of commercial Pt/C (η_{10} = 20 for Ru4PP vs. 27 mV for Pt/C), prepared following the same protocol and reaction conditions.

XPS analyses were performed after reductive treatment in order to elucidate the species responsible for the catalytic activity. As mentioned above, **RuMPT-p** and **Ru2PP-p** samples were superficially passivated, with a mixture of Ru(0) and RuO_2 (**Figure 5**). After 30 minutes of bulk electrolysis at j = -10 mA·cm^{-2} in aqueous 1 M H_2SO_4, the disappearance of the peak centred at 280.6 eV, corresponding to RuO_2, was observed for both **RuMPT-a$_H$** and **Ru2PP-a$_H$**, the XPS signals being due solely to the presence of metallic Ru (peak centred at 278.8 eV) (**Figure 9**) [27].

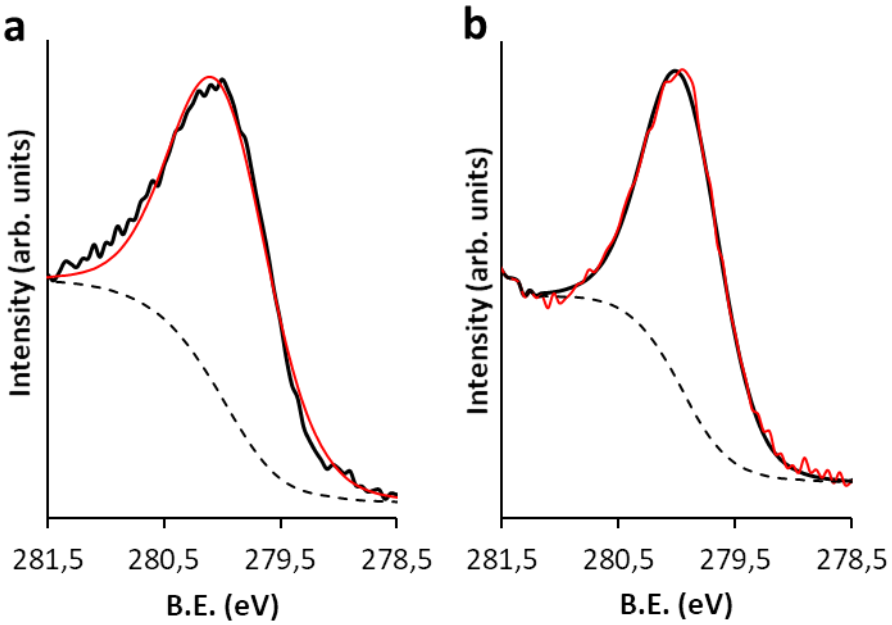

Figure 9. XPS analysis of a) **RuMPT-a$_H$** (red) and b) **Ru2PP-a$_H$** (red) after 30 minutes of bulk electrolysis at j = -10 mA·cm^{-2} in 1 M H_2SO_4. Fit for the signals: in red line, metallic Ru (Ru 3d$_5$/2 280.2 eV); in bold, envelope; in dashed line, background.

Not only the catalytic performance of a catalyst is relevant for its consideration as potentially useful for the HER, but also stability should come into consideration. Long-term stability of **RuMPT-a$_H$** was tested by a current-controlled experiment lasting 12 hours, applying a constant current density of j = -10 mA·cm^{-2} and monitoring the change on the required overpotential. This system did not show significant changes in the value of η_{10}, obtaining a practically identical LSV polarization curve after the experiment (**Figure 10a**). TEM analyses were performed after recovering and redispersing the NPs from the electrode, confirming the presence of Ru NPs after the catalytic experiments (**Figure 10b**). Analogous results were obtained when testing the long-stability of the **Ru2PP-a$_H$** system in 1

M H_2SO_4 (**Figure S2**). EDX analyses of both samples also confirmed the presence of Ru after the electrocatalytic experiments (**Figure S3**).

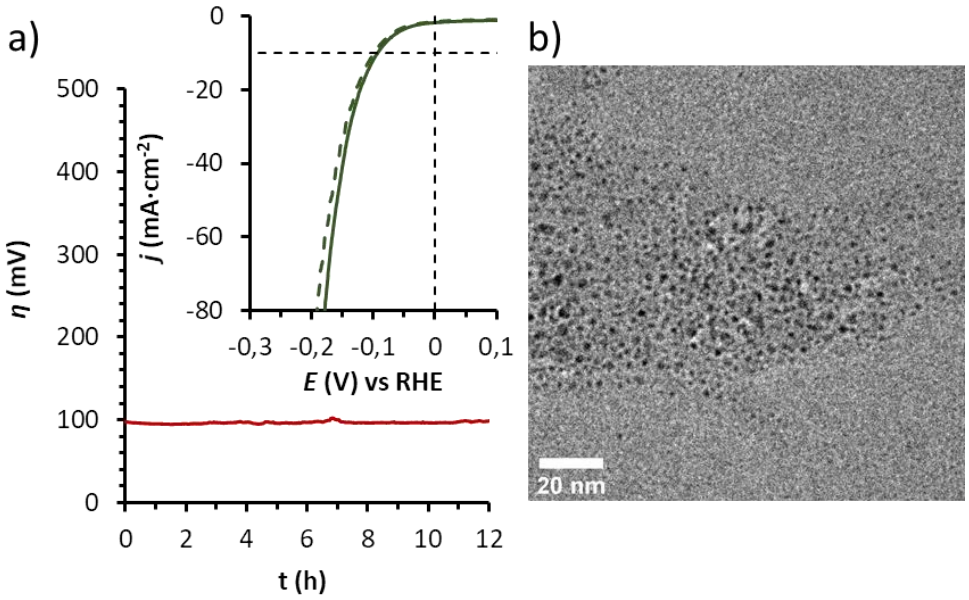

Figure 10. a) 12 hours bulk electrolysis of **RuMPT-a$_H$** at j = -10 mA·cm^{-2} in 1 M H_2SO_4 solution. Inset: polarization curves before (bold) and after (dashed) 12 h bulk electrolysis; b) TEM micrograph after 12 h bulk electrolysis experiment.

Additionally, Faradaic efficiencies ($\mathcal{E}$) were determined after quantifying the amount of H_2 released during electrolysis, using a H_2-probe, and comparing it with the maximum amount of H_2 calculated using the total charge passing through the electrode during the experiment, giving a result of 98% for **RuMPT-a$_H$** (**Figure 11**) and 97% for **Ru2PP-a$_H$** (**Figure S4**). These results confirmed hydrogen production as the sole reaction taking place during the electrocatalytic experiments.

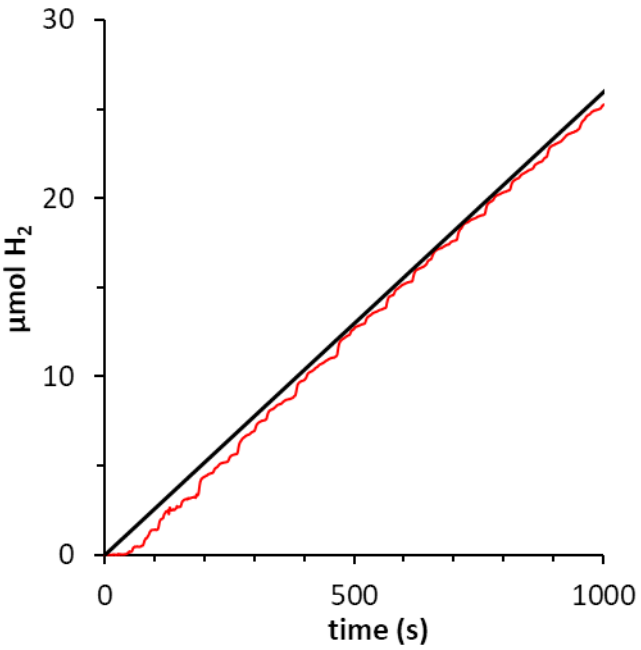

Figure 11. H_2-monitored (red) current-controlled bulk electrolysis (black) of **RuMPT-a$_H$** at j = -10 mA·cm^{-2} in 1 M H_2SO_4. H_2 production was monitored in gas phase (red curve), using a Clark-type electrode, yielding a Faradaic efficiency ($\mathcal{E}$) > 98%.

Another parameter that could be extracted from LSV polarization curves is the corresponding Tafel plot. As introduced in Chapter I, this analysis provides information about the mechanism and rate-determining step (rds) in the HER [34,35]. In this case, they also served to demonstrate the different nature and catalytic performance of the **RuMPT-p** and **Ru2PP-p** species with respect to **RuMPT-a$_H$** and **Ru2PP-a$_H$**. Both **RuMPT-p** and **Ru2PP-p** showed a high value for the Tafel slope of 133 mV·dec^{-1} (**Figure 12**, dark green) and 109 mV·dec^{-1} (**Figure 12**, dark blue), respectively, typical values for catalysts displaying the Volmer step (hydrides adsorption on the surface of the NPs, with slope values ≈ 120 mV·dec^{-1}) as the rds. After bulk electrolysis, Tafel slope value lowered to 93 mV·dec^{-1} for **RuMPT-a$_H$,** a value in between the Volmer step and Heyrovsky step (H_2 desorption after recombination of one adsorbed hydride with a proton from solution, typical slope values ≈ 40 mV·dec^{-1}) as the rsd. For **Ru2PP-a$_H$,** the slope was of 42 mV·dec^{-1}, thus indicating Heyrovsky step as the rds of the reaction. A similar shift was also observed in the reference system Ru4PP, with a change in the Tafel slope from 106 mV·dec^{-1} to 29 mV·dec^{-1} , the latter value indicated Tafel step as rds (also the

formation and desorption of H_2, as the Heyrovsky step, but in this case after recombination of two adsorbed hydrides (**Table S1**). The reorganization on the surface state after the activation of the NPs (e.g., the disappearance of the superficial RuO_2 or the change on the active sites, estimated later by Cu UPD), may be some of the reasons to explain this change in the mechanism, .

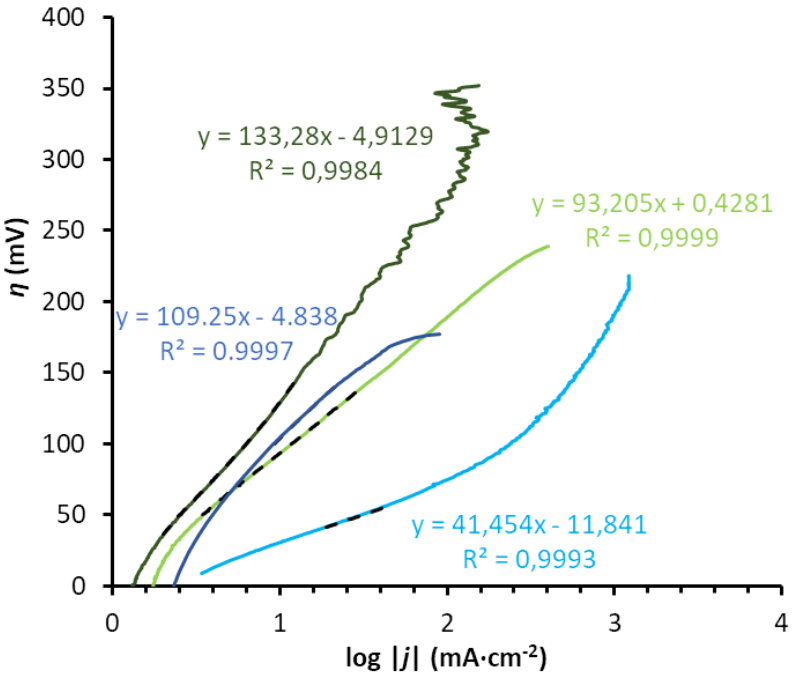

Figure 12. Tafel plot of **RuMPT-p** (dark green), **RuMPT-a$_H$** (light green), **Ru2PP-p** (dark blue) and **Ru2PP-a$_H$** (light blue) in 1 M H_2SO_4.

3.4.3 Electrocatalytic HER studies in 1 M NaOH

HER performance of both **RuMPT-p** and **Ru2PP-p** was also tested in alkaline conditions (1 M NaOH) using the same procedure and electrochemical set-up as for the study in acidic medium. **RuMPT-p** delivered a η_0 of ca. 100 mV and η_{10} of 131 mV, and **Ru2PP-p** overpotential values were η_0 ca. 75 mV and η_{10} = 86 mV. For the latter, as was the case with the Ru4PP system, no activation was observed after applying a current density of j = -10 mA·cm^{-2} during at least 30 min, whereas **RuMPT-p** experienced an improvement in its activity after being kept under reductive conditions (η_0 ca. 50 mV and η_{10} = 61 mV) (**Figure 13**).

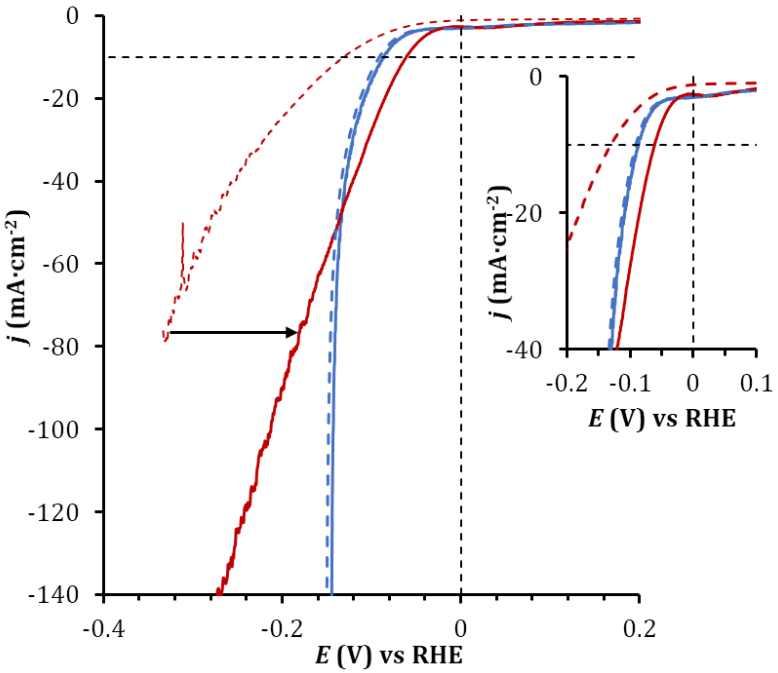

Figure 13. Polarization curves of **RuMPT-p** and **Ru2PP-p** before (dashed red and dashed blue, respectively) and after 30 min bulk electrolysis at j = -10 mA·cm^{-2} (bold red and bold blue, respectively), in 1 M NaOH. Inset: Onset overpotential area enlarged.

After applying the reductive treatment, XPS analyses were carried out to notice possible changes in the oxidation state of the NPs. For **Ru2PP-p**, in which no activation was observed after 30 min, the same mixture of Ru and RuO_2 (peaks centred at 278.8 eV and 280.6 eV, respectively) was present as in the passivated NPs (Note: As no evolution under electrochemical conditions or change in the chemical composition of the sample were observed, the label **Ru2PP-p** is maintained when discussing the **2PP** stabilized system in alkaline conditions, thus assuming that is the same system). Surprisingly, the same mixture was also observed in the case of **RuMPT-**activated in basic medium(**a$_{OH}$**), which is activated after applying j = -10 mA·cm^{-2} for 30 min (**Figure 14**). Some examples can be found in the literature that explain this difference in behaviour for the **RuMPT-a$_{OH}$**, apparently unrelated to the oxidation state of the NPs. Zhang *et al.* reported a carbon-supported RuO_2 NPs system which was activated in 1 M H_2SO_4 under reductive conditions, attributed to a possible structural deformation of RuO_2 [36]. On the other hand, although not in the nanoscale, Näslund *et al.* studied the evolution of a RuO_2-coated electrode under HER conditions in 1 M NaOH. Through an exhaustive study involving XPS and XRD

analyses, they demonstrated that, in fact, RuO_2 was used in the catalytic cycle in favour of the metallic Ru during 24 h of catalysis (reductive conditions), with the formation of intermediate active species like $RuO(OH)_2$ [37].

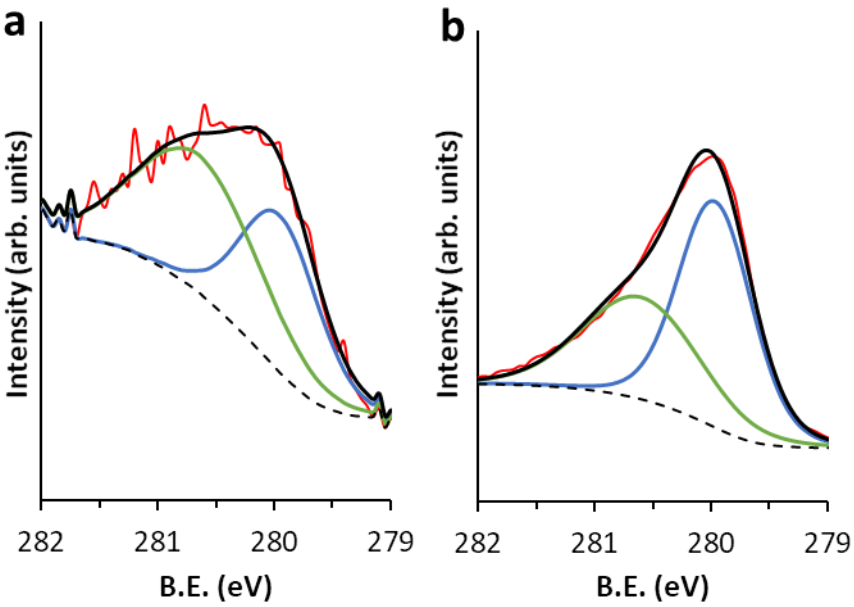

Figure 14. XPS analysis of a) **RuMPT-a$_{OH}$** (red) and b) **Ru2PP-p** (red) after 30 minutes of bulk electrolysis at j = -10 mA·cm^{-2} in 1 M NaOH. Fit for the signals: in blue line, metallic Ru (Ru 3d$_{5/2}$ 278.8 eV); in green line, RuO_2 (Ru 3d$_{5/2}$ 280.6 eV); in bold, envelope; in dashed line, background.

Regarding long-term stability, current-controlled experiments were performed at j = -10 mA·cm^{-2}. **RuMPT-a$_{OH}$** showed good stability, with an increase on η_{10} of only 14 mV after 12 hours (**Figure 15a**), a change similar to that observed for **Ru2PP-p**, although in this case after 6 h of bulk electrolysis (**Figure S5a**). This behavior is due to mechanical stability issues of **Ru2PP-p** over the GC-RDE electrode in alkaline conditions, even when using fixation agents such as Nafion®, probably motivated by the tendency of this system to aggregate, as seen in the TEM analyses. In both cases, Ru NPs were still visible after 12 h and 6 h stability tests (**Figure 15b** and **Figure S5b** respectively). Ruthenium was also detected by EDX analyses after the experiments for both nanocatalysts (**Figure S6**). Faradaic efficiencies close to 100% were determined by measuring the amount of hydrogen released during electrolysis (**Figure S7**), confirming also in 1 M NaOHthat H_2 production was the sole reaction taking place.

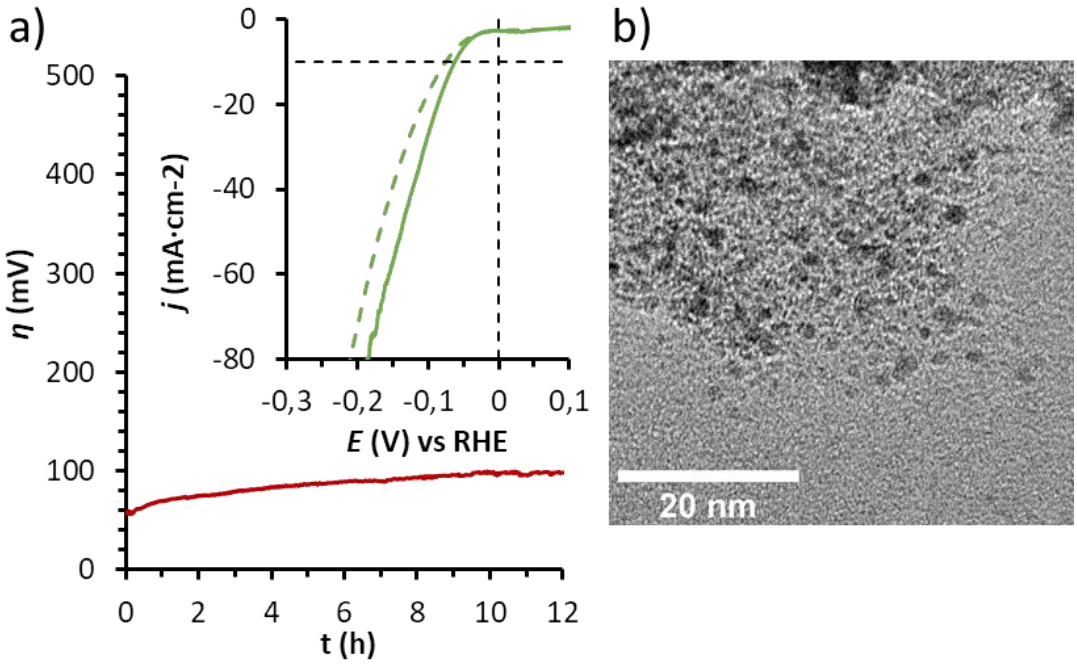

Figure 15. 12 hours bulk electrolysis of **RuMPT-a$_{OH}$** at j = -10 mA·cm^{-2} in 1 M NaOH solution. Inset: polarization curves before (bold) and after (dashed) 12 h bulk electrolysis; b) TEM micrograph after 12 h bulk electrolysis experiment.

Tafel plot analyses in 1 M NaOH solution show a change on the slope of **RuMPT-a$_{OH}$** after activation (from 123 to 87 mV·dec^{-1}), values similar to those expected for catalyst with hydrogen adsorption as the rds (Volmer step), whereas **Ru2PP-p** shows a slope of 72 mV·dec^{-1} (practically the same value before and after the 30 min bulk electrolysis at j = -10 mA·cm^{-2}), closer to the typical values for catalysts with Heyrovsky step as rds (hydrogen formation and desorption), a value comparable to the **Ru4PP** reference system with a Tafel slope of 56 mV·dec^{-1} in 1 M NaOH (**Table S2**).

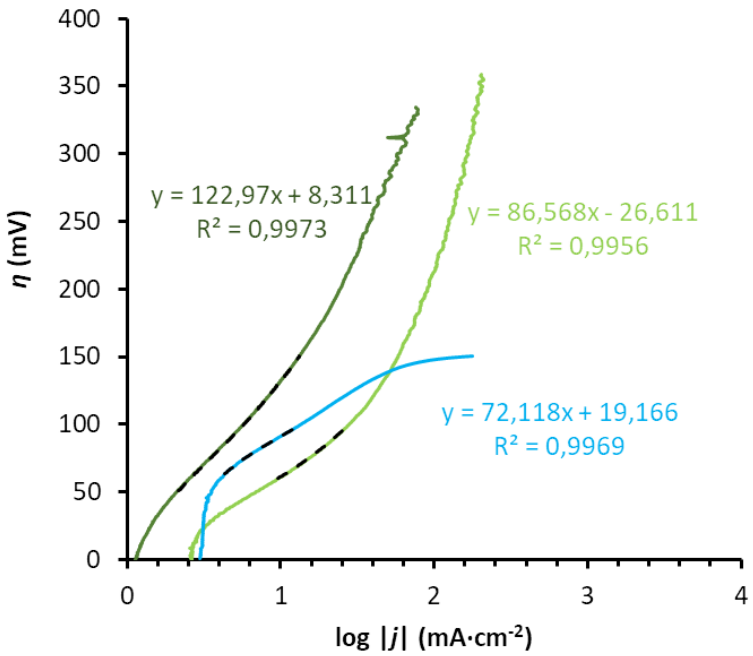

Figure 16. Tafel plot of **RuMPT-p** (dark green), **RuMPT-a$_{OH}$** (light green) and **Ru2PP-p** (light blue) in 1 M NaOH.

3.4.4 Electrocatalytic performance benchmarking

The benchmarking methodology reported by Jaramillo *et al.*[38] (described in Chapter I) was employed to characterize the electrocatalytic performance and its short-term stability of **RuMPT-a$_{H}$** and **Ru2PP-a$_{H}$** (1 M H_2SO_4) and **RuMPT-a$_{OH}$** and **Ru2PP-p** (1 M NaOH), in order to be able to compare them with other catalytic systems reported in the literature. First, the electrochemically active surface area (*ECSA*) of the four electrodes was calculated from the double-layer capacitance (C_{DL}), estimated from the capacitive current in a non-Faradaic zone (see Experimental part for calculation details) (**Figure 17** for **RuMPT-a$_{H}$** in 1 M H_2SO_4 (a) and **RuMPT-a$_{OH}$** in 1 M NaOH (b); **Figure S8** for for **Ru2PP-a$_{H}$** 1 M H_2SO_4 (a) and **Ru2PP-p** in 1 M NaOH (b)). After dividing the calculated *ECSA* values by the geometric area of the electrode (S = 0.07 cm^2), roughness factor (*RF*) could be estimated. These values of *ECSA* allowed to know the real electroactive area of each system, and thus to calculate the value of the specific current densities (j_s) by normalizing the measured current densities with the estimated RF values. **Table S3** (acidic medium) and **Table S4** (basic medium) show the obtained values of overpotential η_{10} at t = 0 and after 2 hours, and j_s at η = 100 mV, together with the

values obtained for Ru4PP and other systems reported by the research group, and Pt for comparison.

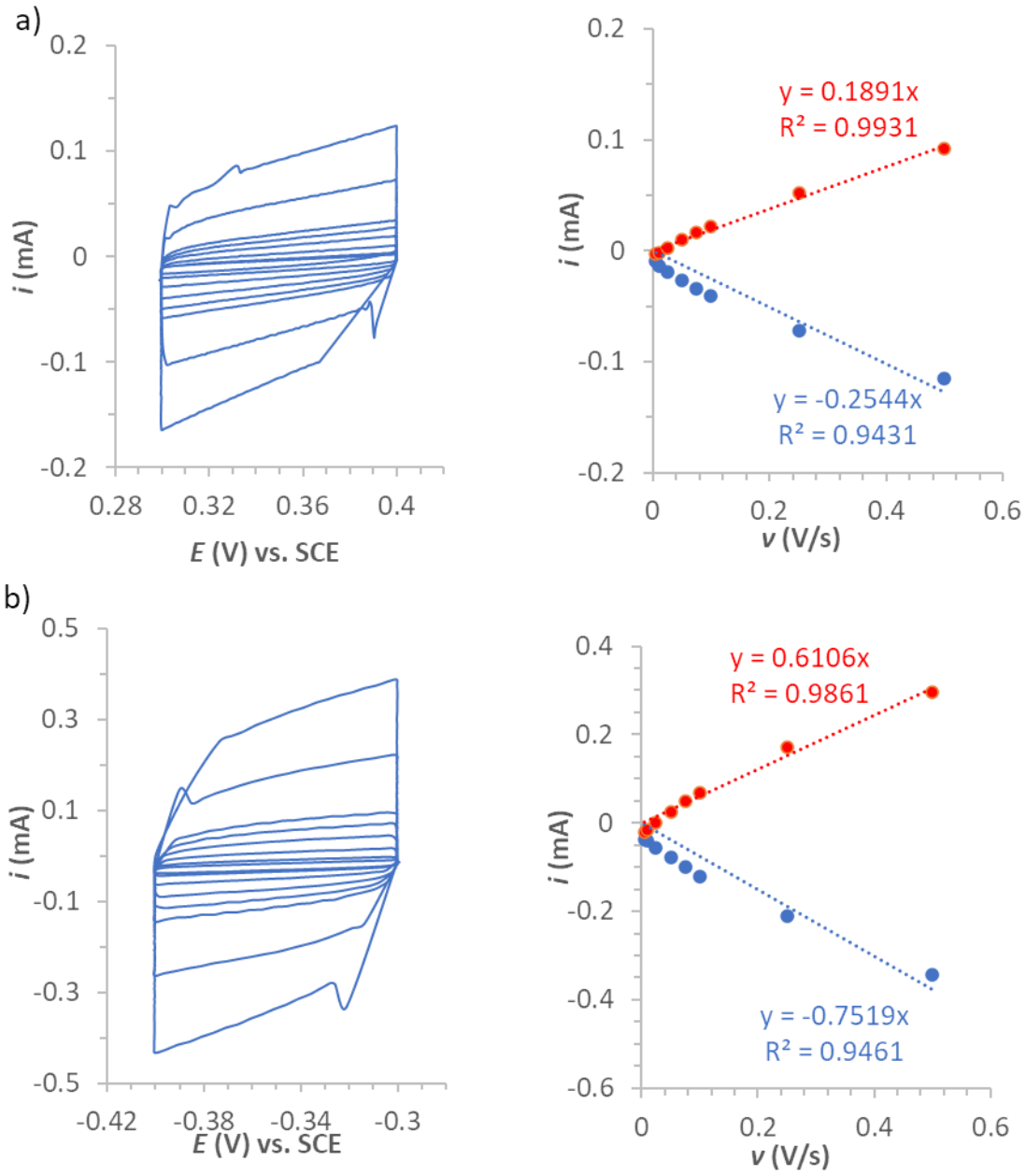

Figure 17. Multi cyclic voltammetry (CV) experiments at different scan rates (*v*) (left) and current values plotted at the middle of the potential range values (V vs. SCE) for the different scar rates for the C_{DL} determination of a) **RuMPT-a$_{H}$** in 1 M H_2SO_4 and b) **RuMPT-a$_{OH}$** in 1 M NaOH.

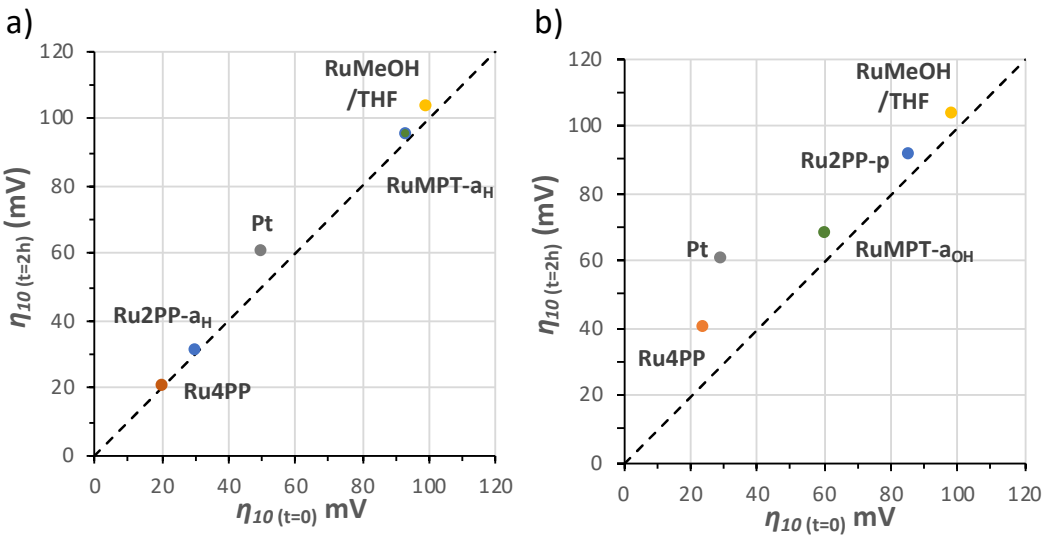

Figure 18. Graphical comparison of different hydrogen evolution electrocatalysts by Jaramillo's methodology in a) 1 M H_2SO_4 and b) 1 M NaOH.

In acidic conditions, **Ru2PP** follows the same trend as Ru4PP, with low overpotentials and outperforming Pt, while **RuMPT** shows larger overpotentials (ca. 100 mV) although excellent stability (**Figure 18a**). In alkaline conditions, neither of the **RuMPT-a$_{OH}$** and **Ru2PP-p** systems stands out, with overpotentials much higher than those reached by **Ru4PP**, which tops Pt, although with a better stability than either of these two reported systems, with an increase in the η_{10} of ca. 15 mV in both cases after 2 h of electrolysis (**Figure 18b**). Regarding the specific current density values at η = 100 mV, in acidic conditions only **Ru2PP-a$_H$** (0.542 mA·cm^{-2}) can compete with Ru4PP (0.550 mA·cm^{-2}) and Pt (2.500 mA·cm^{-2}) whereas in alkaline conditions j_s values for both **RuMPT-a$_{OH}$** (0.103 mA·cm^{-2}) and **Ru2PP-p** (0.113 mA·cm^{-2}) are in the same order as the benchmarked catalysts Ru4PP (0.191 mA·cm^{-2}) and Pt (0.540 mA·cm^{-2}) (**Table S3** and **Table S4**).

A more detailed study about the electrocatalytic activity of Ru NPs systems can be made by calculating the TOF values, which is carried out by estimating active sites through the copper underpotential deposition (Cu UPD). This technique consists of submerging the electrodes of the electrochemical set-up in a 5 mM $CuSO_4$ solution, and applying a reductive potential in the working electrode (WE), thus promoting the electroreduction of Cu^0 on top of the active sites on the electrode (Ru^0). After carrying out a polarization curve in a Cu-free acid solution, the appearance of a wave due to the re-oxidation of Cu^0 to Cu^{2+} could be observed, with the area below being

proportional to the number of electrons required for the oxidative process, and therefore proportional to the Cu deposited and the active sites (Ru^0) of the catalyst in WE. LSV curves before and after the Cu UPD in acidic solution are collected in **Figure 19** for **RuMPT-a$_H$** and **RuMPT-p**. Almost no oxidation of Cu after the Cu UPD was observed in the case of **RuMPT-p**, confirming the passivation on the surface of the NPs, thus decreasing the number of Ru^0 active sites. Same behaviour was observed for **Ru2PP-a$_H$** and **Ru2PP-p** (**Figure S9**). According to these curves, the area was higher for the **Ru2PP-a$_H$** than for **RuMPT-a$_H$**, thus indicating than the former has a greater number of actives sites in the surface of the NPs, which may explain its better electrocatalytic output.

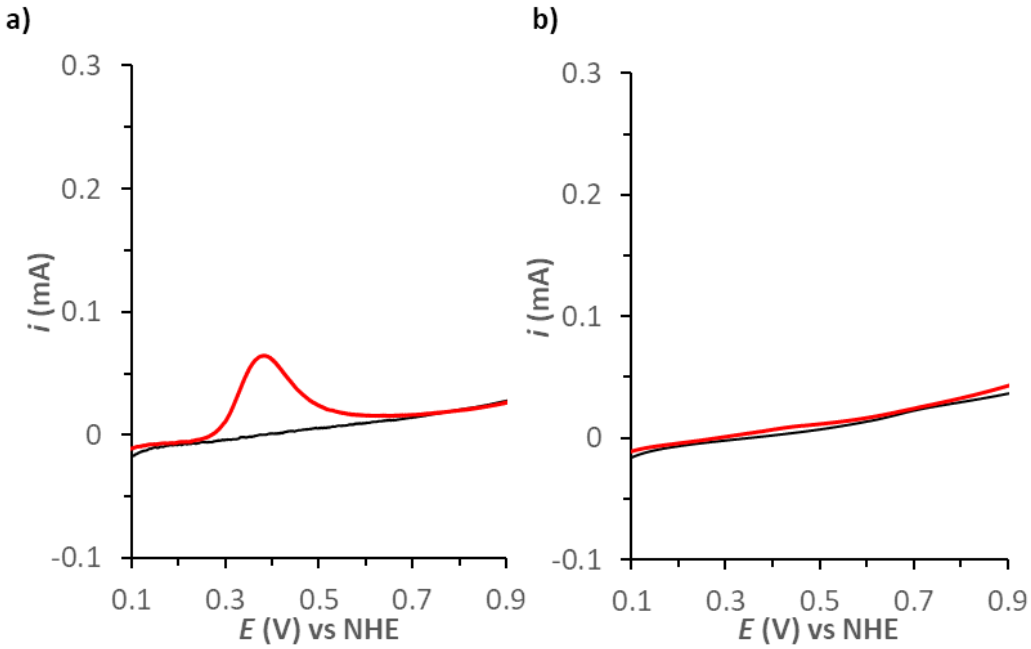

Figure 19. LSV curves (from 0.1 to 0.9 V vs NHE) before (black) and after copper underpotential deposition (Cu UPD) in 1 M H_2SO_4 solution of a) **RuMPT-a$_H$** and b) **RuMPT-p**.

TOF values were calculated at different overpotentials in 1 M H_2SO_4, the values being 0.18, 0.28 and 0.95 s^{-1} (at 25, 50, and 100 mV, respectively) for **RuMPT**, and 0.32, 1.37 and 10.3 s^{-1} for **Ru2PP** (**Figure 20**). Again, **Ru2PP** showed a behaviour more similar to Ru4PP (0.55, 3.06 and 17.38 s^{-1}), which was even comparable with Pt (1.65, 5.60 and 23.36 s^{-1}) under the same reaction conditions (**Table S1**).

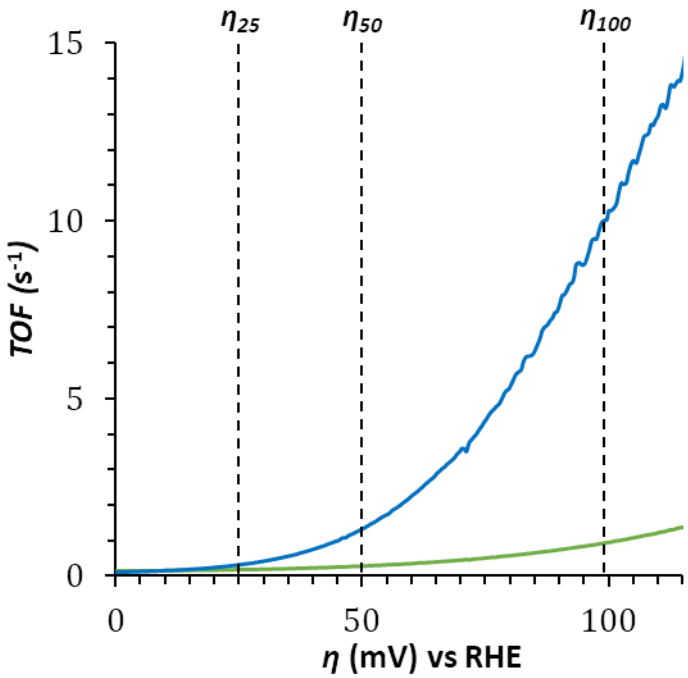

Figure 20. TOF vs. η (mV) graph of **RuMPT-a$_H$** (green) and **Ru2PP-a$_H$** (blue) systems in 1 M H_2SO_4 solution. TOF calculations were obtained by dividing the value of current intensity (i, mV) by the charge under the Cu UPD wave in each case.

3.5 Conclusions

The use of the organometallic approach as synthetic method has allowed the preparation of pyridine-type ligand-capped ruthenium nanoparticles with a narrow size distribution.

Through TEM micrographs it has been possible to study the effect of the L/M ratio on the size of the nanoparticles, demonstrating that, when using **MPT** as ligand, the size of the nanoparticles was highly dependent on L/M ratio used, while for **2PP** the size was not so affected. For the latter, the agglomeration of the NPs became more noticeable by increasing the amount of ligand. This highlights the importance of both ligand nature and L/M in stabilizing the nanoparticles.

Other characterization techniques have allowed us to know the composition of the isolated nanoparticles. Through WAXS and XPS studies, it has been shown that, initially, the nanoparticles of Ru prepared consisted only of metallic Ru, and that after subjecting them to a passivation process when exposed to air, a mixture of Ru/RuO_2 was obtained. EA and TGA analyses allowed to demonstrate the presence of ligand even after the passivation process, validating the good role of MPT and 2PP as stabilizing ligands.

Selected systems **RuMPT-p** and **Ru2PP-p** were tested as electrocatalysts for HER in both acidic and alkaline conditions. In acidic medium (1 M H_2SO_4), the performance of both systems can be improved by applying a reductive treatment for a short period of time, in which Ru^0 is recovered as the only species present in the catalyst. **Ru2PP-a$_H$** outperformed **RuMPT-a$_H$** offering lower overpotentials ($\eta_0 \approx 0$ mV and η_{10} = 30 mV vs. η_0 = 60 mV and η_{10} = 93 mV), lower Tafel slope (42 mV·dec^{-1} vs. 93 mV·dec^{-1}) and achieved higher TOF at a 100 mV of overpotential (10.3 s^{-1} vs. 0.95 s^{-1}), being competitive with the previously reported Ru4PP system ($\eta_0 \approx 0$ mV and η_{10} = 20 mV; Tafel slope of 29 mV·dec^{-1} and TOF value of 17 s^{-1} at η = 100 mV). Both **Ru2PP-a$_H$** and **RuMPT-a$_H$** were capable to produce a current density (j_0) of -10 mA·cm^{-2} during 12 h with hardly any deactivation and preserving the morphology of the nanoparticles.

In contrast, in alkaline conditions (1 M NaOH), only **RuMPT-p** experienced an improvement in catalytic performance after applying the reductive treatment. However, the original Ru/RuO_2 mixture was detected after subjecting both samples to catalytic conditions. Both **Ru2PP-p** (η_0 = 75 mV and η_{10} = 86 mV, Tafel slope of 72 $mV \cdot dec^{-1}$) and **RuMPT-a$_{OH}$** (η_0 = 50 mV and η_{10} = 61 mV, Tafel slope of 87 $mV \cdot dec^{-1}$) systems were outperformed by Ru4PP ($\eta_0 \approx 0$ mV and η_{10} = 25 mV, Tafel slope of 65 $mV \cdot dec^{-1}$) in basic medium, although exhibiting a superb stability when compared with state-of-the-art Pt under the same conditions.

3.6 Supporting Information

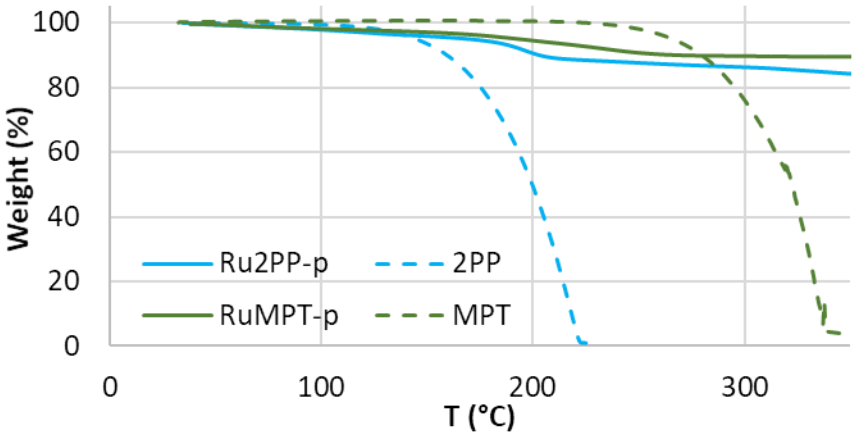

Figure S1. TGA curves for **RuMPT-p** (green) and **Ru2PP-p** (blue) samples and the corresponding **MPT** (dashed green) and **2PP** (dasedh blue) ligands.

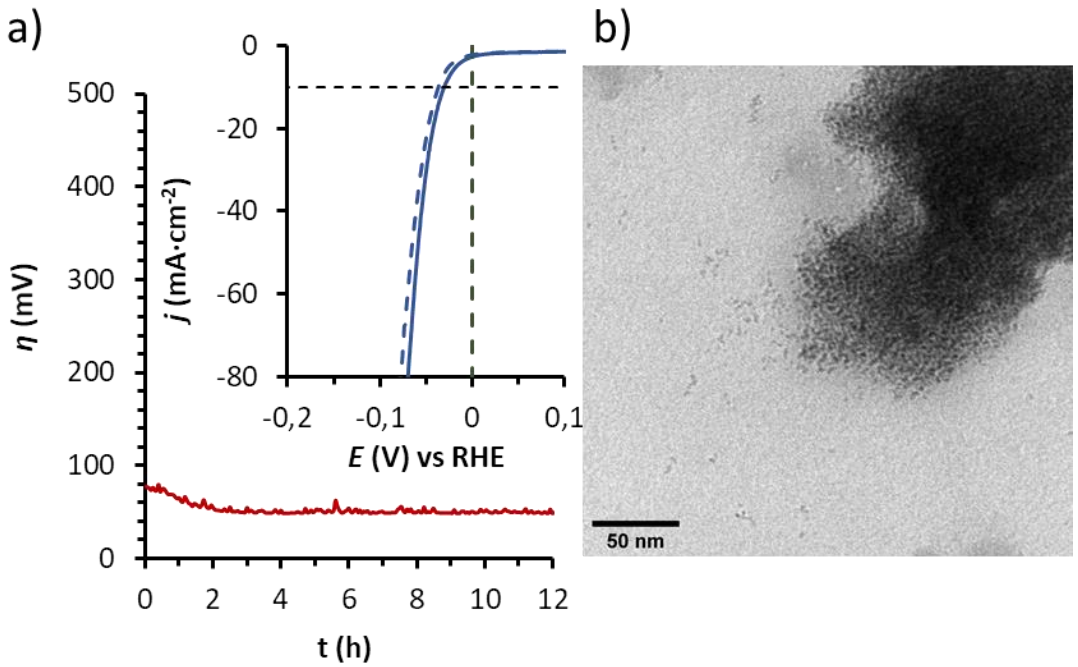

Figure S2. a) 12 hours bulk electrolysis of **Ru2PP-a$_H$** at j = -10 mA·cm^{-2} in 1 M H_2SO_4 solution. Inset: polarization curves before (bold) and after (dashed) 12 h bulk electrolysis; b) TEM micrograph after 12 h bulk electrolysis experiment.

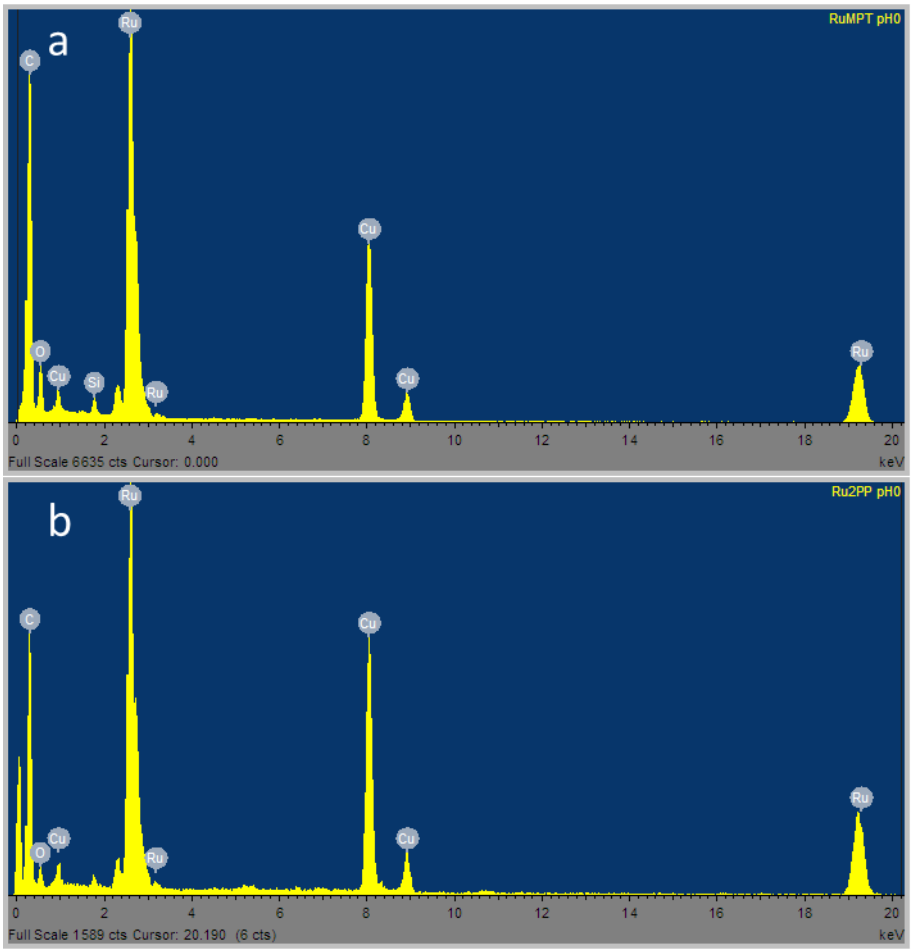

Figure S3. EDX analyses of a) **RuMPT** and b) **Ru2PP** after stability tests in 1 M H_2SO_4.

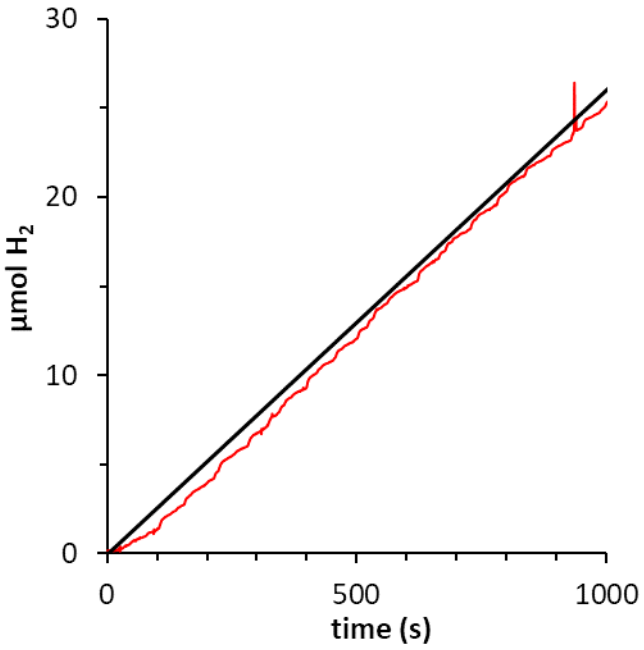

Figure S4. H_2-monitored (red) current-controlled bulk electrolysis (black) of **Ru2PP-a$_H$** at j = -10 mA·cm^{-2} in 1 M H_2SO_4. H_2 production was monitored in gas phase (red curve), using a Clark-type electrode, yielding a Faradaic efficiency ($\mathcal{E}$) > 97%

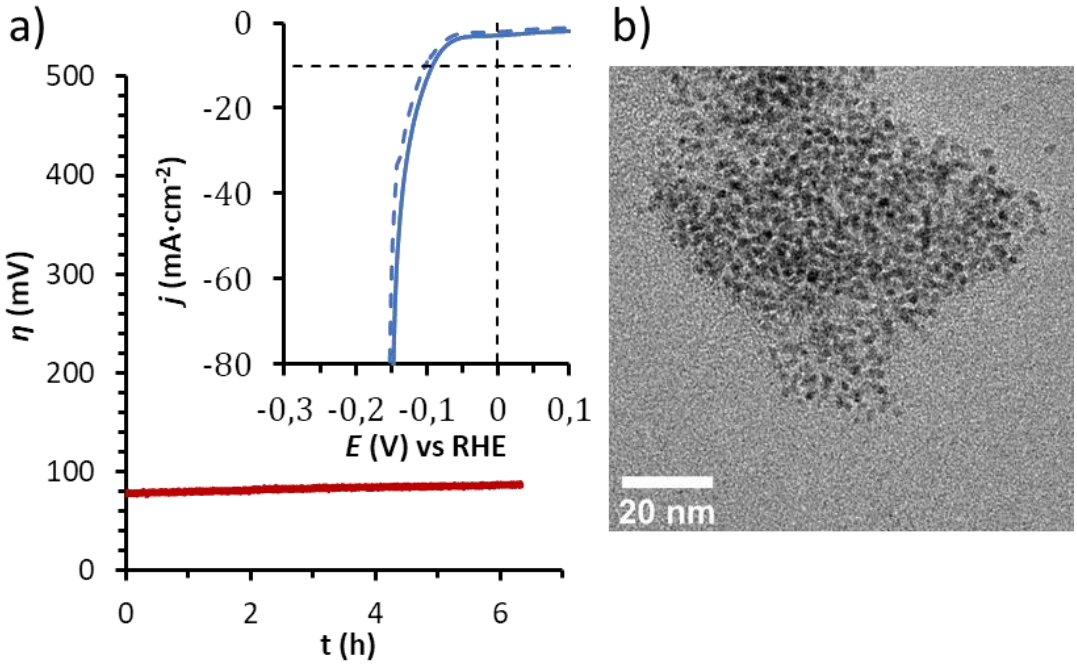

Figure S5. a) 6 hours bulk electrolysis of **Ru2PP-p** at j = -10 mA·cm^{-2} in 1 M NaOH solution. Inset: polarization curves before (bold) and after (dashed) 6h bulk electrolysis; b) TEM micrograph after 6 h bulk electrolysis experiment.

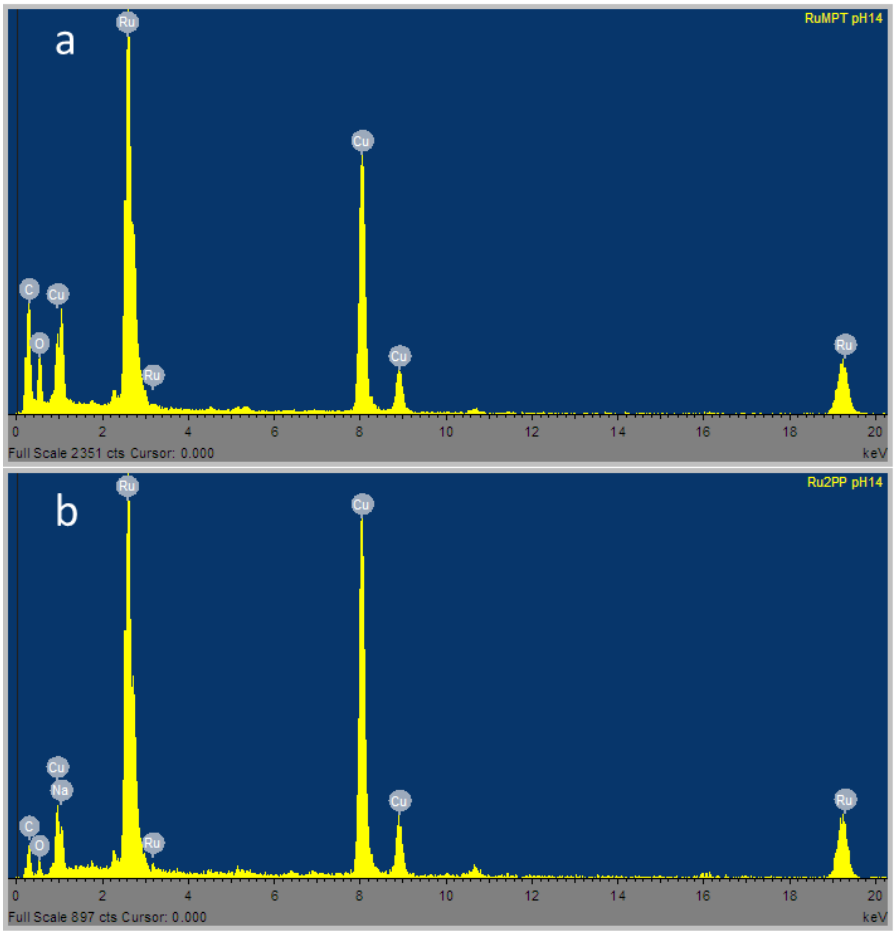

Figure S6. EDX analyses of a) **RuMPT** and b) **Ru2PP** after stability tests in 1 M NaOH.

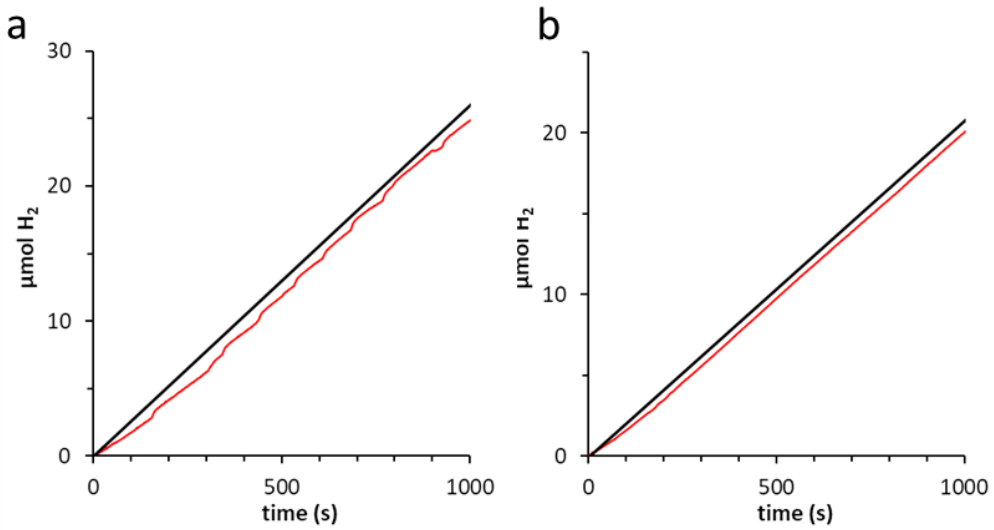

Figure S7. H_2-monitored (red) current-controlled bulk electrolysis (black) of a) **RuMPT-a$_{OH}$** and b) **Ru2PP-p** at at j = -10 mA·cm^{-2} in 1 M NaOH. H_2 production was monitored in gas phase (red curve), using a Clark-type electrode, yielding a Faradaic efficiency ($\mathcal{E}$) of ca. 96 % (**RuMPT-a$_{OH}$**) and 98 % (**Ru2PP-p**)

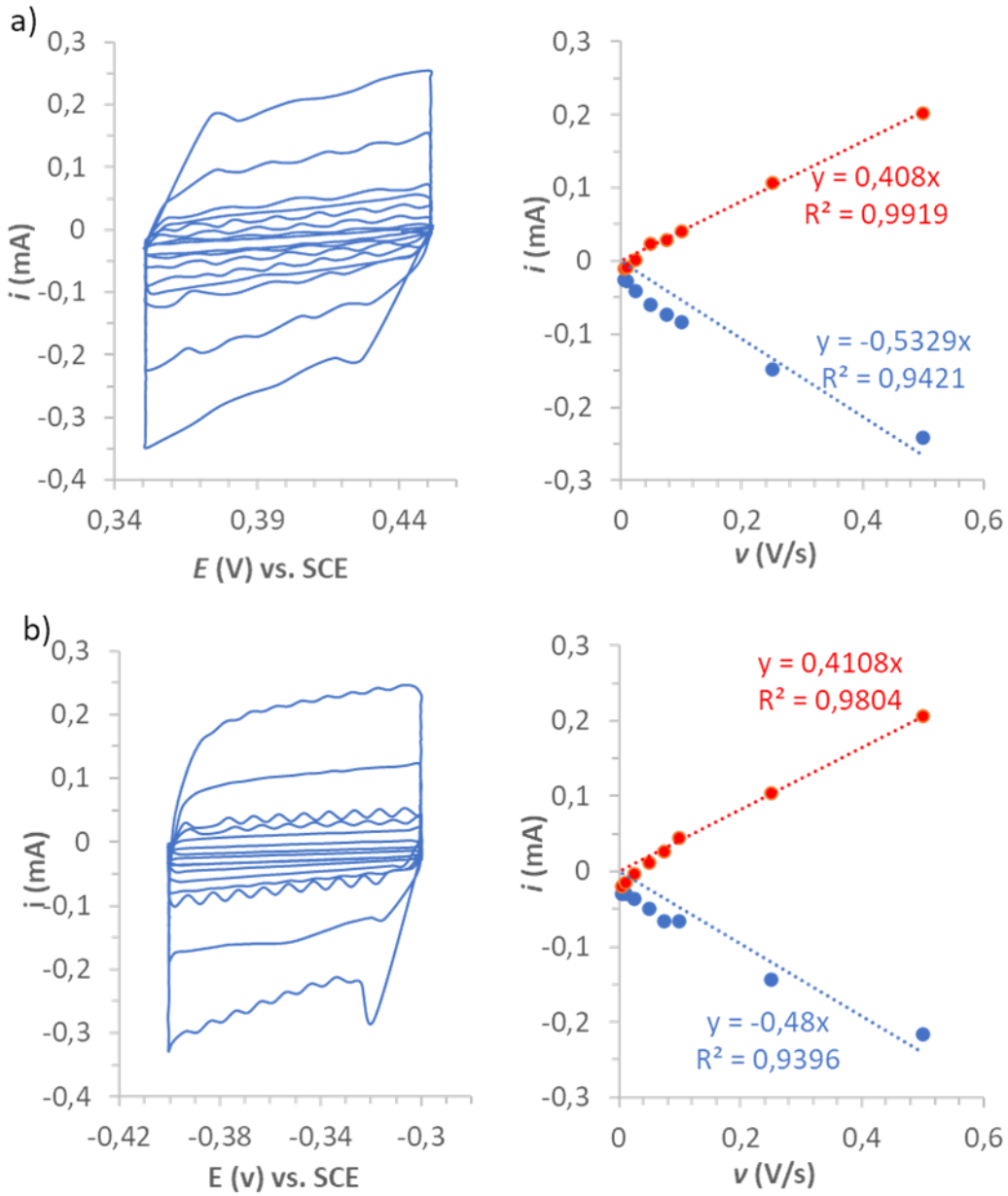

Figure S8. Multi cyclic voltammetry (CV) experiments at different scan rates (*v*) (left) and current values plotted at the middle of the potential range values (V vs. SCE) for the different scan rates for the CDL determination of a) **Ru2PP-a$_H$** in 1 M H_2SO_4 and b) **Ru2PP-p** in 1 M NaOH.

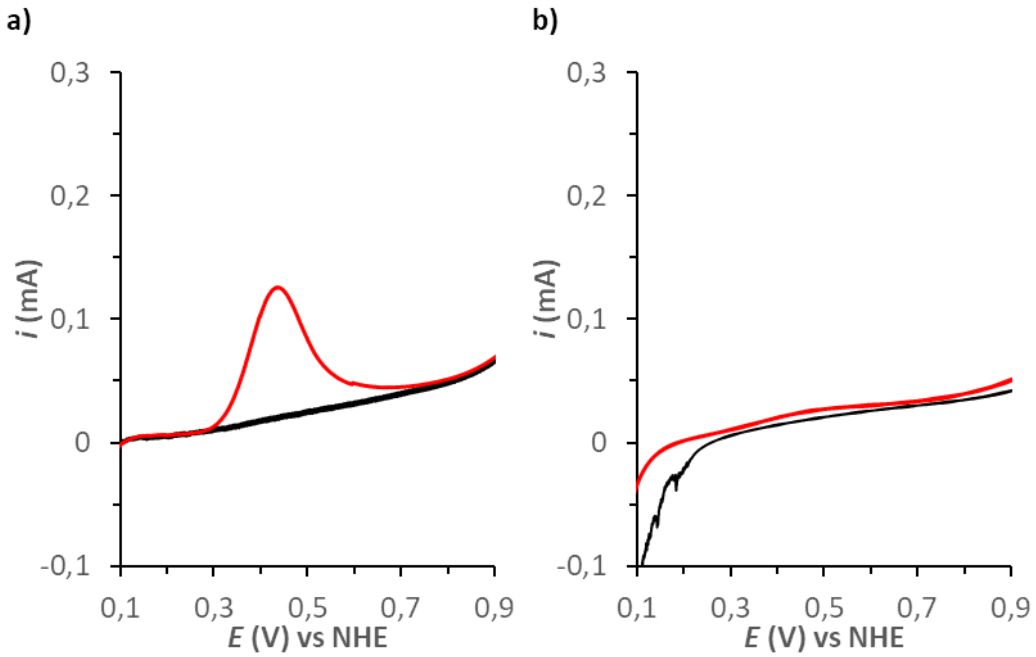

Figure S9. LSV curves (from 0.1 to 0.9 V vs NHE) before (black) and after (red) copper underpotential deposition (Cu UPD) in 1 M H_2SO_4 solution of a) **Ru2PP-a$_H$** and b) **Ru2PP-p**.

HEC	Size (nm)	η_0 (mV)	η_{10} (mV)	b (mV·dec^{-1})	j_0 (mA·cm^{-2})	TOF (s^{-1})	Ref.
RuMPT-a_H	1.4	60	93	42	0.99	0.18 (25 mV) 0.28 (50 mV) 0.95 (100 mV)	This work
Ru2PP-a_H	1.8	≈ 0	30	93	1.93	0.32 (25 mV) 1.37 (50 mV) 10.3 (100 mV)	This work
Ru4PP	1.5	0	20	29	2.04	0.55 (25 mV) 3.06 (50 mV) 17.38 (100 mV)	[13]
Pt/C		0	27	32	1.40	1.65 (25 mV) 5.60 (50 mV) 23.36 (100 mV)	[13]
Ru-black		70	150	65	0.14	0.12 (25 mV) 0.31 (50 mV) 1.81(100 mV)	[13]
Ru-MeOH/ THF	20	0	83	46	0.36	0.07 (25 mV) 0.10 (50 mV) 0.87 (100 mV)	[39]

Table S1. Comparison of complementary electrocatalytic parameters of different HEC in 1 M H_2SO_4. Size (nm), onset overpotential (η_0), overpotential at j = -10 mA·cm^{-2} (η_{10}), Tafel slope (b), exchange current density (j_0) and turnover frequency (TOF).

Catalyst	Size (nm)	η_0 (mV)	η_{10} (mV)	b (mV·dec^{-1})	j_0 (mA·cm^{-2})	TOF (s^{-1})	Ref.
RuMPT-a_{OH}	1.4	50	61	87	2.03	-	This work
Ru2PP-p	1.8	75	86	72	0.54	-	This work
Ru4PP	1.5	0	25	65	0.19	0.55 (25 mV) 3.06 (50 mV) 17.38 (100 mV)	[13]
Pt/C		5	35	56	2.40		[13]
Ru-black		50	125	80	0.65		[13]

Table S2. Comparison of complementary electrocatalytic parameters of different HEC in 1 M NaOH. Size (nm), onset overpotential (η_0), overpotential at j = -10 mA·cm^{-2} (η_{10}), Tafel slope (b), exchange current density (j_0) and turnover frequency (TOF).

Catalyst	RF	η_{10} (t=0) (mV)	η_{10} (t=2h) (mV)	$j_{(\eta=100)}$ (mA·cm^{-2})	$j_{s(\eta=100)}$ (mA·cm^{-2})	Ref.
RuMPT-a_H	211 ± 44	93	95	12	0.056	This work
Ru2PP-a_H	448 ± 85	30	31	243	0.542	This work
Ru4PP	895 ± 95	20	20	496	0.550	[13]
Pt-(b)	90 ± 20	50	60	220	2.500	[40]
Ru-MeOH/THF	645 ± 87	99	103	43	0.067	[39]
RuPP@pCF	-	-	-	-	0.028	[41]

Table S3. Comparison of electrocatalytic parameters of different HEC following the methodology of Jaramillo in 1 M H_2SO_4. RF (Roughness Factor), overpotential at j = -10 mA·cm^{-2} (η_{10}) at t = 0 and t = 2h, current density (j) and specific current density at η = 100 mV (j_s).

Catalyst	RF	η_{10} (t=0) (mV)	η_{10} (t=2h) (mV)	$j_{(\eta=100)}$ (mA·cm^{-2})	$j_{s(\eta=100)}$ (mA·cm^{-2})	Ref.
RuMPT-a_{OH}	272 ± 50	61	68	28	0.103	This work
Ru2PP-p	159 ± 18	86	91	16	0.113	This work
Ru4PP	320 ± 140	25	40	61	0.191	[13]
Pt-(b)	130 ± 50	30	60	70	0.540	[40]

Table S4. Comparison of electrocatalytic parameters of different HEC following the methodology of Jaramillo in 1 M NaOH. RF (Roughness Factor), overpotential at j = -10 mA·cm^{-2} (η_{10}) at t = 0 and t = 2h, current density (j) and specific current density at η = 100 mV (j_s).

3.7 References

[1] Barber, J. and Tran, P. D. "From natural to artificial photosynthesis" *J. R. Soc. Interface*, **2013** (10)

[2] Brandon, N. P. and Kurban, Z. "Clean energy and the hydrogen economy" *Philos. Trans. R. Soc. A Math. Phys. Eng. Sci.*, **2017** (375)

[3] Zeng, M. and Li, Y. "Recent advances in heterogeneous electrocatalysts for the hydrogen evolution reaction" *J. Mater. Chem. A*, **2015** (3) 14942–62

[4] Zou, X. and Zhang, Y. "Noble metal-free hydrogen evolution catalysts for water splitting" *Chem. Soc. Rev.*, **2015** (44) 5148–80

[5] Eftekhari, A. "Electrocatalysts for hydrogen evolution reaction" *Int. J. Hydrogen Energy*, **2017** (42) 11053–77

[6] Bae, S.-Y.; Mahmood, J.; Jeon, I.-Y. and Baek, J.-B. "Recent advances in ruthenium-based electrocatalysts for the hydrogen evolution reaction" *Nanoscale Horizons*, **2019** 43–56

[7] Li, C. and Baek, J. B. "Recent Advances in Noble Metal (Pt, Ru, and Ir)-Based Electrocatalysts for Efficient Hydrogen Evolution Reaction" *ACS Omega*, **2020** (5) 31–40

[8] Creus, J.; De Tovar, J.; Romero, N.; García-Antón, J.; Philippot, K.; Bofill, R. and Sala, X. "Ruthenium Nanoparticles for Catalytic Water Splitting" *ChemSusChem*, **2019** (12) 2493–514

[9] Kweon, D. H.; Okyay, M. S.; Kim, S. J.; Jeon, J. P.; Noh, H. J.; Park, N.; Mahmood, J. and Baek, J. B. "Ruthenium anchored on carbon nanotube electrocatalyst for hydrogen production with enhanced Faradaic efficiency" *Nat. Commun.*, **2020** (11) 1–10

[10] Peng, Y.; Lu, B.; Chen, L.; Wang, N.; Lu, J. E.; Ping, Y. and Chen, S. "Hydrogen evolution reaction catalyzed by ruthenium ion-complexed graphitic carbon nitride nanosheets" *J. Mater. Chem. A*, **2017** (5) 18261–9

[11] Magdić, K.; Kvastek, K. and Horvat-Radošević, V. "Impedance approach to activity of hydrogen evolution reaction on spatially heterogeneous GC electrode surfaces: Metal free vs. Ru catalysed case" *Electrochim. Acta*, **2015** (167) 455–69

[12] Amiens, C.; Chaudret, B.; Ciuculescu-Pradines, D.; Collière, V.; Fajerwerg, K.; Fau, P.; Kahn, M.; Maisonnat, A.; Soulantica, K. and Philippot, K. "Organometallic approach for the synthesis of nanostructures" *New J. Chem.*, **2013** (37) 3374–401

[13] Creus, J.; Drouet, S.; Suriñach, S.; Lecante, P.; Collière, V.; Poteau, R.; Philippot, K.; García-Antón, J. and Sala, X. "Ligand-Capped Ru Nanoparticles as Efficient Electrocatalyst for the Hydrogen Evolution Reaction" *ACS Catal.*, **2018** (8) 11094–102

[14] Rahm, J. M. and Erhart, P. "Beyond Magic Numbers: Atomic Scale Equilibrium Nanoparticle Shapes for Any Size" *Nano Lett.*, **2017** (17) 5775–81

[15] Wang, J.; Mbah, C. F.; Przybilla, T.; Apeleo Zubiri, B.; Spiecker, E.; Engel, M. and Vogel, N. "Magic number colloidal clusters as minimum free energy structures" *Nat. Commun.*, **2018** (9)

[16] Zheng, Y.; Jiao, Y.; Zhu, Y.; Li, L. H.; Han, Y.; Chen, Y.; Jaroniec, M. and Qiao, S. Z. "High Electrocatalytic Hydrogen Evolution Activity of an Anomalous Ruthenium Catalyst" *J. Am. Chem. Soc.*, **2016** (138) 16174–81

[17] Gao, K.; Wang, Y.; Wang, Z.; Zhu, Z.; Wang, J.; Luo, Z.; Zhang, C.; Huang, X.; Zhang, H. and Huang, W. "Ru nanodendrites composed of ultrathin fcc/hcp nanoblades for the hydrogen evolution reaction in alkaline solutions" *Chem. Commun.*, **2018** (54) 4613–6

[18] Zhao, M.; Chen, Z.; Lyu, Z.; Hood, Z. D.; Xie, M.; Vara, M.; Chi, M. and Xia, Y. "Ru Octahedral Nanocrystals with a Face-Centered Cubic Structure, {111} Facets, Thermal Stability up to 400 °C, and Enhanced Catalytic Activity" *J. Am. Chem. Soc.*, **2019** (141) 7028–36

[19] Aiken, J. D. and Finke, R. G. "A review of modern transition-metal nanoclusters: Their synthesis, characterization, and applications in catalysis" *J. Mol. Catal. A Chem.*, **1999** (145) 1–44

[20] Qiao, L. and Swihart, M. T. "Solution-phase synthesis of transition metal oxide nanocrystals: Morphologies, formulae, and mechanisms" *Adv. Colloid Interface Sci.*, **2017** (244) 199–266

[21] Green, C. L. and Kucernak, A. "Determination of the platinum and ruthenium surface areas in platinum-ruthenium electrocatalysts by underpotential deposition of copper. 2: Effect of surface composition on activity" *J. Phys. Chem. B*, **2002** (106) 11446–56

[22] Pelzer, K.; Vidoni, O.; Philippot, K.; Chaudret, B. and Collière, V. "Organometallic synthesis of size-controlled polycrystalline ruthenium nanoparticles in the presence of alcohols" *Adv. Funct. Mater.*, **2003** (13) 118–26

[23] Creus, J. "Electrocatalytic water splitting with ruthenium nanoparticles" PhD Dissertation, Departament de Química, Universitat Autònoma de Barcelona, Barcelona, Spain, **2018**
[24] Lara, P.; Philippot, K. and Chaudret, B. "Organometallic Ruthenium Nanoparticles: A Comparative Study of the Influence of the Stabilizer on their Characteristics and Reactivity" *ChemCatChem*, **2013** (5) 28–45
[25] Favier, I.; Massou, S.; Teuma, E.; Philippot, K.; Chaudret, B. and Gómez, M. "A new and specific mode of stabilization of metallic nanoparticles" *Chem. Commun.*, **2008** 3296–8
[26] Guerrero, M.; García-Antón, J.; Tristany, M.; Pons, J.; Ros, J.; Philippot, K.; Lecante, P. and Chaudret, B. "Design of new N,O hybrid pyrazole derived ligands and their use as stabilizers for the synthesis of Pd nanoparticles" *Langmuir*, **2010** (26) 15532–40
[27] Morgan, D. J. "Resolving ruthenium: XPS studies of common ruthenium materials" *Surf. Interface Anal.*, **2015** (47) 1072–9
[28] Guerrero, M.; Roucoux, A.; Denicourt-Nowicki, A.; Bricout, H.; Monflier, E.; Collire, V.; Fajerwerg, K. and Philippot, K. "Alkyl sulfonated diphosphines-stabilized ruthenium nanoparticles as efficient nanocatalysts in hydrogenation reactions in biphasic media" *Catal. Today*, **2012** (183) 34–41
[29] Martínez-Prieto, L. M.; Urbaneja, C.; Palma, P.; Cámpora, J.; Philippot, K. and Chaudret, B. "A betaine adduct of N-heterocyclic carbene and carbodiimide, an efficient ligand to produce ultra-small ruthenium nanoparticles" *Chem. Commun.*, **2015** (51) 4647–50
[30] Axet, M. R. and Philippot, K. "Catalysis with Colloidal Ruthenium Nanoparticles" *Chem. Rev.*, **2020** (120) 1085–145
[31] Pery, T.; Pelzer, K.; Buntkowsky, G.; Philippot, K.; Limbach, H. H. and Chaudret, B. "Direct NMR evidence for the presence of mobile surface hydrides on ruthenium nanoparticles" *ChemPhysChem*, **2005** (6) 605–7
[32] Debouttière, P. J.; Coppel, Y.; Denicourt-Nowicki, A.; Roucoux, A.; Chaudret, B. and Philippot, K. "PTA-stabilized ruthenium and platinum nanoparticles: Characterization and investigation in aqueous biphasic hydrogenation catalysis" *Eur. J. Inorg. Chem.*, **2012** 1229–36
[33] García-Antón, J.; Axet, M. R.; Jansat, S.; Philippot, K.; Chaudret, B.; Pery, T.; Buntkowsky, G. and Limbach, H. H. "Reactions of olefins with ruthenium hydride nanoparticles: NMR characterization, hydride titration, and room-temperature C-C bond activation" *Angew. Chemie - Int. Ed.*, **2008** (47) 2074–8
[34] Murthy, A. P.; Theerthagiri, J. and Madhavan, J. "Insights on Tafel Constant in the Analysis of Hydrogen Evolution Reaction" *J. Phys. Chem. C*, **2018** (122) 23943–9
[35] Shinagawa, T.; Garcia-Esparza, A. T. and Takanabe, K. "Insight on Tafel slopes from a microkinetic analysis of aqueous electrocatalysis for energy conversion" *Sci. Rep.*, **2015** (5) 1–21
[36] Cheng, J.; Zhang, H.; Ma, H.; Zhong, H. and Zou, Y. "Study of carbon-supported IrO2 and RuO2 for use in the hydrogen evolution reaction in a solid polymer electrolyte electrolyzer" *Electrochim. Acta*, **2010** (55) 1855–61
[37] Näslund, L. Å.; Ingason, Á. S.; Holmin, S. and Rosen, J. "Formation of RuO(OH)2 on RuO2-based electrodes for hydrogen production" *J. Phys. Chem. C*, **2014** (118) 15315–23
[38] McCrory, C. C. L.; Jung, S.; Ferrer, I. M.; Chatman, S. M.; Peters, J. C. and Jaramillo, T. F. "Benchmarking Hydrogen Evolving Reaction and Oxygen Evolving Reaction Electrocatalysts for Solar Water Splitting Devices" *J. Am. Chem. Soc.*, **2015** (137) 4347–57
[39] Drouet, S.; Creus, J.; Collière, V.; Amiens, C.; García-Antón, J.; Sala, X. and Philippot, K. "A porous Ru nanomaterial as an efficient electrocatalyst for the hydrogen evolution reaction under acidic and neutral conditions" *Chem. Commun.*, **2017** (53) 11713–6
[40] Walton, D. J.; Burke, L. D. and Murphy, M. M. "Sonoelectrochemistry: Chlorine, hydrogen and oxygen evolution at platinised platinum" *Electrochim. Acta*, **1996** (41) 2747–51
[41] Creus, J.; Mallón, L.; Romero, N.; Bofill, R.; Moya, A.; Fierro, J. L. G.; Mas-Ballesté, R.; Sala, X.; Philippot, K. and García-Antón, J. "Ruthenium Nanoparticles Supported on Carbon Microfibers for Hydrogen Evolution Electrocatalysis" *Eur. J. Inorg. Chem.*, **2019** (2019) 2071–7

Chapter IV

Graphitic Carbon Nitride-supported Platinum Nanoparticles as CO_2 Reduction Photocatalysts

Two carbon nitride-supported Pt-based nanoparticles systems have been prepared, following the organometallic approach, and characterized through a multi-technique process. Both hybrid materials have been tested as photocatalysts in the reduction of CO_2 under UV and visible light irradiation, studying the effect of the Pt loading and the light source in their photocatalytic output and the selectivity of the CO_2 reduction towards different carbon products.

Table of contents

4.1 Abstract

Platinum nanoparticles (Pt NPs) have been directly deposited on the surface of mesoporous graphitic carbon nitride (mpg-CN) semiconductor, using the organometallic approach synthetic method with two different Pt loadings. After full characterization of the hybrid materials, well-dispersed, small (ca. 2.5 nm) and homogeneous Pt-based nanoparticles were observed on the surface of the mpg-CN, consisting predominantly of metallic Pt with a slight contribution of oxidic species on the surface. After loading mpg-CN with Pt NPs, the semiconductor experimented an enhancement in its charge separation properties upon bandgap excitation. This enhancement was attributed to the electron extraction from the conduction band of the semiconductor induced by the deposited Pt NPs, as confirmed by fluorescence lifetime measurements. Both hybrid materials showed photocatalytic activity in the reduction of CO_2 under UV and visible irradiation, and an improved selectivity towards highly reduced carbon products such as methanol or methane, whereas bare mpg-CN led to the formation of CO as the main product. These results lead to new pathways to control the selectivity in the photocatalytic reduction of carbon dioxide, thus contributing to develop selective photocatalysts, which is one of the key issues in this rising technology for direct solar-to-chemical energy conversion.

4.2 Introduction

The extreme economic and energy dependence on fossil fuels has led to a huge environmental impact, like global warming, caused by the excessive emission of gases, such as CO_2, into the atmosphere [1]. Despite the growing interest in more sustainable energy sources, the prospect of having a dominant cleaner energy alternative is still far-off. In this regard, part of the research has focused on developing techniques for CO_2 capture and storage (CCS) [2] and even transforming it into useful chemicals [3]. Among various strategies, photocatalytic reduction of CO_2 to fuels and other value-added products emerge as a solution to stabilize the concentration of CO_2 in the atmosphere, thus minimizing the environmental side-effects, and, at the same time, directly converting solar energy into chemical energy [4–6]. Inoue and co-workers reported in 1979 the first examples of photocatalyzed CO_2 reduction, employing an aqueous suspension of semiconductor powders, such as TiO_2 [7]. Since then, the work of many pieces of research in the field of energy have focused on improving the efficiency of the complex transformation that is the CO_2 reduction [8]. As introduced in Chapter I (section 1.7), although TiO_2 is one of the most widely used materials in photocatalyzed reactions, other semiconductors, such as Ga_2O_3, ZrO_2, CuO, $LaCoO_3$, CdS, GaP or SiC, have been tested as photocatalyst for the reduction of carbon [4–9]. However, the main drawback of most of these semiconductors, including TiO_2, is that they absorb predominantly in the UV range, thus restricting their potential application as sunlight-driven photocatalysts, considering the fact that UV light barely represents 4% of the solar radiation reaching the Earth crust [10]. Therefore, the design of visible light-triggered photocatalysts for CO_2 reduction is required.

Graphitic carbon nitride, also presented in the introduction chapter, is a semiconductor material with a stacked structure (resembling graphite), and a suitable band structure that can be activated by visible light irradiation (bandgap ~2.7 eV). Depending on the preparation method, there are different types of graphitic carbon nitride with distinct morphological features. Among them, mesoporous graphitic carbon nitride (mpg-CN) is very interesting given its porosity, which further increases its surface area, thus increasing the amount of active sites in the material [11]. Its affordable and facile preparation, Earth-abundance, non-

toxic elemental composition, and thermal and chemical stability make it a very promising semiconductor to be used as a photocatalyst in the reduction of CO_2 [12–14]. However, extended light absorption does not necessarily lead to an enhanced photocatalytic output, because a highly efficient charge separation/transfer at the semiconductor and fast catalysis are also needed in order to avoid charge recombination undesired deactivation processes [15]. The major challenge of CO_2 reduction is to achieve control over process selectivity towards the different possible carbon products, typically CO, HCOOH, CH_3OH and CH_4, just addressing C_1 products [1,16,17]. A simple and versatile manner to enhance the photocatalytic output and the selectivity of the materials is to load fitting co-catalysts on the surface of the semiconductor [1,17]. Supported metal nanoparticles (NPs) have proved to be effective in this role as co-catalysts [1,17,18] as they can improve activity by acting as electron transfer centers and catalytically active sites, but also they can help tuning the product selectivity. Noble-metals, and specifically Pt NPs, are remarkably effective in CO_2 reduction due to their outstanding activity and selectivity [19]. However, not only the chemical nature of the co-catalyst is relevant, but also their morphological properties and its stability under reaction conditions. In this regard, the organometallic approach is a reproducible method that allows the preparation of small metal nanoparticles with narrow size distribution, with a well-controlled surface state under mild reaction conditions [20].

In this chapter, Pt nanoparticles have been directly deposited on the surface of mesoporous graphitic carbon nitride, through the organometallic approach method, and using two different metal loadings, achieving well-distributed and narrow-sized NPs all over the surface of the semiconductor. The obtained hybrid materials were studied as photocatalysts in the reduction of CO_2 under UV and visible light irradiation, correlating their physical and chemical features with their photocatalytic output and selectivity.

4.3 Experimental part

4.3.1 Reagents and materials

All procedures involved in the handling of reagents and the synthesis of the hybrid materials were carried out inside a glovebox (MBRAUN Unilab), or using standard Schlenk-line and Fisher-Porter vessel techniques, under Ar atmosphere. All glassware were pre-dried before use, either at 120 °C in the oven or using a heat gun. The following reagents were used as purchased: $[Pt(dba)_3]$ (dba = dibenzylideneacetone) (Strem Chemicals), hydrogen gas (Abelló Linde, H_2 >99%), $^{13}CO_2$ (Cambridge Isotope Laboratories, ^{13}C 99%). Tetrahydrofuran (THF) and hexane, used as solvents (both from Scharlab), were distilled, dried and degassed by freeze–pump–thaw cycling.

4.3.2 Synthesis of mpg-CN

Synthesis of mesoporous graphitic carbon nitride (mpg-CN) was carried out via the sol-gel route, according to a procedure previously reported [21], consisting on the use of precursors cyanamide and triethyl orthosilicate (TEOS), yielding a mixture of carbon nitride and silica. After treating this mixture with NH_4HF_2 and washing with water and ethanol, SiO_2, which serves as template, is removed, yielding the final mpg-CN.

4.3.3 Synthesis of mpg-CN-supported Pt nanoparticles

200 mg of mpg-CN and 16 mL of THF were added in a pre-dried Fisher-Porter bottle connected to the Schlenk-line. $[Pt(dba)_3]$ was weighed and placed into the reactor inside the glovebox, either 11.2 mg (0.012 mmol) or 4.5 mg (0.005 mmol) for **Pt-NPs@mpg-CN(H)** and **Pt-NPs@mpg-CN(L)**, respectively, where (H) and (L) stand for the high or low metal loading employed in each case. The reactor was then pressurized with 3 bars of H_2, and the mixture was kept under vigorous magnetic stirring at room temperature (r.t.) for 16 h. After removing the H_2 pressure, a sample for Transmission Electron Microscopy (TEM) was prepared. The Pt NPs / mpg-CN hybrid materials were washed with hexane, isolated by centrifugation, and dried under vacuum, thus yielding a brownish powder.

4.3.4 Characterization techniques

Transmission Electron Microscopy (TEM) and Energy-dispersive X-ray spectroscopy (EDX). TEM and EDX analyses were performed at the Servei de Microscòpia at the UAB, using a JEM-2011 unit with an acceleration voltage of 200 kV, equipped with an EDX detector model X-Max EDS with 136 eV energy resolution (Oxford Instruments). TEM samples were prepared after drop-casting a single drop of the crude colloidal solution on the surface of a carbon-coated copper grid (400 mesh). Mean size and distribution of the Pt nanoparticles (NPs) contained in **Pt-NPs@mpg-CN(H)** and **Pt-NPs@mpg-CN(L)** were estimated after measuring ca. 200 NPs on the TEM micrographs, using the freeware Fiji-ImageJ.

X-ray Powder Diffraction (XRD). X-ray diffractograms were measured in an Empyrean diffractometer (Malvern Panalytical) using Cu K_α radiation at a scanning rate of 0.01 $°s^{-1}$.

X-Ray Photoelectron Spectroscopy (XPS). XPS measurements were carried out at the Institut Català de Nanociència i Nanotecnologia (ICN2, Barcelona), using a Phoibos 150 analyzer (SPECS GmbH) at ultra-high vacuum conditions (base pressure of $5 \cdot 10^{-10}$ mbar), with a monochromatic aluminium Kα X-ray source (1486.74 eV). The energy resolution was measured by the half-maximum intensity (FWHM) of the Ag $3d_{5/2}$ peak from a sputter cleaned silver foil (0.62 eV).

Inductively Coupled Plasma - Optical Emission Spectrometry (ICP-OES). Pt content (wt.%) on each hybrid material was determined by ICP-OES analyses at the Servei d'Anàlisi Química (SAQ) at the UAB, using an equipment from Perkin-Elmer, model Optima 4300DV.

Specific Surface Area (SSA) determination. SSA measurements were carried out on a Quantachrome Autosorb-1 apparatus. Nitrogen adsorption–desorption isotherms were measured at 77.3 K after degassing the samples at 120 °C for 6 h. SSAs were estimated through the Brunauer-Emmett-Teller (BET) method.

UV–vis Diffuse Reflectance Spectroscopy (DRS). UV-vis diffuse reflectance spectra were obtained in a UV/Vis/NIR spectrometer model Lambda 1050 (Perkin Elmer), coupled with a Praying Mantis® diffuse reflectance accessory.

Fluorescence-Lifetime Imaging Microscopy (FLIM). Time-correlated single photon counting (TCSPC) was employed to carry out the measurement of the fluorescence-lifetime, using Mini-τ equipment (Edinburgh Instruments), with a pulsed UV laser diode (372.2 nm, 61.2 ps pulse width, repetition rate of 1 MHz) as excitation source, also including a band-pass filter at 450 or ± 25 nm. After repeating each experiment three times, experimental data were fitted to bi-exponential decay curves, calculating the average fluorescence lifetime as $<\tau>= [\Sigma(A_i\tau_i^2)]/\Sigma(A_i\ \tau_i)$, where A_i is the amplitude and τ_i the lifetime of each contribution.

4.3.5 Photocatalytic CO_2 reduction experiments and calculations.

All experiments towards CO_2 photocatalytic reduction and data treatment were performed by Dr. Fernando Fresno at the Photoactivated Processes Unit in IMDEA Energy Institute (Madrid, Spain).

Gas-phase CO_2 photoreduction experiments were carried out in a continuous-flow mode, using a stainless-steel reactor (280 mL of effective volume), with a borosilicate window, which allowed irradiation. 100 mg of the photocatalyst material were used to prepare a suspension, and deposited on a glass microfiber filter. After drying at 100 °C under vacuum, the filter supporting the photocatalyst was placed in the reactor. UV and visible light were used as irradiation sources, using fluorescent lamps (6 W, maximum wavelength λ_{max} = 365 nm and an average irradiance of 71.7 W/m^2) or LED white lamps (30 W, emitting from 400 to 800 nm, with maxima at 445 and 540 nm and with an irradiance of 78.7 W/m^2), respectively. Pure CO_2 and water (CO_2:H_2O 7.25 molar ratio) were fed into the reactor using a Controlled Evaporation and Mixing (CEM) unit. Reaction products were determined in-line by gas chromatography (GC Bruker 450), equipped with two separation branches and two sampling loops. The first separation branch consisted on two semi-capillary columns (BR-Q Plot and BR-Molesieve5A), a thermal conductivity detector (TCD), a flame ionization detector (FID) and a methanizer. The second one was equipped with a capillary column (Agilent CP-Sil5B) and an FID. Before conducting the experiments, the reactor was evacuated at 50 °C for 1h and then purged with Ar (100 mL/min) for an extra hour, in order to remove any residual organic compounds weakly adsorbed on the surface of the catalyst. After that, both

CO_2 and H_2O were continuously fed in the dark during 1h, thus establishing an adsorption–desorption balance at the reaction temperature. Before light irradiation, the reactor was pressurized (2 bar) and kept at a reaction flow rate of 2 mL/min for another hour. **Figure S1a** shows a scheme of the reaction set-up.

Selectivity towards each carbon-containing reaction product was calculated as the cumulative production of each product, divided by the total amount of all of them. Irradiance measurements were conducted using a fiber optics spectroradiometer (StellarNet Inc.) to calculate photonic efficiencies (utilized electrons divided by incident photons in a given wavelength interval), considering the different electron number required to yield each product from CO_2. ^{13}C isotope tracing experiments were carried out in stainless steel reactor (10.8 of effective volume), with a borosilicate window on top to irradiate through (**Figure S1b).** 20 mg of photocatalyst deposited on a glass microfiber filter (prepared following the procedure described above) were placed in the reactor, which was evacuated under vacuum (P < 1 mbar) at 50 °C during 30 min, and filled first with 3 µL of ultrapure water under static vacuum conditions, and then with $^{13}CO_2$ until a total pressure of 2 bars was reached. After that, the reactor was finally irradiated in batch mode during an hour with two 6 W fluorescent lamps (λ_{max} 365 nm), after which the gas was introduced to a gas chromatograph (Agilent 7820A) fitted with a GS-Carbon-PLOT column (Agilent) and coupled with a mass spectrometry detector (Agilent 5977B) with electron impact ionization.

4.4 Results and discussion

4.4.1 Photocatalysts synthesis and characterization

The synthesis of the platinum nanoparticles (Pt NPs) supported on mesoporous graphitic-carbon nitride (mpg-CN) was performed following the organometallic approach (**Figure 1**). The Pt precursor [Pt(dba)$_3$] and mpg-CN were placed, under inert conditions, in a Fisher-Porter bottle, using THF as solvent. After pressurizing the reactor (3 bar H_2) the mixture was left under vigorous magnetic stirring for 16 h. A colour change in the suspension, from purple to brownish, was observed during this time. The obtained material was washed with hexane, isolated by centrifugation and dried under vacuum, thus yielding a brownish powder. As two different loads of metal precursor were employed, the materials were labelled as **Pt-NPs@mpg-CN(H)** or **Pt-NPs@mpg-CN(L)**, referring to the higher (H) or lower (L) metal loading, respectively.

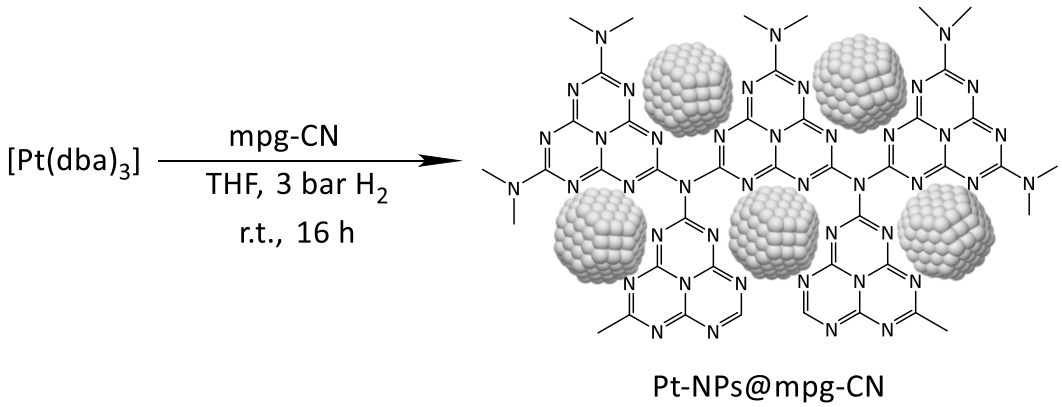

Figure 1. Schematic representation of the organometallic approach for the synthesis of **Pt-NPs@mpg-CN(H)** and **Pt-NPs@mpg-CN(L)**.

The presence of Pt NPs on the surface of the mpg-CN material was first studied by TEM and EDX analysis. TEM micrographs in **Figure 2** show the presence of small and well-dispersed Pt NPs on the surface of the mpg-CN material, with no apparent influence of the initial concentration of Pt precursor in the mean size of the NPs (2.7 ± 0.5 nm and 2.6 ± 0.4 nm for **Pt-NPs@mpg-CN(H)** and **Pt-NPs@mpg-CN(L)**, respectively). These results prove the suitability of mpg-CN as stabilizer for Pt NPs following the organometallic approach, as it does not require an additional stabilizing ligand to control the size and dispersibility of the nanoparticles. EDX

analyses (**Figure S2**) further confirmed the presence of Pt on the surface of the mpg-CN material.

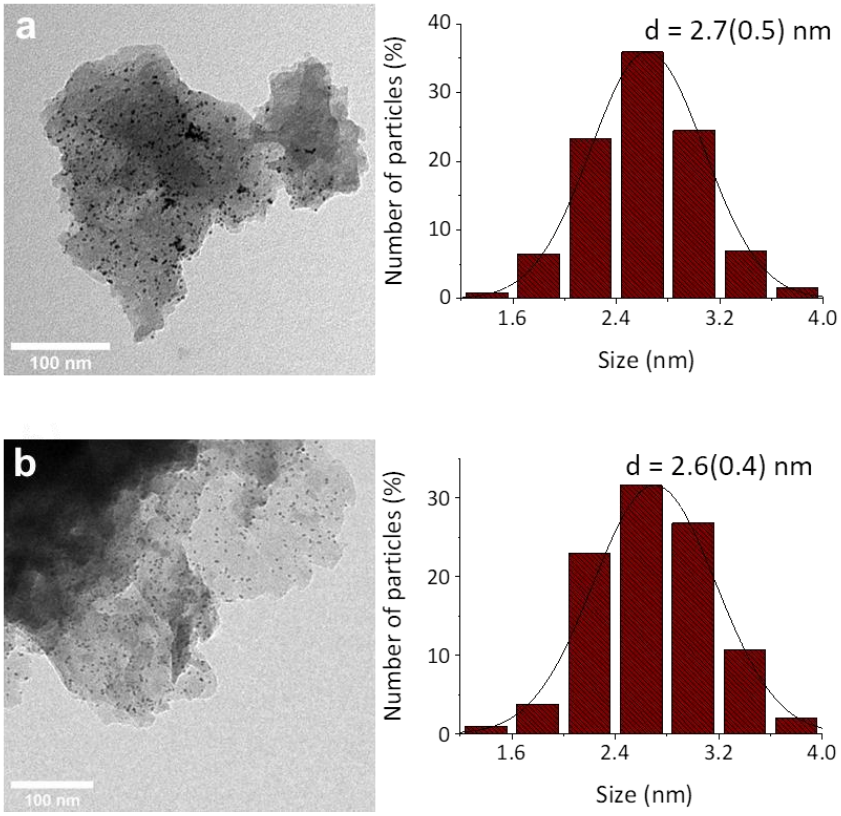

Figure 2. TEM micrographs (left) and size distribution histograms (right) of the as-synthesized a) **Pt-NPs@mpg-CN(H)** and b) **Pt-NPs@mpg-CN(L)**.

X-ray diffraction analyses were performed after synthesizing the hybrid materials. The obtained diffractograms (**Figure 3**) show the reflections typically attributed to mpg-CN, with an intense peak at ca. 27.3 °, related to the stacking of carbon nitride layers with 0.326 nm of interplanar distance, and a weaker peak at ca. 13.1 °, due to the inter-planar repetition of the interconnected triazine units [22]. Two additional reflections, less intense and wider, can be observed for the **Pt-NPs@mpg-CN(L)** material, that can be indexed as the (111) and (002) planes of the platinum cubic structure (pattern also displayed, as vertical black bars, in **Figure 3**). Those signals become more prominent in the case of **Pt-NPs@mpg-CN(H)** sample, with NPs of the same size but with a higher Pt content. In good accordance with TEM images (see above), average Pt particle size calculation, after applying the Scherrer equation to the (111) peak in the **Pt-NPs@mpg-CN(H)** sample diffractogram, gave a value of 3.0 nm.

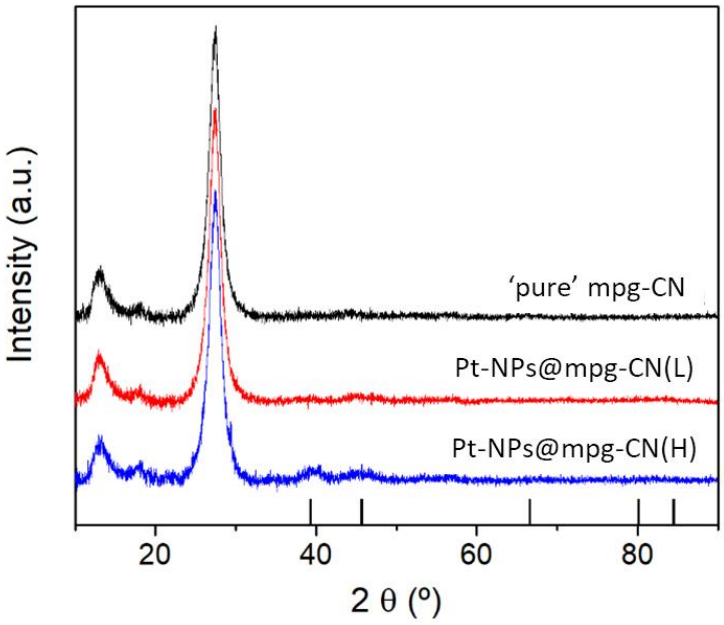

Figure 3. X-ray difractograms of 'pure' mpg-CN (black), **Pt-NPs@mpg-CN(L)** (red) and **Pt-NPs@mpg-CN(H)** (blue). Black vertical bars indicate reference Pt cubic structure reflections (ICDD PDF #01-088-2343).

The specific amount of Pt in each sample was measured by ICP-OES. The obtained results were in accordance witch those expected based on the initial concentration of Pt in each synthesis, being the experimental values 1.2 wt.% Pt for **Pt-NPs@mpg-CN(H)** and 0.6 wt.% for **Pt-NPs@mpg-CN(L)**, and 1.2 and 0.5 wt.% Pt the estimated ones, respectively.

Additionally, XPS measurements helped to understand the chemical nature of the Pt NPs in the freshly prepared hybrid materials (**Figure 4**). Two Pt species were detected, corresponding to Pt^0 ($4f_{7/2}$ peak at 70.6 eV and $4f_{5/2}$ peak at 73.9 eV) and PtO, whose $4f_{7/2}$ and $4f_{5/2}$ peaks are shifted compared to metallic Pt (72.9 eV and 76.6 eV respectively). Previous research in the literature involving Pt NPs demonstrate that they can be partially oxidized [17].

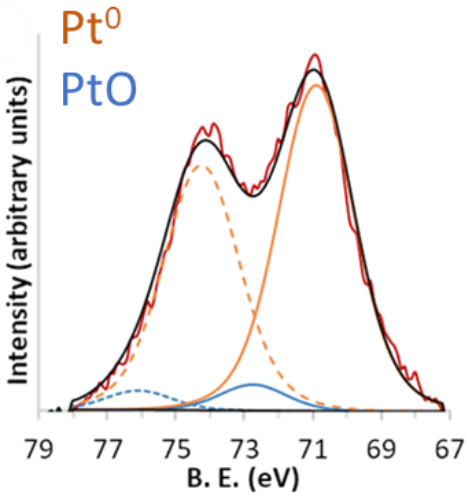

Figure 4. XPS analyses of **Pt-NPs@mpg-CN(H)** after synthesis. In red, the experimental XPS spectra. Fit for the signals: orange lines, the metallic-Pt components (Pt 4f); blue lines, the Pt^{II} components (Pt 4f); bold black lines, the envelope.

Specific surface areas (S_{BET}) measurements were carried out to study possible changes in the structural properties of the mpg-CN after depositing the Pt NPs (N_2 isotherms are collected in **Figure 5**). 'Pure' mpg-CN displays a S_{BET} of 147.0 $m^2 \cdot g^{-1}$, thus confirming its mesoporosity nature. After depositing Pt NPs, a decrease in the specific surface area values was observed (109.9 and 114.7 $m^2 \cdot g^{-1}$ for **Pt-NPs@mpg-CN(H)** and **Pt-NPs@mpg-CN(L)**, respectively), possibly due to a partial blocking of the mesopores of the mpg-CN by the Pt NPs.

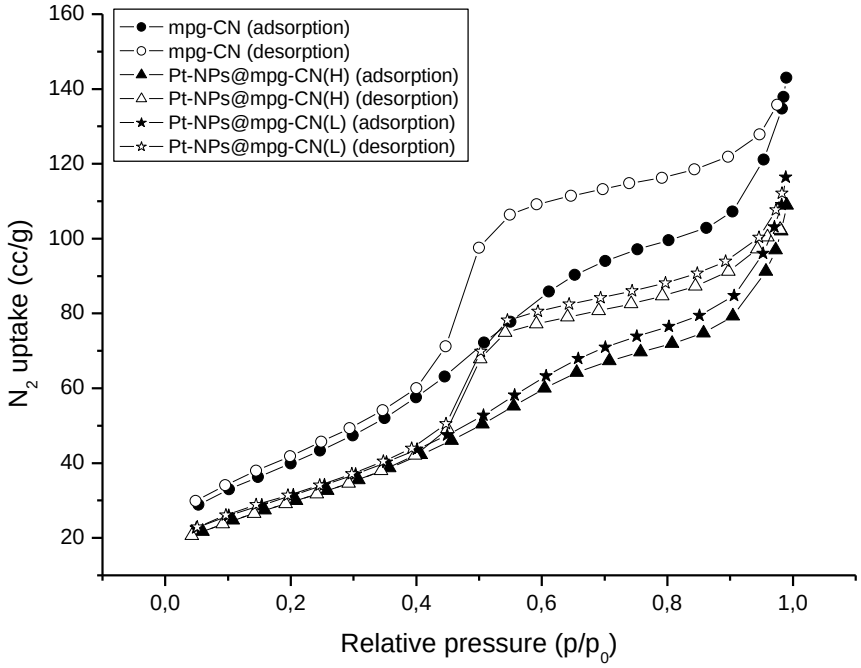

Figure 5. N_2 isotherms corresponding to 'pure' mpg-CN, Pt-NPs@mpg-CN(H) and RuNPs@mpg-CN(L).

UV-vis diffuse reflectance spectra (**Figure 6**) displayed the typical profile of mpg-CN semiconductors, with a steep absorption onset at ca. 450 nm (corresponding to a 2.7-2.8 eV bandgap). A slight variation in the absorption edge could be observed in the spectra, probably attributed to the baseline of the visible region caused by the Pt NPs.

Fluorescence lifetime measurements were performed on the mpg-CN material before and after the incorporation of Pt nanoparticles. The fluorescence decay curves (**Figure 7**) show a reduction of the estimated mean fluorescence lifetime after the decoration with Pt. The presence of metal NPs can induce electron withdrawal from the conduction band (CB) of the mpg-CN semiconductor upon excitation, reducing the CB population and consequently shortening the band-to-band transition lifetime, involved in the fluorescence [23,24]. For the **Pt-NPs@mpg-CN(H)**, the decrease of the fluorescence lifetime is larger compared to **Pt-NPs@mpg-CN(L)** sample, thus indicating that increasing the number of NPs can induce electron transfer to a larger extent.

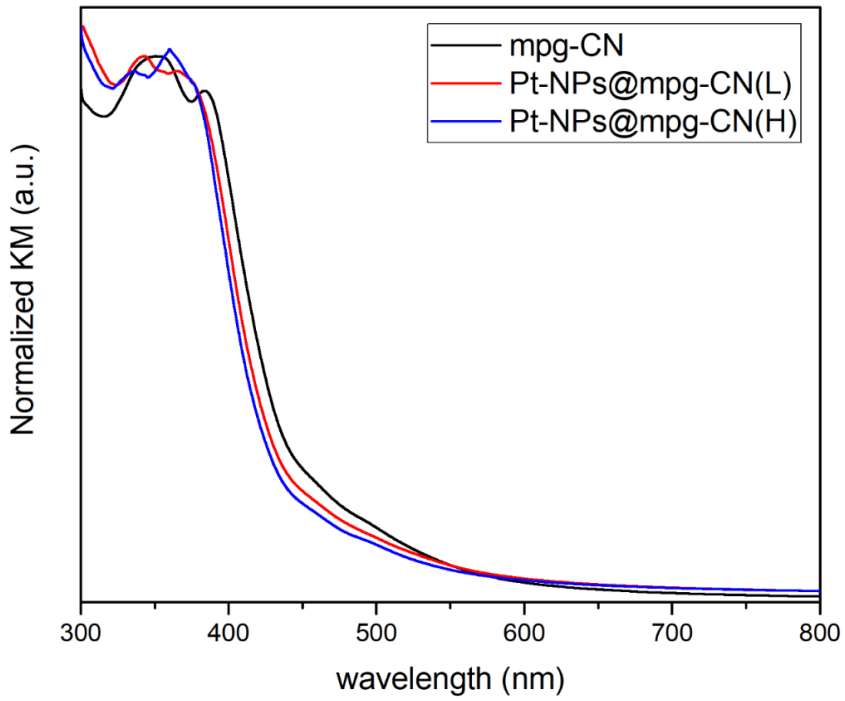

Figure 6. UV-vis diffuse reflectance spectra of mpg-CN before and after Pt decoration

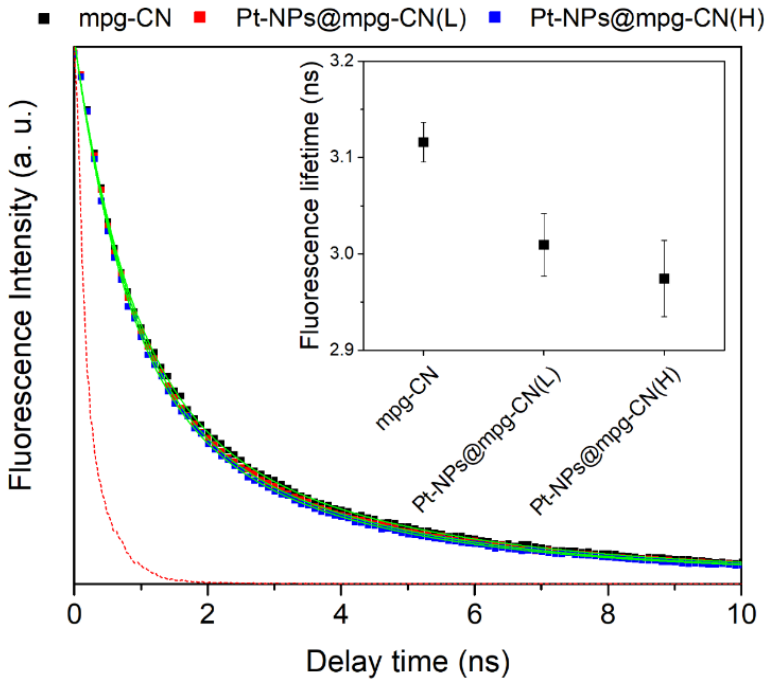

Figure 7. Fluorescence decay curves of mpg-CN before and after Pt NPs deposition. Decay curves fitted to each dataset are represented in green lines, whereas dotted red curve corresponds to the instrument response function (IRF). Inset: Mean fluorescence lifetimes, estimated from the fitted decay curves.

4.4.2 CO_2 photocatalytic reduction under UV and visible irradiation

Both **Pt-NPs@mpg-CN(H)** and **Pt-NPs@mpg-CN(L)** were tested as gas-phase CO_2 reduction photocatalysts, using water as electron donor. Under UV irradiation, CO, CH_3OH, CH_4 and H_2 were detected as the main reaction products (**Figure 8**). As expected, the presence of Pt NPs in the mpg-CN largely boosted the production of H_2 through water reduction, competing with that of CO_2 [25]. Regarding carbon-based products, Pt shifted the selectivity from CO to CH_4, reaching its maximum (ca. 65%, **Figure 9a**) in the case of **Pt-NPs@mpg-CN(L)** photocatalyst. A remarkable selectivity was also observed towards CH_3OH, with a maximum in this case for the **Pt-NPs@mpg-CN(H)** photocatalyst, which also delivered almost total selectivity towards CH_4 and CH_3OH (ca. 60% vs. 40% respectively), with CO production virtually suppressed (**Figure 9a**). This suggests that the selectivity of mpg-CN photocatalyst in the CO_2 reduction under UV irradiation may be roughly tuned by the election of the suitable co-catalyst. Nevertheless, further studies will be required to modulate the carbon product outcome. Thereby, the organometallic approach postulates as a powerful tool for the preparation of metal nanoparticles, allowing the fine-tuning of the catalytic features of the nanocatalysts by using a limitless variety of ligands for their surface stabilization, as done for molecular catalysts [26,27].

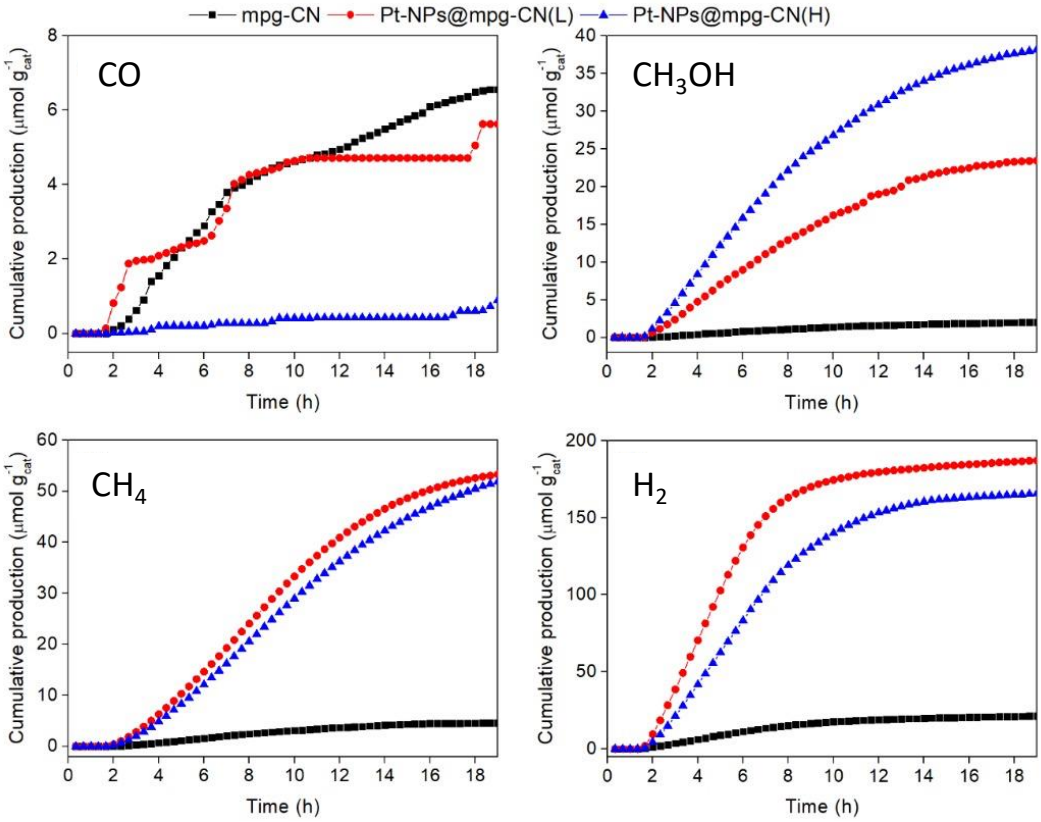

Figure 8. Evolution of the main products obtained in the photocatalytic reduction of CO_2 with water as electron donor, under UV irradiation: CO, CH_3OH, CH_4, H_2.

Figure 9a confirms that the shift in selectivity after deposition of the Pt nanoparticles took place together with an increase of CO_2 conversion (from less than 20 $\mu mol \cdot g_{cat}^{-1}$ with bare mpg-CN to 80-90 $\mu mol \cdot g_{cat}^{-1}$ with both Pt-based nanomaterials) thanks to a much better electron utilization, either in total terms (C-products and H_2 production) or just regarding electrons transferred into carbon products, moving from a value, in this scenario, of ca. 100 $\mu mol \cdot g_{cat}^{-1}$ when using mpg-CN to above 500 $\mu mol \cdot g_{cat}^{-1}$ with either **Pt-NPs@mpg-CN(H)** or **Pt-NPs@mpg-CN(L)**. Accordingly, the calculated photonic efficiency between λ = 300 - 400 nm increased by an order of magnitude in the presence of Pt, from ca. 0.003 % for 'pure' mpg-CN to ca. 0.03% in both Pt-decorated mpg-CN photocatalysts.

Despite these promising results under UV irradiation, as stated in the introduction, the most appealing photocatalytic applications of carbon nitride are those involving visible light. **Figure 10** shows the evolution of the main reaction products under visible irradiation (λ > 400 nm). The utilization of 'pure' mpg-CN as photocatalysts yielded mainly CO and H_2, being the latter a product of the competitive water

reduction process, in a ratio ca. 7:1, thus indicating a higher selectivity towards CO_2 reduction when compared to UV irradiation conditions. Traces of CH_3OH and CH_4 were also detected, giving rise to a larger carbon selectivity towards CO (ca. 82 %) when using bare mpg-CN as photocatalyst, as shown in **Figure 9b**.

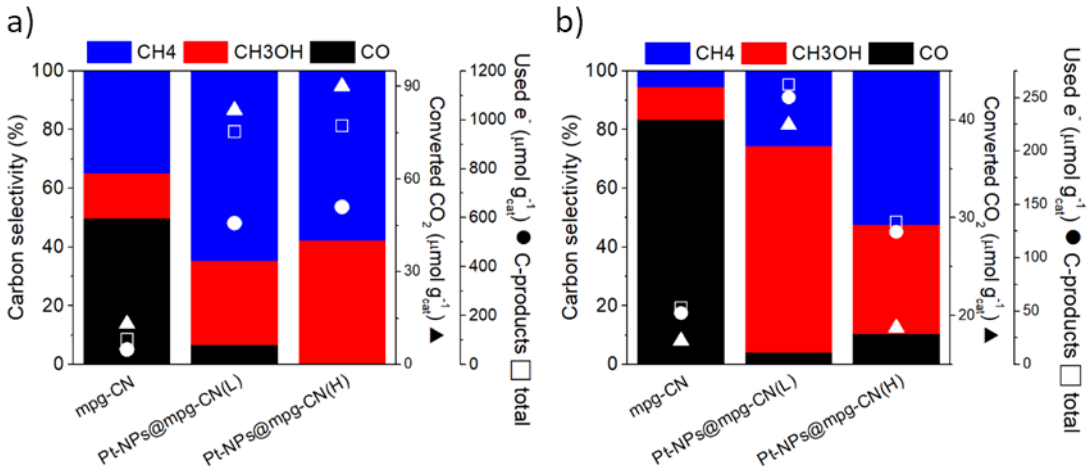

Figure 9. Product selectivity (coloured bars), CO_2 converstion (triangles) and electron utilization (circles: in C-products; square: in C-products and H_2) obtained with the mpg-CN, **Pt-NPs@mpg-CN(H)** and **Pt-NPs@mpg-CN(L)** photocatalysts in the photocatalytic reduction of CO_2 using H_2O as electron donor under a) UV and b) visible irradiation.

As observed under UV irradiation, loading the mpg-CN material with Pt NPs induced an increase in H_2 production, although to a lesser extent than the former (**Figure 10**). This demonstrated that a higher selectivity towards CO_2 reduction vs H_2O reduction takes place under visible light, one of the keystones of this reaction [8]. This is supported by estimated values of total electron use and electron transfer to carbon products, showed in **Figure 9**, which under visible excitation are practically equal, as opposed to UV conditions. Regarding C-products, the incorporation of Pt NPs clearly shifted the selectivity from CO to CH_3OH and CH_4. Interestingly, while with **Pt-NPs@mpg-CN(L)** the selectivity was clearly favorable towards CH_3OH (ca. 70% vs. 25% for CH_4), increasing the amount of Pt led to a higher selectivity towards methane, the most reduced carbon product (50% vs. 40% for CH_3OH when using **Pt-NPs@mpg-CN(H)**). This could be explained as an enhancement of the electron transfer motivated by the increase of Pt centers, as also pointed out by the fluorescence lifetime measurements discussed above. Comparing both Pt-loaded

photocatalysts, the total CO_2 conversion was noticeably lower when using **Pt-NPs@mpg-CN(H)** sample (ca. 10 μmol · g_{cat}^{-1}, very similar to that of the 'pure' mpg-CN), than the conversion obtained with **Pt-NPs@mpg-CN(L)** (approximately 40 μmol · g_{cat}^{-1}) photocatalyst. Accordingly, the estimated photonic efficiency under visible irradiation (up to 450 nm as corresponds to the photocatalyst absorption spectrum) was maximum with the **Pt-NPs@mpg-CN(L)** sample (ca. 0.01%). Thus, the latter hybrid material postulates a promising photocatalyst for visible CO_2 reduction, considering not only the total CO_2 conversion and electron use, but also its selectivity towards CH_3OH, a directly usable fuel.

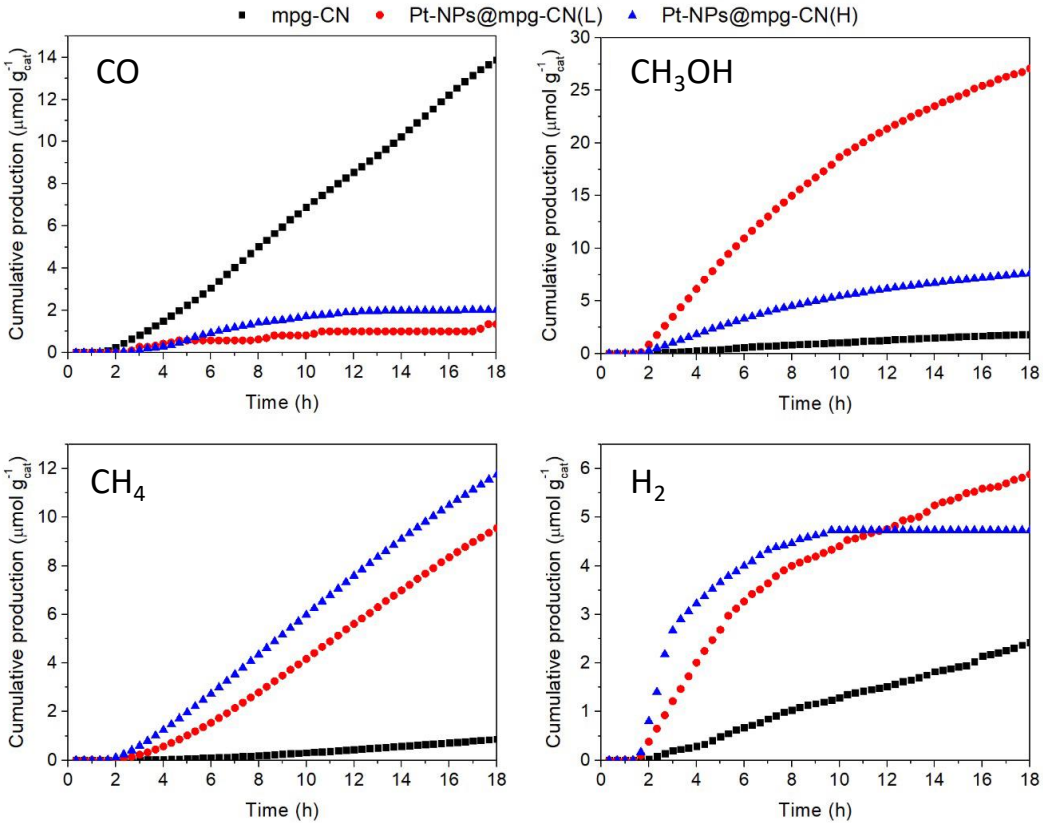

Figure 10. Evolution of the main products obtained in the photocatalytic reduction of CO_2 with water as electron donor, under visible light irradiation: CO, CH_3OH, CH_4, H_2.

When studying the differences in terms of selectivity between UV and visible excitation conditions, it is interesting to remark that the selectivity towards CO_2 reduction compared to H_2O reduction is superior under visible light, even after deposition of Pt NPs, a widely studied hydrogen evolution catalyst, on the mpg-CN. Considering carbon products, visible irradiation seems to favour the production of

CH_3OH to the detriment of CH_4. It is worth highlighting that **Pt-NPs@mpg-CN(L)** photocatalyst delivered a selectivity toward methanol as high as 70% under these conditions. In this regard, it has been previously studied that irradiation with higher photon energy may induce the transfer of a higher number of electrons simultaneously, which could be one of the keys in determining the formation of a more or less reduced product (CH_4 or CH_3OH in this case), based on the excitation wavelength [28]. Similarly, when using Ag/TiO_2 photocatalysts a change in selectivity was also observed when shifting from UV to visible excitation [29].

At the same time, with the aim of finding out the origin of the C-products, ^{13}C tracing studies were performed, by carrying out a photocatalytic $^{13}CO_2$ reduction, and analysing the as-formed products by GC-MS. The obtained chromatogram (**Figure 11**) confirmed that the $^{13}CO_2$ was being reduced to methane.

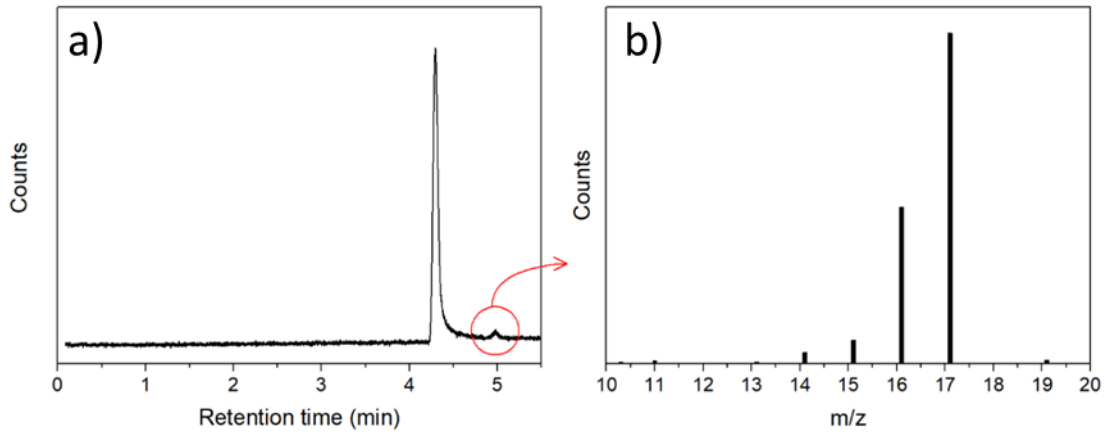

Figure 11. GC-MS analysis after photocatalytic $^{13}CO_2$ reduction, using Pt-NPs@mpg-CN(H) sample as photocatalyst, under UV irradiation. a) Chromatogram; b) MS spectra of the highlighted peak.

Finally, the study of the fate of the Pt-based mpg-CN materials after the photocatalytic experiment was carried out through TEM, EDX and XPS analyses. In TEM micrographs (**Figure 12**), nanoparticles could still be observed, showing good dispersibility on the mpg-CN surface and with a negligible change in their size (**Table 1**), with EDX analyses (**Figure S3**) confirming the presence of Pt. The XPS studies also supported this chemical stability of the materials after photocatalytic experiments (**Figure 13a** and **b**).

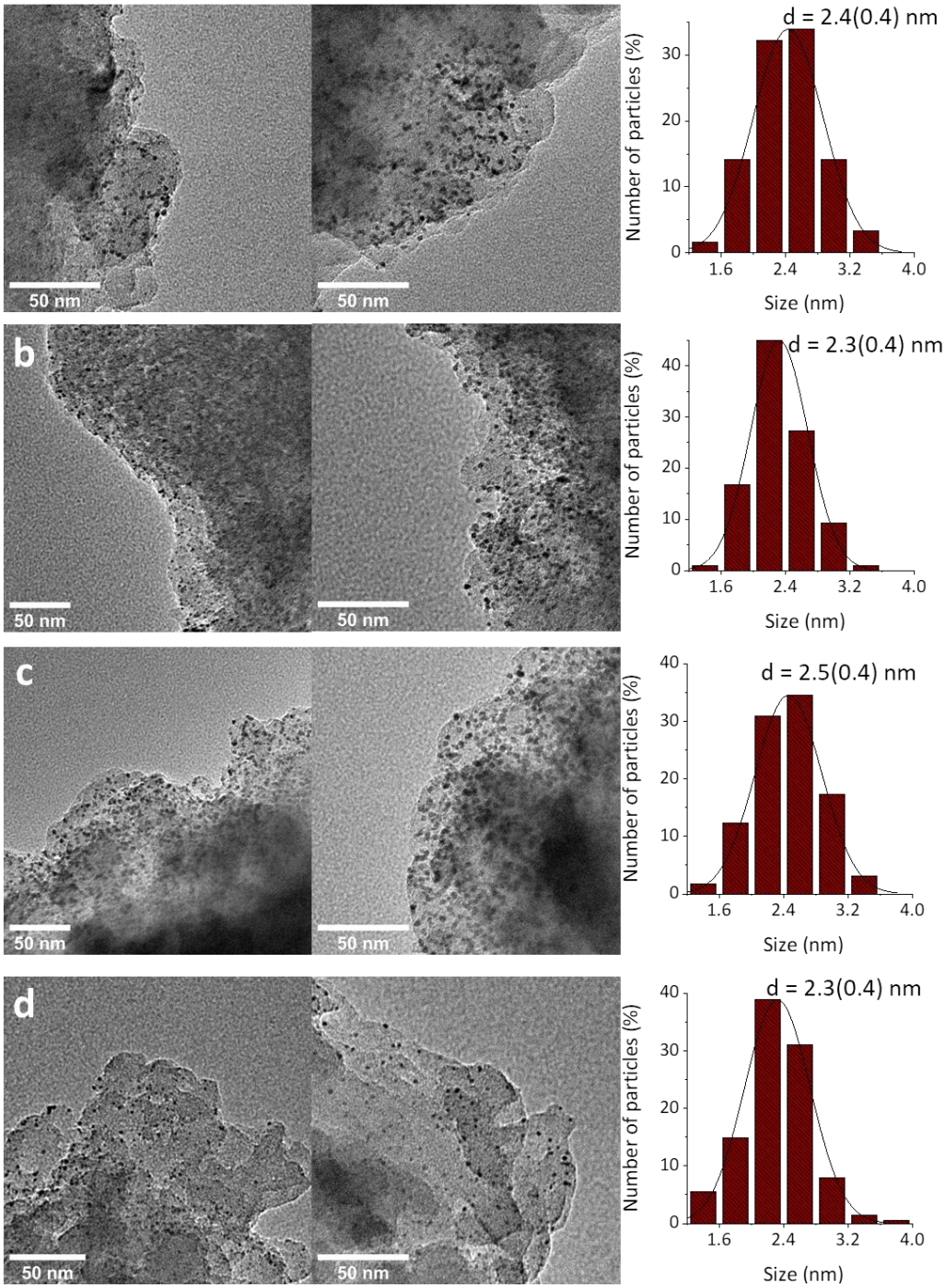

Figure 12. TEM micrographs corresponding to **Pt-NPs@mpg-CN(H)** and b) **Pt-NPs@mpg-CN(L)** after UV-irradiated photocatalytic reaction; c) **Pt-NPs@mpg-CN(H)** and d) **Pt-NPs@mpg-CN(L)** after visible-irradiated photocatalytic reaction.

Photocatalyst	Particle size (nm)		
	As synthesized	After photocatalytic test	
		UV light	Visible light
Pt-NPs@mpg-CN(H)	2.7 ± 0.5	2.4 ± 0.4	2.5 ± 0.4
Pt-NPs@mpg-CN(L)	2.6 ± 0.4	2.3 ± 0.4	2.3 ± 0.4

Table 1. Nanoparticle size comparision of the Pt NPs supported on the mpg-CN before and after photocatalytic test.

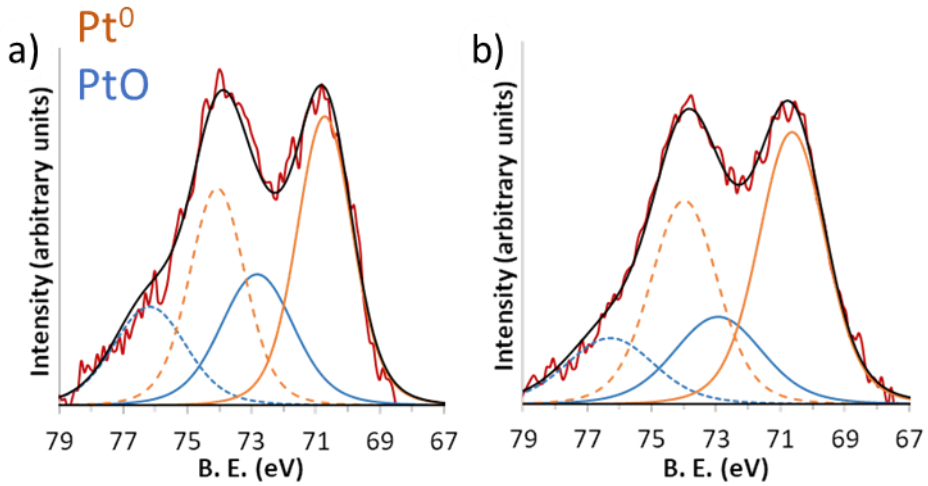

Figure 13. XPS analyses of **Pt-NPs@mpg-CN(H)** (a) after photocatalytic reaction experiment under UV irradiation (b) after photocatalytic reaction test under visible irradiation. In red, the experimental XPS spectra. Fit for the signals: orange lines, the metallic-Pt components (Pt 4f); blue lines, the Pt^{II} components (Pt 4f); bold black lines, the envelope.

4.5 Conclusions

Two mpg-CN supported Pt-based materials have been prepared following the organometallic approach, and studied as photocatalyst in the reduction of CO_2 under UV and visible light excitation, in a continuous flow reactor. Both **Pt-NPs@mpg-CN(H)** and **Pt-NPs@mpg-CN(L)** materials were subjected to a thorough characterization process, involving techniques such as TEM, ICP-OES, EDX and XPS. These studies revealed the presence of well-distributed nanoparticles on the surface of the mpg-CN, with a mean size of ca. 2.5 nm regardless of the metal loading, whose chemical composition was mainly Pt^0 with a minor contribution of oxidized surface species. Photophysical characterization revealed that electron transfer process takes place between the mpg-CN semiconductor and the metal NPs. Consequently, Pt-loaded mpg-CN delivered improved photocatalytic features in terms of conversion and selectivity towards highly reduced (and directly usable) fuels such as methanol or methane, in both UV and visible irradiation, when compared to the bare mpg-CN, which yielded CO as the main product. **Pt-NPs@mpg-CN(L)** system particularly stood out, delivering a selectivity towards methanol of ca. 70% upon visible light irradiation. It is important to note that, under visible light conditions, the selectivity towards CO_2 reduction was higher, whereas under UV irradiation the competitive H_2O reduction played a more relevant role. The election of the organometallic approach as synthetic method, together with the utilization of mpg-CN as support, have facilitated the preparation of stable and reproducible Pt NPs with clean surface, key features in the selectivity and photocatalytic output of the **Pt-NPs@mpg-CN(H)** and **Pt-NPs@mpg-CN(L)** hybrid materials here presented.

4.6 Supporting Information

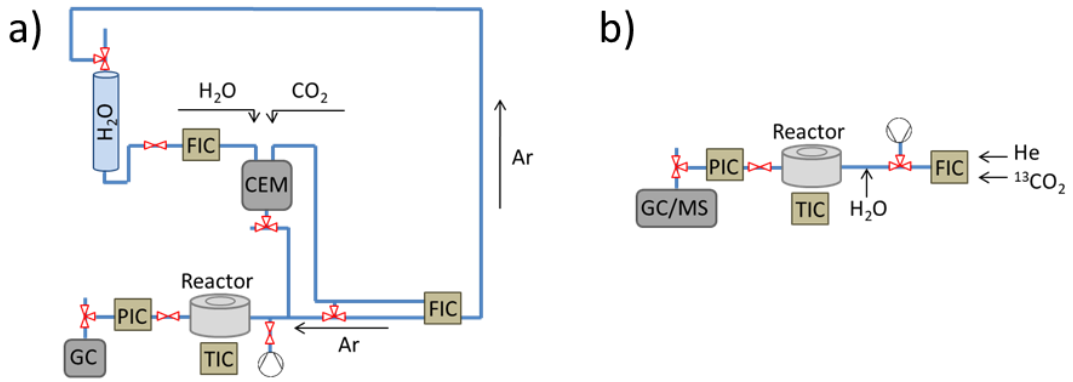

Figure S1. Schematic representation of the set-ups for a) photocatalytic tests and b) isotope tracing experiments. Controlled evaporation and mixing (CEM); flow indicator and controller (FIC): pressure indicator and controler (PIC); temperature indicator and controller (TIC).

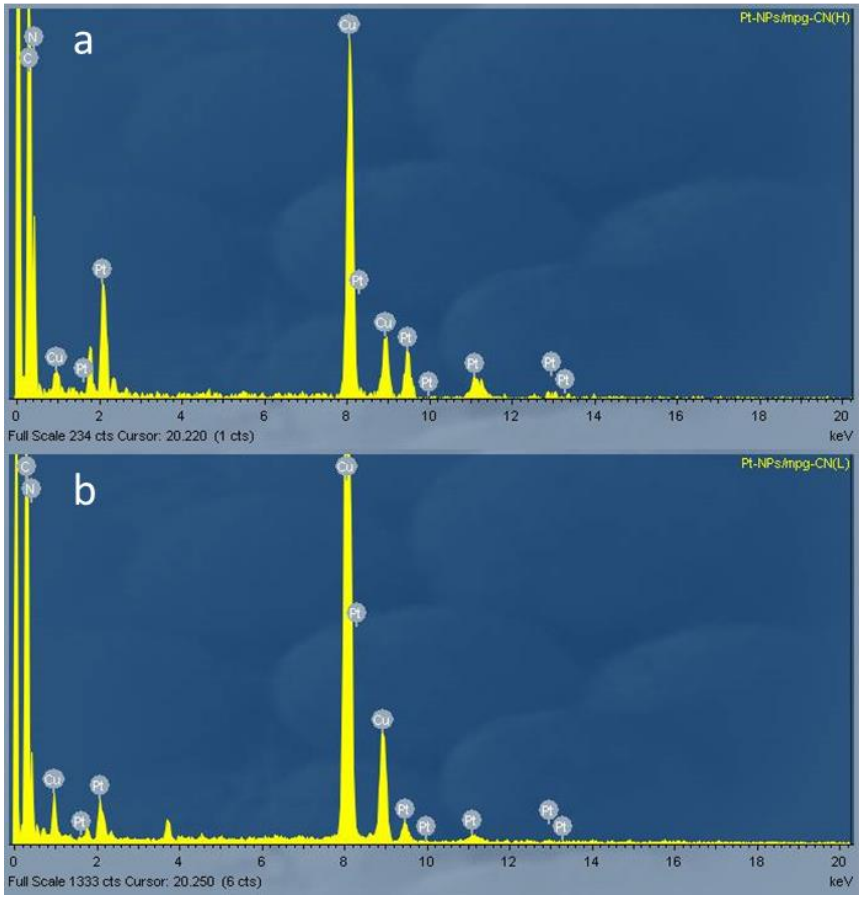

Figure S2. EDX analyses of a) **Pt-NPs@mpg-CN(H)** and b) **Pt-NPs@mpg-CN(L)** before the photocatalytic experiments.

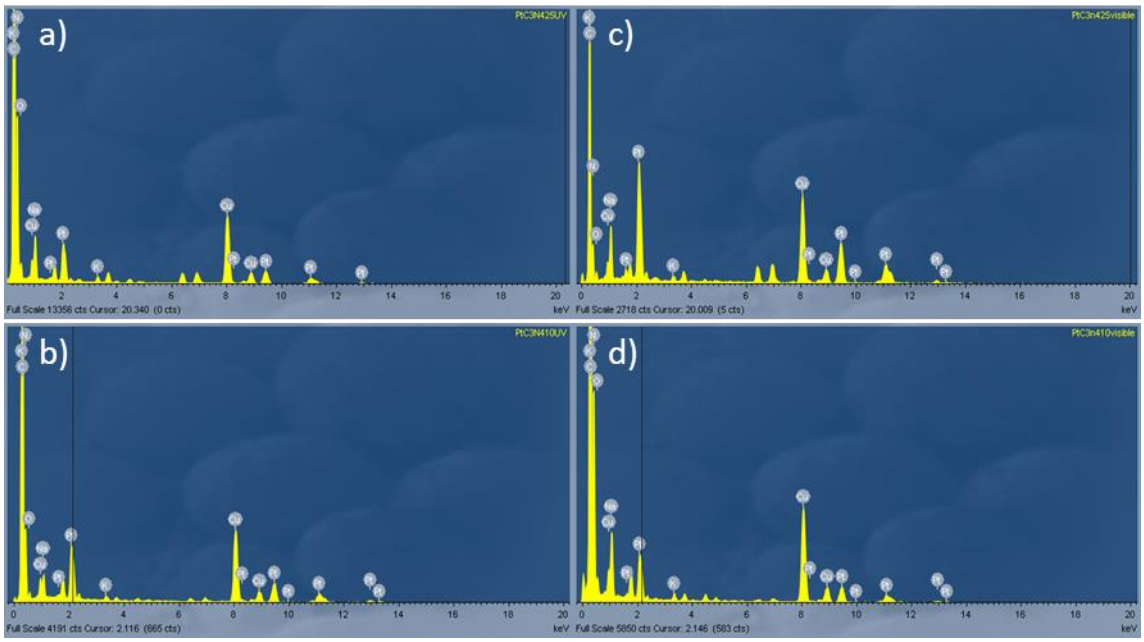

Figure S3. EDX analyses after photocatalytic studies of a) **Pt-NPs@mpg-CN(H)** and b) **Pt-NPs@mpg-CN(L)** under UV irradiation; c) **Pt-NPs@mpg-CN(H)** and d) **Pt-NPs@mpg-CN(L)** under visible irradiation

4.7 References

[1] Fu, J.; Jiang, K.; Qiu, X.; Yu, J. and Liu, M. "Product selectivity of photocatalytic CO2 reduction reactions" *Mater. Today*, **2020** (32) 222–43

[2] Leung, D. Y. C.; Caramanna, G. and Maroto-Valer, M. M. "An overview of current status of carbon dioxide capture and storage technologies" *Renew. Sustain. Energy Rev.*, **2014** (39) 426–43

[3] Centi, G.; Quadrelli, E. A. and Perathoner, S. "Catalysis for CO2 conversion: a key technology for rapid introduction of renewable energy in the value chain of chemical industries" *Energy Environ. Sci.*, **2013** (6) 1711

[4] Fu, Z.; Yang, Q.; Liu, Z.; Chen, F.; Yao, F.; Xie, T.; Zhong, Y.; Wang, D.; Li, J.; Li, X. and Zeng, G. "Photocatalytic conversion of carbon dioxide: From products to design the catalysts" *J. CO2 Util.*, **2019** (34) 63–73

[5] Ola, O. and Maroto-Valer, M. M. "Review of material design and reactor engineering on TiO2 photocatalysis for CO2 reduction" *J. Photochem. Photobiol. C Photochem. Rev.*, **2015** (24) 16–42

[6] Abdullah, H.; Khan, M. M. R.; Ong, H. R. and Yaakob, Z. "Modified TiO 2 photocatalyst for CO 2 photocatalytic reduction: An overview" *J. CO2 Util.*, **2017** (22) 15–32

[7] Inoue, T.; Fujishima, A.; Konishi, S. and Honda, K. "Photoelectrocatalytic reduction of carbon dioxide in aqueous suspensions of semiconductor powders [3]" *Nature*, **1979** (277) 637–8

[8] Fresno, F.; Villar-García, I. J.; Collado, L.; Alfonso-González, E.; Renones, P.; Barawi, M. and De La Pena O'Shea, V. A. "Mechanistic View of the Main Current Issues in Photocatalytic CO 2 Reduction" *J. Phys. Chem. Lett.*, **2018** (9) 7192–204

[9] Wang, Y.; He, D.; Chen, H. and Wang, D. "Catalysts in electro-, photo- and photoelectrocatalytic CO2 reduction reactions" *J. Photochem. Photobiol. C Photochem. Rev.*, **2019** (40) 117–49

[10] Shen, M.; Zhang, L.; Wang, M.; Tian, J.; Jin, X.; Guo, L.; Wang, L. and Shi, J. "Carbon-vacancy modified graphitic carbon nitride: enhanced CO 2 photocatalytic reduction performance and mechanism probing" *J. Mater. Chem. A*, **2019** (7) 1556–63

[11] Sun, S.; Gou, X.; Tao, S.; Cui, J.; Li, J.; Yang, Q.; Liang, S. and Yang, Z. "Mesoporous graphitic carbon nitride (g-C 3 N 4) nanosheets synthesized from carbonated beverage-reformed commercial melamine for enhanced photocatalytic hydrogen evolution" *Mater. Chem. Front.*, **2019** (3) 597–605

[12] Ong, W. J.; Tan, L. L.; Ng, Y. H.; Yong, S. T. and Chai, S. P. "Graphitic Carbon Nitride (g-C3N4)-Based Photocatalysts for Artificial Photosynthesis and Environmental Remediation: Are We a Step Closer to Achieving Sustainability?" *Chem. Rev.*, **2016** (116) 7159–329

[13] Kumar, S.; Karthikeyan, S. and Lee, A. "g-C3N4-Based Nanomaterials for Visible Light-Driven Photocatalysis" *Catalysts*, **2018** (8) 74

[14] Wang, A.; Wang, C.; Fu, L.; Wong-Ng, W. and Lan, Y. "Recent Advances of Graphitic Carbon Nitride-Based Structures and Applications in Catalyst, Sensing, Imaging, and LEDs" *Nano-Micro Lett.*, **2017** (9)

[15] Cao, S.; Huang, Q.; Zhu, B. and Yu, J. "Trace-level phosphorus and sodium co-doping of g-C 3 N 4 for enhanced photocatalytic H 2 production" *J. Power Sources*, **2017** (351) 151–9

[16] Ye, R. P.; Ding, J.; Gong, W.; Argyle, M. D.; Zhong, Q.; Wang, Y.; Russell, C. K.; Xu, Z.; Russell, A. G.; Li, Q.; Fan, M. and Yao, Y. G. "CO2 hydrogenation to high-value products via heterogeneous catalysis" *Nat. Commun.*, **2019** (10) 5698

[17] Wang, H.; Wang, Y.; Zhu, Z.; Sapi, A.; An, K.; Kennedy, G.; Michalak, W. D. and Somorjai, G. A. "Influence of Size-Induced Oxidation State of Platinum Nanoparticles on Selectivity and Activity in Catalytic Methanol Oxidation in the Gas Phase" *Nano Lett.*, **2013** (13) 2976–9

[18] Bhavani, K. S.; Anusha, T. and Brahman, P. K. "Platinum nanoparticles decorated on graphitic carbon nitride-ZIF-67 composite support: An electrocatalyst for the oxidation of butanol in fuel cell applications" *Int. J. Hydrogen Energy*, **2021** (46) 9199–214

[19] Wang, Y.; Arandiyan, H.; Scott, J.; Aguey-Zinsou, K. F. and Amal, R. "Single Atom and Nanoclustered Pt Catalysts for Selective CO 2 Reduction" *ACS Appl. Energy Mater.*, **2018** (1) 6781–9

[20] Amiens, C.; Ciuculescu-Pradines, D. and Philippot, K. "Controlled metal nanostructures: Fertile ground for coordination chemists" *Coord. Chem. Rev.*, **2016** (308) 409–32

[21] Kailasam, K.; Epping, J. D.; Thomas, A.; Losse, S. and Junge, H. "Mesoporous carbon nitride-silica composites by a combined sol-gel/thermal condensation approach and their application as photocatalysts" *Energy Environ. Sci.*, **2011** (4) 4668–74

[22] Thomas, A.; Fischer, A.; Goettmann, F.; Antonietti, M.; Müller, J. O.; Schlögl, R. and Carlsson, J. M. "Graphitic carbon nitride materials: Variation of structure and morphology and their use as metal-free catalysts" *J. Mater. Chem.*, **2008** (18) 4893–908

[23] Noomnarm, U. and Clegg, R. M. "Fluorescence lifetimes: fundamentals and interpretations" *Photosynth. Res.*, **2009** (101) 181–94

[24] López-Calixto, C. G.; Barawi, M.; Gomez-Mendoza, M.; Oropeza, F. E.; Fresno, F.; Liras, M. and De La Penã O'Shea, V. A. "Hybrids Based on BOPHY-Conjugated Porous Polymers as Photocatalysts for Hydrogen Production: Insight into the Charge Transfer Pathway" *ACS Catal.*, **2020** (10) 9804–12

[25] Maeda, K. and Domen, K. "Photocatalytic Water Splitting: Recent Progress and Future Challenges" *J. Phys. Chem. Lett.*, **2010** (1) 2655–61

[26] Creus, J.; Drouet, S.; Suriñach, S.; Lecante, P.; Collière, V.; Poteau, R.; Philippot, K.; García-Antón, J. and Sala, X. "Ligand-Capped Ru Nanoparticles as Efficient Electrocatalyst for the Hydrogen Evolution Reaction" *ACS Catal.*, **2018** (8) 11094–102

[27] De Tovar, J.; Romero, N.; Denisov, S. A.; Bofill, R.; Gimbert-Suriñach, C.; Ciuculescu-Pradines, D.; Drouet, S.; Llobet, A.; Lecante, P.; Colliere, V.; Freixa, Z.; McClenaghan, N.; Amiens, C.; García-Antón, J.; Philippot, K. and Sala, X. "Light-driven water oxidation using hybrid photosensitizer-decorated Co3O4 nanoparticles" *Mater. Today Energy*, **2018** (9) 506–15

[28] Yu, S.; Wilson, A. J.; Heo, J. and Jain, P. K. "Plasmonic Control of Multi-Electron Transfer and C–C Coupling in Visible-Light-Driven CO 2 Reduction on Au Nanoparticles" *Nano Lett.*, **2018** (18) 2189–94

[29] Collado, L.; Reynal, A.; Fresno, F.; Barawi, M.; Escudero, C.; Perez-Dieste, V.; Coronado, J. M.; Serrano, D. P.; Durrant, J. R. and de la Peña O'Shea, V. A. "Unravelling the effect of charge dynamics at the plasmonic metal/semiconductor interface for CO2 photoreduction" *Nat. Commun.*, **2018** (9) 4986

Chapter V

Graphitic Carbon Nitride-supported Metal Nanoparticles for Photocatalytic Hydrogen Evolution Reaction

Different hybrid materials, consisting of carbon nitride-supported Ru or Pt nanoparticles, have been prepared following the organometallic approach, with and without the stabilization of further carbon materials or 4-phenylpyridine ligand. After an in-depth characterization, all of the hybrid systems have been tested as photocatalysts in the reduction of H_2 under visible light irradiation. The effect of the co-catalyst load and the additional stabilization on the nanoparticles were revealed. Photophysical studies were also performed to elucidate on the different photocatalytic behaviours observed.

Table of contents

5.1 Abstract

Mesoporous graphitic carbon nitride (mpg-CN), a semiconductor typically employed in photo-induced catalytic reactions, has been used as infrastructure for the preparation of hybrid materials, either after mixing with Ru nanoparticles previously synthesized on carbon-based allotropes (nano)materials, or by direct deposition of metal nanoparticles (MNP; M= Ru or Pt), in both cases by the organometallic method. After fully characterizing the resulting **RuNPs@CNM/mpg-CN** and **MNP@mpg-CN** systems, these hybrid materials were used in the photocatalytic hydrogen evolution reaction (HER), displaying an enhanced performance, especially the Pt-decorated material, when compared with the bare mpg-CN without any co-catalyst addition. All Ru-based photocatalysts surprisingly delivered similar output in the HER, independently of the use or not of the CNM support or further stabilizing ligands (4-phenylpyridine). The use of CNM has shown to be useful in controlling the stability and dispersibility of the nanoparticles, while direct deposition on the semiconductor has simplified the preparation of the photocatalysts. Additional photophysical experiments, carried out with the **MNP@mpg-CN** samples, indicated that an improvement on the electron transfer kinetics (from the mpg-CN to the MNP) could be the reason behind the enhanced photocatalytic performance of the Pt-based material over the Ru-based analogues.

5.2 Introduction

As it has already been addressed in the previous chapters, there is a growing need to develop a cleaner, sustainable and carbon-free energy alternative to the fossil fuels, to minimize the effects of the climate change that humankind has already triggered, amid other economic and political issues derived from the fossil fuel dependence [1]. In this regard, hydrogen emerges as an ideal energy carrier able to meet the increasing energy needs of the population, but also requires a cleaner production strategy. Thus, artificial photosynthesis, which involves the storage of solar energy in the chemical bonds of a substance that can be used a fuel, has become a hot topic in the recent decades, with the aim of developing an environmentally sustainable energy supply [2].

The optimization of the light-driven water splitting reaction into molecular H_2 and O_2 is attracting crescent interest from energy researches [3]. This water splitting process can be divided into two half-reactions, the oxygen evolution reaction (OER) and the hydrogen evolution reaction (HER), requiring, in both cases, a suitable catalyst (or one for each half-reaction) in order to yield acceptable reaction rates.

Focusing just in the photocatalytic HER, besides the catalyst, a photoactive species is required, with the adequate bandgap to be visible-light responsive. This is important to note as many of the materials typically used are more active under UV irradiation, which only represents ca. 4 % of the solar radiation reaching Earth surface [4]. Graphitic carbon nitride emerges as a candidate as photoactive semiconductor material for its visible-light photo-responsive features, but needs a suitable co-catalyst to speed up the reaction, overcoming the undesired electron-hole recombination [5–7]. After harvesting (sun)light, excited electrons in the valence band (VB) of the semiconductor will move to the conduction band (CB), where, in the presence of the co-catalyst, will be used in the proton reduction to H_2. Pt, due to its outstanding performance for this reaction, even at low concentrations, is the most employed co-catalyst. However, there is an urgent need to look for equally efficient alternatives, due to its high cost, scarcity and low stability in alkaline environments [8,9]. In this context, Ru nanoparticles (NPs) have recently proven to be good substitutes for this process, with high catalytic activity and

stability in a wide range of pH, even under extreme acidic or alkaline conditions [10]. However, the application of Ru NPs in photocatalytic HER triggered by visible light has been hindered by the apparent inefficient electron transfer from the typical molecular photoactive species to the Ru NPs, which, in most cases, has been overcome by the use of a photosensitizer coupled with an electron mediator, such as methyl viologen or derivatives [11].

A key factor after the election of metal nanoparticles as the co-catalyst in the light-driven HER is its preparation, as surface environment, size, morphology, dispersibility and homogeneity of the selected NPs will play a role in their performance. Thus, the organometallic approach postulates as a powerful synthetic method, yielding small nanoparticles, with homogeneous size distribution and controlled surface state, under mild reaction conditions (generally at room temperature and under 3 bar of H_2), by the decomposition of an organometallic precursor in the presence of a stabilizing ligand or support [12,13]. This also facilitates to link the catalytic output of these systems with their physical and chemical features.

In this chapter, different hybrid materials were prepared using the photoactive mpg-CN semiconductor as stabilizer, following the organometallic method by two different approaches. The first set of hybrid materials were prepared by physically mixing mpg-CN with Ru NPs directly synthesized on the surface of different carbon allotropes (nano)nanomaterials (CNM = 0D carbon nanohorns, CNH; 1D single-walled carbon nanotubes, CNT; 2D reduced graphene oxide, rGO; and 3D graphite, GP). The second set was prepared by direct deposition of Ru, with and without further stabilizing pyridine-type ligand, and Pt NPs on the surface of mpg-CN. Both hybrid systems sets were tested as photocatalyst in the HER under visible light. Additionally, the latter set was utilized to carry out photophysical experiments with the aim of elucidate about their photocatalytic behaviour.

5.3 Experimental part

5.3.1 Reagents and materials

All procedures involving either handling the reagents and the preparation of the hybrid materials were performed under inert conditions (Ar), using a glovebox (MBRAUN Unilab) and/or standard Schlenk-line and Fisher-Porter bottle techniques. Glassware was dried prior to use at 120 °C. The following chemicals were used as purchased: [Ru(cod)(cot)] (cod = 1,5-cyclooctadiene; cot = 1,3,5-cyclooctatriene) from NanoMePS, [Pt(dba)$_3$] (dba = dibenzylideneacetone) from Strem Chemicals; 4-phenylpyridine (PP) from Sigma-Aldrich; Carbon Nanohorns (CNH) and flaked Graphite (GP) were purchased from Sigma-Aldrich; reduced graphene oxide (rGO) was synthesized by some collaborators from GP, following a previously reported methodology [14]; single-walled carbon nonotubes (CNT) were provided by SES ResearchM; hydrogen (H_2) gas from Abelló Linde; Mesoporous graphitic carbon nitride (mpg-CN) was prepared by the group of Prof. Arne Thomas (TU Berlin) as described in the following section. Tetrahydrofuran (THF) and hexane, purchased in Scharlab, were dried, distilled and degassed via freeze–pump–thaw cycles before using them as solvents.

5.3.2 Synthesis of mpg-CN

Synthesis of mesoporous graphitic carbon nitride (mpg-CN) was carried out via a sol-gel route, according to a procedure previously reported [15], based on the use of cyanamide and triethylorthosilicate as precursors, yielding a mixture of carbon nitride and silica. Treating this mixture with NH_4HF_2 and washing with water and ethanol lead to the removal of the SiO_2 template, obtaining the desired mpg-CN.

5.3.3 Synthesis of carbon-supported (CNH, CNT, rGO or GP) Ru-based nanoparticles

10 mg of the carbon material (either CNH, CNT, rGO or GP) were weighed and transferred into a Fisher-Porter bottle under inert conditions, with 40 mL of THF. The reactor was sonicated during 30 min before adding 40 mg (0.128 mmol) of [Ru(cod)(cot)] inside the glovebox. The Fisher-Porter bottle was then pressurized with 3 bar of H_2, and the reaction mixture was kept under vigorous stirring for 2 h

at room temperature. After evacuating the H_2 pressure, a sample for Transmission Electron Microscopy (TEM) analysis was prepared. The carbon-supported Ru NPs were cleaned with hexane and isolated after being centrifuged and dried under vacuum, yielding a black powder corresponding to each material, being **RuNP@CNH**, **RuNP@CNT**, **RuNP@rGO** or **RuNP@GP** depending on the carbon support employed.

5.3.4 Synthesis of mpgCN-supported Ru and Pt-based nanoparticles

200 mg of mpg-CN were placed into a Fischer-Porter bottle, together with 3.9 mg (0.013 mmol) of [Ru(cod)(cot)] (for **RuNP@mpg-CN** and for in-**RuPPNP@mpgCN**) or 11.3 mg (0.013 mmol) of $[Pt(dba)_3]$ (for **PtNP@mpg-CN**) and 16 mL of THF. Additionally, for **in-RuPPNP@mpgCN**, 0.4 mg (0.003 mmol) of 4-PP were dissolved in the solvent prior to the precursor addition. The reactor was used pressurized with 3 bar of H_2 at room temperature, and the reaction was kept under vigorous magnetic stirring for 16h. Hydrogen pressure was then removed, a TEM sample was prepared, and the hybrid materials were isolated by centrifugation, cleaned with hexane and dried under vacuum, obtaining a brownish powder for each sample.

For the preparation of the **ex-RuPPNP@mpgCN**, the same procedure as for **in-RuPPNP@mpgCN** was followed, but the mpg-CN material was not added until the H_2 pressure was removed. Then, the mixture was left stirring for 24 h, and the brownish powder corresponding to this hybrid material was recovered as described above.

5.3.5 Characterization techniques

Transmission Electron Microscopy (TEM), Energy-Dispersive X-ray spectroscopy (EDX), and Scanning Electron Microscopy-Field Emission Gun (SEM-FEG). Electron microscopy characterization was carried out in Servei de Microscòpia at the UAB. For the TEM analyses, a JEM-2011 unit with an acceleration voltage of 200 kV, equipped with an X-Max EDS detector with 136 eV energy resolution (Oxford Instruments) for the EDX analyses. SEM-FEG analyses were carried out in a MERLIN FE-SEM unit with an EDS detector model LINCA X-Max (Oxford Instruments). TEM samples were prepared by drop-casting method, depositing a single drop of the colloidal solution after synthesis on the surface of a

carbon-coated copper grid (400 mesh). TEM micrographs were treated with the Fiji-ImageJ image processing freeware, in order to obtain the size distribution of each Ru and Pt-based NPs system after measuring ca. 200 NPs. SEM-FEM samples were prepared by depositing the redispersed carbon-supported Ru-based NPs in a SEM specimen pin stub.

X-Ray Photoelectron Spectroscopy (XPS). Chemical composition of the (photo)catalyst was determined by XPS at Institut Català de Nanociència i Nanotecnologia (ICN2, Barcelona), using a Phoibos 150 analyzer (SPECS GmbH) at ultra-high vacuum conditions (base pressure of $5 \cdot 10^{-10}$ mbar), with a monochromatic aluminium Kα X-ray source (1486.74 eV). The energy resolution was measured by the FWHM of the Ag 3d5/2 peak, which for a sputtered silver foil was 0.62 eV. Samples were studied after synthesis and, in some cases, after photocatalytic experiments.

Inductively Coupled Plasma - Optical Emission Spectrometry (ICP-OES). The estimated concentrations (wt.%) of Ru or Pt on each metal-based carbon/mpg-CN supported system were determined using an ICP-OES equipment from Agilent (model Optima) at the Servei d'Anàlisi Química (SAQ) of the UAB.

X-ray Powder Diffraction (XRD). XRD patterns of the as-synthesised (photo)catalysts were obtained in the Servei Difracció Raigs X (SDRX) at the UAB, using a PANalytical X'Pert Pro Powder Diffraction with Cu Kα radiation and PIXcel^{1D} detector.

Specific Surface Area (SSA) determination. Surface area determination was carried out on a Quantachrome Autosorb-1 equipment. Nitrogen adsorption–desorption isotherms were measured at 77.350 K once samples were degassed at 120 °C for 6 h. SSAs were calculated applying the Brunauer-Emmett-Teller (BET) method.

5.3.6 Photocatalytic and photophysical experiments.

Photocatalytic tests in the screening reactor. Preliminary photocatalytic experiments were carried out with the RuNPs@CNH sample to adjust the optimal co-catalyst loading. 26.3 mg of 'pure' mpg-CN were physically mixed in a mortar with the selected amount of of RuNPs@CNH (ca. 0.16, 0.41, 0.81, or 1.62 mg) and the mixture was placed into the reactor (35 mL of effective volume, **Figure S1**), together with 20 mL of a 10 vol.% triethanolamine (TEOA) aqueous solution, which acted as the sacrificial electron donor (SED) for the reaction. The system was purged with argon during 10 minutes. The cell was closed with a septum and then irradiated using a Xenon lamp (L.O.T. Oriel QuantumDesign, with a 395 nm filter). The distance from the lamp to the reactor was 10 cm and the temperature of the reactor was controlled using a thermostat (Huber, ministat 125) set at 19 °C. After 4 h of irradiation, 8 mL of the gas confined in the headspace was collected with a syringe and analysed in a gas chromatograph, through two 4 mL injections, in order to determine the amount of hydrogen generated during the photocatalytic studies. The equipment used was a gas chromatograph from Agilent, model 7890 A, fitted with a Thermal Conductivity Detector (TCD). The column was a Carboxen 1000 unit, using argon as carrier gas. TON and TOF values were calculated by estimating the amount of Ru after mixing each sample with the mpg-CN, based on the ICP results for the RuNPs@CNM materials.

Photocatalytic tests in the standard reactor. 25 mg of 'pure' mpg-CN were physically mixed in a mortar with the selected amount of each RuNPs@CNM sample (ca. 0.15 or 0.39 mg) before placing them into the reactor (51.3 mL of effective volume; **Figure S2** and **Figure S3** for photocatalytic set-up and schematic representation of the reactor chamber, respectively). For the MNP@mpg-CN hybrid materials, ca. 26 mg of the samples were introduced in the reactor. The system was sealed with a lid made of quartz glass. The reactor was connected to a Schlenk-Line in order to purge the system under Ar. After that, 38 mL of a 10% TEOA aqueous solution as SED, previously degassed using argon, was added with a syringe through a channel on the top of the reactor with an argon counter current. The reactor chamber was then

irradiated with a Xenon lamp (L.O.T. Oriel QuantumDesign, with a 395 nm filter), and the mixture was kept under vigorous stirring of 24 h, at 30 °C (using a thermostat unit LAUDA ECO RE 630). The distance between the Xe lamp and the reactor was 10 cm. The pressure variation inside the reactor was measured using a pressure sensor (Type-P30, Δp = ±0.1, WIKA Alexander Wiegand SE & Co. KG). Since the temperature is a constant parameter, the amount of hydrogen produced can be determined through the ideal gas equation. Additionally, the amount of H_2 generated was determined also by GC, using the same procedure described for the screening reactor. TON and TOF values were calculated by estimating the amount of Ru after mixing each sample with the mpg-CN, based on the ICP results for the RuNPs@CNM materials. In the case of the MNP@mpg-CN, the amount or Ru was estimated directly using the ICP analyses of the samples.

Stability tests. A third set-up was employed to carry out the stability experiments for the mpg-CN directly supporting Pt or Ru-based NPs (**Figure S4**). In this case, the set-up configuration consisted on a glass-cell thermostated at 25 °C, containing 4 mL of 10% TEOA aqueous solution as SED, in which the selected photocatalyst was dispersed. A septum was used to seal the cell. Hydrogen evolution was monitored using a Clark hydrogen electrode (Unisense H2-NP-9463), whose tip was introduced in the cell through the septum, using grease to ensure the correct sealing of the system. The reaction mixture was purged using Ar for at least 10 min or until stabilization of the signal from the Clark electrode. The cell was then irradiated using a solar simulator (Abet 10500), consisting on a Xe lamp placed at exactly 1 sun (100 $mW \cdot cm^{-2}$) distance. Once the stability test was over, the system was again purged using Ar, and the amount of H_2 was determined after calibration, injecting known volumes of (e.g., 50, 100, 150, 200, 250, 300, 350 and 400 µL) of H_2. The amount of H_2 in µmols were estimated with the ideal gas law.

Photophysical tests. All experiments and data treatment involving the photophysical studies of the samples were carried out by Dr. Mirco Natali from the University of Ferrara (Ferrara, Italy). Absorption spectra in diffuse-reflectance mode were recorded in a Jasco V-570 spectrophotometer using an integrating

sphere setup. A spectrofluorometer from Edinburgh Instrument was employed to perform the steady-state luminescence measurements. Time-resolved emission measurements were carried out in a TC-SPC (Time-Correlated Single Photon Counting) unit (PicoQuant Picoharp 300) equipped with a sub-nanosecond LED source (380 nm, 500–700 ps pulse width) with a variable (2.5–40 MHz) pulsed power supply (PicoQuant PDL 800-B). PicoQuant FluoFit Global Fluorescence Decay Analysis Software was used to analyse the decays. Transient absorption measurements were carried out in a custom laser spectrometer comprised of a Continuum Surelite II Nd:YAG laser (FWHM 6 – 8 ns) with frequency tripled (355 nm) option, a Xe lamp (Applied Photophysics) including a mod. 720 150W lamp housing, a mod. 620 power-controlled lamp supply and a mod. 03 –102 arc lamp pulser. Laser excitation was carried out at 90° with respect to the white light probe beam. Light transmitted by the sample was focused onto the entrance slit of a 300 mm focal length Acton SpectraPro 2300i triple grating, flat field, and double exit monochromator fitted with a photomultiplier detector (Hamamatsu R3896). Signals from the photomultiplier were processed using TeledyneLeCroy 604Zi (400 MHz, 20 GS/s) digital oscilloscope. The excitation pulse (355 nm wavelength) was defocused using a diverging lens and set to an average energy of ~5 mJ/pulse using a combination of neutral density filters (Edmund Optics).

5.4 Results and discussion

5.4.1 Synthesis and characterization of carbon-supported (CNH, CNT, rGO or GP) Ru-based nanoparticles

Ruthenium nanoparticles (Ru NPs) have been synthesized using four different carbon (nano)materials (CNM) as stabilizing surfaces, namely 0D carbon nanohorns (CNH), 1D carbon nanotubes (CNT), 2D reduced graphene oxide (rGO) and 3D graphite (GP) (structures displayed in **Figure 1**), following the organometallic approach as synthetic method [12]. The preparation of the Ru NPs was carried out in a Fisher-Porter reactor, by hydrogenation of the organometallic Ru precursor [Ru(cod)(cot)] in mild conditions (3 bar or H_2 and room temperature, for 2 h). THF was used as solvent and the selected carbon material was present in the medium since the start of the reaction (**Figure 2**). After removing the hydrogen pressure, a sample for TEM analysis was prepared, and the resulting materials were cleaned with hexane, isolated by centrifugation and dried under vacuum, yielding a black powder corresponding to either **RuNPs@CNH**, **RuNPs@CNT**, **RuNPs@rGO** or **RuNPs@GP** depending on the carbon support used.

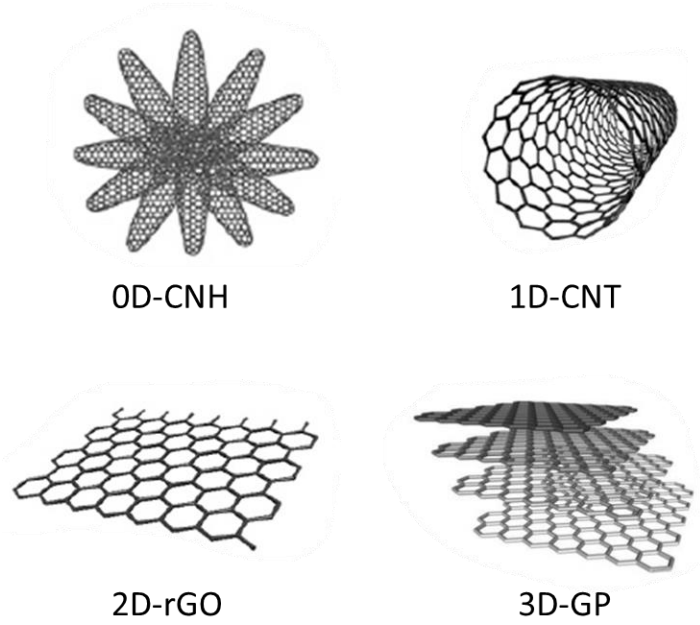

Figure 1. Chemical structures of the different carbon materials used as supports in the synthesis of the Ru NPs-based materials: 0D carbon nanohorns (CNH), 1D carbon nanotubes (CNT), 2D reduced graphene oxide (rGO) and 3D graphite (GP). Based on reference [16].

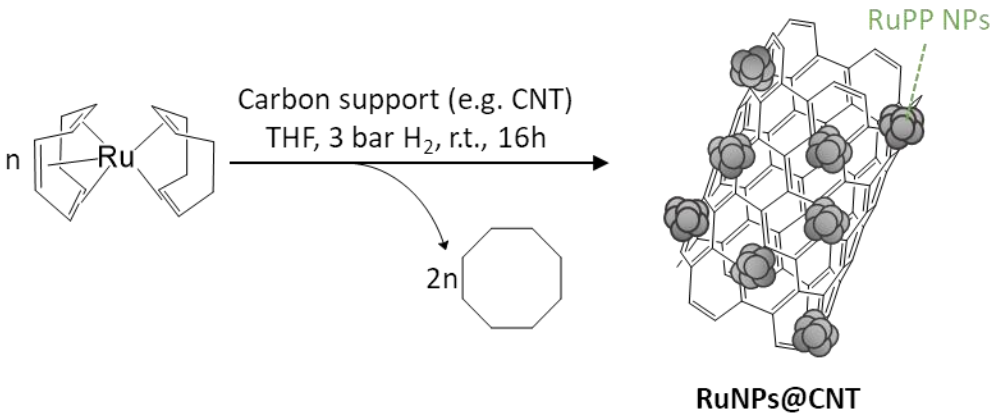

Figure 2. Organometallic approach for the synthesis of **RuNPs@CNM**, using CNT material as example.

TEM analyses of the four samples revealed the presence of tiny NPs on the surface of each CNM (**Figure 3**). For the CNH and the CNT, isolated Ru NPs were partially covering the surface of the carbon material, whereas the surface of rGO and GP were totally covered by NPs, observing even a slight agglomeration. This could be explained considering that, for the same amount of CNM, the total surface area is higher for the 0D (CNH) and 1D (CNT) materials than for the 2D and 3D materials (rGO and GP respectively). The nanoparticles were manually measured from each micrograph being the estimated mean sizes, in ascending order, of: 1.3 nm (CNH), 1.5 nm (rGO), 2.0 nm (GP), and 2.3 nm (CNT). Although the size of the nanoparticles could be affected by the nature of the carbon material, it does not differ much between the different samples.

The experimental Ru loading (wt.%) on each CNM was estimated by ICP-OES, resulting in 42, 41, 37 and 32 wt.% of Ru for **RuNPs@CNH**, **RuNPs@CNT**, **RuNPs@rGO** and **RuNPs@GP**, respectively, an interesting result considering that the increase in the surface to volume ratio of the CNM is accompanied by an increase in the metal load.

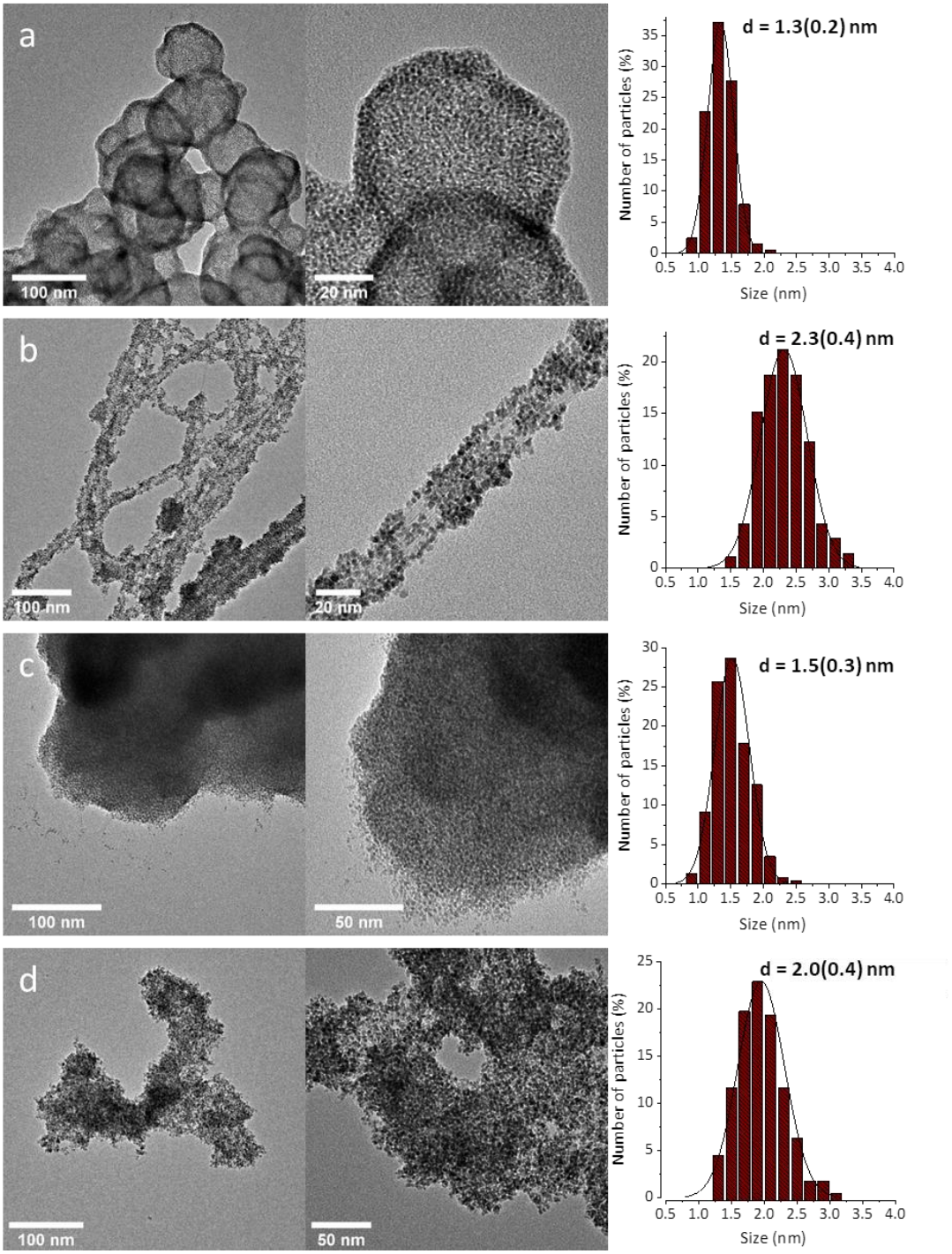

Figure 3. TEM micrographs and size distribution of Ru NPs supported on a) CNH, b) CNT, c) rGO and d) GP.

XPS measurements led to an in-deep understanding of the chemical composition of the samples (**Figure 4**). For all samples, two Ru species could be encountered, Ru^0 ($3d_{5/2}$ peak at 279.8 eV, $3d_{3/2}$ peak at 284.0 eV) and Ru^{IV} ($3d_{5/2}$ peak at 280.8 eV, $3d_{3/2}$ peak at 285.0 eV). Additionally, other peaks could be found in the spectra (centered at ca. 284.0 and 290.3 eV), which can be attributed to aliphatic, aromatic

and partially oxidized C atoms. The presence of the Ru^{IV} species was ascribed to the partial oxidation of the metallic Ru on the surface of the NPs to RuO_2, a behaviour already observed for Ru NPs prepared following the organometallic approach [17]. In this case, the Ru NPs required a controlled passivation process, analogous for the ligand-stabilized Ru NPs presented in Chapter III, in order to avoid the directly air exposure of the nanoparticles and their subsequent burning. As this behaviour was not observed with these hybrid materials, the reductive properties of the CNM were thought to be responsible of preventing the rapid oxidation of the nanoparticles.

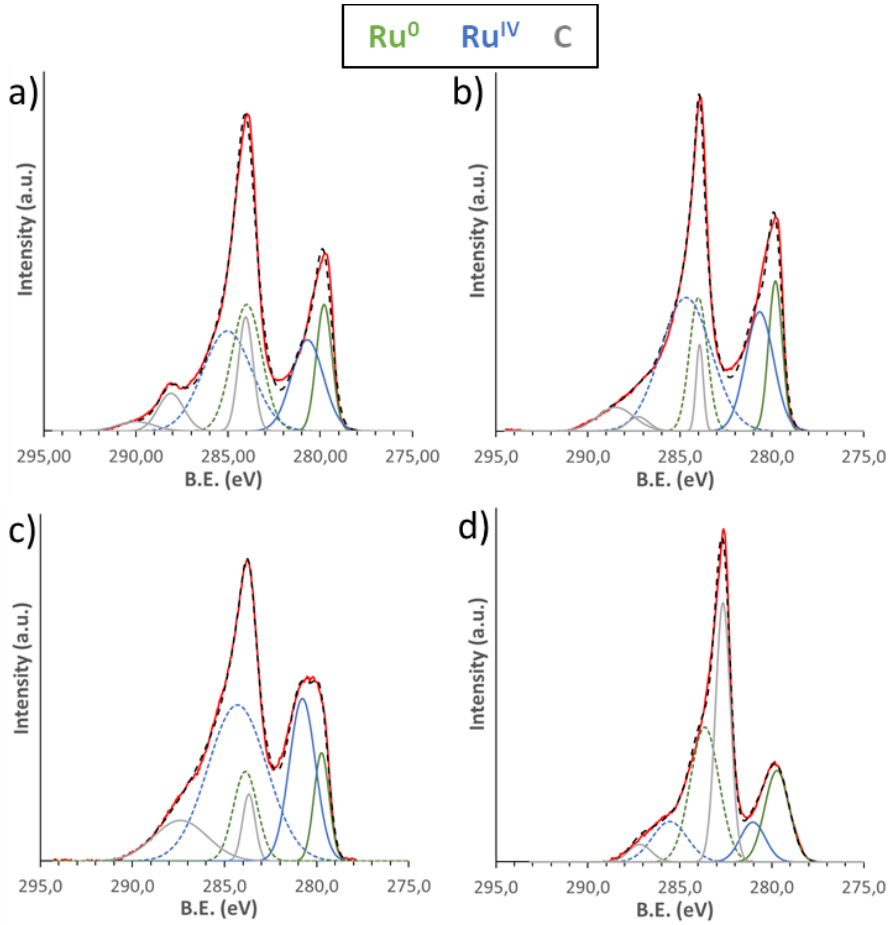

Figure 4. XPS spectra corresponding to a) **RuNPs@CNH**, b) **RuNPs@CNT**, c) **RuNPs@rGO** and d) **RuNPs@GP** after synthesis. In red, the experimental XPS spectra. Fit for the signals: green lines, metallic-Ru components (Ru 3d); blue lines, Ru^{IV} components (Ru 3d); grey lines, carbon components. Dashed black lines, envelope.

Further characterization was performed on these samples after mixing the RuNPs@CNM for their use as co-catalysts with the mpg-CN semiconductor. For the preliminary tests in the standard reactor, 26.3 mg of mpg-CN were mixed with four

different loads of each RuNPs@CNH sample (0.16, 0.41, 0.81, or 1.62 mg, with a final Ru wt.% in each case, estimated using the ICP values, of ca. 0.26, 0.63, 1,24 and 2,39 wt.%). Specific surface areas (S_{BET}) measurements were performed, confirming a decrease in the measured SSAs values after loading mpg-CN with each RuNPs@CNM. S_{BET} decreased from 134.3 $m^2 \cdot g^{-1}$ for the 'pure' mpg-CN to 83.1 $m^2 \cdot g^{-1}$ for the lower load in **RuNPs@CNT/mpg-CN** sample (0.16 mg), or 49.7 $m^2 \cdot g^{-1}$ with a higher load (0.39 mg) of the same material. Similar tendencies were observed for the rest of the samples (**Figure S5, Table S1**), thus suggesting the partial blocking of the mesopores of the mpg-CN material after the co-catalyst loading.

SEM-FEG micrographs (**Figure S6a** to **Figure S9a**) showed the presence of big mpg-CN particles (> 1 µm), partially covered by the corresponding RuNPs@CNM materials, which could be observed as white dots because of the use of a backscattered-electrons detector. EDX analyses confirmed the presence of Ru in the surface of these RuNPs@CNM/mpg-CN hybrid materials (**Figure S6b** Figure **S9b**). Finally, Powder XRD patterns confirmed the crystallinity of mpg-CN after loading each co-catalyst (0.16 mg), although the low Ru concentration (0.63 µmol) prevented the observation of any reflection corresponding to the metal NPs (**Figure 5**).

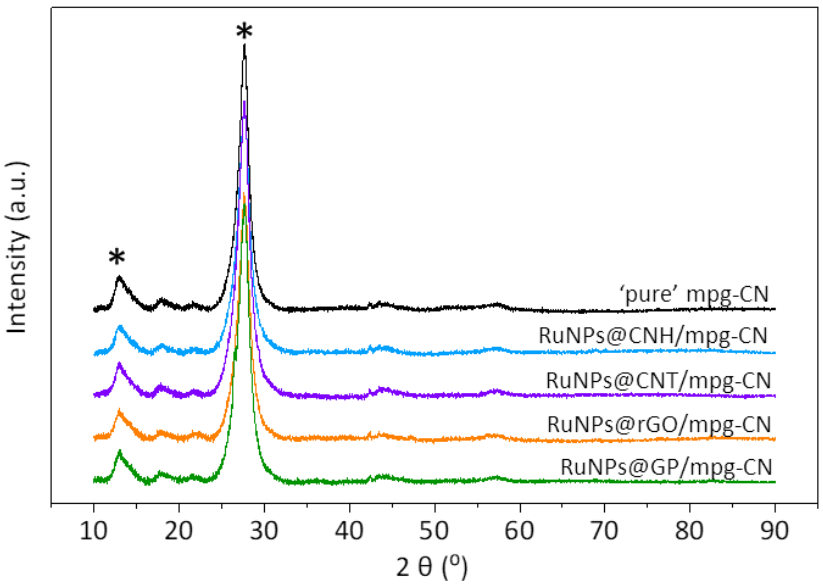

Figure 5. X-ray difractograms of 'pure' mpg-CN (black), **RuNPs@CNH/mpg-CN** (blue), **RuNPs@CNT/mpg-CN** (purple), **RuNPs@rGO/mpg-CN** (orange) and **RuNPs@GP/mpg-CN** (green). (*) indicates typical signals of mpg-CN.

5.4.2 Synthesis and characterization of mpg-CN-supported Pt and Ru-based nanoparticles

The photoactive mpg-CN semiconductor served as support for the preparation of four different hybrid materials, after depositing metal nanoparticles (MNP, M = Ru or Pt) through the organometallic approach [12] (**Figure 6**). The preparation of the mpg-CN supported Pt NPs was already described in Chapter IV. Essentially, the metal precursor, either [Ru(cod)(cot)] or [$Pt(dba)_3$], was placed in the Fisher-Porter reactor together with THF as solvent and mpg-CN as support for the preparation of the MNP. For the *in-situ* preparation of Ru NPs stabilized by 4-phenylpyridine (PP), the ligand was previously dissolved in the THF before the precursor addition. The reactor was pressurized then with 3 bar of H_2 and the mixture was left at room temperature and under vigorous stirring for 16 h, yielding either **RuNP@mpg-CN** (Ru NPs directly stabilized onto mpg-CN surface), **in-RuPPNP@mpg-CN** (Ru NPs directly stabilized onto mpg-CN surface with additional 4-PP stabilization), or **PtNP@mpg-CN** (Pt NPs directly stabilized onto mpg-CN surface). The fourth system consisted on an *ex-situ* preparation of RuPP NPs (this NPs were already reported by our group [17]). The obtained colloidal solution was used to impregnate the surface of the mpg-CN, obtaining the **ex-RuPPNP@mpg-CN** sample. In all cases, a TEM sample was prepared before washing the hybrid materials with hexane, and centrifuging and drying the samples under vacuum.

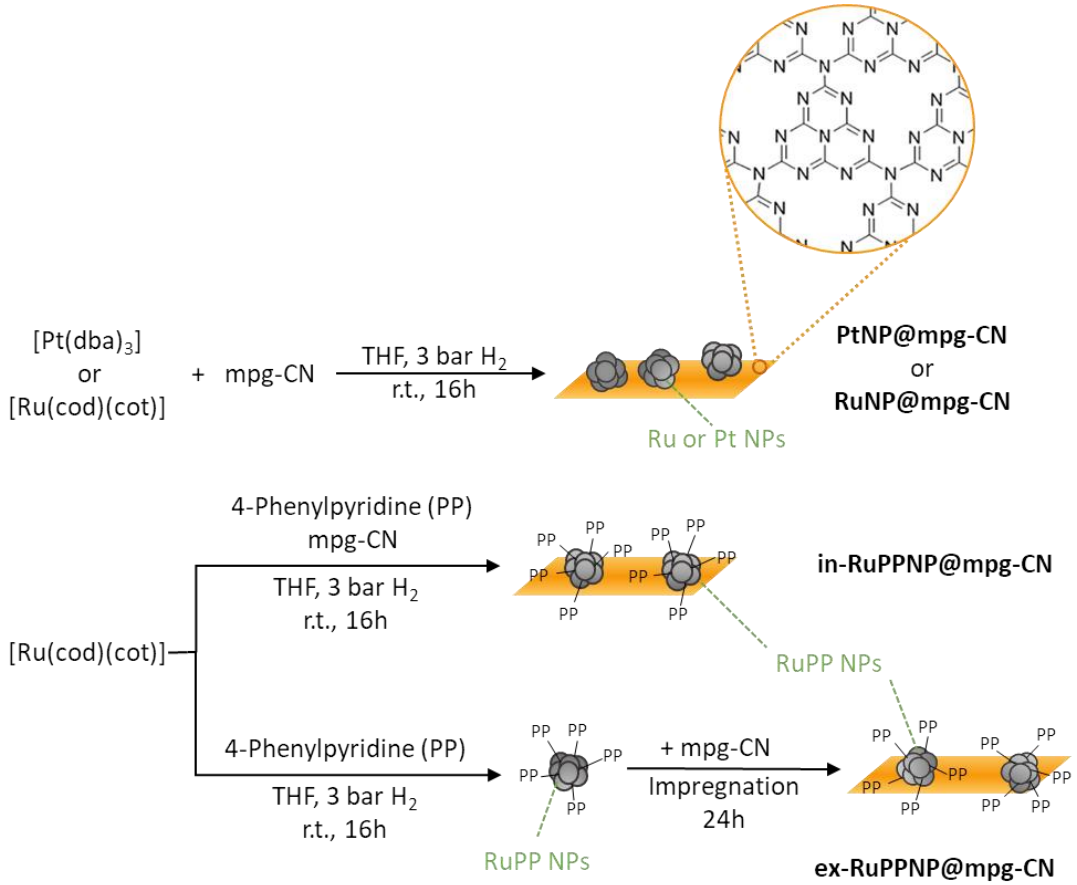

Figure 6. Organometallic approach for the preparation of Pt and Ru-based NPs supported by mpg-CN.

TEM micrographs (**Figure 7**) confirmed the presence of small Pt NPs on the surface of the mpg-CN for the **PtNP@mpg-CN** (as already seen in Chapter IV, where this sample was labelled as Pt-NPs@mpg-CN(H)), with a mean size of 2.7 ± 0.5 nm. Similar results were observed with the **RuNP@mpg-CN** (2.9 ± 0.9 nm). When the 4-phenylpyridine ligand is introduced into the synthesis, a decreased in the size of the Ru NPs was observed for the **in-RuPPNP@mpg-CN** system (1.6 ± 0.4 nm), due to the extra stabilization provided by the PP ligand. However, a certain level of aggregation was observed, suggesting the higher affinity of the Ru precursor towards the PP ligand than to the surface of the mpg-CN. Thus, once the NPs have been formed, their access into the small pores of the mpg-CN would be restrained, leading to the formation of aggregates on the surface of the semiconductor. The same trend was observed for the **ex-RuPPNP@mpg-CN**, yielding smaller nanoparticles (1.7 ± 0.3 nm) but forming agglomerates after the impregnation on the surface of the mpg-CN. Some isolated nanoparticles could be observed for both

of the PP-stabilized systems, but to a lesser extent than **RuNP@mpg-CN**. EDX confirmed the presence of Ru in these three systems (**Figure S10**, for **PtNP@mpg-CN** the analysis was already shown in Chapter IV).

The experimental load of Ru and Pt (wt.%) was measured by ICP-OES, which determined a metal content of 0.52, 0.69, 0.55 and 1.2 wt.% for **RuNP@mpg-CN**, **in-RuPPNP@mpg-CN**, **ex-RuPPNP@mpg-CN**, and **PtNP@mpg-CN** respectively, while the expected values were 0.6 wt.% for the Ru-based hybrid materials and 1.2 wt.% for the Pt-based one (note that these theoretical concentrations were considered to obtain equimolar percentages), confirming a comparable molar concentration of metal in all samples.

Powder XRD analyses were performed for all the samples and the obtained diffractograms were compared to that of 'pure' mpg-CN (**Figure 8**). As described in Chapter IV for the **PtNP@mpg-CN**/Pt-NPs@mpg-CN(H) sample, two peaks centred at 13.1˚ and 27.4˚ were observed, thus confirming the crystallinity of mpg-CN after, in this case, Ru loading. No reflections corresponding to the metal were observed, due to the low Ru concentration.

Specific surface areas (S_{BET}) measurements were carried out to monitor possible changes in the structural properties of the mpg-CN after depositing the Pt or Ru-based NPs. Whereas 'pure' mpg-CN displayed a specific surface area of 147 $m^2 \cdot g^{-1}$, thus confirming its mesoporosity nature, a decrease in the S_{BET} values was observed for each metal-loaded mpg-CN hybrid materials (102 $m^2 \cdot g^{-1}$ for **RuNP@mpg-CN**; 134 $m^2 \cdot g^{-1}$ for **in-RuPPNP@mpg-CN**; 89 $m^2 \cdot g^{-1}$ for ex-**RuPPNP@mpg-CN** and 110 $m^2 \cdot g^{-1}$ for **PtNP@mpg-CN**), probably derived from the partial blocking of the mesopores of the mpg-CN.

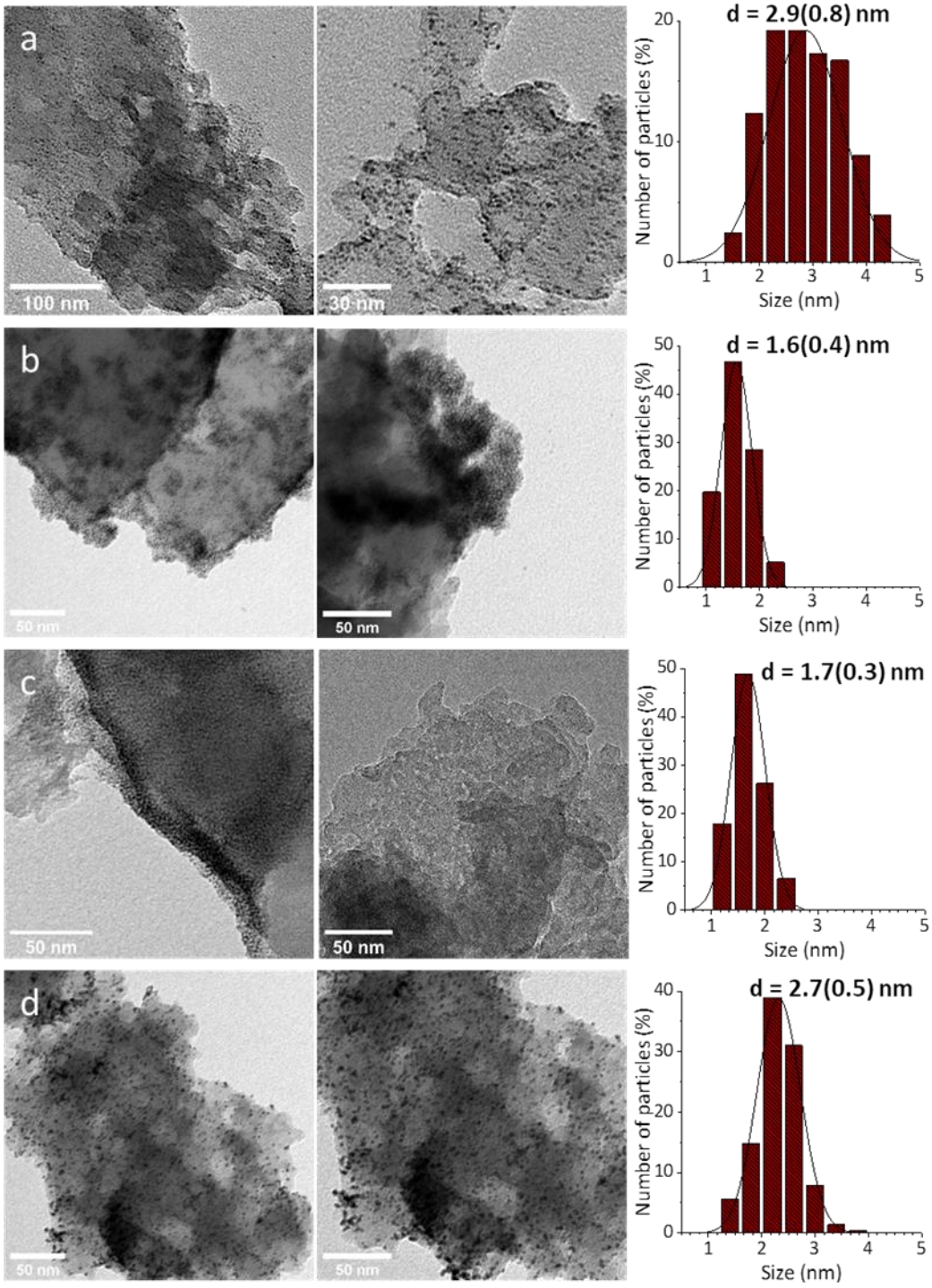

Figure 7. TEM micrographs and size distributions of a) **RuNP@mpg-CN,** b) **in-RuPPNP@mpg-CN**, c) **ex-RuPPNP@mpg-CN** and d) **PtNP@mpg-CN**

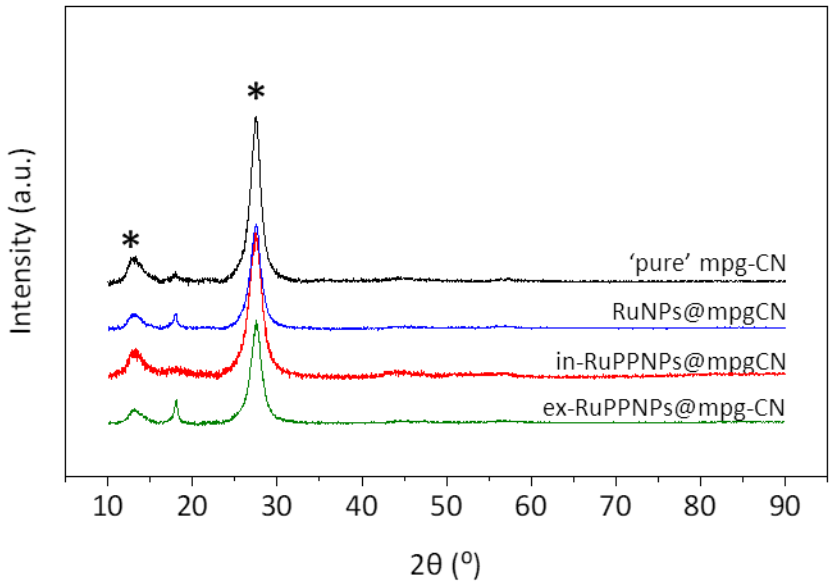

Figure 8. X-ray difractograms of 'pure' mpg-CN (black), **RuNP@mpg-CN** (blue), **in-RuPPNP@mpg-CN** (red), **ex-RuPPNP@mpg-CN** (green). (*) indicates typical signals of mpg-CN.

5.4.3 Photocatalytic HER in the screening reactor

In order to have an idea of the H_2 evolved by the hybrid materials, a screening test was performed with RuNPs@CNH/mpg-CN. The photocatalytic experiments were carried out under visible light irradiation ($\lambda > 395$ nm), using a 300 W Xe lamp in the screening quartz glass reactor (**Figure S1**) with 10% TEOA aqueous solution as SED. The amount of hydrogen generated was measured by GC by collecting an aliquot from the headspace of the reactor after 4 h of photoreaction (**Table 1, Figure 9**). This screening was performed to optimize the co-catalyst loading. The aim is to achieve a balance between better catalytic performance (increasing the amount of co-catalyst is beneficial) and prevention of the darkening of the mpg-CN material (increasing the amount of co-catalyst is detrimental). For these screening tests, different loads (0.16, 0.41, 0.81, or 1.62 mg) of the **RuNPs@CNH** were incorporated to 26.3 mg of mpg-CN. The amount of Ru present in each sample (**Table 1)** expressed in µmol in order to calculate TON values was determined based on the estimated values of Ru wt.% (0.26, 0.63, 1,24 and 2,39 wt.%, respectively). Noteworthy is the fact that the use of 'pure' mpg-CN, **RuNPs@CNH**

without mpg-CN or bare-CNH mixed with mpg-CN led to negligible hydrogen production (**Figure 9** and **Table 1**, entries 1, 2, 3, respectively).

Thus, regarding the **RuNPs@CNH/mpg-CN** samples with different metal loadings, the best photocatalytic results in terms of H_2 production were attributed to the two lowest Ru concentrations. Whereas the sample **RuNPs@CNH/mpg-CN(b)** led to the highest hydrogen production (41.0 µmol of H_2 with 1.69 µmol of Ru; **Table 1**, entry 5), **RuNPs@CNH/mpg-CN(a)** sample (36.2 of H_2 produced with 0.68 µmol of Ru; **Table 1**, entry 4) delivered the fastest photocatalytic reaction, regarding TON and TOF values. Contrary, worse results were obtained with the two highest Ru loadings in the mpg-CN material (31.9 and 10.6 µmol of hydrogen produced, with Ru loadings of 3.38 and 6.75 µmol; entries 6 and 7 in **Table 1** respectively). An explanation for this behaviour would be that, for the higher **RuNPs@CNH** loading, the excessive darkening of the **RuNPs@CNH/mpg-CN** hybrid material prevents light from reaching the surface of the semiconductor, thus decreasing the hydrogen photogeneration. The darkening is also observed by the naked eye (**Figure 10**)

Entry	mpg-CN (mg)	RuNPs@CNH (mg)	Ru (µmol)	H_2 (µmol)	H_2 evol. rate (µmol/g·h)[b]	TON[c] (-)	TOF[c] (h^{-1})
1	26.3	-	–	1.6	17	–	–
2	-	1.62	6.75	-	-	–	–
3	26.3	1.51[a]	–	0.5	5	–	–
4	26.3	0.16	0.68	36.2	340	53	13.3
5	26.3	0.41	1.69	41.0	420	24	6.1
6	26.3	0.81	3.38	31.9	324	9	2.4
7	26.3	1.62	6.75	10.6	105	2	0.4

Table 1. Photocatalytic H_2 production carried out in the screening reactor, under visible light irradiation (300 W Xe lamp; $\lambda > 395$ nm), during 4 h, using TEOA (10%) as SED, for different loads of **RuNPs@CNH**. ([a] only CNH as co-catalyst; [b] µmol of H_2 released per hour and per g of catalyst (including mpg-CN and RuNPs@CNH if applicable); [c] TON and TOF calculated considering molar concentration of Ru).

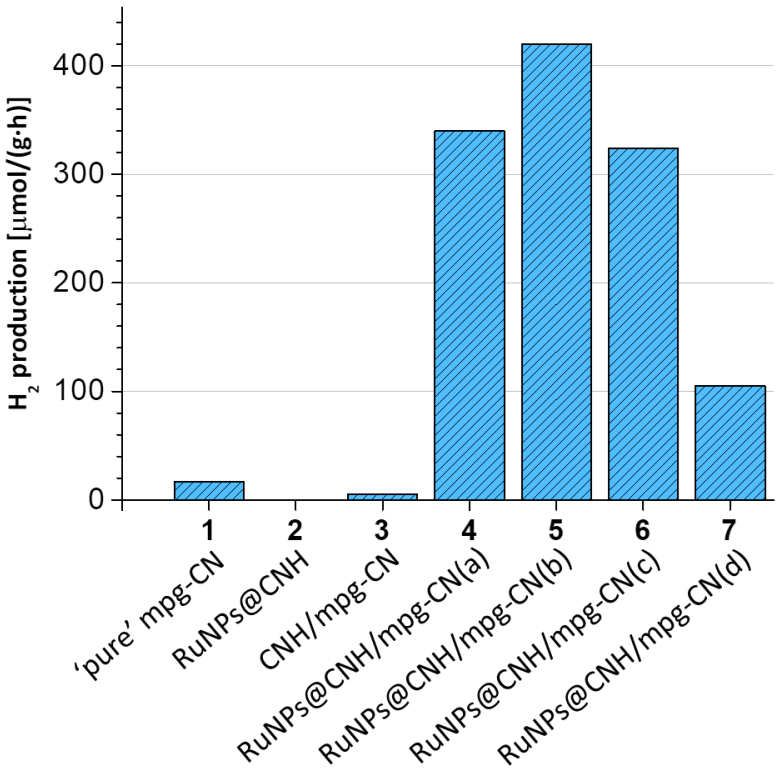

Figure 9. Hydrogen production after the photocatalytic experiments performed in the screening reactor, under visible light irradiation (300 W Xe lamp; λ > 395 nm), during 4 h, using TEOA (10%) as SED, using different loads of **RuNPs@CNH** in mpg-CN. Total Ru content in **RuNPs@CNH/mpg-CN** samples: a) 0.68 µmol, b) 1.69 µmol, c) 3.38 µmol and d) 6.75 µmol.

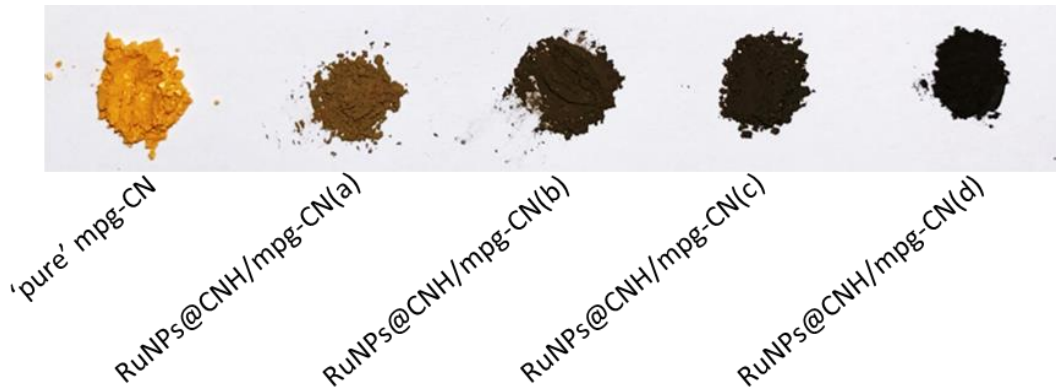

Figure 10. Darkening observed for the **RuNPs@CNT/mpg-CN** samples with diferent RuNPs@CNT loads, from a) the lowest to d) the highest load, compared to the bare mpg-CN.

5.4.4 Photocatalytic HER in the standard reactor

Further photocatalytic experiments were performed for RuNPs@CNM/mpg-CN and MNP@mpg-CN after optimizing the co-catalyst loading. Starting from the former, Ru concentrations of 0.68 μmol (indicated by letter *a* in **Table 2**) and 1.69 μmol (indicated by letter *b* in **Table 2**) were selected for the different **RuNPs@CNM/mpg-CN** materials, prepared by mixing the corresponding amount of RuNPs@CNM with 25 mg of mpg-CN. All samples were placed in the standard reactor (**Figure S2**) with 38 mL of TEOA (as electron donor) and irradiated under visible light, using a 300 W Xe lamp (λ > 395 nm) during 24 h. Hydrogen evolution rate (**Table 2** and **Figure 11**) was measured from the slope of the "mol of H_2 vs. time" curves (**Figure S11**), expressed per hour and per g of photocatalyst ($\mu mol \cdot h^{-1} \cdot g^{-1}$). The total amount of H_2 generated was confirmed by GC. TON values were calculated at 24 h considering the total amount of Ru present in each sample (**Table 2** and **Figure 11**).

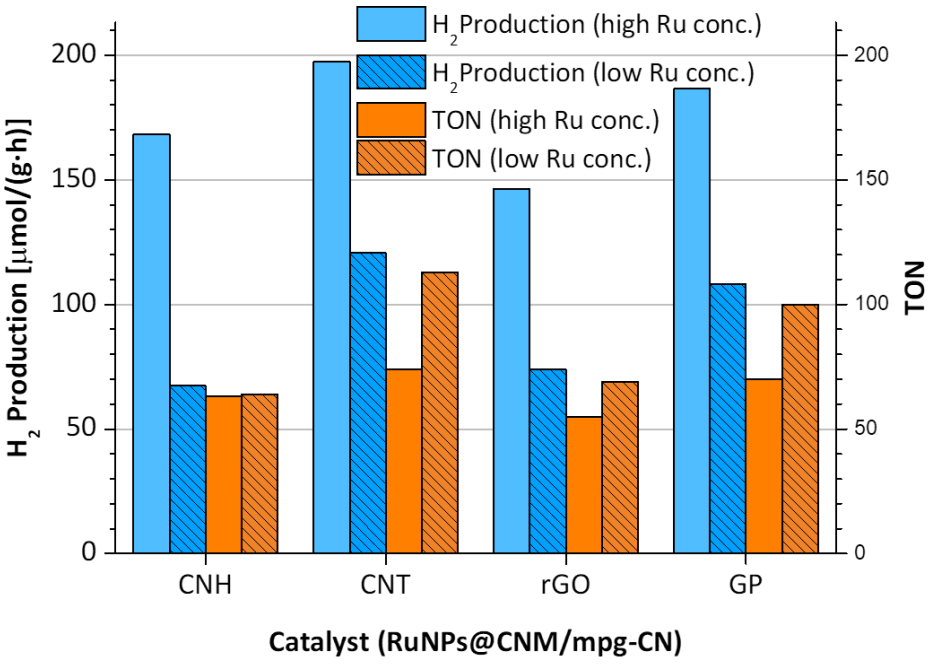

Figure 11. Photocatalytic hydrogen production and TON (considering total μmol of Ru in the hybrid materials) calculated after 24 h of visible light irradiation (300 W Xe lamp; λ > 395 nm, 10% TEOA as SED) for the **RuNPs@CNM/mpg-CN** (CNM = CNH, CNT, rGO or GP) samples. Higher Ru load: 1.69 μmol. Lower Ru load: 0.68 μmol.

Entry	Hybrid Material	RuNPs @CNM (mg)	Ru (μmol)	H_2 evol. rate ($\mu mol \cdot h^{-1} \cdot g^{-1}$)[a]	H_2 (μmol)	TON[b] (-)	TOF[b] (h^{-1})
1	mpg-CN	–	–	2.0	1.2	–	–
2	RuNPs@CNH/mpg-CN (b)	0.15	0.63	67.4	40.1	64	2.7
3	RuNPs@CNH/mpg-CN (a)	0.39	1.62	168.3	101.3	63	2.6
4	RuNPs@CNT/mpg-CN (b)	0.16	0.64	120.6	72.5	113	4.7
5	RuNPs@CNT/mpg-CN (a)	0.39	1.60	197.4	118.0	74	3.1
6	RuNPs@rGO/mpg-CN (b)	0.18	0.64	73.8	44.3	69	2.9
7	RuNPs@rGO/mpg-CN (a)	0.44	1.60	146.5	87.4	55	2.3
8	RuNPs@GP/mpg-CN (b)	0.21	0.65	108.2	65.1	100	4.2
9	RuNPs@GP/mpg-CN (a)	0.51	1.60	186.6	112.9	70	2.9

Table 2. Photocatalytic H_2 production conducted in the standard reactor, under visible light irradiation (300 W Xe lamp; $\lambda > 395$ nm), during 24 h, in the presence of 38 mL of TEOA (10%) as SED, for the different **RuNPs@CNM/mpg-CN** (CNM = CNH, CNT, rGO or GP; mixed with 25 mg of mpg-CN) with two different Ru loadings: (a) means low loading and (b) high loading. ([a] μmol of H_2 released per hour and per g of catalyst (hybrid material); [b] TON and TOF calculated at 24 h considering the molar concentration of Ru).

In all cases, the highest amount of hydrogen was produced when using the highest Ru loading (**Table 2**, entries 3, 5, 7 and 9), in agreement with the results obtained from the screening reactor. The best results with the standard reactor, in terms of hydrogen generation after 24 h, have been obtained with the **RuNPs@CNT/mpg-CN** (118.0 μmol of H_2; **Table 2**, entry 5) and the **RuNPs@GP/mpg-CN** (112.9 μmol of H_2; **Table 2**, entry 9) samples. Nevertheless, the material with the lowest performance using the same Ru load, which corresponds to **RuNPs@rGO/mpg-CN** (87.4 μmol of H_2; **Table 2**, entry 7) generates only ca. 25% less hydrogen than the top-performance material, **RuNPs@CNT/mpg-CN**, thus indicating that the nature of the carbon support is not decisive for the activity of the catalysts, although the CNM itself is influential in the stabilization of the nanoparticles. On the other hand, for a given carbonaceous support, samples with the lower Ru content yielded the highest TON and TOF values (**Table 2**, entries 2, 4, 6 and 8). Again, **RuNPs@CNT/mpg-CN** (with the low Ru loading) delivered the best TON and TOF values (113 and 4.7 h^{-1}).

The optimization of the Ru loading in the **RuNPs@CNM/mpg-CN** samples helped in the design of the **MNP@mpg-CN** materials, prepared with metal NPs directly synthesized or loaded on the surface of the semiconductor, with no utilization of the carbonaceous supports. In fact, the concentration of metal precursor (either Ru or Pt) used in the synthesis (described in the experimental part) of this second set of hybrid materials, was calculated in order to obtain a final concentration of ca. 1.69 μmol of metal (either ca. 0.6 wt.% of Ru or 1.2 wt.% of Pt) in ca. 26 mg of mgp-CN. This is the loading that yielded the best hydrogen production with the **RuNPs@CNM/mpg-CN** samples.

Thus, the **MNP@mpg-CN** hybrid materials were tested as photocatalyst in the hydrogen evolution reaction. The selected sample was introduced in the standard reactor, with 38 mL of 10% TEOA aqueous solution as SED, and irradiated for 24 h under visible light, using a 300 W Xe lamp (>395 nm). Hydrogen evolution rate (**Table 3** and **Figure 12**) was measured from the slope of the "mol of H_2 vs time" curves (**Figure S12** and **Figure S13**), expressed per hour and per g of photocatalyst ($\mu mol \cdot h^{-1} \cdot g^{-1}$). The total amount of H_2 generated in 24 h was also confirmed by GC.

TON values were calculated at 24 h considering the total amount of Ru or Pt present in each sample (**Table 3** and **Figure 12**).

The H_2 production value for **PtNP@mp-CN** (870 $\mu mol \cdot h^{-1} \cdot g^{-1}$) outperformed those of any of the Ru samples (137, 155 and 129 $\mu mol \cdot g^{-1} \cdot h^{-1}$ for **RuNP@mpg-CN**, **in-RuPPNP@mpg-CN** and **ex-RuPPNP@mpg-CN**, respectively). Following this trend, **PtNP@mp-CN** (**Table 3**, entry 5) material delivered, the best final activity out of all the samples, more than 5-fold the total amount of H_2 generated (522 µmol) and TON value after 24 h (339) when compared to any of the Ru samples.

Regarding only the Ru-loaded samples (**RuNP@mpg-CN**, **in-RuPPNP@mpg-CN**, and **ex-RuPPNP@mpg-CN**; **Table 3**, entries 2, 3 and 4, respectively), it can be observed that after 24 h of photocatalytic HER, both hydrogen production and TON values were close (87, 96 and 82 µmol of H_2 and 64, 54, 57 TON values for **RuNP@mpg-CN**, **in-RuPPNP@mpg-CN**, and **ex-RuPPNP@mpg-CN,** respectively). Better photocatalytic output was expected for the 4-phenylpyridine (PP)-stabilized materials (**in-RuPPNP@mpg-CN**, and **ex-RuPPNP@mpg-CN**), as it has been reported that the stabilization with PP ligand outstandingly enhances the electrocatalytic performance of Ru NPs towards the HER [17]. The lower-than-expected performances for these hybrid materials could be explained with the TEM micrographs: isolated Ru NPs are barely visible in the surface of the mpg-CN for **in-RuPPNP@mpg-CN**, and **ex-RuPPNP@mpg-CN**; instead, they are forming aggregates, whose connectivity with the semiconductor would not be as good as if they were isolated, thus explaining the similar photocatalytic performance observed for the Ru samples.

Entry	Hybrid Material	MNP@mpg-CN (mg)	Metal (µmol)	H_2 (µmol·h^{-1}·g^{-1})[a]	H_2 (µmol)	TON[b] (–)	TOF (h^{-1})
1	mpg-CN	–	–	2	1	–	–
2	RuNP@ mpg-CN	26.4	1.36	137	87	64	2.7
3	in-RuPPNP @mpg-CN	25.9	1.77	155	96	54	2.3
4	ex-RuPPNP @mpg-CN	26.6	1.45	129	82	57	2.4
5	PtNP@ mpg-CN	25.0	1.54	870	522	339	14.1

Table 3. Photocatalytic H_2 evolution in the standard reactor, under visible light irradiation (300 W Xe lamp; λ > 395 nm), during 24 h, with 38 mL of TEOA (10%) as SED, using **MNP@mpg-CN** (MNP = Ru, RuPP or Pt) samples as photocatalysts. ([a] µmol of H_2 released per hour and per g of catalyst (hybrid material); [b] TON and TOF calculated at 24h considering the molar concentration of Ru or Pt).

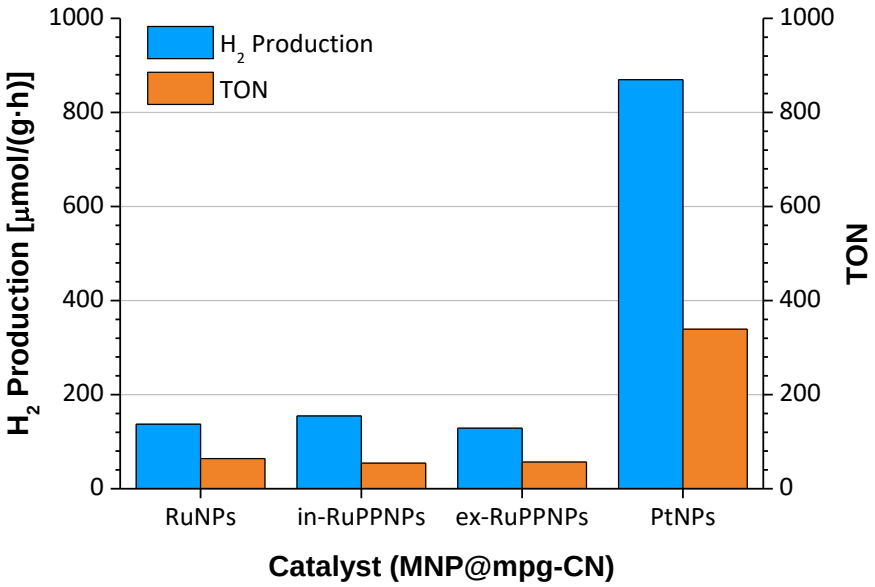

Figure 12. Photocatalytic H_2 evolution and TON (considering total µmol of Ru or Pt in the hybrid materials) calculated after 24 h of visible light irradiation (300 W Xe lamp; λ > 395 nm, 10% TEOA as SED) using the **MNP@mpg-CN** (MNP = Ru, RuPP or Pt) samples as photocatalysts.

Excluding the Pt-based photocatalyst, which overshadowed all of the other materials here presented, if we compare the **RuNP@mp-CN** and **in/ex-RuPPNP@mpg-CN** samples with the previously studied **RuNPs@CNM/mpg-CN** materials, it can be observed that both hydrogen production and TON values, considering the same Ru content, are similar (**Figure 13**). This fact highlights, on the one hand, the need to load the mpg-CN with the appropriate co-catalyst so the photocatalytic performance in the HER would be efficient enough, and on the other, that the two strategies to prepare photocatalytic mpg-CN-based materials have proven to be equally useful, each offering different advantages. The use of CNM as supports allowed a greater control over the stability and dispersibility of the NPs, before and after mixing the materials with mpg-CN, whereas direct deposition of the metal NPs on the surface, as seen for the **MNP@mpg-CN** materials, significantly simplified the preparation and characterization of the hybrid materials.

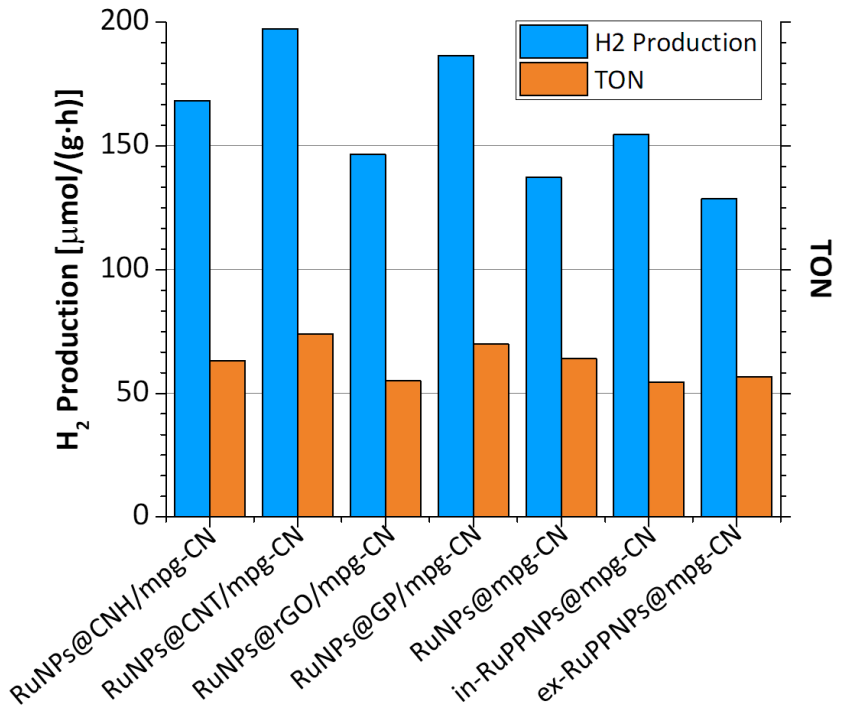

Figure 13. Photocatalytic hydrogen production and TON (considering total μmol of Ru in the hybrid materials) calculated after 24 h of visible light irradiation (300 W Xe lamp; λ > 395 nm, 10% TEOA as SED) for the **RuNPs@CNM/mpg-CN** (CNM = CNH, CNT, rGO or GP; Ru loading: 1.69 μmol) and the **RuNP@mp-CN** and **in/ex-RuPPNP@mpg-CN** samples.

The main photocatalytic data for **RuNPs@CNM/mpg-CN** and **MNP@mpg-CN** are collected in **Table S2**, where they are compared with other examples found in the literature based on carbon nitride-supported nanocatalysts, which consist mainly on Pt, but also Pd and Ni (and their corresponding alloys with Co or Au) nanoparticles. The work presented here is up to date the only example of, carbon nitride-supported Ru NPs for photocatalytic HER. Pt-based photocatalysts display superior HER activities, including our **PtNP@mpg-CN** system, which outperformed most of the Pt-based photocatalyst reported under similar conditions, whereas the supported Ru-based systems here presented outperform Ni-based photocatalysts.

5.4.5 Stability tests

The long-term stability of the photocatalytic materials was studied with the **RuNPs@CNT/mpg-CN** sample, with Ru loading of 1.60 μmol, with the same reaction setup described for the standard reactor, but during 75 h of visible light irradiation. No sign of deactivation could be detected after this time (**Figure 14**), thus confirming the high stability of these materials.

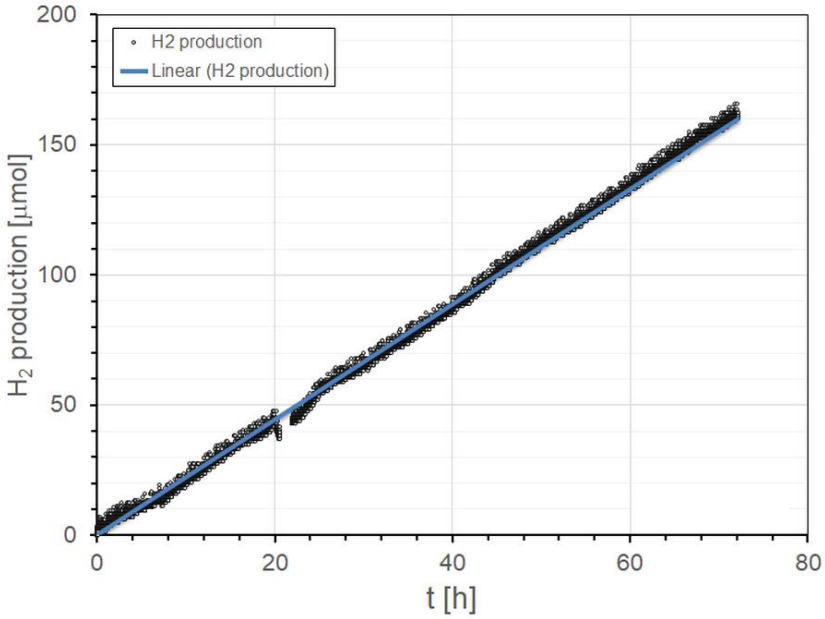

Figure 14. Photocatalytic H_2 evolution using RuNPs@CNT/mpg-CN under visible irradiation (300 W Xe lamp; λ > 395 nm) in the standard reactor (38 mL of 10% TEOA as electron donor) during 75 h.

Additionally, the fate of the materials after the photocatalytic measurements was studied by TEM, with the systems with the highest amount of Ru, in order to facilitate their characterization. TEM micrographs confirmed the presence of Ru NPs (supported on the CNM and embedded onto the mpg-CN), with similar size and shape as those observed just after synthesis (**Figure S14**).

The long-term stability of the MNP@mp-CN was also studied, using the RuNP@mpg-CN and PtNP@mpg-CN samples, experiments carried out using a Clark hydrogen electrode (**Figure S4**), to follow the H_2 evolution under visible light irradiation (300 W Xe lamp; $\lambda > 395$ nm), with TEOA as SED. No sign of deactivation was observed for the PtNP@mpg-CN material after 65 h of reaction. In the case of the RuNP@mpg-CN, although a decay on the slope could be observed, the system was still active after 65 h (**Figure 15**).

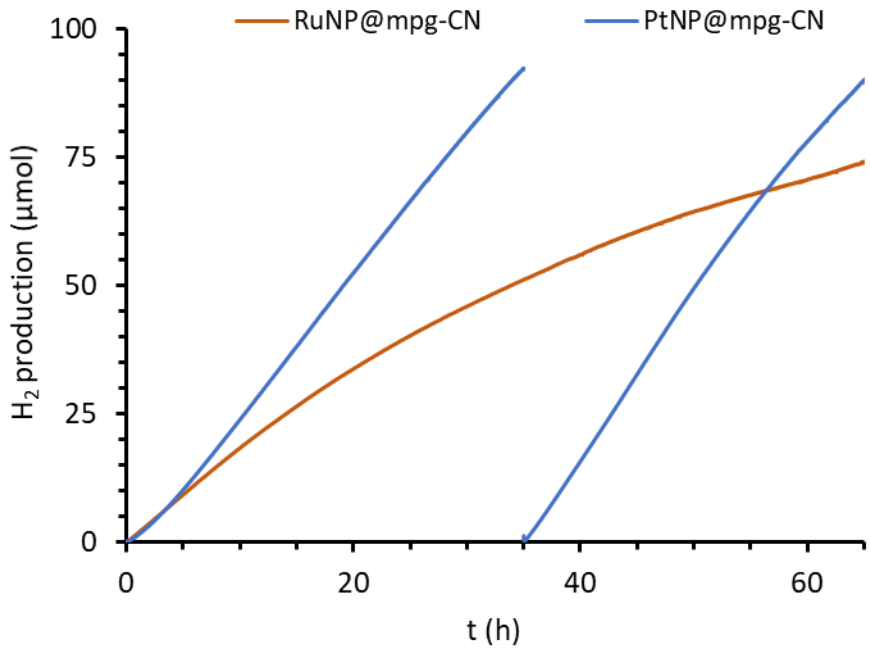

Figure 15. Photocatalytic H_2 evolution with **PtNP@mpg-CN** and **RuNP@mpg-CN**) samples as photocatalysts, after more than 60 h of visible light irradiation (300 W Xe lamp; $\lambda > 395$ nm, 10% TEOA as SED).

5.4.6 Photophysical studies

Photophysical studies were carried out with the **MNP@mpg-CN** hybrid materials. The first step was to study the absorption and emission properties of the bare mpg-CN, with no co-catalyst loading, whose diffuse-reflectance absorption profile discloses an intense absorption at $\lambda < 420$ nm and a tail at longer wavelengths [18,19]. Tauc method was applied to the diffuse-reflectance spectra, in order to determine the bandgap energy of the semiconductor, estimating a value of ca. 2.7 eV (**Figure 16**).

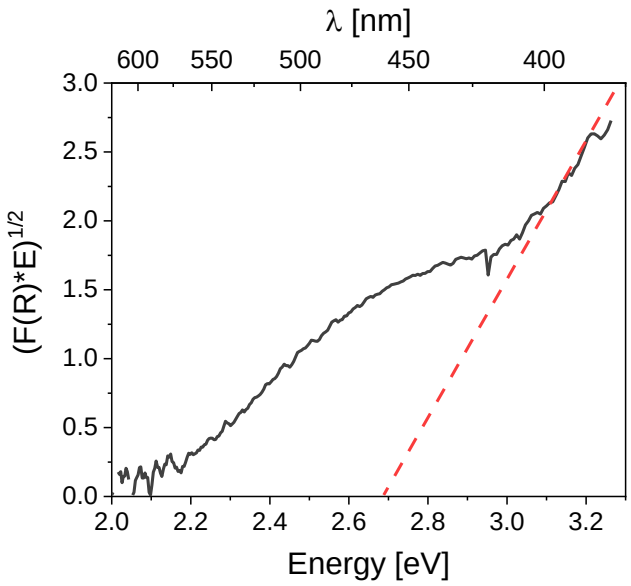

Figure 16. Tauc plot for bandgap energy dermination of the bare mpg-CN in water; The linear part of the plot is extrapolated to the x-axis; F(R) represents the optical absorption based on the the Kubelka-Monk function.

The emission spectrum corresponding to the bare mpg-CN in water was recorded after excitation under $\lambda = 390$ nm. The wide luminescence band emitted, peaking near 475 nm (**Figure 17**), could be fitted using two Gaussian functions [20]. The high energy peak, centred at 465 nm (2.7 eV), was attributed to emissions from band edges, while the low-energy component at 524 nm (2.4 eV) was assigned to intra bandgap states. The time-resolved emission decay (**Figure 18**), measured by Time-Correlated Single Photon Counting (TC-SPC) (monitored at 470 nm after excitation at 380 nm), can be fitted using a tri-exponential function, yielding an amplitude-weighted average lifetime of $\langle\tau\rangle = 2.04$ ns.

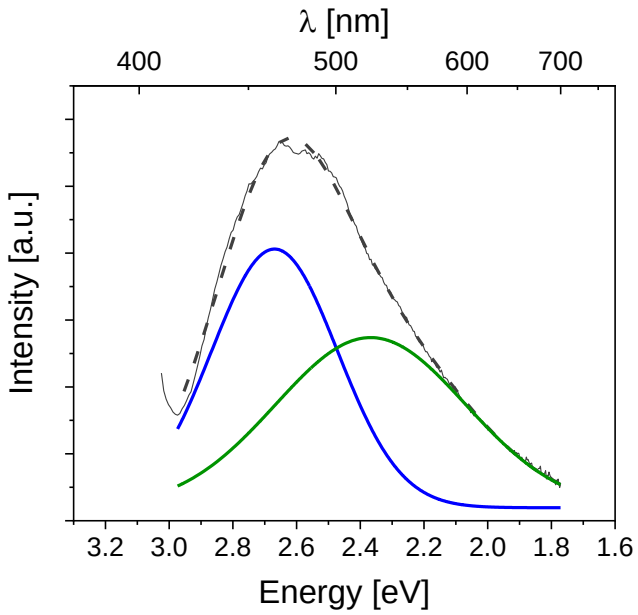

Figure 17. Gaussian fit of photoluminiscence spectrum of bare mpg-CN in water after excitation under λ = 390 nm. In blue, high-energy component (465 nm; 2.7 eV); in green, low-energy component (524 nm; 2.7 eV); In grey, experimental data; In black, the cumulative fit.

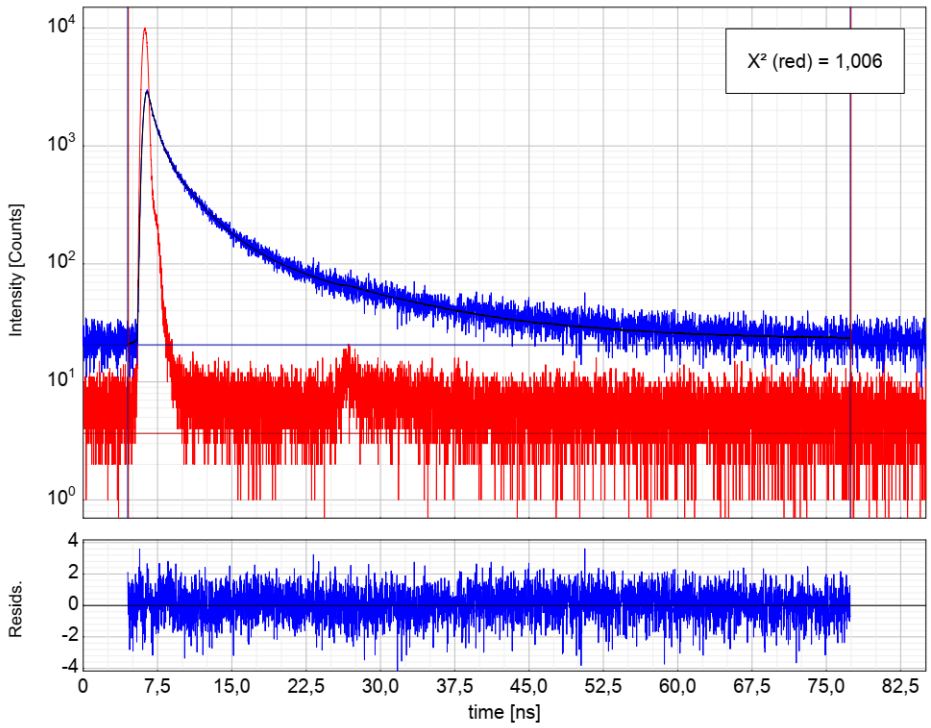

Figure 18. Time-resolved emmision decay of mpg-CN in water, obtained by TC-SPC (excitation at 380 nm, monitored at 470 nm), and corresponding fitting using a tri-exponential function.

The semiconductor delivered similar emission lifetimes (ca. 2 ns) without TEOA after the different co-catalyst loading (**Table S3**), although a tiny decrease was observed for **PtNP@mpg-CN** and **ex-RuPPNP@mpg-CN** samples, thus suggesting that the co-catalyst quenches the emissive states with low efficiency (<14%). This slight decrease was also observed after the incorporation of the sacrificial donor, attributed to hole transfer efficiencies between 4-7% (**Figure 19**). The tenuous degree of luminescence quenching by either Ru and Pt NPs or the TEOA donor indicates the low efficiency of the charge carrier transfer from the emissive excited states.

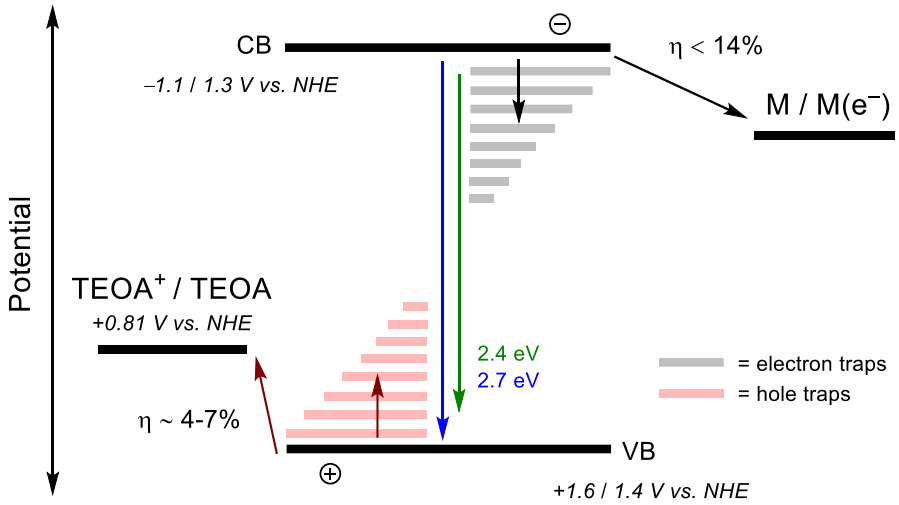

Figure 19. Scheme of the photophysical processes in the mpg-CN system, involving charge carriers in emissive excited states (potentials corresponding to conduction (CB) and valence (VB) bands of the mpg-CN semiconductor, and TEOA have been extracted from literature [21–24]).

Transient absorption spectroscopy (TAS) helped with the elucidation on the charge carrier dynamics. A relevant decay pathway of charge carriers in 'bare' mpg-CN sample is thus expected to involve gradual trapping into deep trap levels. The related charge trapped states are usually non-emissive [20,25]. A laser pulse (355 nm) was used to photoexcite the bare semiconductor sample. The observed transient signal in the μs-to-ms timescale, exhibiting a maximum at ca. 750 nm, as shown in **Figure 20**, was attributed to photogenerated charge carriers [20,21,26]. An analogous profile could be observed after the incorporation of 10% TEOA in the medium, but with an increased amplitude and longer lifetime (**Figure 20**), which

can be explained taking into account that the transient profile is mainly related to photogenerated electrons and that reaction of trapped holes with TEOA takes place in a time scale below the resolution limits of the experiment [20]. The sacrificial donor was expected to react with photogenerated holes, thus leaving long-lived electrons, which decay through complex kinetics [27].

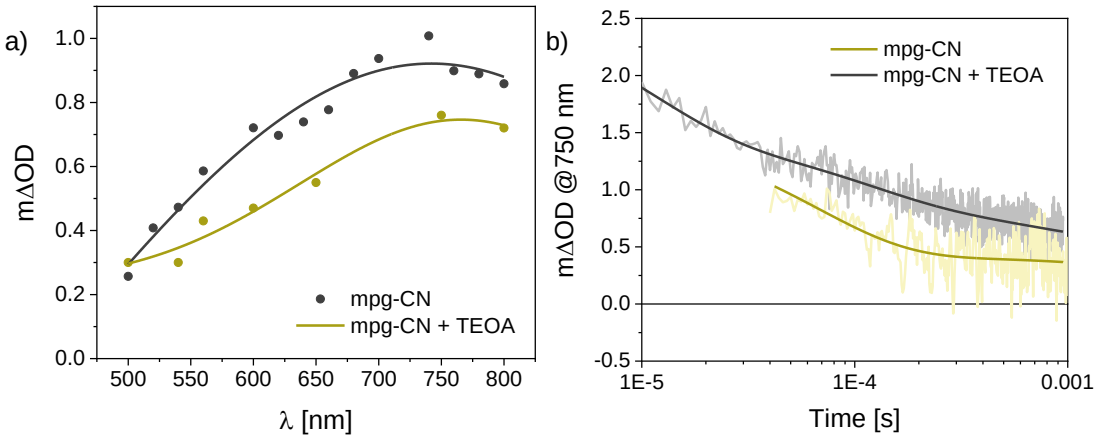

Figure 20. a) Transient absorption spectra at 100 μs time-delay obtained by laser flash photolysis after excitation at λ = 355 nm, for the 'pure' mpg-CN sample in water with and without TEOA (10%) in the medium. (dots corresponds to experimental data; lines corresponds to the best fits in each case, using gaussian functions); b) TAS kinetic decay at λ = 750 nm.

TAS analyses were also employed to study the dynamics of the photogenerated electrons after loading the mpg-CN with metal NPs (Ru or Pt) (**Figure 21**). The TAS kinetics decays were apparently unaltered after the incorporation NPs. On the contrary, the amplitude of the transient signal (prompt ΔOD at ca. 10 μs) was quenched in the presence of the metal NPs, thus indicating that trapped electrons could be transferred to the co-catalyst within a comparable timescale of the hole-scavenging by the TEOA [20]. The amount of prompt transient quenching changes according to the nature of the co-catalyst, following the descending sequence: **PtNP@mpg-CN** (78%) >> **in-RuPPNP@mpg-CN** (48%) > **ex-RuPPNP@mpg-CN** (32%) ~ **RuNP@mpg-CN** (31%), and could be linked to the efficiency of the electron transfer processes from mpg-CN to the metal co-catalyst (**Figure 22**). It is important to note that the same trend was also detected after the photocatalytic hydrogen evolution reaction experiments previously discussed, indicating that the electron transfer from the photoexcited mpg-CN to the metal NPs, represents the rate determining step for this reaction.

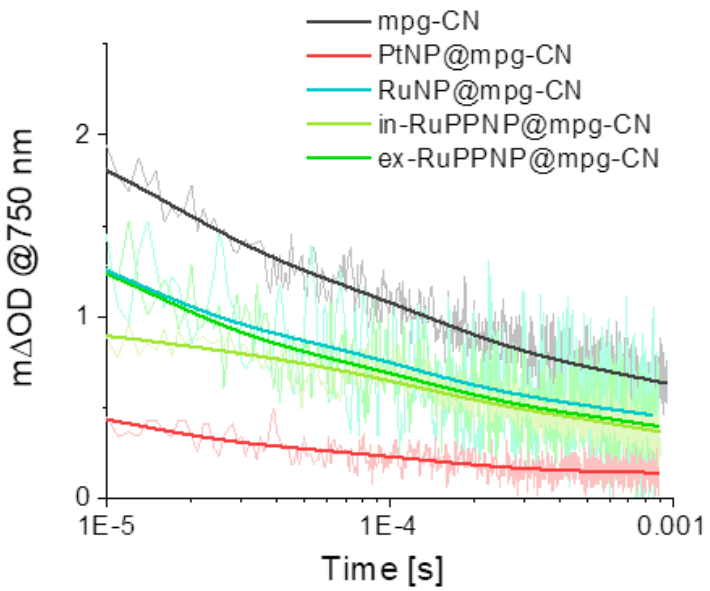

Figure 21. TAS kinetic decays probed at 750 nm, following excitation at 355 nm (measured by laser flash photolysis) corresponding to the bare mpg-CN, and the **PtNP@mpg-CN**, **RuNP@mpg-CN**, **in-RuPPNP@mpg-CN**, and **ex-RuPPNP@mpg-CN** hybrid materials in water (10% TEOA solution). A tri-exponential function, whose lifetimes in the order of $\tau 1 \sim 10\text{-}5$ s, $\tau 2 \sim 10\text{-}4$ s, and $\tau 3 \sim 10\text{-}3$ s, was used to fit the kinetic traces in all cases.

Therefore, the superior photocatalytic performance of **PtNP@mpg-CN** came from a more efficient electron transfer, when compared to all Ru-decorated systems. A similar behaviour as the latter systems was observed at the research group when studying Ru NPs supported onto sensitized TiO_2 for HER [28]. Considering just the Ru-based samples, the slightly higher electron transfer yields determined for the **in-RuPPNP@mpg-CN,** could be due to the smaller size of the NPs, thus yielding a higher surface-area-to-volume ratio and therefore a larger number of active sites when compared to the **RuNP@mpg-CN** sample, as well as to enhanced interactions and electronic connectivity with the semiconductor, when compared to the **ex-RuPPNP@mpg-CN** material. But even in the case of the Pt-based hybrid material, the reduction of the transient signal is not quantitative, indicating that electron transfer from the mpg-CN to the metal NPs always occurs in competition with further trapping. As already stated, the corresponding decaying kinetics seem to be practically independent of the metal NPs, indicating that progressively trapped electrons lose their energy and do not have sufficient driving force to reduce the

metal NPs regardless of their nature. **Figure 22** summarizes the mechanistic scenario involving non-emissive states.

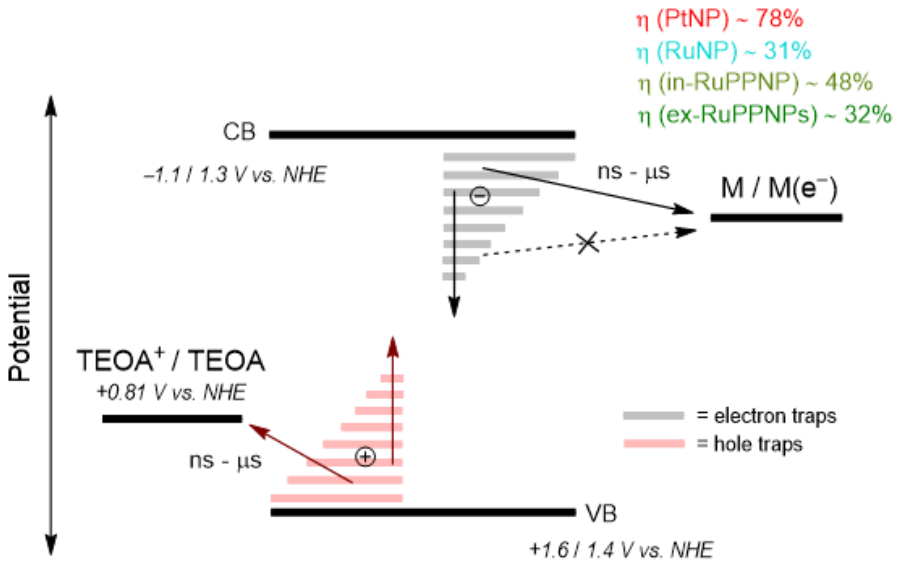

Figure 22. Scheme of the main processes involving trapped charge carriers in non-emissive states (potentials corresponding to conduction (CB) and valence (VB) bands of the mpg-CN semiconductor, and TEOA have been extracted from literature [21–24]).

5.5 Conclusions

Two sets of mpg-CN supported metal NPs-based hybrid materials have been prepared, via the organometallic approach. The first set, **RuNPs@CNM/mpg-CN** (CNM = carbon nanohorns, CNH; single-walled carbon nanotubes, CNT; reduced graphene oxide, rGO; and graphite, GP), was prepared after depositing the Ru NPs on the surface of CNM, by physically mixing them with the mpg-CN. For the second set, **MNP@mpg-CN** (M= Ru or Pt), metal NPs were deposited directly on the surface of the mpg-CN. For the Ru NPs, syntheses were carried out in the absence/presence of 4-phenylpyridine (PP) ligand as stabilizer, either with the mpg-CN also present in the medium or with an impregnation process afterwards. Both sets of hybrid materials were subjected to an in-depth characterization process, using techniques as diverse as TEM, SEM-FEG, EDX, ICP-OES, XRD, XPS, and specific surface area measurements. In all cases, small Ru or Pt NPs were detected, with sizes from ca. 1.3 to 2.9, depending on the metal precursor, and the use or not of further carbon support or PP ligand.

Initial photocatalytic test in the HER were performed using the **RuNPs@CNH/mpg-CN** hybrid material, demonstrating that higher loads of Ru led to a darkening in the material, thus preventing light from reaching the surface of the semiconductor. Therefore, a compromise was reached between maintaining the light-absorbing properties of the material, and using enough Ru load to deliver an efficient photocatalytic performance.

After optimizing the Ru load (0.68 and 1.69 μmol of Ru), **RuNPs@CNM/mpg-CN** were tested as photocatalyst in the HER for 24 h, under visible light irradiation and using a 10 % TEOA aqueous solution as sacrificial electron donor. In all the materials, the highest loading of Ru (1.69 μmol) led to the highest amounts of H_2 released, whereas the best TON values were obtained with the lowest loading of Ru (0.68 μmol). More specifically, **RuNPs@CNT/mpg-CN** delivered the best performance, producing between 4 and 26 % more hydrogen, and with a TON value 12-43 % higher than the rest of the hybrid systems.

Interestingly, similar results, in terms of H_2 generation and calculated TON at 24 h, were obtained when using the second set of hybrid materials (**MNP@mpg-CN**, M =

Ru), for photocatalytic HER under the same experimental conditions, using 1.69 µmol of Ru loading. Nevertheless, as expected, **PtNP@mpg-CN** stood out, with a hydrogen production as high as 558.1 $\mu mol \cdot h^{-1} \cdot g^{-1}$, 5-fold higher than its Ru counterparts, which despite the variations in their preparation, delivered comparable results.

Photophysical experiments were employed to rationalize the observed photocatalytic behaviour for the **MNP@mpg-CN** hybrid materials (M = Ru or Pt). The tendency was related with the estimated electron transfer efficiency, which follows the sequence **PtNP@mpg-CN** >> **in-RuPPNP@mpg-CN** > **ex-RuPPNP@mpg-CN** (32%) ~ **RuNP@mpg-CN.** Again, **PtNP@mpg-CN** outshined, offering the highest electron transfer yield which, in combination with the small size and high dispersibility of the Pt NPs on the material, led to a much higher hydrogen production when compared to the Ru-decorated mpg-CN materials. On the other hand, no notable differences were observed for these Ru-based hybrid materials, although for the **in-RuPPNP@mpg-CN**, given its higher electron transfer yield and larger number of active sites, derived from the smaller size of the NPs, better photocatalytic output was expected. An explanation to this lower-than-expected performance may lie in the agglomeration of the NPs observed on the surface of the mpg-CN, which probably hampers the connectivity between the NPs and the mpg-CN support. . In the case of the **RuNP@mpg-CN**, while presenting larger nanoparticles (and thus fewer active sites), the Ru NPs are isolated and well dispersed all over the surface of the mpg-CN. These differences in NPs' size and agglomeration may explain their similar outputs in H_2 production.

As a final remark, the incorporation of metal NPs as co-catalyst has improved the performance of the bare mpg-CN in the photocatalytic HER, in terms of activity, H_2 production and stability, as the prepared hybrid materials remain active after more than 60 h of photocatalysis. Regarding the Ru NPs-based systems here presented, they are among the few examples available in the literature where the photo-responsive material, mpg-CN, is able to carry out the electron-transfer process towards the Ru NPs without the utilization of an electron mediator.

5.6 Supporting Information

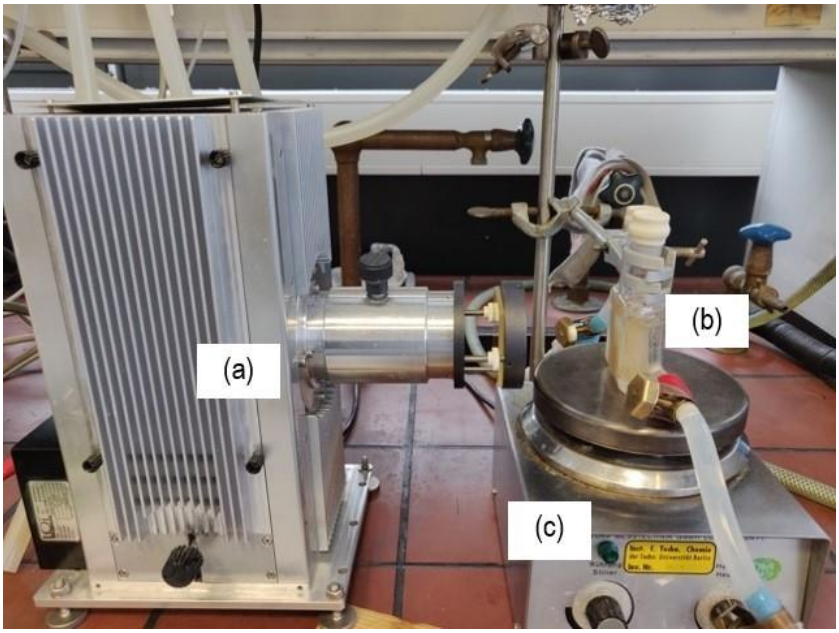

Figure S1. Experimetal set-up corresponding to the screening reactor for the photocatalytic experiments, consisting mainly on a) light source; b) fused quartz reactor; c) magnetic stirrer.

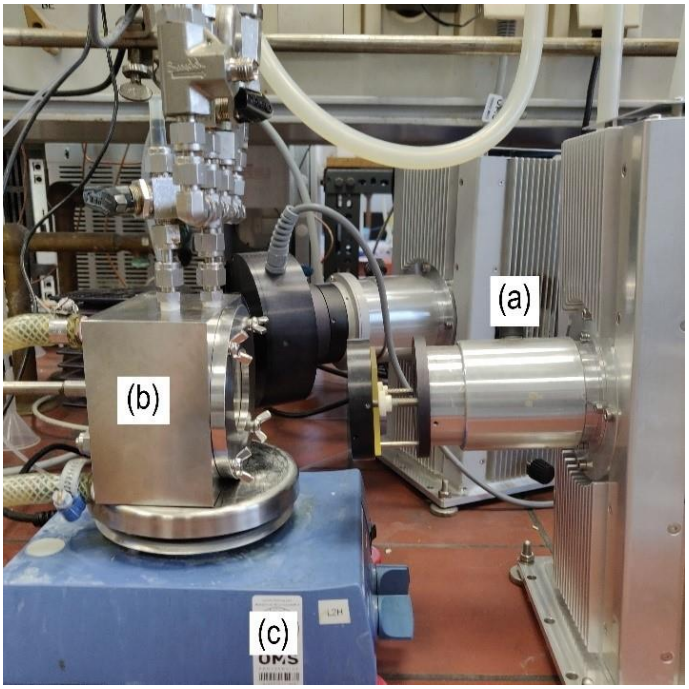

Figure S2. Experimetal set-up corresponding to the standard reactor for the photocatalytic experiments, consisting mainly on a) light source; b) reactor; c) magnetic stirrer.

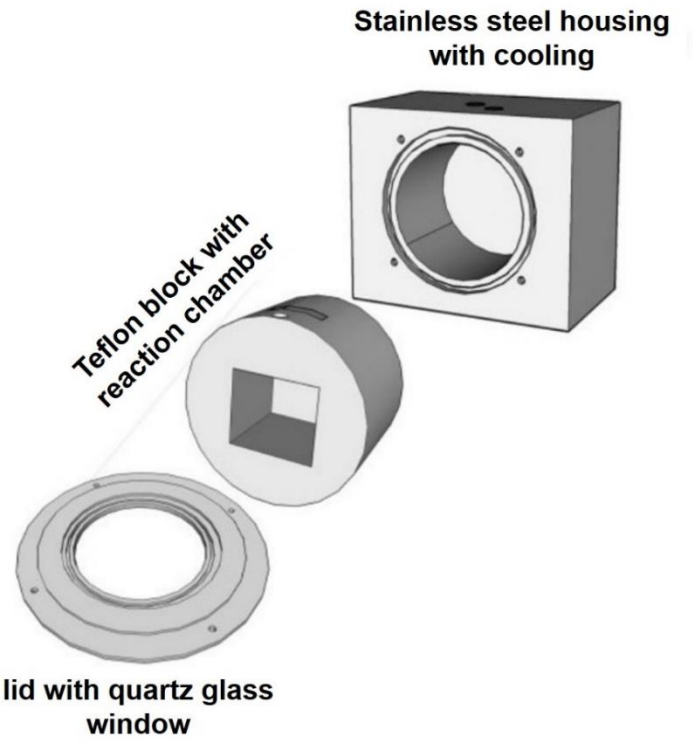

Figure S3. Schematic design for the different components of the standard reactor for the photocatalytic experiments. The reactor consist on a main body made of Teflon, with a reaction chamber and thermocouples inside. This block is attached to a stainless-steel housing with cooling. The window oof the reactor is a 6 mm thick round piece of quartz glass. In the top part of the reactor two channels allow the addition of (liquid) substances and the measurement of the pressure, using a pressure sensor and a manometer. A third hole fitted with a temperature sensor allows the control over the temperature inside the reactor [29].

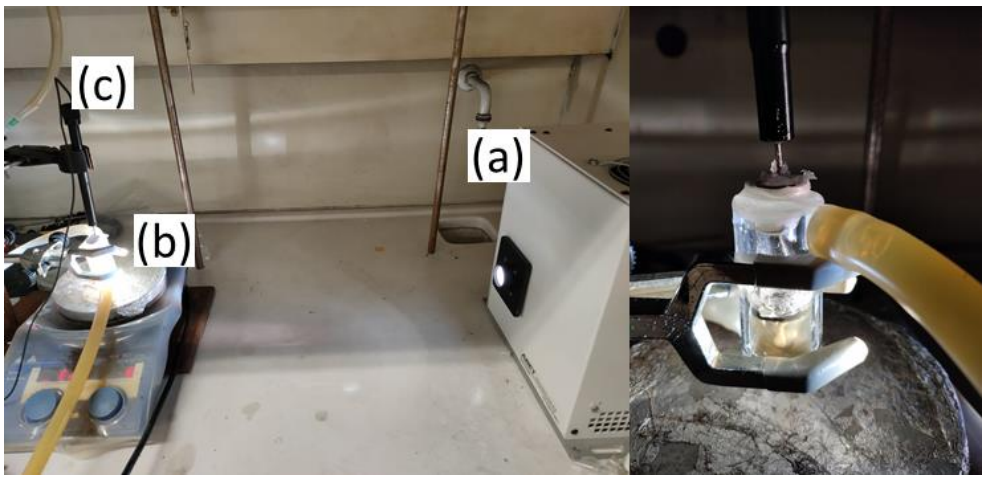

Figure S4. (Right) Experimetal set-up corresponding to carry out the stabilization tests of the photocatalytic experiments, consisting on (a) light source; b) reactor; c) Clark electrode. (Left) Close-up of the Clark electrode inside the reactor.

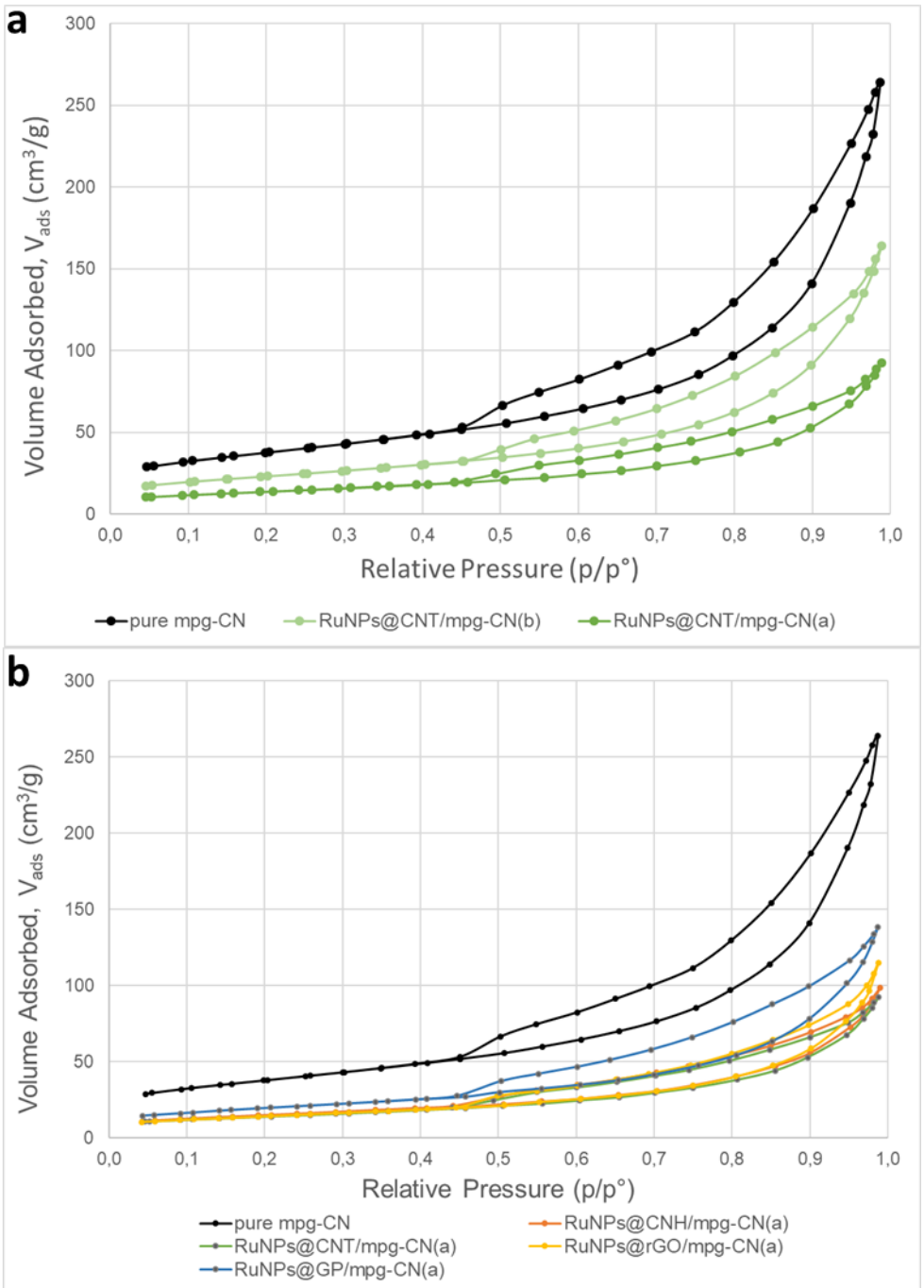

Figure S5. a) BET isotherms corresponding to 'pure' mpg-CN and RuNPs@CNT/mpg-CN(a; 0.39 mg co-cat., 1.60 µmol Ru) and RuNPs@CNT/mpg-CN(b; 0.16 mg co-cat; 0.64 µmol Ru); b) BET isotherms for each RuNPs@CNM/mpg-CN with a co-catalyst load of 0.39 (ca. 1.60 µmol Ru).

Sample	**RuNPs@CNM (mg)**	**Ru (µmol)**	**S_{BET} ($m^2 \cdot g^{-1}$)**
mpg-CN	-	-	134.3
RuNPs@CNT/mpg-CN (b)	0.16	0.64	83.1
RuNPs@CNT/mpg-CN (a)	0.39	1.60	49.7
RuNPs@CNH/mpg-CN (a)	0.39	1.62	51.8
RuNPs@rGO/mpg-CN (a)	0.44	1.60	51.4
RuNPs@GP/mpg-CN (a)	0.51	1.60	70.4

Table S1. Specific surface area (S_{BET}) values for each RuNPs@CNM/mpg-CN hybrid materials determined after certain co-catalyst loads.

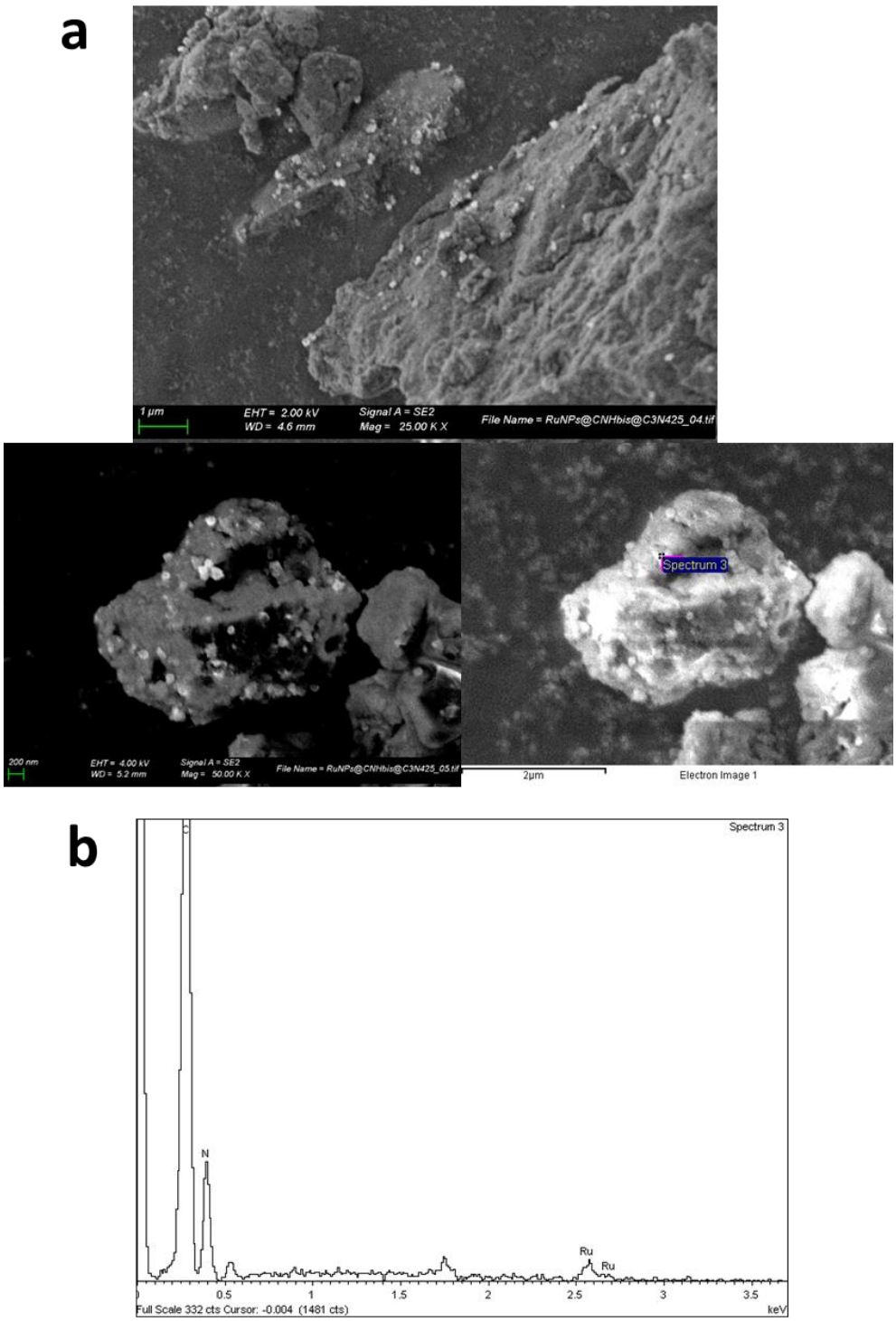

Figure S6. a) SEM-FEG micrographs corresponding to **RuNPs@CNH/mpg-CN** using secondary and back-scattered electrons (75 and 25 % respectively). b) EDX analysis confirming the presence of the **RuNPs@CNH** nanohybrids on the surface of the mpg-CN (area marked as spectrum 3).

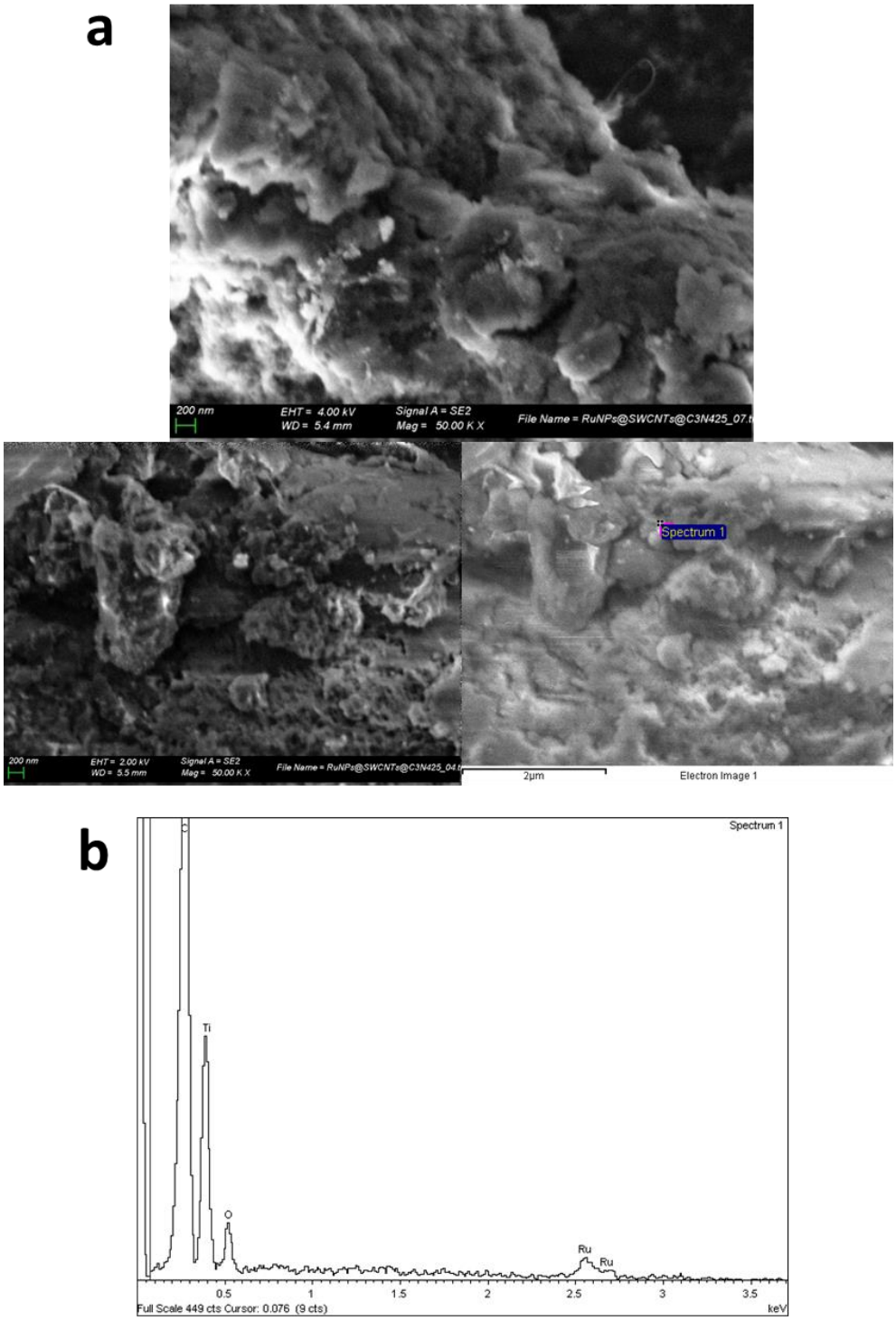

Figure S7. a) SEM-FEG micrographs corresponding to **RuNPs@CNT/mpg-CN** using secondary and back-scattered electrons (75 and 25 % respectively). b) EDX analysis confirming the presence of the **RuNPs@CNT** nanohybrids on the surface of the mpg-CN (area marked as spectrum 1).

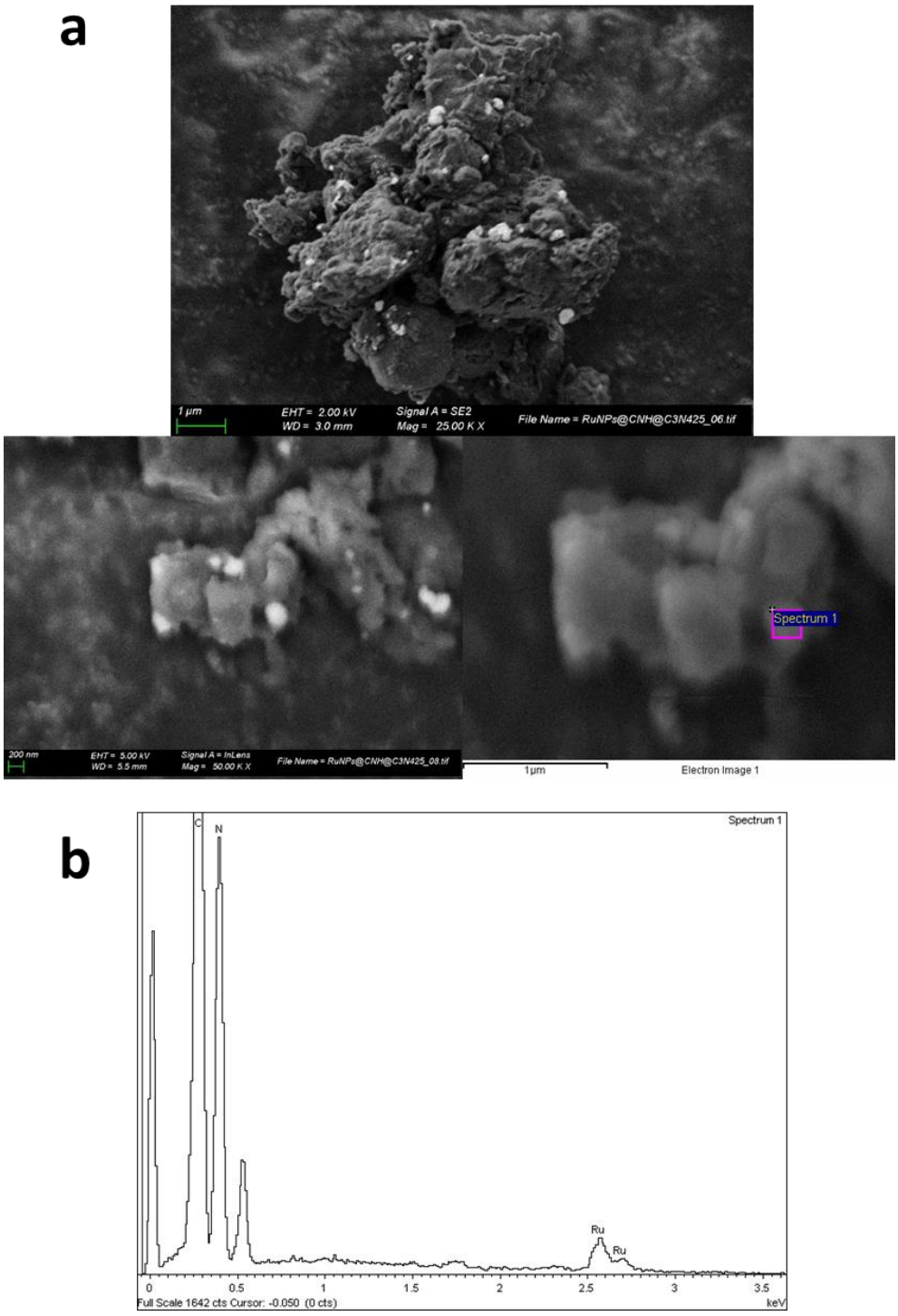

Figure S8. a) SEM-FEG micrographs corresponding to **RuNPs@rGO/mpg-CN** using secondary and back-scattered electrons (75 and 25 % respectively). b) EDX analysis confirming the presence of the **RuNPs@rGO** nanohybrids on the surface of the mpg-CN (area marked as spectrum 1).

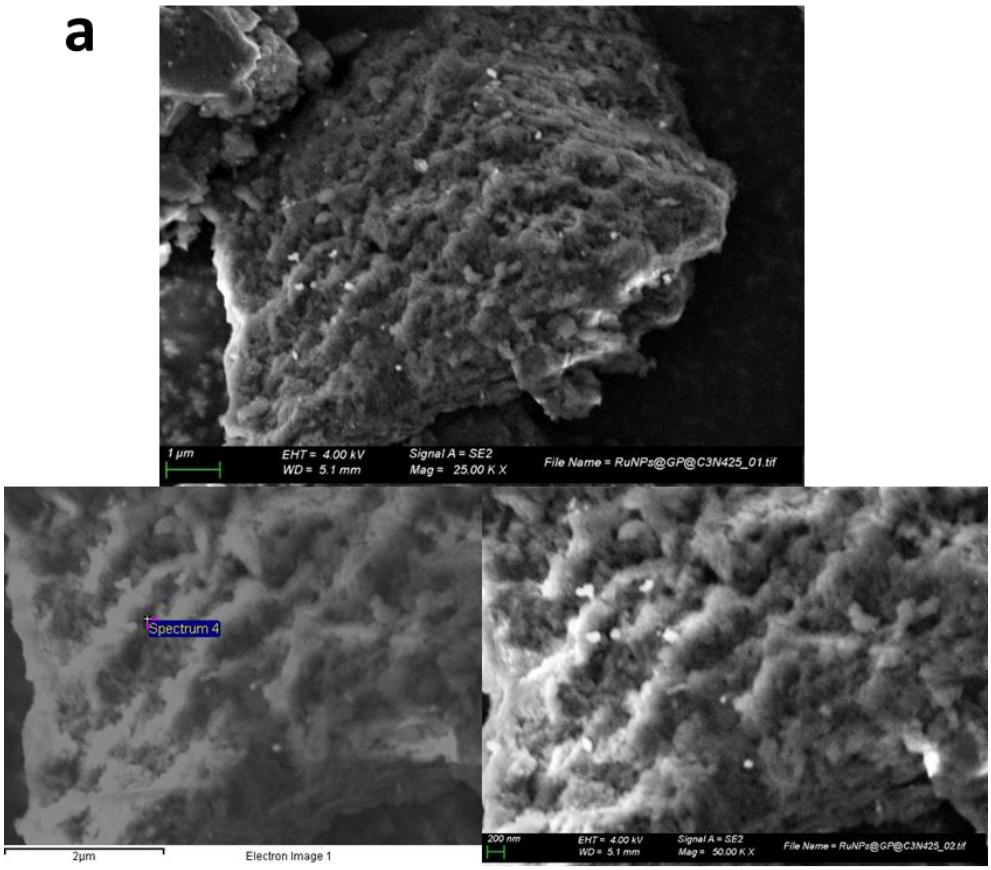

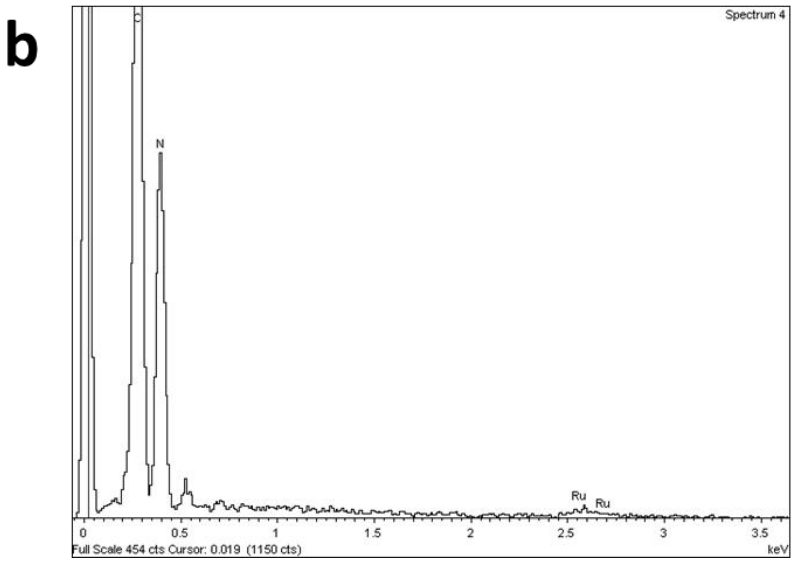

Figure S9. a) SEM-FEG micrographs corresponding to **RuNPs@GP/mpg-CN** using secondary and back-scattered electrons (75 and 25 % respectively). b) EDX analysis confirming the presence of the **RuNPs@GP** nanohybrids on the surface of the mpg-CN (area marked as spectrum 4).

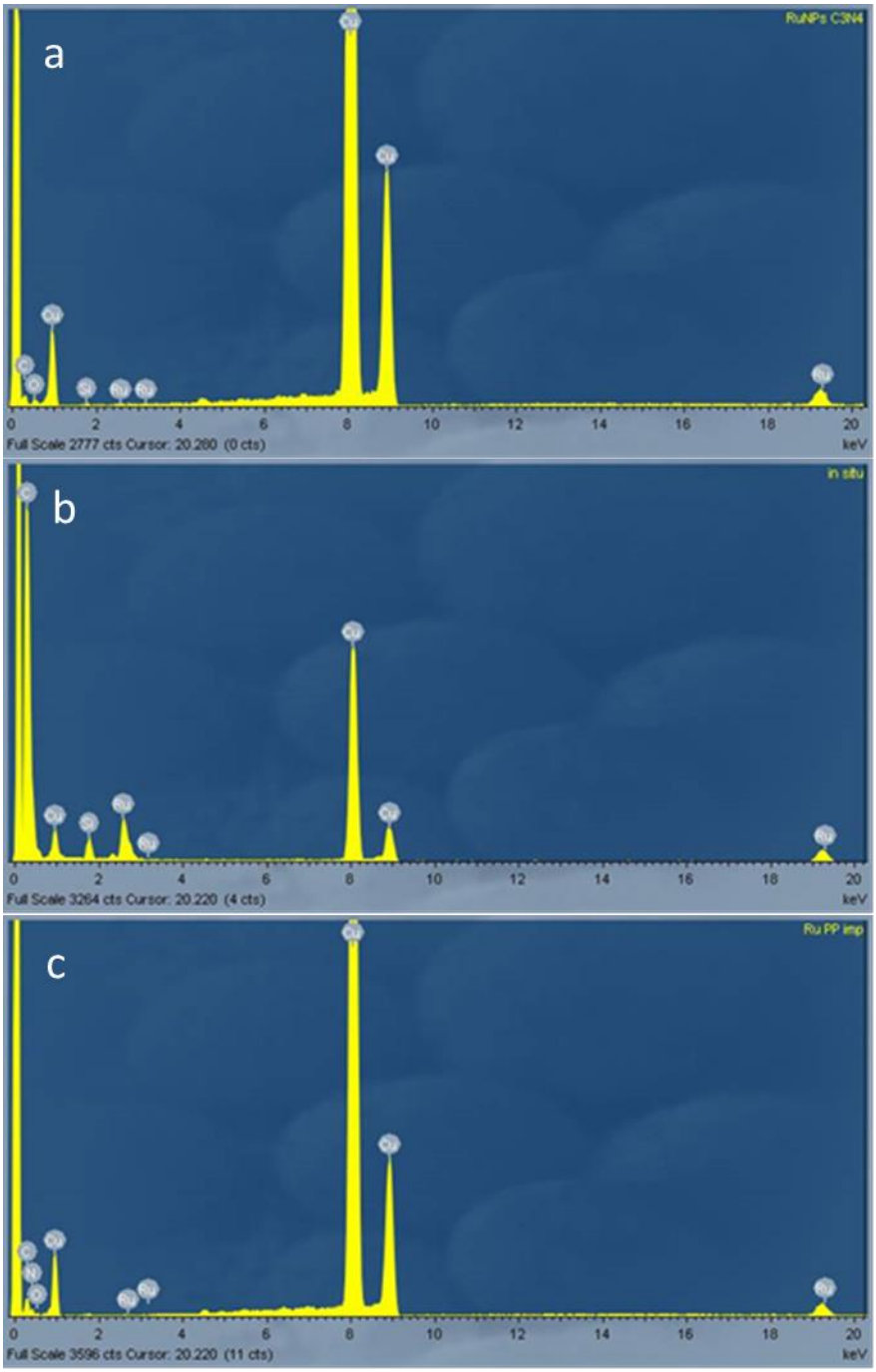

Figure S10. EDX analyses of a**) RuNPs@mpg-CN**, b) **in-RuPPNPs@mpg-CN**, and c) **ex-RuPPNPs@mpg-CN**

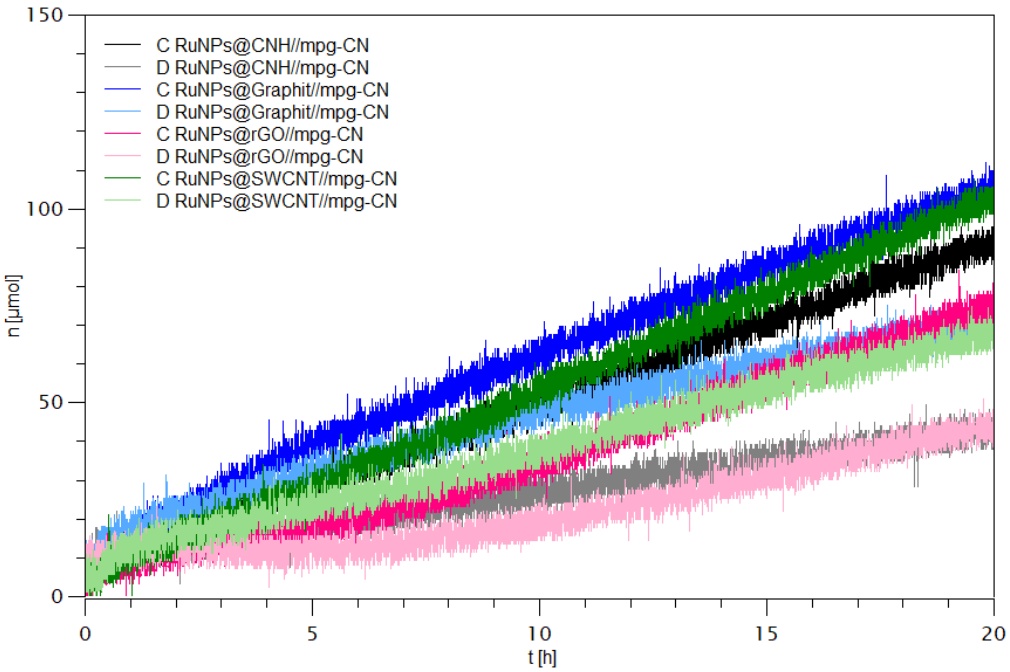

Figure S11. Photocatalytic H_2 evolution for the different samples after 24 h of visible irradiation (300 W Xe lamp; λ > 395 nm, 10% TEOA as electron donor) in the standard reactor. C and D correspond to the Ru load on each material (1.69 and 0.68 µmol respectively).

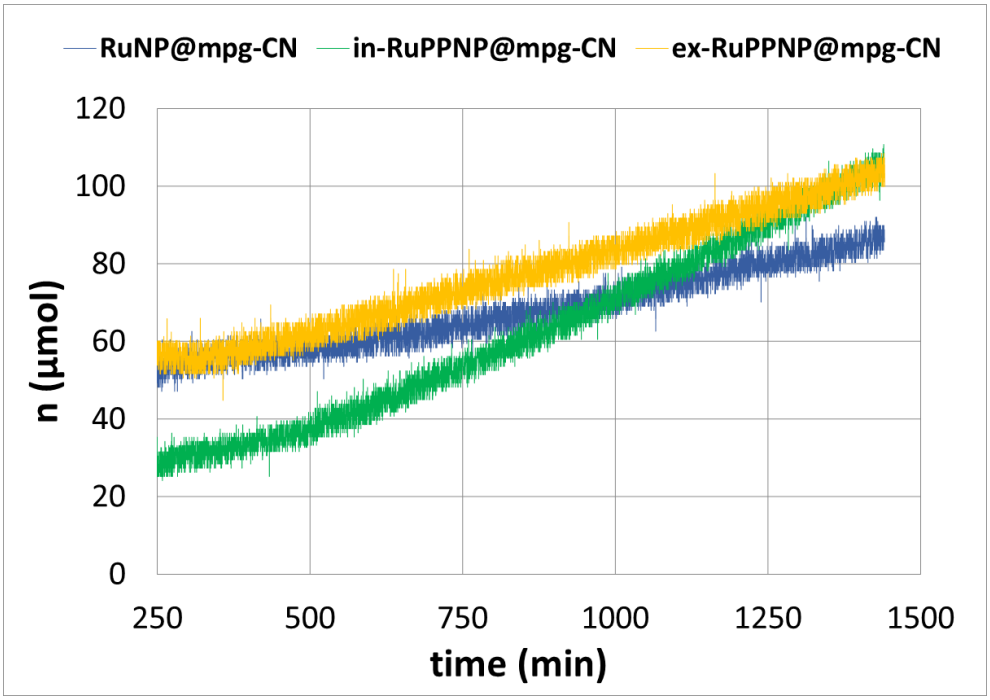

Figure S12. Photocatalytic H_2 evolution with **RuNPs@mpg-CN**, **in-RuPPNPs@mpg-CN**, and **ex-RuPPNPs@mpg-CN** as photocatalysts, after 24 h of visible irradiation (300 W Xe lamp; λ > 395 nm, 10% TEOA as electron donor) in the standard reactor.

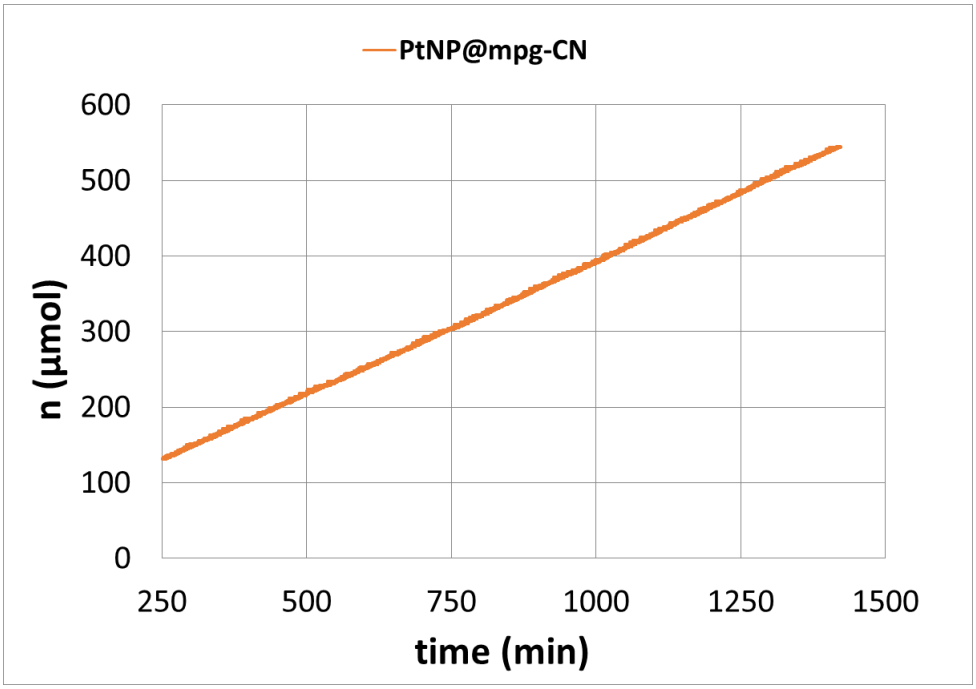

Figure S13. Photocatalytic H_2 evolution with **PtNPs@mpg-CN** as photocatalyst, after 24 h of visible irradiation (300 W Xe lamp; $\lambda > 395$ nm, 10% TEOA as electron donor) in the standard reactor.

Entry	Ref.	Photocat.	Co-catalyst (loading)	SED	Light source	t (h)	TOF (h^{-1})
1	*This work*	mpg-CN	RuNPs@CNH (0.26 wt% Ru)	TEOA (10%)	300 W Xe lamp λ > 395 nm	24	2.7
2	*This work*	mpg-CN	RuNPs@CNT (0.26 wt% Ru)	TEOA (10%)	300 W Xe lamp λ > 395 nm	24	4.7
3	*This work*	mpg-CN	RuNPs@rGO (0.26 wt% Ru)	TEOA (10%)	30W Xe lamp λ > 395 nm	24	2.9
4	*This work*	mpg-CN	RuNPs@GP (0.26 wt% Ru)	TEOA (10%)	300 W Xe lamp λ > 395 nm	24	4.2
5	*This work*	mpg-CN	Ru NPs (0.52 wt% Ru)	TEOA (10%)	300 W Xe lamp λ > 395 nm	24	2.7
6	*This work*	mpg-CN	In-RuPP NPs (0.69 wt% Ru)	TEOA (10%)	300 W Xe lamp λ > 395 nm	24	2.3
7	*This work*	mpg-CN	ex-RuPP NPs (0.55 wt% Ru)	TEOA (10%)	30W Xe lamp λ > 395 nm	24	2.4
8	*This work*	mpg-CN	Pt NPs (1.2 wt% Ru)	TEOA (10%)	300 W Xe lamp λ > 395 nm	24	14.1
9	[30]	g-CN nanosheets	Pt (3 wt%)	TEOA (10%)	150 W Xe lamp λ > 420 nm	4	31.6
10	[31]	g-CN	Pt (0.87 wt%)	TEOA (10%)	350 W Xe lamp λ > 400 nm	3	13.2
11	[32]	g-CN	Pt (3.2 wt%)	TEOA (10%)	300 W Xe lamp λ > 420 nm	6	83.0
12	[33]	mpg-CN	Pt (3 wt%)	TEOA (10%)	300 W Xe lamp λ > 420 nm	4	15.5
13	[34]	g-CN	Pt (3 wt%)	TEOA (10%)	Xe lamp λ > 420 nm	6	6.3
14	[35]	g-CN (single layer)	Pt (3 wt%)	TEOA (10%)	500 W Xe lamp λ > 420 nm	4	1.5
15	[36]	mpg-CN (S-doped)	Pt (3 wt%)	TEOA (15%)	300 W Xe lamp λ > 420 nm	4	8.9
16	[37]	g-CN	Pt, Co (1 wt%)	TEOA (10%)	300 W Xe lamp λ > 400 nm	5	4.3
17	[38]	g-CN	Pd (0.1 wt%)	TEOA (20%)	300 W Xe lamp λ > 400 nm	3	77.5
18	[39]	g-CN	Pd, Au, (0.5 wt%)	TEOA (10%)	300 W Xe lamp λ > 400 nm	6	4.5
19	[40]	g-CN (N-doped)	Ni (1.9 wt%)	TEOA (10%)	300 W Xe lamp λ > 420 nm	3	1.0
20	[41]	g-CN (porous)	Ni (10 wt%)	TEOA (10%)	500 W Xe lamp	-	0.2

Table S2. Photocatalytic H_2 evolution data of RuNPs@CNM/mpg-CN, MNP@mpg-CN, and other carbon nitride-supported nanocatalysts reported in the literature.

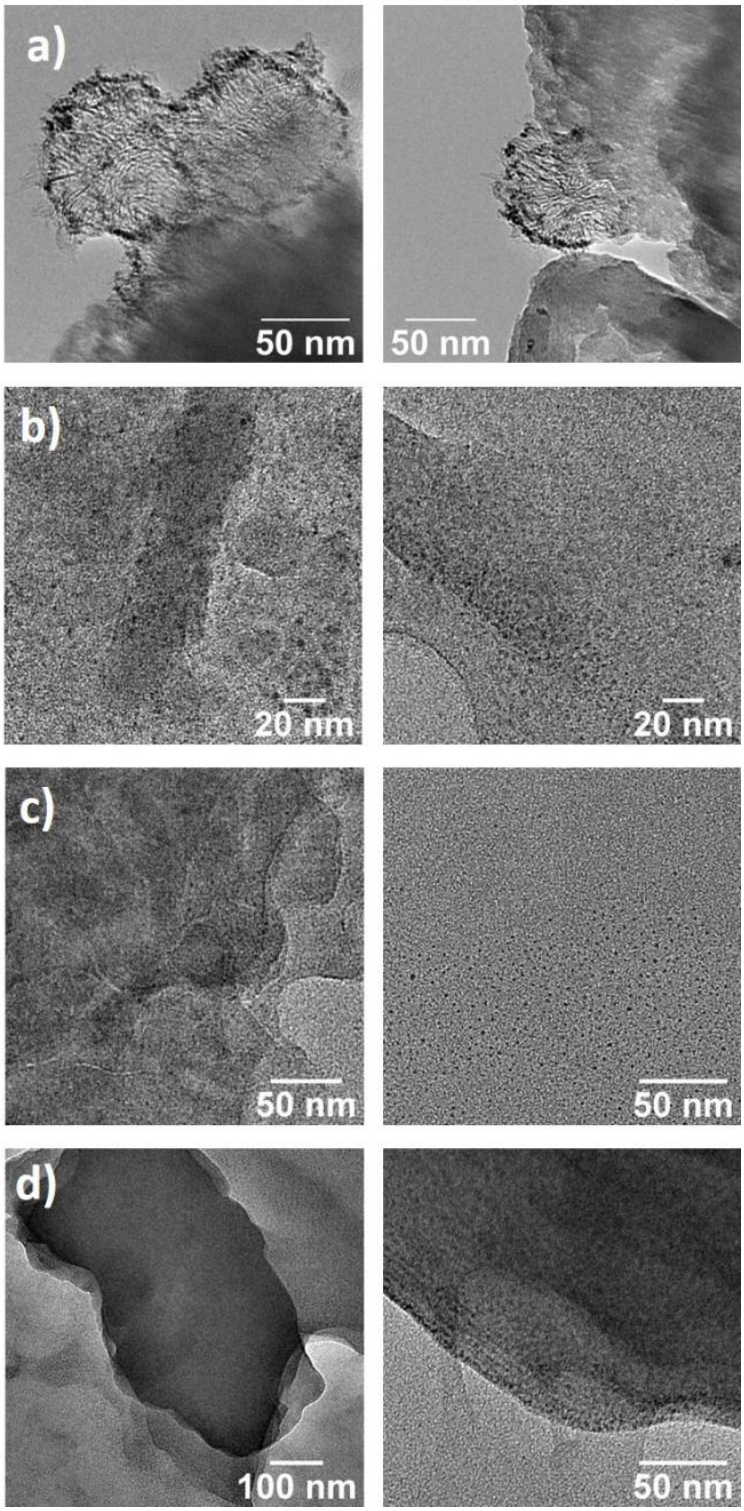

Figure S14. TEM images corresponding to a) **RuNPs@CNH/mpg-CN**, b) **RuNPs@CNT/mpg-CN**, c) **RuNPs@rGO/mpg-CN** and d) **RuNPs@GP/mpg-CN** after the photocatalytic studies in the standard reactor (24 h).

	τ_1	τ_2	τ_3	$<\tau>$
mpg-CN	0.75 (68%)	3.28 (28%)	14.92 (4%)	2.04
mpg-CN + TEOA	0.75 (69%)	3.27 (27%)	14.00 (4%)	1.97
PtNP@mpg-CN	0.72 (69%)	3.17 (27%)	13.78 (4%)	1.95
PtNP@mpg-CN + TEOA	0.67 (68%)	2.94 (28%)	13.30 (4%)	1.81
RuNP@mpg-CN	0.70 (66%)	3.14 (29%)	14.00 (5%)	2.02
RuNP@mpg-CN + TEOA	0.71 (68%)	3.17 (28%)	14.30 (4%)	1.94
in-RuPPNP@mpg-CN	0.74 (65%)	3.17 (30%)	13.26 (5%)	2.09
in-RuPPNP@mpg-CN + TEOA	0.75 (68%)	3.19 (28%)	14.23 (4%)	2.00
ex-RuPPNP@mpg-CN	0.62 (68%)	2.87 (28%)	13.22 (4%)	1.76
ex-RuPPNP@mpg-CN + TEOA	0.61 (69%)	2.77 (27%)	12.01 (4%)	1.67

Table S3. Compilation of the emission lifetimes of the different MNP@mpg-CN materials in water, obtained via TC-SPC (excitation at λ = 380 n, analysis at 470 nm).

5.7 References

[1] Burke, M. J. and Stephens, J. C. "Political power and renewable energy futures: A critical review" *Energy Res. Soc. Sci.*, **2018** (35) 78–93

[2] Lewis, N. S. "Research opportunities to advance solar energy utilization" *Science (80-.).*, **2016** (351)

[3] Qi, J.; Zhang, W. and Cao, R. "Solar-to-Hydrogen Energy Conversion Based on Water Splitting" *Adv. Energy Mater.*, **2018** (8) 1–16

[4] Shen, M.; Zhang, L.; Wang, M.; Tian, J.; Jin, X.; Guo, L.; Wang, L. and Shi, J. "Carbon-vacancy modified graphitic carbon nitride: enhanced CO 2 photocatalytic reduction performance and mechanism probing" *J. Mater. Chem. A*, **2019** (7) 1556–63

[5] Zheng, Y.; Liu, J.; Liang, J.; Jaroniec, M. and Qiao, S. Z. "Graphitic carbon nitride materials: Controllable synthesis and applications in fuel cells and photocatalysis" *Energy Environ. Sci.*, **2012** (5) 6717–31

[6] Zheng, Y.; Lin, L.; Wang, B. and Wang, X. "Graphitic Carbon Nitride Polymers toward Sustainable Photoredox Catalysis" *Angew. Chemie Int. Ed.*, **2015** (54) 12868–84

[7] Zhang, J.; Chen, Y. and Wang, X. "Two-dimensional covalent carbon nitride nanosheets: Synthesis, functionalization, and applications" *Energy Environ. Sci.*, **2015** (8) 3092–108

[8] Zou, X. and Zhang, Y. "Noble metal-free hydrogen evolution catalysts for water splitting" *Chem. Soc. Rev.*, **2015** (44) 5148–80

[9] Eftekhari, A. "Electrocatalysts for hydrogen evolution reaction" *Int. J. Hydrogen Energy*, **2017** (42) 11053–77

[10] Creus, J.; De Tovar, J.; Romero, N.; García-Antón, J.; Philippot, K.; Bofill, R. and Sala, X. "Ruthenium Nanoparticles for Catalytic Water Splitting" *ChemSusChem*, **2019** (12) 2493–514

[11] Fukuzumi, S. and Yamada, Y. "Catalytic activity of metal-based nanoparticles for photocatalytic water oxidation and reduction" *J. Mater. Chem.*, **2012** 24284–96

[12] Amiens, C.; Chaudret, B.; Ciuculescu-Pradines, D.; Collière, V.; Fajerwerg, K.; Fau, P.; Kahn, M.; Maisonnat, A.; Soulantica, K. and Philippot, K. "Organometallic approach for the synthesis of nanostructures" *New J. Chem.*, **2013** (37) 3374–401

[13] Amiens, C.; Ciuculescu-Pradines, D. and Philippot, K. "Controlled metal nanostructures: Fertile ground for coordination chemists" *Coord. Chem. Rev.*, **2016** (308) 409–32

[14] Muñoz, J.; Brennan, L. J.; Céspedes, F.; Gun'ko, Y. K. and Baeza, M. "Characterization protocol to improve the electroanalytical response of graphene-polymer nanocomposite sensors" *Compos. Sci. Technol.*, **2016** (125) 71–9

[15] Kailasam, K.; Epping, J. D.; Thomas, A.; Losse, S. and Junge, H. "Mesoporous carbon nitride-silica composites by a combined sol-gel/thermal condensation approach and their application as photocatalysts" *Energy Environ. Sci.*, **2011** (4) 4668–74

[16] Adorinni, S.; Cringoli, M. C.; Perathoner, S.; Fornasiero, P. and Marchesan, S. "Green approaches to carbon nanostructure-based biomaterials" *Appl. Sci.*, **2021** (11) 1–20

[17] Creus, J.; Drouet, S.; Suriñach, S.; Lecante, P.; Collière, V.; Poteau, R.; Philippot, K.; García-Antón, J. and Sala, X. "Ligand-Capped Ru Nanoparticles as Efficient Electrocatalyst for the Hydrogen Evolution Reaction" *ACS Catal.*, **2018** (8) 11094–102

[18] Deifallah, M.; McMillan, P. F. and Corà, F. "Electronic and structural properties of two-dimensional carbon nitride graphenes" *J. Phys. Chem. C*, **2008** (112) 5447–53

[19] Jorge, A. B.; Martin, D. J.; Dhanoa, M. T. S.; Rahman, A. S.; Makwana, N.; Tang, J.; Sella, A.; Corà, F.; Firth, S.; Darr, J. A. and McMillan, P. F. "H2 and O2 evolution from water half-splitting reactions by graphitic carbon nitride materials" *J. Phys. Chem. C*, **2013** (117) 7178–85

[20] Godin, R.; Wang, Y.; Zwijnenburg, M. A.; Tang, J. and Durrant, J. R. "Time-Resolved Spectroscopic Investigation of Charge Trapping in Carbon Nitrides Photocatalysts for Hydrogen Generation" *J. Am. Chem. Soc.*, **2017** (139) 5216–24

[21] Ye, C.; Li, J. X.; Li, Z. J.; Li, X. B.; Fan, X. B.; Zhang, L. P.; Chen, B.; Tung, C. H. and Wu, L. Z. "Enhanced Driving Force and Charge Separation Efficiency of Protonated g-C3N4 for Photocatalytic O2 Evolution" *ACS Catal.*, **2015** (5) 6973–9

[22] Cui, Y.; Ding, Z.; Liu, P.; Antonietti, M.; Fu, X. and Wang, X. "Metal-free activation of H2O2 by g-C 3N4 under visible light irradiation for the degradation of organic pollutants" *Phys. Chem. Chem. Phys.*, **2012** (14) 1455–62

[23] Kalyanasundaram, K.; Kiwi, J. and Graetzel, M. "Hydrogen Evolution from Water by Visible Light, a Homogeneous Three Component Test System for Redox Catalysis" *Helv. Chim. Acta*, **1978** (61) 2720–30
[24] Pellegrin, Y. and Odobel, F. "Les donneurs d'électron sacrificiels pour la production de combustible solaire" *Comptes Rendus Chim.*, **2017** (20) 283–95
[25] Walsh, J. J.; Jiang, C.; Tang, J. and Cowan, A. J. "Photochemical CO2 reduction using structurally controlled g-C3N4" *Phys. Chem. Chem. Phys.*, **2016** (18) 24825–9
[26] Kuriki, R.; Matsunaga, H.; Nakashima, T.; Wada, K.; Yamakata, A.; Ishitani, O. and Maeda, K. "Nature-Inspired, Highly Durable CO2 Reduction System Consisting of a Binuclear Ruthenium(II) Complex and an Organic Semiconductor Using Visible Light" *J. Am. Chem. Soc.*, **2016** (138) 5159–70
[27] Nelson, J. "Diffusion-limited recombination in polymer-fullerene blends and its influence on photocurrent collection" *Phys. Rev. B - Condens. Matter Mater. Phys.*, **2003** (67) 1–10
[28] Romero, N.; Guerra, R. B.; Gil, L.; Drouet, S.; Salmeron-Sànchez, I.; Illa, O.; Philippot, K.; Natali, M.; García-Antón, J. and Sala, X. "TiO2-mediated visible-light-driven hydrogen evolution by ligand-capped Ru nanoparticles" *Sustain. Energy Fuels*, **2020** (4) 4170–8
[29] Schwarze, M.; Schröder, M.; Stellmach, D.; Kailasam, K.; Thomas, A. and Schomäcker, R. "Entwicklung eines Reaktors zur standardisierten Quantifizierung der photokatalytischen Wasserstofferzeugung" *Chemie-Ingenieur-Technik*, **2013** (85) 500–7
[30] Zhang, J. H.; Wei, M. J.; Wei, Z. W.; Pan, M. and Su, C. Y. "Ultrathin Graphitic Carbon Nitride Nanosheets for Photocatalytic Hydrogen Evolution" *ACS Appl. Nano Mater.*, **2020** (3) 1010–8
[31] Cao, S.; Jiang, J.; Zhu, B. and Yu, J. "Shape-dependent photocatalytic hydrogen evolution activity over a Pt nanoparticle coupled g-C3N4 photocatalyst" *Phys. Chem. Chem. Phys.*, **2016** (18) 19457–63
[32] Li, X.; Bi, W.; Zhang, L.; Tao, S.; Chu, W.; Zhang, Q.; Luo, Y.; Wu, C. and Xie, Y. "Single-Atom Pt as Co-Catalyst for Enhanced Photocatalytic H2Evolution" *Adv. Mater.*, **2016** (28) 2427–31
[33] Li, X.; Masters, A. F. and Maschmeyer, T. "Photocatalytic hydrogen evolution from silica-templated polymeric graphitic carbon nitride-is the surface area important?" *ChemCatChem*, **2015** (7) 121–6
[34] Shiraishi, Y.; Kofuji, Y.; Kanazawa, S.; Sakamoto, H.; Ichikawa, S.; Tanaka, S. and Hirai, T. "Platinum nanoparticles strongly associated with graphitic carbon nitride as efficient co-catalysts for photocatalytic hydrogen evolution under visible light" *Chem. Commun.*, **2014** (50) 15255–8
[35] Xu, J.; Zhang, L.; Shi, R. and Zhu, Y. "Chemical exfoliation of graphitic carbon nitride for efficient heterogeneous photocatalysis" *J. Mater. Chem. A*, **2013** (1) 14766–72
[36] Hong, J.; Xia, X.; Wang, Y. and Xu, R. "Mesoporous carbon nitride with in situ sulfur doping for enhanced photocatalytic hydrogen evolution from water under visible light" *J. Mater. Chem.*, **2012** (22) 15006–12
[37] Han, C.; Lu, Y.; Zhang, J.; Ge, L.; Li, Y.; Chen, C.; Xin, Y.; Wu, L. and Fang, S. "Novel PtCo alloy nanoparticle decorated 2D g-C3N4 nanosheets with enhanced photocatalytic activity for H2 evolution under visible light irradiation" *J. Mater. Chem. A*, **2015** (3) 23274–82
[38] Liu, L.; Wu, X.; Wang, L.; Xu, X.; Gan, L.; Si, Z.; Li, J.; Zhang, Q.; Liu, Y.; Zhao, Y.; Ran, R.; Wu, X.; Weng, D. and Kang, F. "Atomic palladium on graphitic carbon nitride as a hydrogen evolution catalyst under visible light irradiation" *Commun. Chem.*, **2019** (2) 2–9
[39] Han, C.; Wu, L.; Ge, L.; Li, Y. and Zhao, Z. "AuPd bimetallic nanoparticles decorated graphitic carbon nitride for highly efficient reduction of water to H2 under visible light irradiation" *Carbon N. Y.*, **2015** (92) 31–40
[40] Deng, P.; Gan, M.; Zhang, X.; Li, Z. and Hou, Y. "Non-noble-metal Ni nanoparticles modified N-doped g-C3N4 for efficient photocatalytic hydrogen evolution" *Int. J. Hydrogen Energy*, **2019** (44) 30084–92
[41] Bi, L.; Meng, D.; Bu, Q.; Lin, Y.; Wang, D. and Xie, T. "Electron acceptor of Ni decorated porous carbon nitride applied in photocatalytic hydrogen production" *Phys. Chem. Chem. Phys.*, **2016** (18) 31534–41

Chapter VI

Carbon-supported Platinum Nanoparticles for Electrochemical Determination of Parabens

Metal-based hybrid materials have been prepared by decoration of four different carbon (nano)allotropes materials with Pt nanoparticles, through the organometallic method. The materials have been studied, after deposition on a glassy carbon electrode, as electrochemical sensing platforms towards methylparaben determination. The method has been further validated using a standard HPLC technique with commercial samples.

Table of contents

6.1 Abstract

Four different Pt-based carbon (nano)materials (CNM), typically employed for detection applications as they improve the analytical response when embedded into a sensing platform, have been prepared. The organometallic approach was used as an easy and reproducible method to directly deposit small, homogeneous and well-dispersed Pt NPs onto the surface of four carbon (nano)allotropes, namely 0D carbon nanohorns (CNH), 1D carbon nanotubes (CNT), 2D reduced graphene oxide (rGO) and 3D graphite (GP). After being characterized through TEM, XRD and TGA analyses, the obtained **Pt-NP@CNH**, **Pt-NP@CNT**, **Pt-NP@rGO** and **Pt-NP@GP** hybrid (nano)materials were tested for methylparaben (MeP) determination, a potential endocrine-disrupting chemical. **Pt-NP@CNT** material outperformed its CNH, rGO and GP-supported counterparts, yielding the lowest detection limit (5.00 ± 0.03 nM) and the best sensitivity ($4.5 \cdot 10^{11}$ $\mu A \cdot M^{-1}$) towards MeP detection and quantification, which are also among the best carbon-based system reported in the literature. Furthermore, the proposed electrochemical sensing platform has been validated, using commercial samples of shampoo, by a standard bench-top chromatographic technique (HPLC-UV), thus highlighting the suitability of **Pt-NP@CNT** material for sensing applications.

6.2 Introduction

In the previous chapters, we have focused on the design and characterization of nanoparticulate systems, and their use as electrocatalyst in the Hydrogen Evolution Reaction (HER) (Chapter III), or photocatalysts, in both CO_2 and H_2 reduction (Chapers IV and V, respectively). These studies have shown that the organometallic approach is a very versatile synthetic method, easily adaptable to the use of different metal precursors, stabilizing ligands or supports. In the present chapter we want to demonstrate also the versatility of these metal nanoparticles (NPs) prepared with this methodology, beyond the energetic purposes already addressed and which are the core of this work.

(Bio)sensors are one of the most widespread applications of nanomaterials [1]. Conducting nanomaterials are highly demanded since they lead to an increase on the analytical signal, related to the intrinsic electron transfer abilities of the transducer, when incorporated into electrochemical sensing frameworks [2–4]. More specifically, carbon (nano)materials (CNM), which consisted completely of sp^2-bonded graphitic carbon and whose dimensions could be confined in the nanoscale, are very attractive due to their enhanced electrochemical activity by their large surface to area ratio, biocompatibility, stability, electric conductivity and easy tunability [5–9]. 0D carbon nanohorns (CNH), 1D carbon nanotubes (CNT), 2D reduced graphene oxide (rGO) and 3D graphite (GP) are among the most employed carbon (nano)allotropes in electrochemical analysis and catalysis. Their performance can even be improved after the deposition of metal nanoparticles (NPs) [10–15]. Concretely, CNT in combination with platinum nanoparticles have yielded an enhanced sensitivity towards different (bio)analytes [16–18].

Thus, these systems could be very useful in the detection and quantification of substances, like the determination of potentially hazardous chemicals in commercial samples. One example would be parabens (PBs), a type of alkyl esters of *p*-hydroxybenzoic acid that, due to their superb antimicrobial activity, are specifically synthesized to use them as preservatives in food, or in pharmaceutical and cosmetic formulations [19,20]. However, it has been reported that PBs exposure could lead to a harmful effect in human's health, similar to estrogen-like endocrine-

disrupting chemicals, being also detected in human breast tumors [21–23]. That is why many institutions now regulate their utilization. For example, in cosmetic formulations, the maximum allowed concentration of a mixture of PBs is set at 0.8 wt.%, according to European Union Council regulations [24]. Therefore, there is a necessity to design a rapid, simple and sensitive analytical methodology to determine PBs at ultra-trace level. In this regard, these electrochemical sensing frameworks presents an ideal alternative to the traditional methods, such as high-performance liquid chromatography (HPLC). Some advantages include being easy-to-use and more cost-effective. Furthermore, time response is also lower, and this devices can be easily miniaturized, which facilitates their implementation in multiple potential applications [5,25–29].

In this Chapter, addressing the crescent concern about the presence of PBs in commercial products and also aquatic environments, different CNM-supported metal-based hybrid (nano)materials will be prepared and tested for methylparabene (MeP) determination. The hybrid systems will be synthesized by decorating the surface of four CNM (CNH, CNT, rGO and GP) with Pt NPs by means of the simple and reproducible organometallic approach [30]. Then their electrochemical performance towards MeP detection and quantification will be studied, and the method will be validated by means of HPLC-UV, comparing the results with those reported in the literature for analogue systems.

6.3 Experimental part

6.3.1 Reagents and methods

Synthesis of the carbon-based hybrid materials were carried out under inert conditions (Ar), either using a glovebox (MBRAUN Unilab) or standard Schlenk-line and Fisher-Porter vessel techniques. All glassware was pre-dried at 120 °C. All chemicals, except solvents, were used as purchased. Metal precursor [$Pt(dba)_3$] (dba = dibenzylideneacetone) was purchased from Strem Chemicals; Carbon Nanohorns (CNH) and flaked Graphite (GP), from Sigma-Aldrich; reduced graphene oxide (rGO) was synthesized from GP following a previous methodology reported by our collaborators [31]; single-walled carbon nonotubes (CNT) were purchased by SES ResearchM; hydrogen (H_2) gas from Abelló Linde; Tetrahydrofuran (THF) and hexane, used as solvents, were purchased from Scharlab, were dried, distilled and degassed via freeze–pump–thaw cycles.

6.3.2 Synthesis of Pt-NP@CNM

5 mg of CNM (either CNH, CNT, rGO o GP) were weighed and placed, together with 20 mL of THF, inside a Fisher-Porter bottle. The reactor was sonicated for 20 min. Afterwards, 57 mg of the metal precursor [$Pt(dba)_3$] were weighed inside the glovebox, and incorporated into the reactor. The Fisher-Porter bottle was then pressurized with 3 bars of H_2, keeping the mixture under vigorous magnetic stirring at room temperature (r.t.) for ca. 16 h. Once the reactor was depressurized, a sample for Transmission Electron Microscopy (TEM) analysis was prepared, and the yielded black power (corresponding to the **Pt-NP@CNH**, **Pt-NP@CNT**, **Pt-NP@rGO** and **Pt-NP@GP** hybrid materials, depending on the selected CNM) was washed with hexane, isolated by centrifugation, and dried under vacuum.

6.3.3 Characterization techniques

Transmission Electron Microscopy (TEM). TEM analyses were performed at the Servei de Microscòpia in the UAB, using a JEM-2011 unit with an acceleration voltage of 200 kV. TEM samples were prepared after drop-casting a single drop of the crude colloidal solution after synthesis, on the surface of a carbon-coated copper grid (400 mesh). Mean size and distribution of the Pt nanoparticles (NPs) contained

in each CNM were estimated after measuring ca. 200 NPs on the TEM micrographs, treated using the freeware Fiji-ImageJ.

X-ray Powder Diffraction (XRD). XRD patterns Pt-based hybrid (nano)materials were obtained at the Servei Difracció Raigs X (SDRX) at the UAB, using a PANalytical X'Pert Pro Powder Diffraction with Cu Kα radiation and PIXcel^{1D} detector.

Thermogravimetrid Analysis (TGA). TGA measurements were carried out in a STA 449 F1 Jupiter® (NETZSCH) unit. Samples were heated up to 1000 °C under air, at a 10 °C·min^{-1} rate.

6.3.4 Electrochemical characterization and MeP determination

All experiments involved in the electrochemical studies and method validation were performed by Dr. Jose Muñoz at the Institute of Materials Science of Barcelona (ICMAB-CSIC) (Barcelona, Spain).

Preparation of modified Glassy Carbon Electrodes (GCE). The bare GCE were initially polished using aluminium sandpaper. Modified electrodes were prepared by deposition of 5 µL of a dispersion containing 0.1 mg·mL^{-1} of the Pt-NP@CNM in ethanol. For the blank experiments, bare CNM were employed to prepare the modified GCE.

Electrochemical Measurements. Cyclic voltammetry (CV), Electrochemical Impedance Spectroscopy (EIS) and Differential Pulse Voltammetry (DPV) measurements were carried out using the conventional three-electrode cell set-up, in a potentiostat/galvanostat from Metrohm Autolab (PGSTAT128N), with NOVA 2.1.2 software. The modified GCE served as working electrode, whereas Ag/AgCl (sat. KCl) and a Pt wire were employed as reference and counter electrode, respectively. For CV and EIS characterization, a 0.1 M solution of KCl containing 10 mM $[Fe(CN)_6]^{3-/4-}$ served as redox marker. For DPV measurements, the selected electrolyte was a 20 mL phosphate-buffered saline (PBS) pH 7 solution.

Preparation and analysis of methylparabene (MeP). Calibration curves were constructed starting from a stock solution of 1.0 mM MeP in ethanol. Quantification was carried out using both DPV and HPLC-UV techniques. The analysis with the real

sample was carried out by mixing ca. 0.25 mg of a commercial shampoo with 10.0 mL of acetonitrile (ACN). After sonicating the mixture for 15 min, the sample was centrifuged for another 15 min at 300 rpm. An 10 µL aliquot of the supernatant was taken and analysed via HPLC to determine the MeP concentration in the commercial sample. Electroanalytical measurements were performed by DPV. Once the electrochemical set-up was prepared, progressive volume additions of the standard MeP solution were incorporated into the electrolyte. The repeatability of the method was ensured by repeating the measurements in triplicate. Detection limits (LOD) and recoveries are also presented, within a 95 % confidence interval.

High-performance liquid chromatography with ultraviolet detection (HPLC-UV) analysis. HPLC-UV measurements were performed in an equipment from Agilent (1260 Infinity II model), fitted with a Kromasil Eternity C18 column (250 x 4.6 mm ID, 5 µm particle). The measurements were performed isocratically, repeated per triplicate, with the temperature of the column set at 25 °C using a MeOH–ACN–H_2O (15:27:58 $v/v/v$) mobile flowing at 1 mL·min^{-1} (injection volume: 10 µL). Peaks were recorded at 256 nm, the maximum absorbance wavelength for the MeP.

6.4 Results and discussion

6.4.1 Synthesis and characterization of Pt-NP@CNM

The synthesis of the platinum nanoparticles (Pt NPs) supported on different carbon allotropes (nano)materials (CNM = 0D carbon nanohorns (CNH), 1D carbon nanotubes (CNT), 2D reduced graphene oxide (rGO) and 3D graphite (GP)) was performed following the organometallic approach (**Figure 1**) [30]. Essentially, the samples were prepared after decomposition of the organometallic precursor [$Pt(dba)_3$] in a Fisher-Porter reactor, which contained THF as solvent, and the selected carbonaceous support to stabilize the NPs, under 3 bar of H_2. After ca. 16 h of reaction at r.t., a TEM specimen was prepared, and the reaction mixture was cleaned with hexane, centrifuged and dried under vacuum, thus recovering a black powder, corresponding to **Pt-NP@CNH**, **Pt-NP@CNT**, **Pt-NP@rGO** or **Pt-NP@GP**.

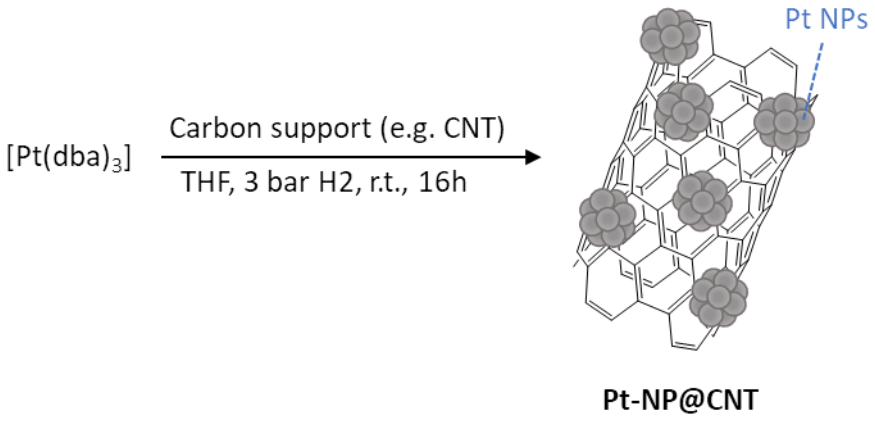

Figure 1. Schematic representation of the organometallic approach for the synthesis of **Pt-NP@CNM** (CNM = CNH, CNT, rGO or GP).

TEM micrographs confirmed the presence of small Pt NPs on the surface of each CNM (**Figure 2**). The estimated mean sizes were found in a range from 2.3-2.7 nm, suggesting that, under these conditions and at the selected Pt load, the nature of the carbon support is not a major differential factor in the stabilization of the Pt NPs, and that the organometallic method is a useful tool to obtain homogenous nanoparticulate systems.

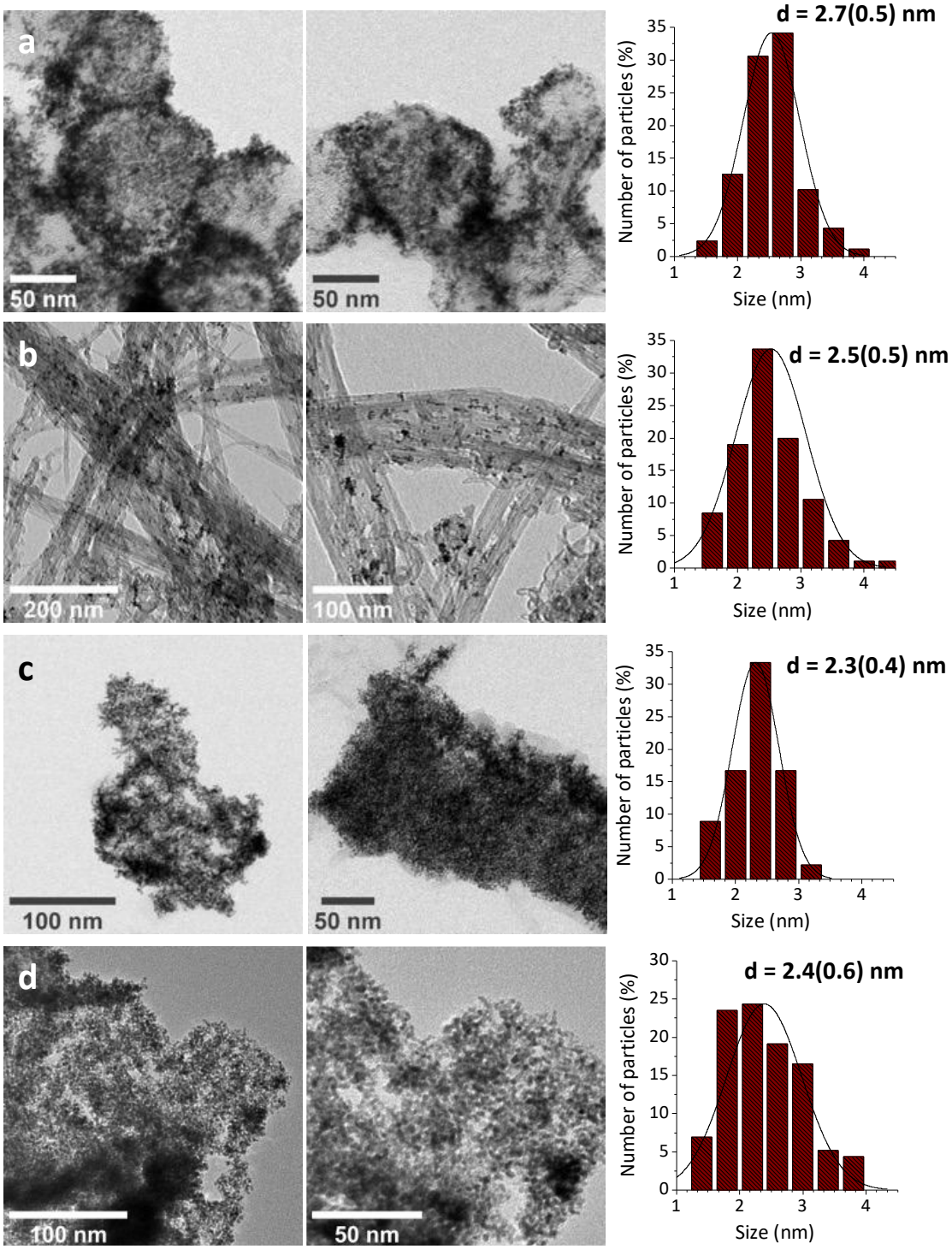

Figure 2. TEM micrographs (left) and size distribution histograms (right) of the as-synthesized a) **Pt-NP@CNH**, b) **Pt-NP@CNT**, c) **Pt-NP@rGO** and d) **Pt-NP@GP**.

Interestingly, in the micrographs of the **Pt-NP@CNT** a lower amount of Pt NPs covering the CNT surface could be observed, whereas the rest of the samples the CNM are almost full-covered. This behaviour was confirmed by TGA analyses, which estimated a 37.6 wt.% of Pt for **Pt-NP@CNT**, in contrast of the 57.5, 53.6 and 56.4

wt.% of Pt found for **Pt-NP@CNH**, **Pt-NP@rGO** and **Pt-NP@GP**, respectively (expected value, according to precursor concentration, of ca. 70 wt.%).

Powder X-ray diffraction analyses helped to study the phase purity and the crystal structure of the different samples (**Figure 3**). The diffractograms revealed the presence of the face-centered cubic (fcc) structure of Pt (characteristic (111), (200), (220), (311) and (222) reflections), thus demonstrating the formation of crystallite Pt NPs. A decrease in the intensity and a shift in the graphite (002) framework to lower 2θ values were also observed, attributed to the presence of amorphous graphite on the walls of the 0D to 2D carbon nanomaterials.

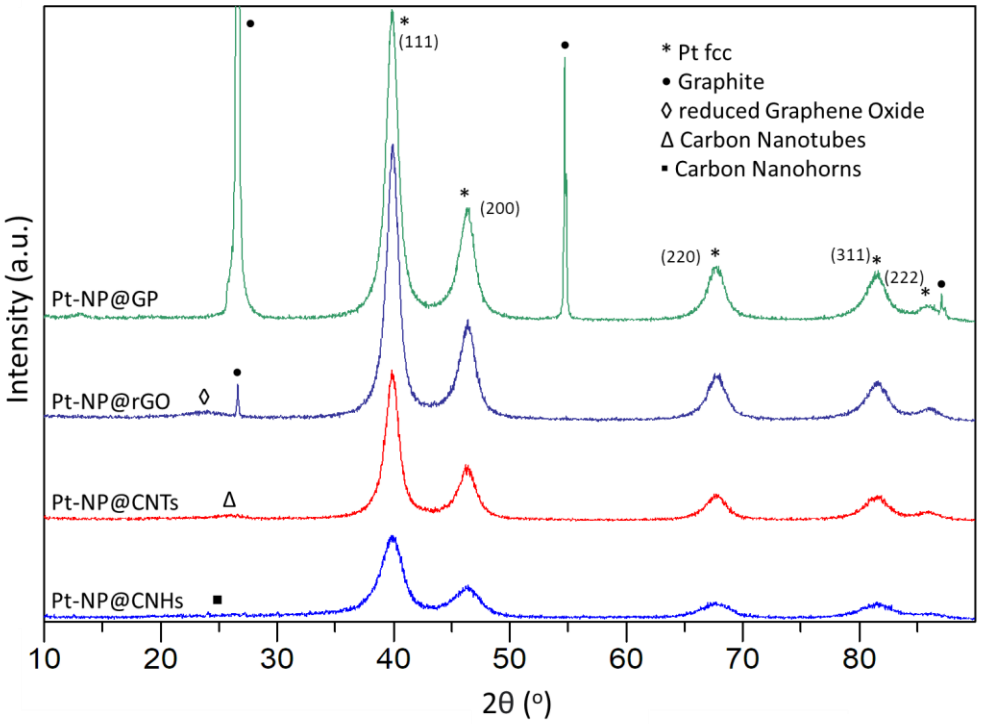

Figure 3. X-ray difractograms of the different **Pt-NP@CNM** (CNM = CNH, CNT, rGO or GP), highlighting the characteristic peaks of the fcc Pt structure, and a basal reflection (002) peak corresponding to bare flaked graphite, whose intensity decreased and position shifted in the corresponding 0D to 2D CNM, due to the presence of amorphous graphite in their structure.

6.4.2 Preliminary electrochemical studies

The electrochemical behaviour of the prepared **Pt-NP@CNM** was first studied through Cyclic Voltammetry (CV) and Electrochemical Impedance Spectroscopy (EIS) experiments, after being deposited on the surface of a glassy carbon electrode (GCE), adding $[Fe(CN)_6]^{3-/4-}$ into the electrochemical cell as redox probe. The experimental data was collected in **Figure 4**, using the results for Pt-NP@CNT/GCE as reference of the Pt-based CNM, and compared to the results of the clean GCE and the bare CNT.

Focusing on the CV experiments (**Figure 4(i)**), a peak current (I_p) increased and a peak-to peak (ΔE) separation were observed after the incorporation of the bare CNT to the GCE. These I_p and ΔE give information about the accessibility of the redox probe to be oxidized/reduced at the surface of the GCE, and about the reversibility of the redox couple, respectively [32]. This enhanced electrochemical performance of the CNT/GCE when compared to the bare GCE could be due to the intrinsic conducting properties of the CNM, and also related with an increased in the electrochemically active surface area, due to the higher roughness. This tendency, but more prominent, was also observed after the deposition of the Pt-loaded CNM onto the GCE.

Figure 4(ii) reflects the EIS results, with the Nyquist plots (imaginary vs. real impedance, Z_{imag} vs. Z_{real}) as an indicator of the electron transfer capabilities in the frequency domain. For the bare GCE, it was observed a semi-circular portion at higher frequencies, attributed to the charge transfer resistance (R_{CT}), which indicates the resistance at the electrode-solution interface [4]. In a similar trend to that of CV experiments, R_{CT} values decrease after depositing either bare CNT or **Pt-NP@CNT** in the GCE (1.58 and 1.21 kΩ, respectively, vs. 4.43 kΩ for the polished GCE), due to the conducting nature of the casted materials. For the rest of the **Pt-NP@CNM**, the charge transfer capabilities were also improved after casting either the bare CNM or the Pt-NP@CNM on the electrode, but the values were a bit higher this time with the latter materials, when compared with the bare CNM ones (**Figure 5**). This could be due to the huge amount of Pt NPs covering the surface of these CNM

observed in the TEM micrographs, unlike the Pt-NP@CNT sample, thus hindering the intrinsic electronic transfer potential of these carbon supports.

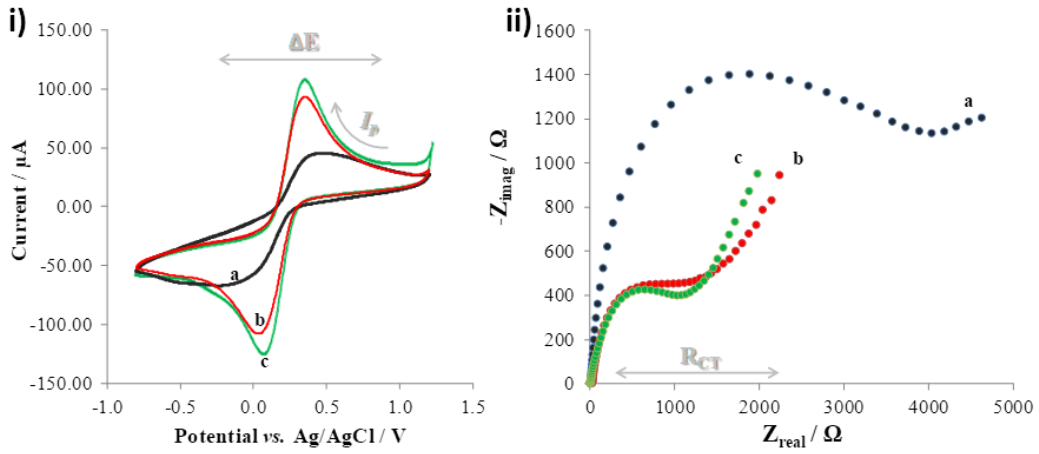

Figure 4. Electrochemical characterization of a) bare GCE (black); b) CNT/GCE (red); c) **Pt-NP@CNT/GCE** (green). i) CV experiments conducted at 50 mV·s^{-1}; ii) EIS experiments conducted at 0.1 Hz to 100 kHz of frequency range; bias potential: +150 mV; AC amplitude: 5 mV.

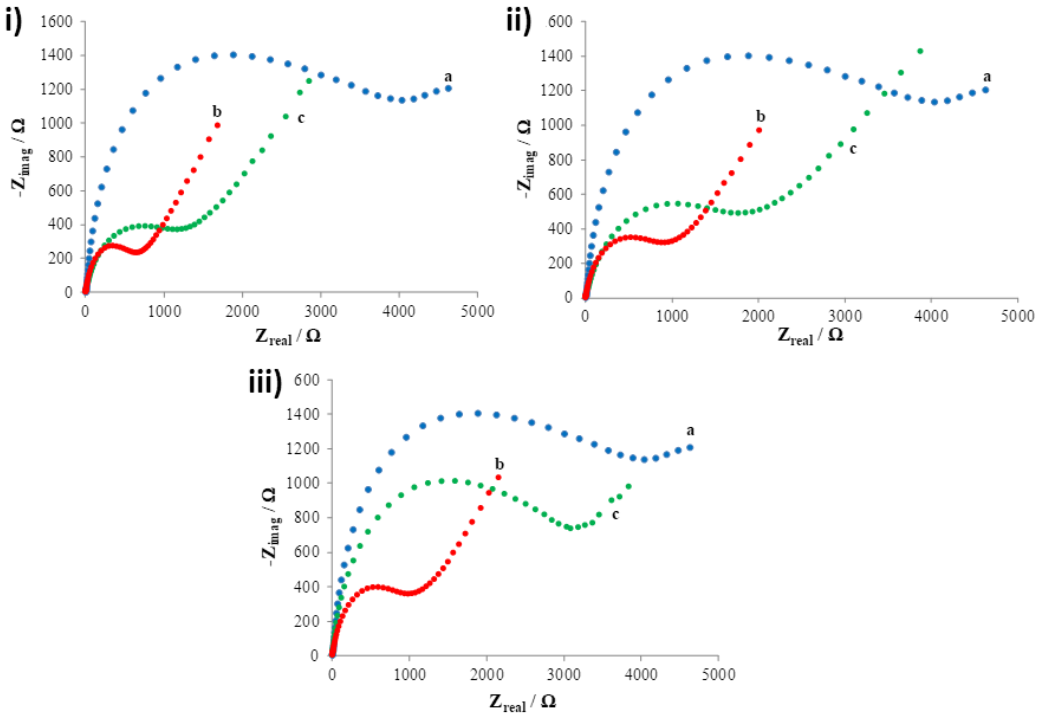

Figure 5. EIS experiments for the Pt-based i)CNH, ii)rGO or iii) GP stabilized systems, conducted at 0.1 Hz to 100 kHz of frequency range; bias potential: +150 mV; AC amplitude: 5 mV). In each graph, results for a) bare GCE (blue), b) CNM/GCE (red) and c) PtNP@CNM@/GCE (green) are shown.

After the initial electrochemical test, the next step was to study the electrochemical response of the **Pt–NP@CNM/GCE** electrodes in the oxidation of methylparabene (MeP) (20 nM), which was measured by Differential Pulse Voltammetry (DPV) (**Figure 6**). As suggested by the previous studies, only the **Pt–NP@CNT/GCE** delivered a well-defined anodic current response (I_{pa}) at 0.89 V vs Ag/AgCl towards MeP oxidation in the nM range. Once again, this behaviour was attributed to the partial covering of the CNT surface by the deposited Pt NPs. For the other materials, the combined effect of the catalytic properties of the Pt NPs and the enhanced electron transfer capability of the carbon material was lost due to the total coating of the CNM surface. This led to a poor electrocatalyst output of the **Pt-NP@CNH**, **Pt-NP@CNH** and **Pt-NP@CNH**, whose performance is comparable to the bare CNT (**Figure 6,** curve b', measured as blank).

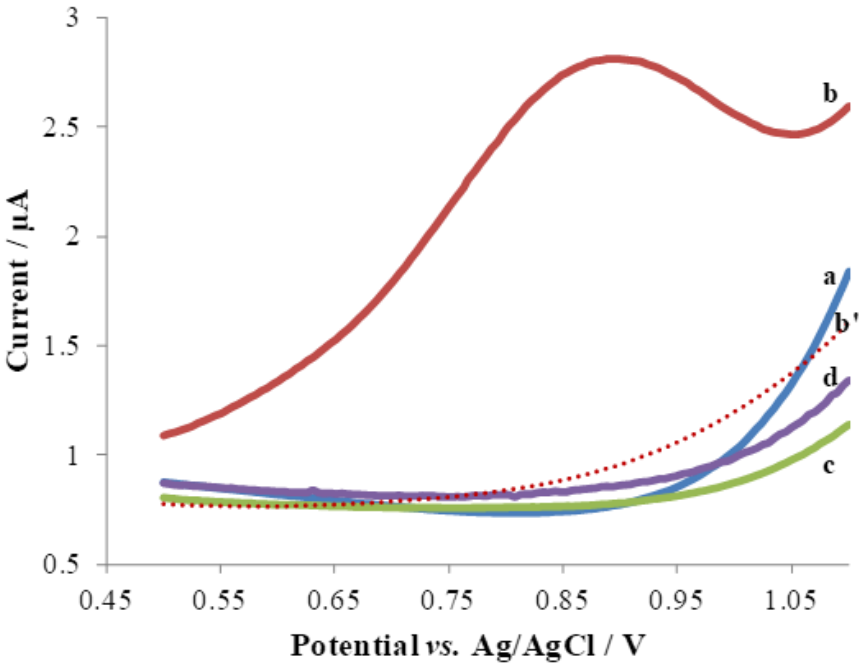

Figure 6. DPV response for a) **Pt-NP@CNH/GCE**, b) **Pt-NP@CNT/GCE,** b') CNT/GCE, as blank, c) **Pt-NP@rGO/GCE** and d) **Pt-NP@GP/GCE**, in presence of MeP (20 nM). Set-up: three electrode configuration in a 20 mL phosphate-buffered saline (PBS) pH 7 electrolyte solution. Scan rate : 50 $mV \cdot s^{-1}$.

This behaviour was confirmed by the calibration curves (**Figure 7**) elaborated, as described in experimental section, for MeP determination, with only **Pt–NP@CNT/GCE** yielding a relevant electrocatalytic signal towards MeP determination at ultra-trace levels. The average I_p values lead to an excellent linear correlation with the MeP concentration in the range of 5.0 to 30.0 nM, with a detection limit (LOD) as low as 5.00 ± 0.03 nM (**Figure 7B**). Blank experiments carried out using bare CNT proved the role that the presence of Pt NPs played on the MeP oxidation, with no signal detected at such low concentrations (**Figure 8**). Regarding the rest of the hybrid materials, their analytical responses fell in the µM linear range, with LODs of 30.0, 2.5 and 5.0 µM for the **Pt–NP@CNH**, **Pt–NP@rGO** and **Pt–NP@GP** samples, respectively. This was also an indicator that the synergistic effect between the CNM and the Pt NPs could be linked to the optimal load of Pt NPs in the CNM, which, according to the TGA measurements, must be lower than 50%.

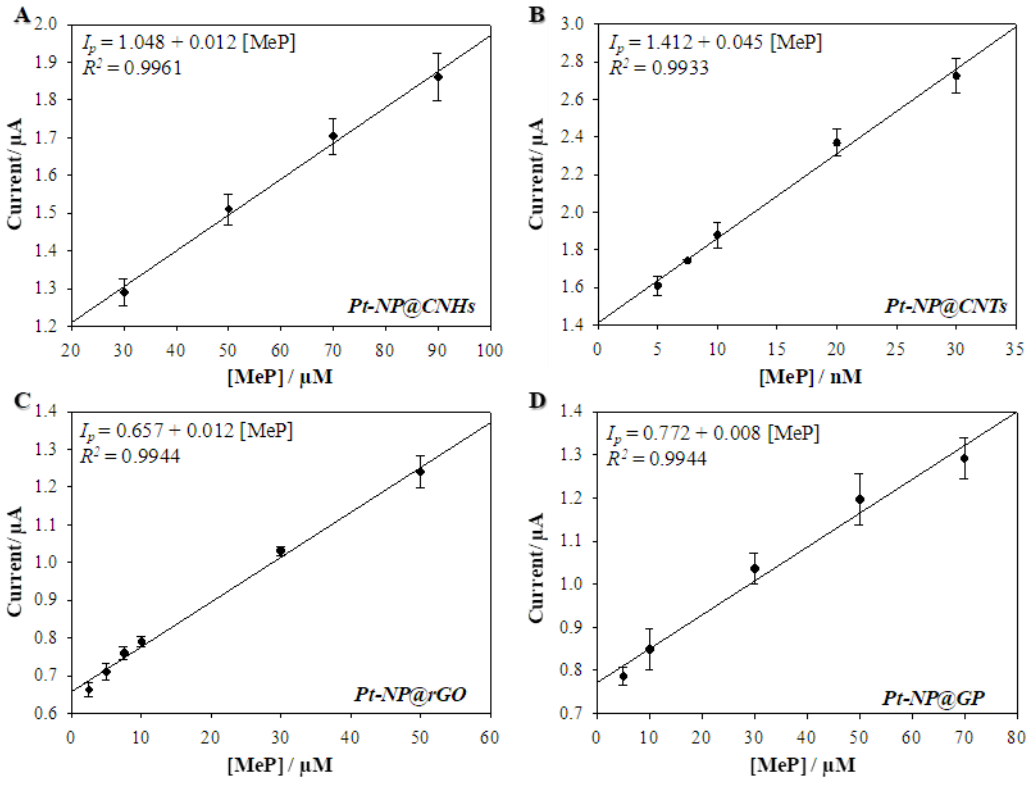

Figure 7. Calibration curves constructed from DPV analyses, for a) Pt-NP@CNH/GCE, b) Pt-NP@CNT/GCE, c) Pt-NP@rGO/GCE and d) Pt-NP@GP/GCE electrodes in the determination of MeP at different concentrations (A-B) in the nM-µM range.

The sensitivity of the **Pt–NP@CNT** material (corresponding to the slope of the calibration curve in **Figure 7**) was also outstanding, with a value of 0.045 $\mu A \cdot nM^{-1}$, ca. $4 \cdot 10^3$ – $6 \cdot 10^3$ times higher than the rest of the Pt-based samples. Therefore, Pt–NP@CNT was the selected hybrid material to carry out the studies with the real samples.

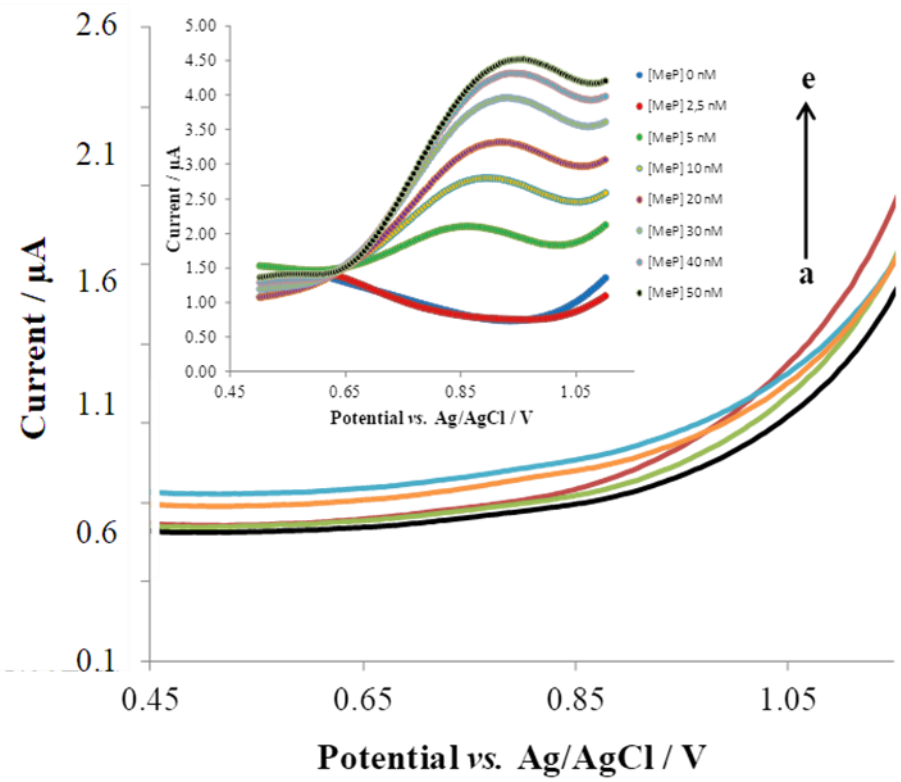

Figure 8. DPV response, using CNT/GCE, for MeP determination at different concentrations: a) 0 nM, b) 5 nM, c) 50 nM, d) 100 nM, e) 500 nM. Inset: Analogous analysis but using Pt-NP@CNT/GCE at different concentrations of MeP. Set-up: three electrode configuration in a 20 mL phosphate-buffered saline (PBS) pH 7 electrolyte solution. Scan rate : 50 $mV \cdot s^{-1}$.

6.4.3 MeP determination in real samples and method validation

The validation of the electrochemical sensing method here presented was carried out using high-performance liquid chromatography with ultraviolet detection (HPLC-UV). The overlapped chromatograms in **Figure 9** obtained at different [MeP], featured a peak area (*A*) increase while increasing the concentration of MeP. With these values, a calibration curve **(Figure 9,** inset) was constructed to quantify the [MeP] in a commercial shampoo sample. 10 µL of the real sample (after the pre-treatment described in the experimental section), were interpolated in the calibration curve, yielding a concentration value of 196.2 ± 0.4 µM.

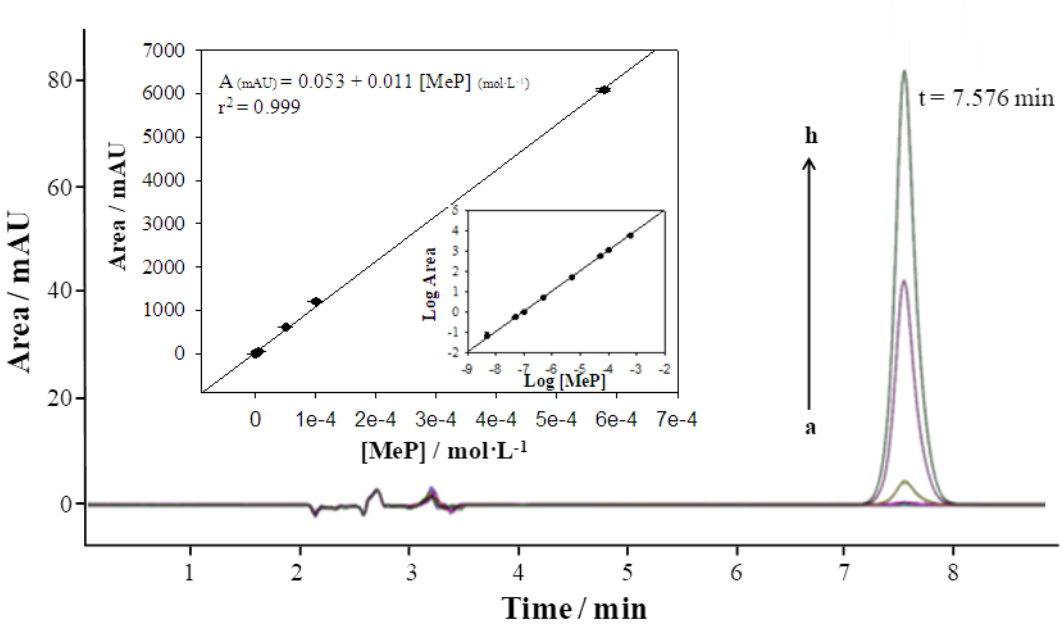

Figure 9. Overlapped HPLC-UV chromatograms for MeP quantification at different concentrations (a) $5.00 \cdot 10^{-9}$, b) $5.00 \cdot 10^{-8}$, c) $1.00 \cdot 10^{-7}$, d) $5.00 \cdot 10^{-7}$, e) $5.00 \cdot 10^{-6}$, f) $5.00 \cdot 10^{-5}$, g) $1.00 \cdot 10^{-4}$ and h) $5.75 \cdot 10^{-4}$ mol·L^{-1}). Inset: Calibration curve, calculated with the logarithmic range amplification.

Five different samples were prepared (SA-1 to SA-5), whose added and found values are displayed in **Table 1**. The concentration for SA-1 is due to a dilution of the MeP concentration initially present in the real shampoo sample. Then, for the preparation of the SA-2 to SA-5 samples, known standard [MeP] solutions were added to SA-1, which lead to notable recoveries using the HPLC technique. Same procedure was employed with the DPV technique for MeP determination, using **Pt-NP@CNT/GCE** as electrode, by incorporating into the electrochemical cell different concentrations of MeP (**Figure 10**). Good recoveries were also obtained with this

method (**Table 1**), thus indicating the selectivity of the method, as the matrix effect that could induce the use of the commercial shampoo did not interfere with the electrochemical sensing signal.

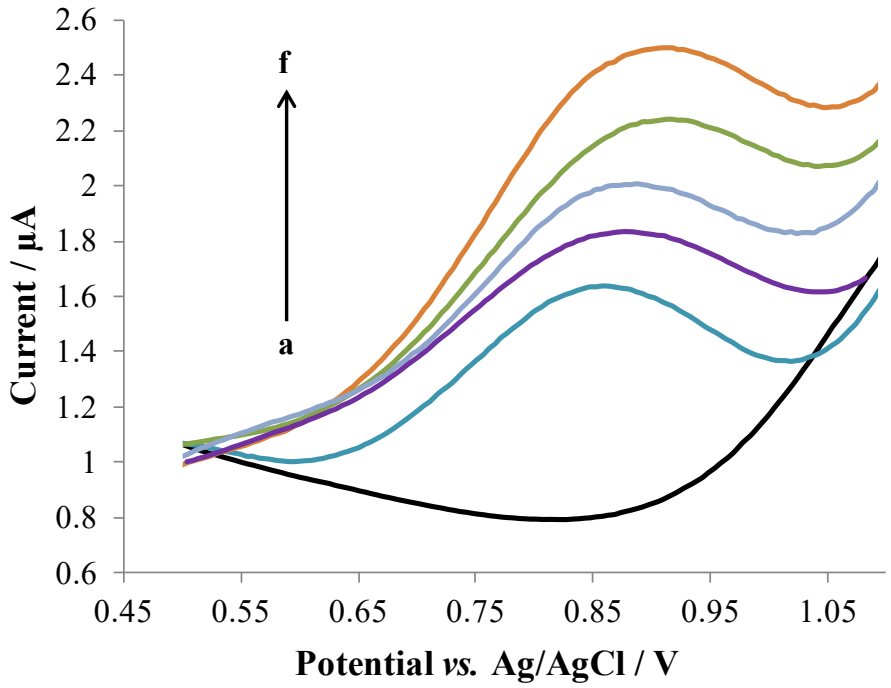

Figure 10. DPV response, using Pt-NP@CNT/GCE, for MeP determination in real samples. Analytical signals corresponding to a) background current, b) to f), SA-1 to SA-5 samples. Set-up: three electrode configuration in a 20 mL phosphate-buffered saline (PBS) pH 7 electrolyte solution. Scan rate : 50 $mV \cdot s^{-1}$.

No significant differences were observed after comparing the results from DPV or HPLC techniques (see $^{HPLC}C_{MeP}/^{DPV}C_{MeP}$ column in **Table 1**), for any of the SA-1 to SA-5 samples. Therefore, it is safe to conclude that the electrochemical sensor here presented is validated, being a suitable platform for the determination of MeP in real samples at ultra-low concentrations.

Sample	C_{MeP} (µM)	C_{MeP} added (µM)	$^{HPLC}C_{MeP}$ found (µM)	^{HPLC}Recovery (%)	$^{DPV}C_{MeP}$ found (µM)	^{DPV}Recovery (%)	$\frac{^{HPLC}C_{MeP}}{^{DPV}C_{MeP}}$
SA-1	4.79	0	4.99 ± 0.18	104.2	4.96 ± 0.02	103.5	1.01
SA-2		4.5	9.45 ± 0.27	101.7	9.49 ± 0.05	102.2	1.00
SA-3		9.0	13.94 ± 0.91	101.1	13.48 ± 0.08	97.8	1.03
SA-4		13.5	18.16 ± 0.28	99.3	18.39 ± 0.06	100.5	0.99
SA-5		18.0	22.75 ± 0.84	99.8	23.48 ± 0.11	103.0	0.97

Table 1. Statistical comparison of MeP quantification, using real shampoo samples, derived from DPV and HPLC-UV techniques.

Additionally, when compared with other carbon-based electrochemical electrodes reported in the literature (**Table 2**), **Pt-NP@CNT** delivered the best sensitivity and one of the lowest delivered the best sensitivity and one the lowest LOD towards MeP determination. This is even more significant considering that the synthetic method for the hybrid material preparation is more simple than other reported systems with comparable performance [33,34].

Carbon material	Detection Method	Linear Range (M)	LOD (M)	Sensitivity ($\mu A \cdot M^{-1}$)	HPLC validation	Ref.
Cellulose Nanocrystals-rGO/	DPV	$2.0 \cdot 10^{-4}$ – $9.0 \cdot 10^{-4}$	$1.0 \cdot 10$	2.79	No	[35]
CNTs-Nafion/GCE	LSV	$3.0 \cdot 10^{-6}$ – $1.0 \cdot 10^{-4}$	$1.0 \cdot 10^{-6}$	$3.38 \cdot 10^{4}$	No	[36]
CNTs-LB/GCE	LSV	$1.0 \cdot 10^{-6}$ – $8.0 \cdot 10^{-5}$	$4.0 \cdot 10^{-7}$	$3.9 \cdot 10^{5}$	No	[37]
Ru–NP@rGO/GCE	SWV	$5.0 \cdot 10^{-7}$ – $3.0 \cdot 10^{-6}$	$2.4 \cdot 10^{-7}$	$4.5 \cdot 10^{6}$	Yes	[15]
Au–NP@rGO/GCE	SWV	$3.0 \cdot 10^{-8}$ – $1.3 \cdot 10^{-6}$	$1.4 \cdot 10^{-8}$	$1.3 \cdot 10^{6}$	No	[14]
CNTs-Hb/CPE	DPV	$1.0 \cdot 10^{-7}$ – $1.3 \cdot 10^{-5}$	$2.5 \cdot 10^{-9}$	$2.5 \cdot 10^{8}$	No	[33]
(Co-Ni-Pd)NP-CNFs/GCE	SWV	$3.0 \cdot 10^{-9}$ – $3 \cdot 10^{-7}$	$1.2 \cdot 10^{-9}$	$1.3 \cdot 10^{11}$	No	[34]
Pt–NP@CNT/GCE	LSV	$5.0 \cdot 10^{-9}$ – $3 \cdot 10^{-8}$	$5.0 \cdot 10^{-9}$	$4.5 \cdot 10^{11}$	Yes	This work

Table 2. Comparison of sensing features for MeP determination of Pt-NP@CNT/GCE with other carbon-based electrochemical electrodes.

6.5 Conclusions

Pt NPs have been successfully deposited on the surface of four different carbon (nano)materials (CNM = CNH, CNT, rGO or GP), following the organometallic approach. Nanoparticles with similar sizes (ca. 2.5 nm) were obtained in all cases, well distributed all over the surface of the CNM, although in the case of the **Pt-NP@CNT** hybrid material, the surface was not fully covered. TGA analysis confirmed an inferior Pt load for the last.

The four hybrid systems were used for MeP determination, where **Pt-NP@CNT** yielded the best electrochemical responses in CV and DPV analyses, after deposition on a GCE. This **Pt-NP@CNT/GCE** electrochemical sensing platform delivered a low detection limit (5.00 ± 0.03 nM), and the best sensitivity found in literature for this type of systems ($4.5 \cdot 10^{11}$ $\mu A \cdot M^{-1}$). This behaviour was related to the Pt load, which was found optimal for the Pt-NP@CNT system. As the CNT were not fully covered by Pt NPs, the resulting hybrid material benefited from the synergic effect achieved by combination of the enhanced electrochemical abilities of the CNM and the catalytic properties of the metal nanoparticles. The electrochemical method was validated, using commercial samples, by means of the conventional HPLC-UV technique.

Furthermore, the electrochemical platform here presented, based on **Pt-NP@CNT**, involves a fast and simple preparation, is reproducible, highly sensitive and precise. Its effectiveness has also been tested with real samples. Thus, this cost-effective and easy to miniaturize system would be an ideal candidate for diverse applications in the pharmaceutical, biomedical or environmental fields.

6.6 References

[1] Abdel-Karim, R.; Reda, Y. and Abdel-Fattah, A. "Review—Nanostructured Materials-Based Nanosensors" *J. Electrochem. Soc.*, **2020** (167) 037554

[2] Maduraiveeran, G.; Sasidharan, M. and Ganesan, V. "Electrochemical sensor and biosensor platforms based on advanced nanomaterials for biological and biomedical applications" *Biosens. Bioelectron.*, **2018** (103) 113–29

[3] Maduraiveeran, G. and Jin, W. "Nanomaterials based electrochemical sensor and biosensor platforms for environmental applications" *Trends Environ. Anal. Chem.*, **2017** (13) 10–23

[4] Muñoz, J.; Montes, R. and Baeza, M. "Trends in electrochemical impedance spectroscopy involving nanocomposite transducers: Characterization, architecture surface and bio-sensing" *TrAC - Trends Anal. Chem.*, **2017** (97) 201–15

[5] Yang, C.; Denno, M. E.; Pyakurel, P. and Venton, B. J. "Recent trends in carbon nanomaterial-based electrochemical sensors for biomolecules: A review" *Anal. Chim. Acta*, **2015** (887) 17–37

[6] Adhikari, B. R.; Govindhan, M. and Chen, A. "Carbon nanomaterials based electrochemical sensors/biosensors for the sensitive detection of pharmaceutical and biological compounds" *Sensors (Switzerland)*, **2015** (15) 22490–508

[7] Wu, S.; He, Q.; Tan, C.; Wang, Y. and Zhang, H. "Graphene-based electrochemical sensors" *Small*, **2013** (9) 1160–72

[8] Muñoz, J.; Navarro-Senent, C.; Crivillers, N. and Mas-Torrent, M. "Study of carbon nanotube-rich impedimetric recognition electrode for ultra-low determination of polycyclic aromatic hydrocarbons in water" *Microchim. Acta*, **2018** (185) 1–21

[9] Zhang, Y. N.; Niu, Q.; Gu, X.; Yang, N. and Zhao, G. "Recent progress on carbon nanomaterials for the electrochemical detection and removal of environmental pollutants" *Nanoscale*, **2019** (11) 11992–2014

[10] Muñoz, J.; Bastos-Arrieta, J.; Muñoz, M.; Muraviev, D.; Céspedes, F. and Baeza, M. "Simple green routes for the customized preparation of sensitive carbon nanotubes/epoxy nanocomposite electrodes with functional metal nanoparticles" *RSC Adv.*, **2014** (4) 44517–24

[11] Gan, T.; Li, J.; Li, H.; Liu, Y. and Xu, Z. "Synthesis of Au nanorod-embedded and graphene oxide-wrapped microporous ZIF-8 with high electrocatalytic activity for the sensing of pesticides" *Nanoscale*, **2019** (11) 7839–49

[12] Muñoz, J.; Bastos-Arrieta, J.; Muñoz, M.; Muraviev, D.; Céspedes, F. and Baeza, M. "CdS quantum dots as a scattering nanomaterial of carbon nanotubes in polymeric nanocomposite sensors for microelectrode array behavior" *J. Mater. Sci.*, **2016** (51) 1610–9

[13] Wang, Y.; Ward, K. R.; Laborda, E.; Salter, C.; Crossley, A.; Jacobs, R. M. J. and Compton, R. G. "A joint experimental and computational search for authentic nano-electrocatalytic effects: Electrooxidation of nitrite and L-ascorbate on gold nanoparticle-modified glassy carbon electrodes" *Small*, **2013** (9) 478–86

[14] Piovesan, J. V.; Santana, E. R. and Spinelli, A. "Reduced graphene oxide/gold nanoparticles nanocomposite-modified glassy carbon electrode for determination of endocrine disruptor methylparaben" *J. Electroanal. Chem.*, **2018** (813) 163–70

[15] Mendonça, C. D.; Prado, T. M.; Cincotto, F. H.; Verbinnen, R. T. and Machado, S. A. S. "Methylparaben quantification via electrochemical sensor based on reduced graphene oxide decorated with ruthenium nanoparticles" *Sensors Actuators, B Chem.*, **2017** (251) 739–45

[16] Yang, M.; Yang, Y.; Liu, Y.; Shen, G. and Yu, R. "Platinum nanoparticles-doped sol-gel/carbon nanotubes composite electrochemical sensors and biosensors" *Biosens. Bioelectron.*, **2006** (21) 1125–31

[17] Baghayeri, M.; Beitollahi, H.; Akbari, A. and Farhadi, S. "Highly Sensitive Nanostructured Electrochemical Sensor Based on Carbon Nanotubes-Pt Nanoparticles Paste Electrode for Simultaneous Determination of Levodopa and Tyramine" *Russ. J. Electrochem.*, **2018** (54) 292–301

[18] Wildgoose, G. G.; Banks, C. E. and Compton, R. G. "Metal nanoparticles and related materials supported on Carbon nanotubes: Methods and applications" *Small*, **2006** (2) 182–93

[19] Azzouz, A.; Kailasa, S. K.; Kumar, P.; Ballesteros, E. and Kim, K. H. "Advances in functional nanomaterial-based electrochemical techniques for screening of endocrine disrupting chemicals in various sample matrices" *TrAC - Trends Anal. Chem.*, **2019** (113) 256–79

[20] Domínguez, J. R.; Muñoz-Peña, M. J.; González, T.; Palo, P. and Cuerda-Correa, E. M. "Parabens abatement from surface waters by electrochemical advanced oxidation with boron doped diamond anodes" *Environ. Sci. Pollut. Res.*, **2016** (23) 20315–30

[21] Li, W.; Shi, Y.; Gao, L.; Liu, J. and Cai, Y. "Occurrence, fate and risk assessment of parabens and their chlorinated derivatives in an advanced wastewater treatment plant" *J. Hazard. Mater.*, **2015** (300) 29–38

[22] Darbre, P. D.; Aljarrah, A.; Miller, W. R.; Coldham, N. G.; Sauer, M. J. and Pope, G. S. "Concentrations of Parabens in human breast tumours" *J. Appl. Toxicol.*, **2004** (24) 5–13

[23] Molins-Delgado, D.; Díaz-Cruz, M. S. and Barceló, D. "Ecological risk assessment associated to the removal of endocrine-disrupting parabens and benzophenone-4 in wastewater treatment" *J. Hazard. Mater.*, **2016** (310) 143–51

[24] Couteau, C. and Coiffard, L. "Regulation no 1223/2009 on cosmetic products" *Nouv. Dermatologiques*, **2010** (29)

[25] Shen, H. Y.; Jiang, H. L.; Mao, H. L.; Pan, G.; Zhou, L. and Cao, Y. F. "Simultaneous determination of seven phthalates and four parabens in cosmetic products using HPLC-DAD and GC-MS methods" *J. Sep. Sci.*, **2007** (30) 48–54

[26] Shanmugam, G.; Ramaswamy, B. R.; Radhakrishnan, V. and Tao, H. "GC-MS method for the determination of paraben preservatives in the human breast cancerous tissue" *Microchem. J.*, **2010** (96) 391–6

[27] Ocaña-González, J. A.; Villar-Navarro, M.; Ramos-Payán, M.; Fernández-Torres, R. and Bello-López, M. A. "New developments in the extraction and determination of parabens in cosmetics and environmental samples. A review" *Anal. Chim. Acta*, **2015** (858) 1–15

[28] Hamzah, H. H.; Shafiee, S. A.; Abdalla, A. and Patel, B. A. "3D printable conductive materials for the fabrication of electrochemical sensors: A mini review" *Electrochem. commun.*, **2018** (96) 27–31

[29] Muñoz, J. and Baeza, M. "Customized Bio-functionalization of Nanocomposite Carbon Paste Electrodes for Electrochemical Sensing: A Mini Review" *Electroanalysis*, **2017** (29) 1660–9

[30] Amiens, C.; Chaudret, B.; Ciuculescu-Pradines, D.; Collière, V.; Fajerwerg, K.; Fau, P.; Kahn, M.; Maisonnat, A.; Soulantica, K. and Philippot, K. "Organometallic approach for the synthesis of nanostructures" *New J. Chem.*, **2013** (37) 3374–401

[31] Muñoz, J.; Brennan, L. J.; Céspedes, F.; Gun'ko, Y. K. and Baeza, M. "Characterization protocol to improve the electroanalytical response of graphene-polymer nanocomposite sensors" *Compos. Sci. Technol.*, **2016** (125) 71–9

[32] Elgrishi, N.; Rountree, K. J.; McCarthy, B. D.; Rountree, E. S.; Eisenhart, T. T. and Dempsey, J. L. "A Practical Beginner's Guide to Cyclic Voltammetry" *J. Chem. Educ.*, **2018** (95) 197–206

[33] Hajian, A.; Ghodsi, J.; Afraz, A.; Yurchenko, O. and Urban, G. "Nanomolar detection of methylparaben by a cost-effective hemoglobin-based biosensor" *Mater. Sci. Eng. C*, **2016** (69) 122–7

[34] Baytak, A. K.; Duzmen, S.; Teker, T. and Aslanoglu, M. "Voltammetric determination of methylparaben and its DNA interaction using a novel platform based on carbon nanofibers and cobalt-nickel-palladium nanoparticles" *Sensors Actuators, B Chem.*, **2017** (239) 330–7

[35] Wan Khalid, W. E. F.; Mat Arip, M. N.; Jasmani, L. and Lee, Y. H. "A New Sensor for Methyl Paraben Using an Electrode Made of a Cellulose Nanocrystal-Reduced Graphene Oxide Nanocomposite." *Sensors (Basel).*, **2019** (19)

[36] Luo, P.; Liu, J.; Li, Y.; Miao, Y. and Ye, B. "Voltammetric Determination of Methylparaban in Cosmetics Using a Multi-Wall Carbon Nanotube/Nafion Composite Modified Glassy Carbon Electrode" *Anal. Lett. - ANAL LETT*, **2012** (45)

[37] Wang, L.; Li, Y.; Li, G. and Ye, B. "A new strategy for enhancing electrochemical sensing from MWCNTs modified electrode with Langmuir-Blodgett film and used in determination of methylparaben" *Sensors Actuators, B Chem.*, **2015** (211) 332–8

Chapter VII

Conclusions

Considering the objectives first exposed, and after discussing the obtained results towards the accomplishment of these goals, this chapter summarize the outputs and reflections of this PhD thesis.

1.1. General conclusions

- ✓ The synthesis and characterization of different metal-based (Ru or Pt) nanoparticle systems have been presented, together with their evaluation as electrocatalyst in the hydrogen evolution reaction (HER), or photocatalyst for both HER and CO_2 reduction.
- ✓ Complementarily, some of these systems have been evaluated for electrochemical determination and quantification of methylparabens (MeP).
- ✓ In all cases, the preparation has been carried out using the organometallic approach, which has proved to be a powerful technique for the preparation of small, well-dispersed and well-stabilized metal nanoparticles (NPs), with a controlled surface environment, key in the catalytic purposes of these nanoparticles.
- ✓ The physical and chemical properties of nanoparticles have been studied through diverse characterization techniques, such as TEM, SEM, EDX, XPS, ICP-OES or TGA.

  Characterization of the materials, not only as-synthesized but also after catalysis, have helped to correlate their different catalytic output with their physical and chemical features, thus highlighting the potential of the organometallic approach to design nanocatalysts, starting from different metal precursors, organic ligands or carbon supports as stabilizers, to fine tune their catalytic properties.

1.2. Chapter III

- ✓ Ru NPs stabilized by pyridine-derived ligands, namely 2-phenylpyridine (**2PP**) and 4'-(4-methylphenyl)-2,2':6',2"-terpyridine (**MPT**), have been prepared.
- ✓ Different ligand-to-metal ratios were explored in the synthesis, demonstrating that the nature of the ligand is a key parameter in the stabilization of the NPs. **MPT**, with three N-coordination sites per molecule, had more impact in the size of the NPs when changing L/M ratio than the **2PP**, with just one N-coordination site per molecule. Thus, in a range of 0.05

to 0.5 molar equivalents of **MPT**, the size of the NPs was drastically reduced from 1.4 to 0.6 nm, while for the **2PP** ligand, the size only decreased from 1.8 to 1.5 nm in a similar concentration range.

- ✓ Optimization of L/M ratio led to two ligand-capped (either **MPT** or **2PP with 0.05 and 0.2 ligand to metal molar ratio, respectively**) Ru NPs system with distinct morphological properties and surface environment, and high Ru content (ca. 85 wt.%) which, after deposition onto a glassy carbon electrode, delivered different catalytic activities towards the HER and, in both cases, with high stability (up to 12 h) in a wide pH range, superior to the state-of-the-art Pt.
- ✓ In acidic medium, an activation of the systems was observed by applying a reductive potential, which later was linked to the reduction of the passivation RuO_2 layer (after air exposure of the as-synthesized Ru NPs), thus recovering the Ru^0 species, more active under these conditions. After this activation, **RuMPT** NPs delivered an overpotential of 93 mV at a current density of j = -10 mA·cm^{-2}, higher than the overpotential of the activated **Ru2PP** system (30 mV) at the same current density. This improved electrocatalytic response of the **Ru2PP** system was supported by Cu underpotential deposition (UPD) analyses, which estimated a higher number of actives sites in the latter NPs system. Additionally, a larger number of hydrides were determined on the surface of the as-synthetized **Ru2PP** (1.0 H/$Ru_{surface}$ vs. 0.7 H/$Ru_{surface}$ for **RuMPT**), which could have an effect facilitating the HER mechanism on the surface of the NPs.
- ✓ Differences observed, in terms of catalytic activity and stabilization, in both **MPT** or **2PP**-stabilized Ru NPs could also be related with the different coordination modes of each ligand. However, DFT calculations (currently in progress) will be required to better understand these coordination modes, and how they affect the catalytic performance of these systems.
- ✓ These results, together with previously reported studies, point to pyridine derivative ligands as a good alternative to stabilize Ru NPs, as the features of the latter could be easily changed by using different ligands, being a simple way to modulate their catalytic behaviour in HER.

1.3. Chapter IV

- ✓ Pt NPs supported on mesoporous graphitic carbon nitride (mpg-CN) have been prepared, using a higher (**Pt-NPs@mpg-CN(L)**) and a lower **(Pt-NPs@mpg-CN(L)**) metal concentration. Both samples have been tested as photocatalyst in the CO_2 reduction.
- ✓ Both Pt-based systems displayed similar sizes of NPs (ca. 2.5 nm) and a good dispersion all over the mpg-CN semiconductor material, thus indicating that the selected metal loads were not determining factors in the synthesis.
- ✓ The importance of the co-catalyst (Pt NPs) in the CO_2 reduction was revealed through photophysical characterization, showing that the presence of the metal NPs induced electron transfer from the semiconductor. This enhancement was even more prominent when increasing the Pt load, thus facilitating the availability of these electrons towards the reduction of CO_2, instead of losing them in electron-hole recombination processes.
- ✓ Photophysical results has been backed by the photocatalytic experiments, with the Pt-loaded samples yielding higher conversion and selectivity towards methanol and methane, more suitable for use as fuels, compared with the non-loaded mpg-CN, under both UV and visible irradiation. Thus, the bare mpg-CN delivered high selectivity towards CO (50% and 80% under UV and visible light, respectively), but after Pt loading these values decreased below 10% in all cases. Lower CO_2 conversions were also observed for the bare mpg-CN under UV (20 $\mu mol \cdot g_{cat}^{-1}$) and visible light (10 $\mu mol \cdot g_{cat}^{-1}$) irradiation. This conversion values increased after Pt loading up to 90 $\mu mol \cdot g_{cat}^{-1}$ and 40 $\mu mol \cdot g_{cat}^{-1}$ under UV and visible light, respectively.
- ✓ Differences in the photocatalytic results were also observed when comparing the Pt-loaded materials, as stated in the specific conclusion for that chapter. Under UV irradiation both systems delivered higher selectivity towards methane (65% and 60% for **Pt-NPs@mpg-CN(L)** and **Pt-NPs@mpg-CN(H)** samples, respectively). In the case of **Pt-NPs@mpg-CN(H)**, this selectivity is almost maintained under visible irradiation (50% vs. 40% for methanol), but a shift was observed for **Pt-NPs@mpg-CN(L)** sample towards methanol (70% of selectivity vs. 25% for methane). This fact indicates that not only the

presence of a co-catalyst is enough to carry out the photoreduction of CO_2 efficiently, but also an optimization of the metal load to achieve high selectivity towards the desired carbon product, and the nature of the light source employed.

1.4. Chapter V

- ✓ mpg-CN has served as support for the preparation of different hybrid materials, based on Ru (with and without 4-phenylpyridine, 4PP, ligand) or Pt NPs, directly deposited on the semiconductor. Additionally, Ru NPs, previously deposited on four different carbon (nano)allotropes (CNM = CNH, CNT, rGO and GP) and later mixed with the carbon nitride material have been prepared. Neither the carbon supports nor the mpg-CN showed a great impact in the size of the NPs (sizes around 1.3-2.3 nm for the former materials, and 2.7-2.9 nm for the latter materials, without further stabilization ligand). However, the incorporation of 4PP ligand led to a decrease in the size of the Ru NPs, when compared to the non-ligand capped Ru NPs directly deposited on the mpg-CN (1.6 and 1.7 nm vs 2.9 nm).
- ✓ All of the hybrid systems were tested as photocatalysts in the HER. Optimization of the metal load was key in order to benefit from the catalytic properties of the metal co-catalyst, and the photosensitive features of the mpg-CN, in terms of hydrogen production or TON/TOF. Thus, using **RuNPs@CNH** hybrid material as the optimization sample, when loading ca. 26 mg of mpg-CN with 1.62 mg of the former material, a H_2 evolution rate of 105 $\mu mol \cdot h^{-1} \cdot g^{-1}$ was obtained, a value that increased up to 420 $\mu mol \cdot h^{-1} \cdot g^{-1}$ when the **RuNPs@CNH** loading was reduced to 0.41 mg. However, the best TON value was obtained after further reducing the metal loading, obtaining a TON value of 53 when incorporating just 0.16 mg of **RuNPs@CNH** to the mpg-CN.
- ✓ Pt NPs directly deposited on mpg-CN (**PtNP@mpg-CN**) displayed the best photocatalytic performance (870 $\mu mol \cdot h^{-1} \cdot g^{-1}$ of H_2 and TON value of 339, using the optimized metal loading).

- ✓ Among the Ru-based hybrid materials, both the pre-supported on CNM or the directly deposited onto mpg-CN, almost no significant photocatalytic differences were observed, considering the same metal loading. Even the 4PP-stabilized systems, whose enhanced catalytic output was studied in Chapter III, did not stand out. This behaviour was attributed to an important agglomeration of NPs observed through TEM, that could diminish their catalytic performance, matching that of larger, but more dispersed, nanoparticle systems.
- ✓ These observations were corroborated after photophysical experiments, which linked their photocatalytic performance with their electron transfer yields. **PtNP@mpg-CN** material was the most efficient towards electron transfer processes, in good accordance with the photocatalytic data, followed by **in-RuPPNP@mpg-CN** (sample prepared in the presence, at the same time, of 4PP and mpg-CN as stabilizers). The higher electron transfer yields observed for this sample could be due to the smaller size of NPs, when compared to the non-ligand-capped hybrid material (**RuPPNP@mpg-CN**), and better interaction and electronic connectivity with the mpg-CN, when compared with the **ex-RuPPNP@mpg-CN** material (NPs prepared with 4PP as stabilizer, and further impregnation in the mpg-CN). However, the aforementioned agglomeration observed for some of these systems likely affects their actual photocatalytic production.
- ✓ Beyond hydrogen production and TON/TOF values, which are comparable to most of the reported systems (based mainly in Pt), it is worth highlighting the fact that the hybrid materials were able to carry out the electron transfer process between the mpg-CN and the co-catalyst efficiently, without an electron mediator, which is rare in the literature concerning Ru-based systems.

1.5. Chapter VI

- ✓ Four different carbon (nano)allotropes (CNM = CNH, CNT, rGO and GP) have served as support for the preparation of Pt NPs-based hybrid materials, with no significant differences in the size of the NPs (from 2.3 to 2.7 nm), suggesting that the presence of each support is essential for nanoparticle dispersibility, but the differences between them are not a critical factor in their growth.
- ✓ When embedded into an electrochemical sensing platform, after immobilization in a glassy carbon electrode, the hybrid systems were tested for the detection and quantification of methylparabens (MeP). Pt-based material using CNT as support yielded the best results, in terms of limit of detection and sensibility (5.00 ± 0.03 nM and $4.5 \cdot 10^{11}$ $\mu A \cdot M^{-1}$, respectively). This was attributed to the higher surface area of carbon material exposed, when compared to the other fully metal-covered samples. Thus, the latter benefited of the synergic effect of the conducting carbon material and the catalytically active Pt NPs, which increased the analytical response. The response was also optimal when validating the method using real samples.
- ✓ These results, and those reported for analogous systems in previous chapters, serve to demonstrate that this type of hybrid materials can efficiently fulfil various purposes, thus making it worth investing in their design and development.

Chapter VIII

Annexes

In the present chapter, three different papers published during the development of this PhD thesis are collected, closely related with the previous PhD work. In the first published work [1] carbon nitride (mpg-CN)-supported Pt nanoparticles are prepared and tested as photocatalysts in the CO_2 reduction, delivering high activity and selectivity for this particular reaction. In the second paper [2], Ru nanoparticles are deposited on the surface of different carbon (nano)allotropes, and tested as co-catalyst of the mpg-CN photoactive material for photocatalytic Hydrogen Evolution Reaction (HER), being one of the few examples in the literature that uses Ru NPs efficiently for this process without requiring an electron mediator. The third paper [3] is focused on the deposition of Pt nanoparticles on the same set of carbon (nano)allotropes already mentioned, but tested for electrochemical determination of parabens, yielding low detection limits and high selectivity, which place them among the best carbon-based systems reported in the literature for electrochemical sensing applications.

[1] "A molecular approach to the synthesis of platinum-decorated mesoporous graphitic carbon nitride as selective CO_2 reduction photocatalyst" *Journal of CO_2 Utilization,* **2021**, *50*, 101574. DOI:10.1016/j.jcou.2021.101574

[2] "Ruthenium nanoparticles supported on carbon-based nanoallotropes as co-catalyst to enhance the photocatalytic hydrogen evolution activity of carbon nitride" R*enewable Energy*, **2021**, *168,* 668–75. DOI:10.1016/j.renene.2020.12.070

[3] "Synthesis of 0D to 3D hybrid-carbon nanomaterials carrying platinum (0) nanoparticles : Towards the electrocatalytic determination of methylparabens at ultra-trace levels" *Sensors & Actuators: B. Chemical*, **2020**, *305***,** 127467. DOI:10.1016/j.snb.2019.127467